

MOHANAKRISHNA R

HYPERSPECTRAL AND SPECTROPOLARIMETRIC
INSTRUMENTATION FOR THE SOLAR ATMOSPHERE

HYPERSPECTRAL AND SPECTROPOLARIMETRIC
INSTRUMENTATION FOR THE SOLAR ATMOSPHERE

MOHANAKRISHNA R



Department of Physics
Indian Institute of Science

DECLARATION

I hereby declare that the work reported in this thesis entitled "Hyperspectral and Spectropolarimetric Instrumentation for the Solar Atmosphere" is entirely original. I have carried out this work at the Space Astronomy Group, ISRO Satellite Centre (ISAC), Bangalore under the guidance of Dr. Sankarasubramanian. K, ISAC, Bangalore and Prof. Chanda J. Jog, Indian Institute of Science, Bangalore under the Joint Astronomy & Astrophysics Program. I further declare that this thesis has not formed the basis for award of any degree, diploma, fellowship, associateship or similar title of any University or Institution.

Bangalore, April 2018

Mohanakrishna
ganathan

Ran-

Mohanakrishna R

Dedicated to –
My Mom, Dad and Keerthi

*We have seen that computer programming is an art,
because it applies accumulated knowledge to the world,
because it requires skill and ingenuity, and especially
because it produces objects of beauty.*

— knuth:1974 [knuth:1974]

ACKNOWLEDGMENTS

I would like to take this opportunity to thank my mom for being very supportive and my dad for his advice and patience and belief in me. I would like to thank my research supervisor Dr. Sankar for constantly checking over me and helping me to develop from a normal individual to a researcher. His innovative ideas and approach to solve a problem have inspired me and in some ways motivated me. His immense belief in my abilities led me to unlock my true potential as a instrumentalist. I would also like to thank Dr. Shibu Mathew and Dr. Raja Bayanna for their support and suggestions during the course of my research. I would like to thank Space Astronomy Group (SAG-ISRO) and Indian Institute of Science (IISc) for giving me an opportunity to peruse my research.

My professional and personal life were filled with joy thanks to my lovely friends. There are way too many people to mention their names individually!. I would also like to thank all the people who helped me in a direct or indirect way to achieve my goals both on a professional and a personal level. Lastly my life would have been incomplete without my little sister and cousins. Thankyou for being so awesome you guys.

ABSTRACT

The Sun is the closest star whose surface can be resolved to a great detail. Understanding the working of Sun helps in understanding a large fraction of the stellar system as it falls under the spectral class G2V, which is the second most abundant type found in our galaxy. It is known that the layers in the solar atmosphere are coupled to each other. The coupling mechanism would reveal a lot about the dynamics of the Sun and the long-standing problem of coronal heating. Thus, the physical parameters of the solar atmosphere should be obtained simultaneously at different heights.

Spectroscopic and polarimetric measurements of spectral lines are used as diagnostics to estimate the physical parameters at a particular region in the solar atmosphere. Traditionally, there are two types of spectrograph used in solar astronomy to perform spectroscopy. They are - the Fabry-Pérot interferometer and Slit-Grating based spectrograph. Both these instruments have their share of advantages and disadvantages.

With telescopes getting bigger, the spatial resolution and light gathering power are increasing. Due to increased size in the telescope aperture, the instruments will be able to resolve small-scale structures of the Sun. But the small-scale structures in the Photosphere and Chromosphere are dynamic in nature and have short timescales. Thus, fast time cadence spectro-polarimetry is a very important capability for new instruments in solar observation. Coupling between the layers of the solar atmosphere can be studied with simultaneous observation at multiple wavelength regions (corresponding to a different height in the solar atmosphere). A traditional grating spectrograph is incapable of achieving high time cadence but can operate at multiple wavelength bands simultaneously. A Fabry-Pérot spectrographs is incapable of simultaneous wavelength measurement but has high time cadence of observation. This thesis aims at addressing the disadvantages of both the instruments and comes up with a solution for the same. An instrument for each type (i. e. Fabry-Pérot and Grating) is built and their capabilities are demonstrated through the data obtained from the engineering run. The slit and grating based spectrograph is extended to include polarimetry in order to measure the vector magnetic field of the solar atmosphere. Although the instruments are developed, and their capabilities are demonstrated for photospheric and chromospheric observations, they can be modified to observe the corona. But the corona is a million times fainter than the photosphere with weak fields of the order of tenths of Gauss (in contrast to the kilo Gauss fields on the photosphere). The polarime-

ters required to measure such field have to be sensitive. A case study of polarimetric accuracy needed to measure the corona polarization, and, the possible sources of noise affecting the signal, is under-taken.

CONTENTS

1	INTRODUCTION	1
1.1	The Sun a star	1
1.2	The formation of spectral lines	3
1.3	The Solar atmosphere	5
1.4	Magnetic field measurement	9
1.4.1	Stokes parameters	9
1.4.2	Zeeman effect	10
1.4.3	Radiative transfer equation for magnetic atmosphere	12
1.5	Motivation and Structure of this thesis	13
I SPECTROPOLARIMETRY		
2	MULTI-SLIT SPECTRO-POLARIMETER	19
2.1	Introduction	19
2.2	Spectrograph Design	24
2.2.1	Grating	25
2.2.2	Collimator and Imager	32
2.2.3	Dense Wavelength Division Multiplexing (DWDM) filter and multi-slit entrance aperture	35
2.2.4	Optics for the detector unit	43
2.3	Polarimeter unit for MSSP	44
2.3.1	Modulator	46
2.3.2	Analyzer	49
2.4	Characterization and calibration of MSSP	54
2.4.1	Spectral resolution and dispersion	57
2.4.2	Polarimeter calibration	59
2.5	Integrating MSSP to MAST	64
2.5.1	Imaging spectro-polarimeter	64
2.5.2	polarization calibration unit (<code>polcal</code>) and Telescope polarization	68
2.6	Data acquisition and analysis	77
2.6.1	Data Acquisition using a GUI	77
2.6.2	Data reduction procedure	79
2.7	Conclusion and future work	85
3	SPECTRO-POLARIMETRIC INVERSION	89
3.1	Introduction	89
3.2	Description of the instrument and data	90
3.2.1	SOLIS-VSM	90
3.2.2	Active region NOAA 12683	90
3.2.3	NICOLE - inversion code	92
3.2.4	Data reduction and input parameters to NICOLE	92
3.3	Results	93

3.3.1	Field values and comparison with standard results	93
3.3.2	Field strength and temperature	97
3.4	Conclusion	100
II SNAPSHOT SPECTROSCOPY		
4	SNAPSHOT SPECTRAL IMAGING	103
4.1	Introduction	103
4.2	Working principle	108
4.3	Optical design	110
4.4	Lenslet Array Spectroscope (LAS)	114
4.4.1	Experiment to validate relation between wavelength and angle of incidence	115
4.4.2	Pupil plane variation in wavelength	116
4.5	Data acquisition and analysis	119
4.6	Design enhancements and future work	125
4.7	Conclusion	132
III POLARIZATION CROSSTALK		
5	EVALUATION OF POLARIZATION CROSSTALK FOR CORONAL FIELD MEASUREMENTS	137
5.1	Introduction	137
5.2	Satellite AOCS - jitter and drift	141
5.3	Polarimeter design	143
5.4	Experimental verification and design enhancement	150
5.5	Conclusion	155
A	APPENDIX	159
BIBLIOGRAPHY		161

LIST OF FIGURES

Figure 1.1	HR diagram of stars.	2
Figure 1.2	Absorption coefficient for a line generated in an atmosphere which is at LTE	5
Figure 1.3	Variation in contribution function as a function of optical depth	6
Figure 1.4	Absorption line providing the field parameters of the atmosphere over a particular range of heights	7
Figure 1.5	The stratification of the solar atmosphere based on temperature, density and plasma β	8
Figure 1.6	Illustration of Zeeman effect and the polarized radiation produced by it	11
Figure 2.1	Solar spectra using grating spectrograph	20
Figure 2.2	Selective transmission of spectra from the spectrograph	21
Figure 2.3	Sample spectra from a grating.	22
Figure 2.4	Multiband spectra from the spectrograph	22
Figure 2.5	Single slit narrow band image of a spectra	22
Figure 2.6	Multiple slit sample of the spectra an example	23
Figure 2.7	A simple reflection grating spectrograph design	26
Figure 2.8	Grating working principle	27
Figure 2.9	Intensity fringe pattern produced from interference of 20 slits.	28
Figure 2.10	Interference pattern modulated by the single slit diffraction pattern	28
Figure 2.11	Blazed grating	31
Figure 2.12	Schematic layout of spectrograph in Littrow configuration	32
Figure 2.13	Schematic layout of the Collimator	33
Figure 2.14	Schematic of off-axis-parabolic mirror	35
Figure 2.15	Transmission window for glass core optical fiber used in optical communication	36
Figure 2.16	Prism as wavelength multiplexer	38
Figure 2.17	filter response function	38
Figure 2.18	Comparison of spectral transmission of DWDM filter and cavity filter for Fe I at 6302 Å	39
Figure 2.19	Conceptual diagram of multiple slit on the FOV	40
Figure 2.20	6 arcmin field drawn to scale with multi-slit on NOAA 12526	42

Figure 2.21	3 arcmin field drawn to scale with multislit on NOAA 12526	42
Figure 2.22	Schematic layout of the spectrograph section of MSSP with pick-off mirror and spectral mask	43
Figure 2.23	Working principle of LCVR	48
Figure 2.24	Schematic drawing of polarimeter unit used in MSSP	50
Figure 2.25	Dual beam analyzer schematic drawing for MSSP	51
Figure 2.26	Concept of spectral mask for dual beam polarimetry	52
Figure 2.27	Multi-slit spectra of Fe I line pair at 6302 taken from pco.2000	53
Figure 2.28	Optical layout of MSSP	55
Figure 2.29	Spot diagram of the chief ray at the 1 st image plane of MSSP for a 34 mm × 34 mm field	56
Figure 2.30	Spot diagram of the chief ray at the detector plane for MSSP	57
Figure 2.31	Fe I spectra obtained from calibration setup of MSSP	58
Figure 2.32	Laser profile fitted with a gaussian function to determine spectral dispersion	59
Figure 2.33	Schematic layout of the optical setup to characterize a polarization modulator	61
Figure 2.34	Front panel of the GUI designed to calibrate the modulator.	62
Figure 2.35	Plot of variation in retardance with voltage for the two LCVRs used in MSSP	62
Figure 2.36	Evaluation of the performance of calcite analyzer used in	63
Figure 2.37	Block diagram of instrument layout at MAST	65
Figure 2.38	Schematic layout of the scanning mechanism used to perform imaging spectropolarimetry for MSSP	66
Figure 2.39	USAF 19 resolution target used to test the imaging capabilities of MSSP	66
Figure 2.40	Raster scan of the resolution target placed at first image plane	67
Figure 2.41	Point spread function of two group 5 element 1 lines in USAF 19 resolution target.	67
Figure 2.42	Focus test along the slit for MSSP	68
Figure 2.43	Optical layout of MAST	71
Figure 2.44	MAST telescope structure consisting of the main frame and coud train to track an object in alt-azimuth plane	73

Figure 2.45	Simulation of polarization introduced by parabolic mirror for an unpolarized input beam	75
Figure 2.46	Simulation of polarization introduced by MAST off-axis parabolic mirror for an unpolarized input beam	76
Figure 2.47	A snapshot of the GUI developed to operate MSSP.	79
Figure 2.48	An example of correction for spectral curvature of the center slit of MSSP	81
Figure 2.49	Master flat image for NOAA 12653	81
Figure 2.50	Stokes data with polcal and telescope polarization correction	83
Figure 2.51	A plot of spectra obtained from MSSP and comparison with BASS solar atlas gives an estimate of stray light fraction	84
Figure 2.52	Vector magnetic field of NOAA 12653 obtained from NICOLE and recorded by MSSP	86
Figure 2.53	Concept of snapshot spectroscopy using a fiber bundle in MSSP	87
Figure 3.1	The synoptic image of sun recorded by SOLIS-VSM on 30 September 2017.	91
Figure 3.2	A Model atmosphere generated by fitting the observed spectra with a synthesized spectra for Fe-I line pair at 6302 Å. The observed and synthesized spectra of 4.242×4.242 arcmin ² field are shown in (a) and (b) respectively.	94
Figure 3.3	Comparison of the inverted field parameters with HMI's results	95
Figure 3.4	Chromospheric field strength	96
Figure 3.5	Comparison of inverted chromospheric field with PFSS	96
Figure 3.6	Comparison of photospheric and chromospheric field parameters	98
Figure 3.7	A map of the atmospheric temperature at various heights as obtained from the inverted model atmosphere	99
Figure 4.1	A hyper spectral data cube with the three axis representing two spatial dimension and one spectral dimension	104
Figure 4.2	A satellite imaging system used to illustration the necessity of fast hyper spectral imaging	105
Figure 4.3	Snapshot spectroscopic concepts used in stellar astronomy	107
Figure 4.4	Concept of parallel plate etalon	109

- Figure 4.5 Blue shift in transmitted wavelength for a ray incident at an angle with respect to the ray incident normally on the etalon 109
- Figure 4.6 Optical design for object pupil sample. 111
- Figure 4.7 Optical design for image pupil sample 113
- Figure 4.8 The experimental validation of variation in wavelength with angle of incidence for LAS 117
- Figure 4.9 Experimental results to validate the variation in wavelength along the pupil for LAS 118
- Figure 4.10 Conceptual diagram of etalon light re-circulation technique where reflected light is circulated back to the etalon at a different angle. The conceptual diagram presented here is borrowed from [113]. 120
- Figure 4.11 GUI to operate LAS. 121
- Figure 4.12 Illustration to determine the location of the starting wavelength 125
- Figure 4.13 Generation of master flat and determining the position of the lenslets using hough transform 126
- Figure 4.14 Absorption line feature sunspot NOAA12526 recorded using LAS 127
- Figure 4.15 Fe-I at 6301.5 Å absorption line obtained from a field point in a single snapshot 128
- Figure 4.16 Comparison of continuum intensity and velocity obtained by LAS with that of HMI 129
- Figure 4.17 Emission line feature recorded at 6562.8 Å and the light re-circulation technique 130
- Figure 4.18 Dynamic events obtained using sequence of snapshot images recorded by LAS 131
- Figure 4.19 Design enhancements for LAS to perform snapshot spectroscopy using a fixed etalon 132
- Figure 4.20 Conceptual diagram of using a spatial light modulator (SLM) to enhance LAS to perform snapshot spectropolarimetry 132
- Figure 5.1 Temperature stratification of the solar atmosphere with height. Nearly a 100 fold jump in temperature can be seen near 2500 km 138
- Figure 5.2 Corona viewed as a halo by occulting the photosphere 140
- Figure 5.3 The three axis of rotation along which a satellite is stabilized 141
- Figure 5.4 Powerspectra of the random motion of a star's image on the star-sensor of the satellite 142
- Figure 5.5 Nearly balanced modulation using a single crystal retarder 144

Figure 5.6	Uniform intensity sampling with farthest spacing between the samples	146
Figure 5.7	Uniform intensity sampling with the closest spacing between samples	147
Figure 5.8	Normalized efficiency of detecting a stokes parameter as a function of retardance	147
Figure 5.9	Normalized efficiency of detecting a stokes parameter with second window position	148
Figure 5.10	The crosstalk from linear to circular polarization is shown as a function of retardance.	149
Figure 5.11	Crosstalk of Q and U into V for second sampling window	150
Figure 5.12	Variation in source intensity for a typical quiet sun corona taken at Fe XIII 1.0746 μm line	152
Figure 5.13	Experimental setup to validate the ability of modulation matrix for EVELC	152
Figure 5.14	A simple GUI developed to test the modulation scheme generated for EVELC	153
Figure 5.15	Plot of residual stokes V signal for a Q input.	154
Figure 5.16	Design enhancement for EVELC polarimeter for higher polarization sensitivity	156
Figure A.1	Procedure followed to obtain field parameters of the solar atmosphere numerically. Image credits Yadav [132]. Concept borrowed from del Toro Iniesta and Ruiz Cobo [23]	159

LIST OF TABLES

Table 2.1	Wavelength order of operation MSSP	31
Table 2.2	Specifications for off-axis parabolic mirror used in MSSP	34
Table 2.3	Specifications of DWDM filter used for Fe I at 6302	37
Table 2.4	Specifications of Multi-slit used in	41
Table 2.5	CCD detector specifications used for the Fe I line pair at 6302	44
Table 2.6	Retardance values of LCVR for balanced modulation	49
Table 2.7	Specifications of dual beam analyzer used in MSSP	54
Table 2.8	Comparison of theoretical spectral performance and experimental value obtained for MSSP	59

Table 2.9	Configuration of Mirror system used in MAST	
	71	
Table 2.10	Field details for engineering run observation of an active region	80
Table 3.1	Spectral parameters for the data set taken from SOLIS on 30 th Sep 2017	92
Table 4.1	Configuration of LAS for monochromatic source	116
Table 4.2	Configuration for field test on cassegrain tele- scope	119
Table 4.3	Configuration of LAS for data observation	122
Table 5.1	Coronal forbidden transition lines in the NIR and MWIR region	139

LISTINGS

ACRONYMS

MSSP	Multi Slit Spectro-Polarimeter
LCVR	Liquid Crystal Variable Retarder
MAST	Multi-Application Solar Telescope
USO	Udaipur Solar Observatory
FP	Fabry-Pérot Interferometer
FOV	Field of View
AO	Adaptive Optics
FWHM	Full Width at Half Maxima
f#	f-ratio or f-number
DWDM	Dense Wavelength Division Multiplexing
PBD	Polarizing Beam Displacer
polcal	polarization calibration unit
PSF	Point Spread Function

- HMI Helioseismic and Magnetic Imager
HSI Hyper Spectral Image
LAS Lenslet Array Spectroscope
ROI Region of Interest
AOCS Attitude and Orbit Control System
LEO Low Earth Orbit
LTE Local Thermodynamic Equilibrium
NLTE Non Linear Local Thermodynamic Equilibrium
CME Coronal Mass Ejection
PFSS Potential Field Source Surface
SNR Signal to Noise Ratio

1

INTRODUCTION

1.1 THE SUN A STAR

Stars are classified into different types based on chromaticity in the Morgan–Keenan (MK) classification. The Sun is a type G2V star according to the MK classification. The G type indicates a surface temperature of the range 5200-6000 K (Habets and Heintze [42]) and numeral “V” indicates that the Sun is in its main sequence. This type of stars are classified as yellow dwarfs and are the second most abundant type after the red dwarfs in the visible portion of the milky way galaxy. Each stellar type occupies a certain region in the Hertzsprung-Russell (HR) diagram that determines the structure of the star, its evolution and chemical composition. The HR diagram also helps in determining the presence of coronae around the star, its rotation and pulsations (Figure 1.1). Stars loose mass through winds, having significant impact on the chemical composition of the interstellar medium and inter planetary medium (Lamers and Cassinelli [60]). These winds also determine the conditions favorable for the presence of life because along with the primary criteria for the planet to be in the habitable zone of its host star, the planet must also be capable of enduring the high energy particles emanating from the star. A well known example for this is planet Mars. Though the planet lies in the goldilocks zone, high energy particles in the solar winds ripped away most of the atmosphere of the planet but at the same time the winds are not strong and gentle enough to be blocked by the earth’s magnetic field. The winds and their acceleration also determines the space weather of the interplanetary system. The mechanism that drives these accelerated outflows involve the star’s magnetic field which is generated through the dynamo action. The magnetic field is also responsible for dynamics of the star like spots and flares. As the Sun is our closest star which can be resolved in great detail, understanding the mechanisms of generation of field, the internal structure etc., gives an insight into the working and evolution of many star systems.

The three sources of information that can be used to understand the Sun are - the solar neutrino generated at the core of our star from nuclear fusion, neutral and charged particles present in the solar wind propagating through the interplanetary medium and the ubiquitous photons (Galvin et al. [34]). Light is the most important source of information used to uncover the working of the sun. Three properties of light namely the intensity, wavelength and polarization are measured

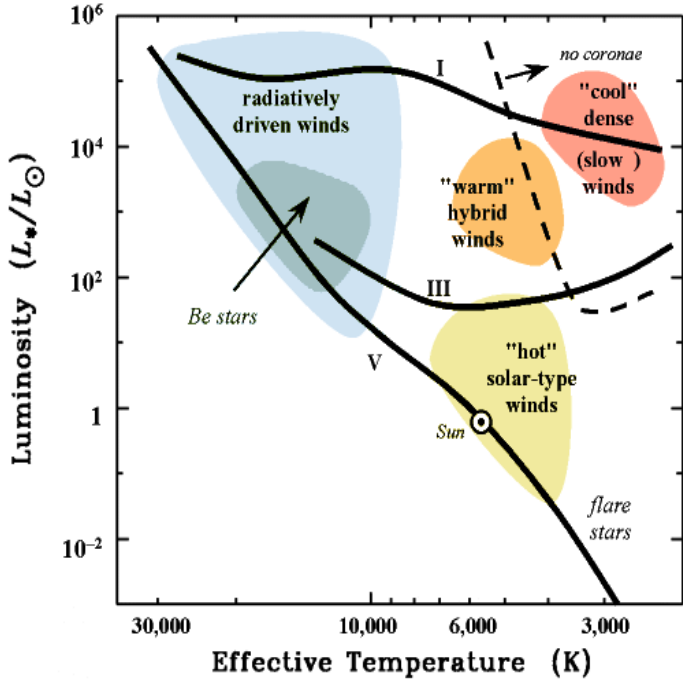


Figure 1.1: HR diagram of stars. The stellar wind type and the presence of a corona are shown in the diagram.

to estimate the physical properties of the source. The measurements are called photometry, spectroscopy and polarimetry respectively.

The interior of the Sun consists of a core extending from its center to $\sim 0.25 R_\odot$ (Garcia et al. [35]). This region has a temperature of 1.5×10^7 K and a density of 150 g/cm^{-3} . At this high temperature, the hydrogen nuclei overcomes the electrostatic barrier through quantum tunneling and undergoes nuclear fusion to generate helium from the proton-proton chain reaction (Bethe and Critchfield [14]) and the CNO cycle (Bethe [13]). The region from $0.25 R_\odot$ to $0.71 R_\odot$ is known as the radiative zone. Here the inward gravitational pull of the gas is in equilibrium with the radiation pressure of photons. Energy produced from fusion in the core is carried outward primarily through radiation and conduction (Ryan and Norton [91]). At $0.71 R_\odot$, the temperature reaches 1.5×10^6 K where the radiative zone ends at the tachocline. The energy is transported through convection from the tachocline to the surface of the sun. During the process of convection the temperature drops from 1.5×10^6 K at the tachocline to 6000 K at the surface. The convective process is visible on the surface as granules of plasma moving upward and then back into the surface. Unlike the internal structure of the Sun which is obtained from the standard solar model, simulations and helioseismology (Deubner and Gough [25] and Duvall et al. [26]), the solar atmosphere can be probed in much greater detail as the photons emitted or scattered by the source can be directly observed. The formation of spectral lines by different

elements and their corresponding excitation potentials can be used to study different regions of the solar atmosphere.

1.2 THE FORMATION OF SPECTRAL LINES

The physical parameters like temperature, density, velocity, magnetic field etc., of a medium have to be inferred from the radiation that passes through it. The radiative transfer equation (RTE) contains the relation between physical properties of the medium and the light that passes through it. The absorption lines formed due to bound-bound transition of electrons in an atomic species give the physical parameters of the the solar atmosphere not just at a single location but a range of heights. The RTE for the propagation of an unpolarized ray is

$$\frac{dI_\nu}{d\tau_\nu} = k(\tau_\nu) [I_\nu - S_\nu] \quad (1.1)$$

where

- τ is the optical depth
- ν is the frequency of the light
- S is the source function

and

$$k_\nu = (1 + \eta\phi_\nu) \quad (1.2)$$

is the propagation function for intensity where η is the ratio of absorption coefficient of line to continuum which determines the strength of the line and ϕ is the absorption profile. It can be seen that [Equation 1.1](#) is a function of optical depth for a constant wavelength. The solution of [Equation 1.1](#) can be written as

$$I_\nu(0) = \int_0^\infty e^{-\int_0^\tau k_\nu(t)dt} k_\nu(\tau) S_\nu(\tau) d\tau \quad (1.3)$$

where $I_\nu(0)$ is the intensity at the observer's location i.e. $\tau=0$. The function within the integral is called the contribution function

$$C(\tau) = e^{-\int_0^\tau k(t)dt} k(\tau) S(\tau) d\tau \quad (1.4)$$

which indicates the evolution of intensity as the radiation propagates through a medium. The exponent $e^{-\int_0^\tau k(t)dt}$ in [Equation 1.4](#) is an attenuation function which defines the probability of detecting a photon originating at some optical depth τ i.e. if the optical depth at which the photon originates is large then the probability of detecting it is low and vice versa. The product of the other two terms $k(\tau) S(\tau)$ in [Equation 1.4](#) is the emission coefficient. In order to determine the

formation of line, the absorption profile ϕ in [Equation 1.2](#) is determined as a function of frequency of radiation.

For a system in thermal equilibrium, the thermodynamic state of any region can be defined just by using temperature T. Then particle/ions will have velocity distribution which is Maxwellian, ionization states with Saha-Boltzmann distribution at T and source function which is a black body curve

$$S_\nu(T) = \frac{2h\nu^3}{c^2(e^{h\nu/kT} - 1)}. \quad (1.5)$$

If a region on the Sun is such that a photon emitted in a particular transition undergoes sufficient collisions such that it is indistinguishable from other transitions in the distribution, then, that local region is said to be in Local Thermodynamic Equilibrium ([LTE](#)). For such a system one can define ϕ_ν in [Equation 1.2](#) for a bound bound transition as

$$\phi_\nu = \frac{\gamma}{\sqrt{\pi}\Delta\nu_D} \int_{-\infty}^{\infty} \frac{e^{-((\nu-\nu')/\Delta\nu_D)^2}}{[2\pi(\nu' - \nu_0)]^2 + (\gamma/2)^2} d\nu' \quad (1.6)$$

which is obtained from the convolution of two profiles, namely, Doppler broadening ϕ_D and natural broadening ϕ_C given by

$$\phi_D(\Delta\nu) = \frac{e^{-(\Delta\nu/\Delta\nu_D)^2}}{\sqrt{\pi}\Delta\nu_D}$$

$$\phi_C(\Delta\nu) = \frac{\gamma}{[2\pi\Delta\nu]^2 + (\gamma/2)^2}$$

where

γ is constant of collisional damping

$\Delta\nu_D$ is Doppler width

$\Delta\nu$ is $\nu - \nu_0$

[Equation 1.6](#) is Voigt profile obtained from a simple dipole oscillator. The derivation of the function can be found in del Toro Iniesta [22]. It must be noted that the line profile defined in [Equation 1.6](#) is derived using Doppler and natural broadening for a [LTE](#) atmosphere. Using [Equation 1.2](#), [1.5](#) and [1.6](#) one can define the emission coefficient for [Equation 1.2](#). [Figure 1.3](#) shows the variation in contribution function with optical depth for a single wavelength point (plot taken from Ruiz Cobo [89]). It can be seen that a range of optical depths give a non zero contribution function and in the solar atmosphere, the optical depth or probability of scattering of a photon decreases as one moves away from the photosphere. If the entire absorption line is considered i.e. if the contribution function is plotted for several wavelength regions along the absorption line then each wavelength

An arbitrary wavelength is chosen for representation purpose only

point on the absorption line profile has the contribution from a range of heights for the atmosphere through which light of that wavelength passes through. Thus in order to study different layers of the solar atmosphere one can observe the absorption line formed by an element at a temperature and density which corresponds to that layer under consideration (see [Figure 1.5a](#)).

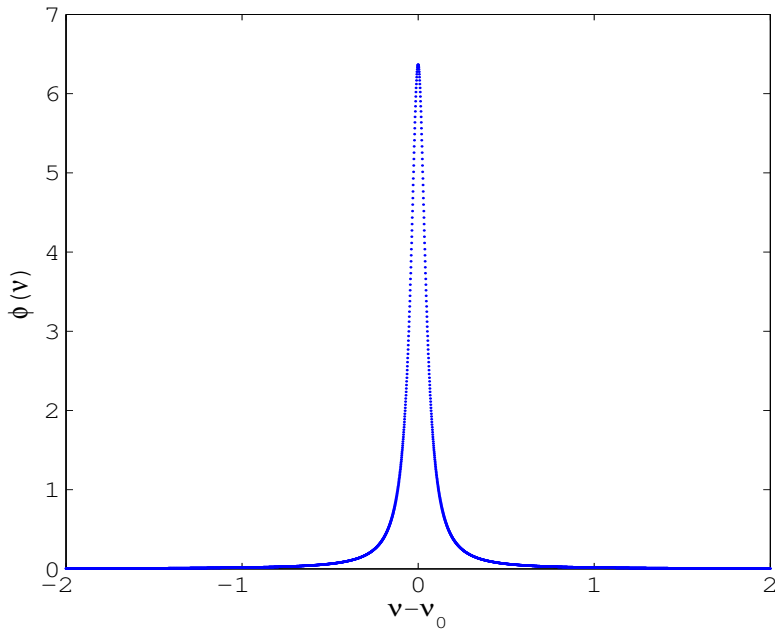


[Figure 1.2](#): Absorption coefficient for a line generated in an atmosphere which is at [LTE](#) for a collision damping of 0.05. The x-axis are in the units of Doppler width to make the plot independent of wavelength.

1.3 THE SOLAR ATMOSPHERE

The Sun is a sphere of gas. But the solar atmosphere starts from a region where the optical depth of the medium reaches unity, and the scattered/emitted photon reaches the observer. The solar atmosphere is broadly divided into four layers based on the stratification of temperature and density. They are the photosphere, chromosphere, transition region and corona. It is well known that the magnetic field is responsible for most of the dynamic activities in the solar atmosphere. Hence the regions are also classified based on plasma β which is the ratio of plasma pressure $p_{plasma} = nkT$ and magnetic pressure $p_{mag} = B^2/2\mu_0$, which determines whether the gas or the field is a dominant component at a given region. If $\beta > 1$, then the gas pressure dominates magnetic pressure and field lines are frozen into the

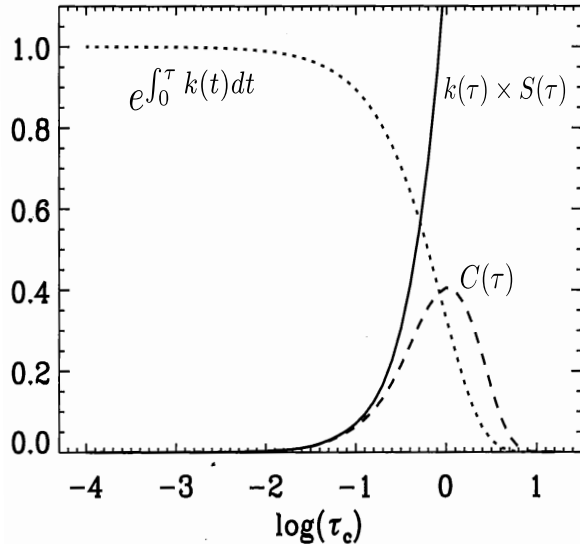
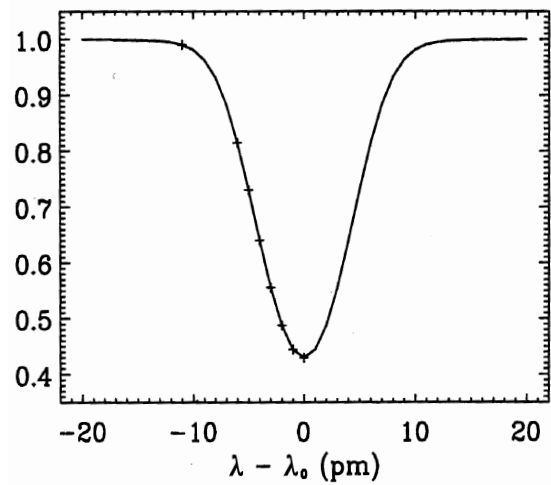


Figure 1.3: Variation in contribution function as a function of optical depth

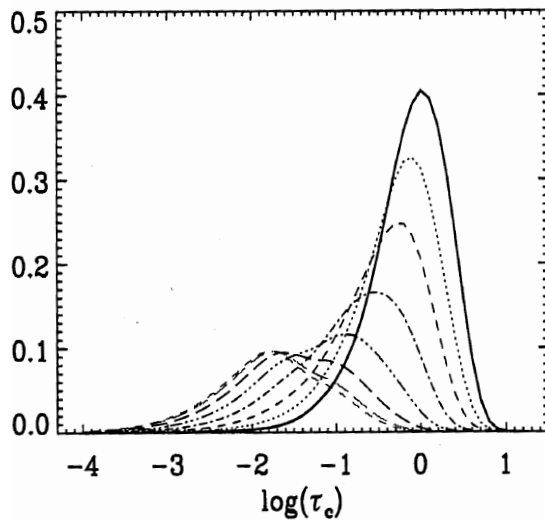
plasma and if $\beta < 1$, then the plasma movement is determined by the motion of field lines. The stratification of the solar atmosphere is shown in Figure 1.5.

The photosphere is the visible layer of the Sun where most of the light reaching the Earth comes from. As optical depth varies for different wavelengths, the base of the photosphere is defined as the region where optical depth τ reaches unity for $\lambda = 500\text{nm}$ (Stix [114]). The temperature decreases linearly from an average of 6000 K to 4000 K in an height range of 500 km. The magnetic fields generated through the solar dynamo (Parker [77] and Zwaan [136]) in the interiors of the convection zone come up due to buoyancy and manifest themselves as sunspots, pores and faculae on the photosphere. As $\beta > 1$ in this region, the field lines get dragged and twisted as the plasma moves, increasing stress in the field lines which when relaxed causes flares and Coronal Mass Ejection (CME)s (Benz [12], Chen [18], Shibata and Magara [104], and Webb and Howard [125]).

The chromosphere is called so because of its famous emission lines called the flash solar spectra obtained during total solar eclipses. The chromospheric region is stratified in hydrostatic manner until an height of 1300 km as $\beta > 1$ with the plasma behavior being hydrodynamic. Although the temperature is increasing gradually with height, the lower chromosphere behaves like an extension of the photosphere with phenomenon like waves in the sunspot umbra and penumbra (seen as 3 and 5 minute oscillations in photospheric region of the sunspot) (Giovanelli [39]). Beyond the $\beta = 1$ region the chromosphere has characteristics similar to the corona with many fine structures (Judge [51]). The chromosphere has several structures of varied size like spicules

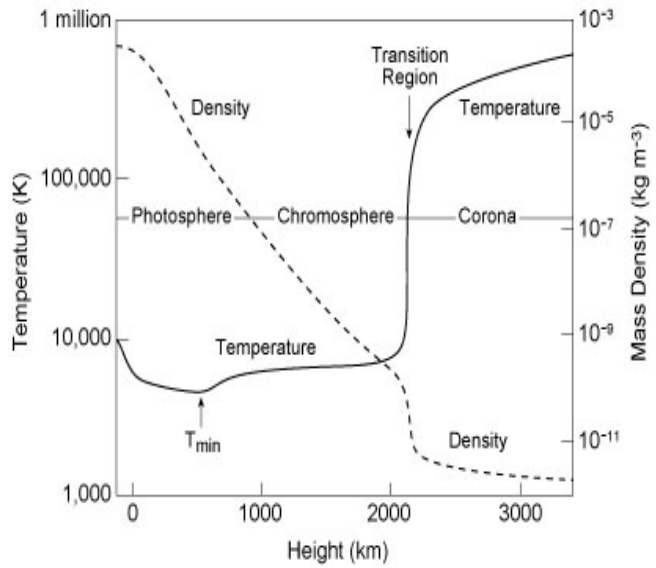


(a) Example of a normalized absorption line as a Voigt profile formed in LTE atmosphere.

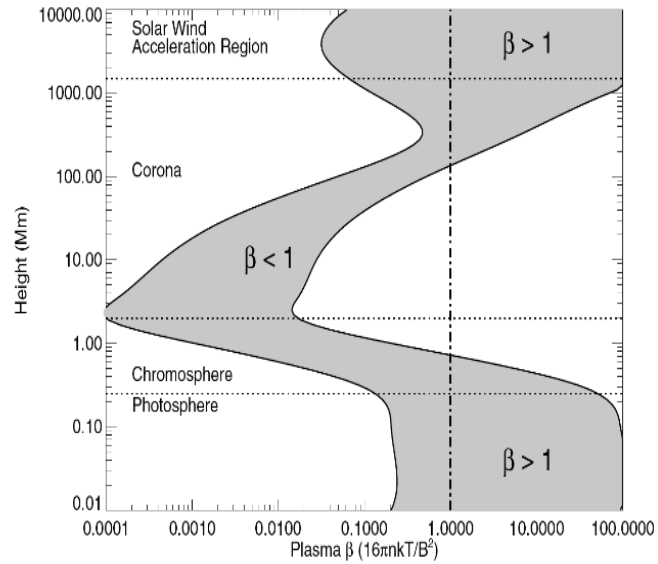


(b) The figure is a plot of contribution function for each point marked by x in Fig (a) as a function of optical depth τ . It can be seen that the wings of the line have contribution at large values of optical depth τ in the atmosphere and the core has maximum contribution for lower values optical depth.

Figure 1.4: Plot of formation of a line at various optical depths. The atmosphere is stratified into different layers with decreasing optical depth hence this plot also shows the ability of an absorption line to provide field parameters at various heights of the solar atmosphere.



(a) The variation in temperature and density of the solar atmosphere with height from the $\tau_{500} = 1$ surface. The figure is adapted from https://ase.tufts.edu/cosmos/print_images.asp?id=28



(b) Variation in plasma beta with height in the solar atmosphere. Regions with $\beta > 1$ is dominated by plasma which controls the position of the magnetic field and vice versa for $\beta < 1$. The figure is adapted from Gary [36]

Figure 1.5: The stratification of the solar atmosphere based on temperature, density and plasma β

and mottles as small scale structures and prominences, plages and super granulation as large scale structures. The solar chromosphere is very important as the study of Ca II K line present in Sun and other population 1 type of stars provide pseudo information of the magnetic structure of the star (Skumanich, Smythe, and Frazier [105] and Wilson [130]). Ca II also helps in determining stellar rotation of even the slowly rotating stars (Vaughan et al. [122]) which in-turn dictates the dynamo, magnetic field generation and star spot cycle (Wilson, Vaughan, and Mihalas [131]). But the photometry of calcium line only act as a pseudo indicators of the fields and the actual vector magnetic fields are obtained through Zeeman effect and solving the RTE in magnetic atmosphere (see [Section 1.4](#)). Sun is the only star where spectro-polarimetric observations can be performed for Ca II K and the relation between the field strength and line intensity can be established.

The transition region is a narrow region where a “transition” in temperature occurs from 25,000 K at the upper chromosphere to 10^6 K in the lower corona. This is the famous coronal heating problem which appears to violate the second law of thermodynamics where there is an increase in temperature as one moves from the photosphere at 6000 K to the corona at 10^6 K. This suggests a non-thermal heating process which dumps the energy from the photosphere to the corona. The proposed carriers of this energy are mechanical waves (Bel and Leroy [10] and Schunker and Cally [98]) and magnetic field lines (Bueno, Shchukina, and Ramos [16] and Kubo, Shimizu, and Lites [57]).

Thus an understanding of the solar atmosphere requires the measurement of magnetic fields. To understand the coupling and dynamics between the layers of the solar atmosphere, the observer needs simultaneous high time cadence observations of several spectral lines forming at different heights in the solar atmosphere.

1.4 MAGNETIC FIELD MEASUREMENT

Different layers of the solar atmosphere are coupled through magnetic field generated through the dynamo action in the convection zone (Parker [77] and Zwaan [136]). They are also responsible for the dynamic activities on the Sun as described in the previous section. Thus it is important to measure the magnetic fields in order to study the dynamic events on the Sun and validate the models which describes the mechanisms that drive these dynamic events.

1.4.1 Stokes parameters

Polarization of light is the plane of vibration of the electric field with respect to a reference observer’s plane. The time averaged po-

larization of light can be expressed completely using four quantities namely the Stokes parameters. The four Stokes parameters are named I, Q, U and V where Stokes-I represents the intensity of the measured light, Q and U together represents the amplitude and orientation of the plane of vibration of the electric field and V represents the direction of rotation of the field plane over time. Beyond the radio wavelength, the electric field oscillates at very high frequencies and cannot be measured directly. Instead the intensity of light which is a manifestation of the electric fields as $I(t) \propto |E(t)|^2$ can be measured. As the information of polarization is lost during such measurements, the three Stokes parameters are modulated into intensity using polarimeters and then demodulated into its constituent components during post processing of the measurements. Polarization is invaluable for the measurement of magnetic field.

1.4.2 Zeeman effect

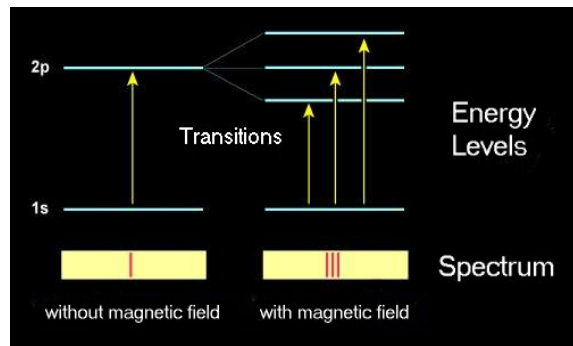
Among the four quantum numbers [L, S, J, M] that define an atomic energy level, the magnetic quantum number (M) determines a component of the total angular momentum (J) in a particular direction with respect to an external magnetic field. In the absence of magnetic field the [M] states are degenerate producing a single wavelength during transitions. This degeneracy is broken when a magnetic field is applied and the atomic levels split ([Figure 1.6b](#)). E.g. the 2p level splits into three sublevels namely σ^+ , π , σ^- in the direction perpendicular to the field. If λ_0 is the central wavelength which corresponds to the transition of π sublevel then, the displacement of spectral lines for σ^\pm sublevels are

$$\Delta\lambda = \frac{e}{4\pi cm_e} g \lambda_0^2 B$$

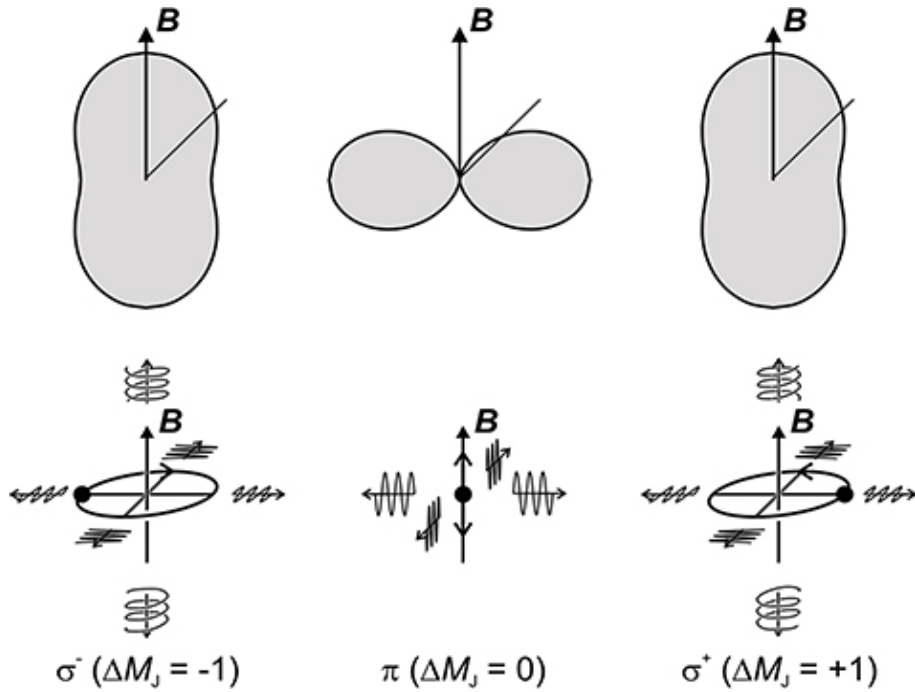
where

- λ is wavelength in Å
- e is charge of electron in columb
- m_e is mass of electron in kg
- c is speed of light
- g is the Landé factors of the transition
- B is field in gauss

Based on the orientation of the observer with respect to the magnetic field, the three spectral components $\lambda_{\sigma^\pm, \pi}$ will have different states of polarization. [Figure 1.6](#) illustrates the plane of vibration of the electric field with respect to the applied magnetic field. For a field line oriented along the observer (longitudinal fields), they see circular polarization in the σ components and no radiation due to π component. Similarly for a transverse field, the σ components are linearly



- (a) An example of Zeeman splitting where the degenerate 2p atomic level splits into 3 levels on the application of magnetic field producing three spectral lines instead of one



- (b) Electrons in the split levels absorb or emit radiation whose electric field is in a preferred orientation. The polarization and radiation pattern of the field is represented in the figure. Image credits Li [63]

Figure 1.6: Illustration of Zeeman effect and the polarized radiation produced by it

polarized in one direction and the π component is polarized linearly in the orthogonal direction. For a field oriented in any other arbitrary direction, the observer sees elliptical polarization (a combination of linear and circular polarization) in the σ components and variable strength of linear polarization in the π component. Further, the separation between the σ components and their handedness gives the strength and polarity of the field. Thus, by using a combination of ellipticity, handedness and separation, one can deduce the vector magnetic field of the atmosphere under observation. The magnetic field of Sun is measured using both Zeeman and inverse Zeeman effect. In the case of inverse Zeeman effect, the absorption lines are partially polarized due to the preferential absorption of the unpolarized black body radiation at that wavelength..

1.4.3 Radiative transfer equation for magnetic atmosphere

The polarization information along with the intensity is used to derive the physical parameters of the magnetic field in the solar atmosphere. Unno [120] initially formulated the RTE which was later generalized by Rachkovsky [82] by including magneto optic effects. Jeffries, Lites, and Skumanich [45] later reformulated the RTE and eliminated the ambiguity in sign conversion. [Equation 1.1](#) is extended to RTE in magnetic medium under LTE and written as

$$\frac{d}{d\tau_v} \begin{pmatrix} I \\ Q \\ U \\ V \end{pmatrix}_v = \begin{pmatrix} \eta_I & \eta_Q & \eta_U & \eta_V \\ \eta_Q & \eta_I & \rho_V & -\rho_U \\ \eta_U & -\rho_V & \eta_I & \rho_Q \\ \eta_V & \rho_U & -\rho_Q & \eta_I \end{pmatrix}_v \begin{pmatrix} I - B(T) \\ Q \\ U \\ V \end{pmatrix}_v \quad (1.7)$$

where the elements of the propagation matrix $K(\tau)$ are -

$$\begin{aligned} \eta_I &= 1 + \frac{\eta_0}{2} [\phi_p \sin^2 \theta + \frac{1}{2} (\phi_l + \phi_r) (1 + \cos^2 \theta)] \\ \eta_Q &= \frac{\eta_0}{2} [\phi_p - \frac{1}{2} (\phi_l + \phi_r)] \sin^2 \theta \cos 2\varphi \\ \eta_U &= \frac{\eta_0}{2} [\phi_p - \frac{1}{2} (\phi_l + \phi_r)] \sin^2 \theta \sin 2\varphi \\ \eta_V &= \frac{\eta_0}{2} (\phi_r - \phi_l) \cos \theta \\ \rho_Q &= \frac{\eta_0}{2} [\psi_p - \frac{1}{2} (\psi_l + \psi_r)] \sin^2 \theta \cos 2\varphi \\ \rho_U &= \frac{\eta_0}{2} [\psi_p - \frac{1}{2} (\psi_l + \psi_r)] \sin^2 \theta \sin 2\varphi \\ \rho_V &= \frac{\eta_0}{2} (\psi_r - \psi_l) \cos \theta \end{aligned}$$

Here ϕ_l, ϕ_r, ϕ_p are left circular, right circular and linear polarization absorption coefficients and ψ_l, ψ_r, ψ_p are dispersion coefficients for radiation traveling in an atmosphere which has magnetic field inclined at an angle θ and azimuth φ with respect to the observer in a spherical co-ordinate system (del Toro Iniesta [22]).

In [Equation 1.7](#) source function $S(\tau)$ and propagation matrix $K(\tau)$ are atmospheric height dependent functions of physical parameters like magnetic field, velocity, temperature etc. By knowing their values one can solve the equation of RTE to obtain I , Q , U and V at different wavelength points. Conversely by measuring the Stokes parameters, the orientation and strength of the magnetic field of the region through which the radiation passed through can be deduced. This is known as the inverse problem. But [Equation 1.7](#) does not have a simple analytical solution and has to be solved numerically. By simplifying the LTE atmosphere to a single layer which is independent of τ , one can obtain an analytical solution (Rachkovsky [83] and Unno [120]) for the inverse problem. The approximation made to obtain this simplified atmosphere is called the Milne-Eddington approximation. Although this approximation does not represent the real solar atmosphere, it serves as an initial guess to obtain numerical solutions for the RTE. The numerical inversions are performed by generating synthetic Stokes profiles with a model atmosphere M and reducing the difference between the observed and computed Stokes profiles using the merit function

$$\chi^2(M) = \frac{1}{4N - F} \sum_{i=1}^N \sum_{j=1}^4 \left\{ I_j^{observed}(\lambda_i) - I_j^{synthetic}(\lambda_i, M) \right\}^2 \frac{w_j^2}{\sigma_j^2} \quad (1.8)$$

where

- N is the number of wavelength points
- F is the number of free parameters of the atmosphere in the model M
- w is the weight factor
- σ is the noise in the observation
- j represents the four Stokes parameters

The atmospheric parameters (M) are difficult to be extracted due to their highly non-linear manifestation into the propagation matrix and source function. Least squares inversion technique is used to obtain numerical solution and minimize [Equation 1.8](#) as they are reliable in deducing atmospheric parameters from polarized spectra (Del Toro Iniesta and Ruiz Cobo [21], del Toro Iniesta and Ruiz Cobo [23], and Rubio [87]). A model atmosphere which provides the best fit or minimum χ^2 is considered to be the actual atmosphere under observation.

1.5 MOTIVATION AND STRUCTURE OF THIS THESIS

This chapter began by stating the role of Sun as a star and the use of understanding its physical processes to interpret the environment in other stellar systems. The dynamic processes due to magnetic field

and the coupling between the layers of the solar atmosphere are defined in [Section 1.3](#). In order to deduce these parameters and understand the working of the Sun, the observers require instruments that can obtain the spectra at multiple wavelength bands and perform polarimetry with high accuracy such that parameters like σ in [Equation 1.8](#) have least contribution in the measurements resulting in accurate interpretation of the physical processes.

The smallest structures that can be resolved on the Sun depends on the photon mean free path (Judge et al. [50]). With the advent of large aperture telescopes, it is now possible to probe the solar atmosphere to a great detail. But small scale structures have short evolving time scales thus the instruments that are used to obtain spectral or polarimetric information of the region must have high time cadence. Further in order to study the evolution of the feature at multiple heights, simultaneous measurements at multiple wavelengths are necessary. Common spectroscopic instruments that are used in solar observation are Fabry-Pérot Interferometer ([FP](#)) based imaging spectrographs or grating based spectrographs. The disadvantage of an [FP](#) imager is that it cannot perform simultaneous observation at different wavelengths and multiple [FP](#) imaging systems have to be used in parallel to achieve multi wavelength capabilities. The disadvantage of a single slit grating spectrograph is the low time cadence of the instrument. The drawbacks of a conventional grating spectrograph and [FP](#) spectrograph are addressed in this thesis by developing instruments that overcome their respective disadvantages to perform high time cadence spectro-polarimetry and snapshot spectroscopy at photospheric and chromospheric heights. Sources of polarization crosstalk while measuring weak coronal fields on a space based observatory and possible solution for the same is devised through an effective modulation scheme to minimize the crosstalks.

The thesis is divided into three parts. The first part deals with spectro-polarimetry and consists of two chapters ([Chapter 2](#) and [Chapter 3](#)). The second part deals with snapshot spectroscopy and consists of one chapter ([Chapter 4](#)). The third part deals with polarization crosstalk and consists of one chapter ([Chapter 5](#)). A brief description of each chapter is as follows -

- **Multislit spectro-polarimeter (MSSP)** - This chapter describes the design, calibration and field testing of a grating based spectro-polarimeter that has 5 slits at the entrance aperture. This design addresses the issue of a single slit spectrograph and achieves a time cadence which is five times faster than a traditional single slit spectrograph. The instrument is designed to work simultaneously at four wavelengths 6302 \AA , 8542 \AA , 10830 \AA and 15653 \AA such that magnetic field and other parameters can be measured at photospheric and chromospheric heights. The instrument is installed at Udaipur Solar Observatory ([USO](#)) and

spectro-polarimetric data is obtained for sunspot NOAA 12653. The Stokes parameters are inverted to obtain magnetic field and the results are compared with Helioseismic and Magnetic Imager ([HMI](#)).

- **Magnetic field of sunspot at photosphere and chromosphere-** In this chapter, the results from the inversion of spectro-polarimetric data obtained from SOLIS-VSM for a nearly simultaneous observation are presented for NOAA12683 which is an alpha type sunspot. Fe I at 6302 Å for photosphere and Ca II at 8542 Å for lower chromosphere are the lines chosen for diagnostics. The field strength of the photosphere obtained from SOLIS-VSM is compared with the field strength obtained from [HMI](#). Non Linear Local Thermodynamic Equilibrium ([NLTE](#)) chromospheric line inversion is carried out using NICOLE and the field strength obtained for the chromospheric region is compared with Potential Field Source Surface ([PFSS](#)) field extrapolation of the photosphere. It is shown that the gradient in the field from photosphere to lower chromosphere obtained from the inversion of two spectral lines formed at different heights is about 4 times lesser than what is obtained from the inversion of a single photospheric line.
- **Snapshot imaging** - Snapshot spectroscopy is the technique of obtaining the spectral information of a 2D field in a single frame. A novel instrument is designed and developed using a lenslet array and Fabry-Pérot interferometer called Lenslet Array Spectroscope ([LAS](#)). This device works on the principle of change in the transmitted wavelength with change in the angle of incidence to achieve hyperspectral imaging capabilities. [LAS](#) is installed at [USO](#) and the snapshot capabilities are demonstrated by measuring Evershed flow in the sunspot penumbra at Fe I 6302 Å and plasma oscillations in the solar prominence at H- α 6562.8 Å.
- **Evaluation of polarization crosstalk for coronal field measurements** - The two instruments described above can also be used for coronal spectro-polarimetry. But the field strength is weak and space based instruments are needed to avoid atmospheric seeing and scatter. Although satellites are stable, temporal attitude corrections introduce jitter which affect polarization measurements and causes crosstalk between the Stokes parameters. Further space based instrumentation has mass restrictions and space qualified components. A rotating retarder based polarimeter is designed and an optimum modulation matrix is generated to reduce crosstalk and improve the efficiency of the weakest Stokes V signal. A laboratory setup is made to experimentally

verify the simulated results of crosstalk for the jitter from a typical Low Earth Orbit ([LEO](#)) satellite.

Each chapter is independent of the contents from the other chapter and is self sustained. As the chapters talk about different instruments, the conclusion of the chapters also contain possible improvements and future work of those instruments. Hence a dedicated chapter for conclusion and future work is not being presented in this thesis.

Part I
SPECTROPOLARIMETRY

2

MULTI-SLIT SPECTRO-POLARIMETER

OVERVIEW

Multi Slit Spectro-Polarimeter ([MSSP](#)) is a 5-slit grating based spectro-polarimeter built for Multi-Application Solar Telescope ([MAST](#)) at [USO](#). In this chapter, the development of [MSSP](#) and characterization of its components are discussed. A GUI is developed to interface [MSSP](#) with [MAST](#) and the raw data obtained from it is reduced to science data using [MSSP](#) reduction codes. The chapter concludes with results obtained from the inversion of Fe I at 6302 Å for sunspot NOAA 12653 obtained from the instrument.

2.1 INTRODUCTION

Our aim is to build a spectro-polarimeter capable of simultaneously measuring the photospheric and chromospheric vector magnetic field with fast time cadence. Two most commonly used types of spectrographs in solar observation are [FP](#) based imaging spectrograph and grating based spectrograph. An [FP](#) spectrograph is useful to study dynamics with short time scales of evolution like umbral and penumbral waves (Giovanelli [39] and Zirin and Stein [135]), umbral flashes or global mode oscillations on Sun at high spatial resolution (Duvall et al. [26]). But the Field of View ([FOV](#)) is imaged at different wavelength points of an emission or absorption line by tuning the [FP](#). This wavelength tuning is temporal and in order to extract the parameters like velocity or magnetic field, seeing should be good or an adaptive-optics system is necessary for image stabilization or else the advantage of high spatial resolution is nullified. Another disadvantage of [FP](#) based spectrographs is the low spectral resolution. In order to increase spectral resolution multiple [FPs](#) have to be used in tandem which results in reduced light throughput. Based on response function of the radiating plasma (del Toro Iniesta [22]), different emission or absorption lines form at different heights of the solar atmosphere (For e.g., study of sunspots at different wavelength (Lin [65], Socas-Navarro et al. [108], and Wang et al. [124]))). As [FP](#) tunes to a single wavelength at a given time, this spectrograph can observe only a single region of the solar atmosphere at any instance. Change in wavelength region requires a change in transmission prefilter i.e. a modification in optical setup. Thus incapability of simultaneous observation at multiple wavelength bands is another short-coming of

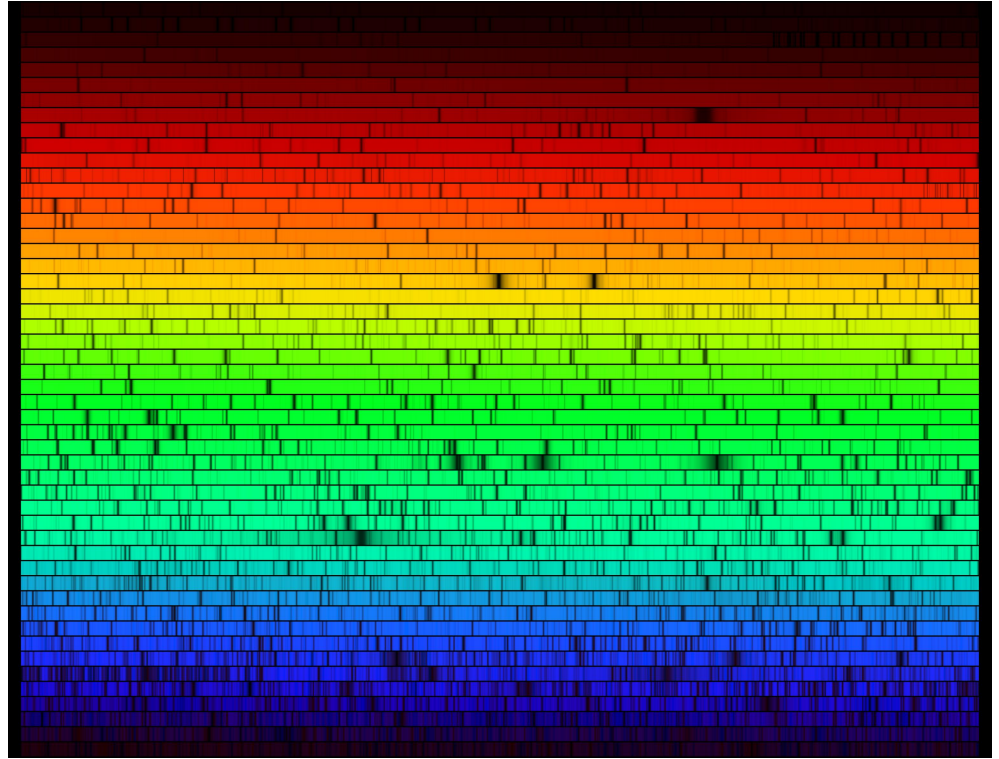


Figure 2.1: Solar spectra of a quiet Sun region obtained from cross dispersion grating at McMath-Pierce observatory

this spectrograph. Further most of the light incident on the FP gets wasted as back reflection or transmission of undesired orders.

A slit and grating based spectrograph on the other hand can sample a broad wavelength band of a particular region (Socas-Navarro et al. [108]). [Figure 2.1](#) is a spectral sample of quiet Sun region taken from a cross dispersion grating using a 2 mm slit which covers 3,630 km (5") on the Sun. The entire visible range is covered by it, the dark bands in the spectra are the absorption lines/Fraunhofer lines. For a field region within the slit, all the wavelength information is obtained simultaneously, thus field parameters like velocity, magnetic field can be extracted with higher accuracy. The spectral resolution of gratings can be high of the order of 5×10^5 - 6×10^5 and it is relatively simple to manufacture and operate. But it is not always desirable to sample all wavelength points within a spectral band. E. g. to extrapolate vector magnetic fields from photosphere to lower chromosphere, photospheric vector magnetic field map can be generated using specific lines like Fe I 6302 Å (Wang et al. [124]) or Fe I 15653 Å while lower chromospheric vector magnetic field can be generated using Ca II 8542 Å from the calcium infrared triplet (Leenaarts et al. [61]) or H- α 6562.8 Å hydrogen balmer line. Fe I 6302 Å line pair have a Full Width at Half Maxima ([FWHM](#)) ≈ 100 mÅ each and Ca II 8542 Å has a 13 Å blue continuum to red continuum line width. So for a grating spectrograph operating in the range between 6302 Å and 8542 Å

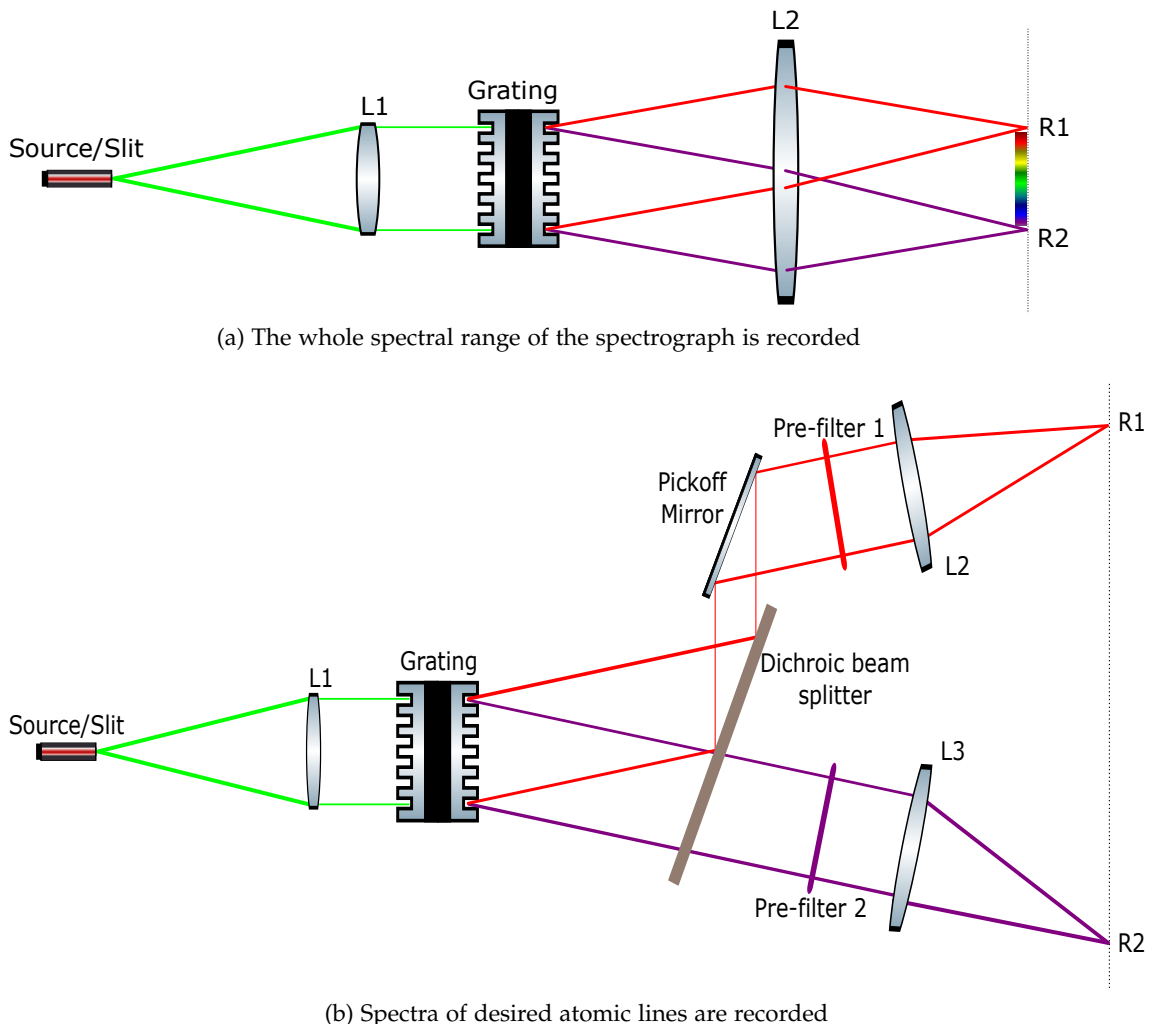


Figure 2.2: Effective utilization of spectra from a grating spectrograph

(Figure 2.3) band pass of about 3 \AA for Fe I and 15 \AA for Ca II are necessary while the rest can be discarded (Figure 2.5). Consider Figure 2.2, if R_1 is the pass band for region 1 (say Ca II) and R_2 is the pass band of second region (say Fe I), then, a dichroic beam splitter can be introduced in the dispersed light from the grating such that the beam splitter's transmission band allows R_1 while R_2 gets reflected and imaged at a separate location (Figure 2.4). Multiple spectral lines can be imaged in a similar manner by using several dichroics allowing for simultaneous observation of multiple heights in the solar atmosphere. This configuration in Figure 2.2b can be used to overcome one of the biggest disadvantages of a slit and grating spectrograph.

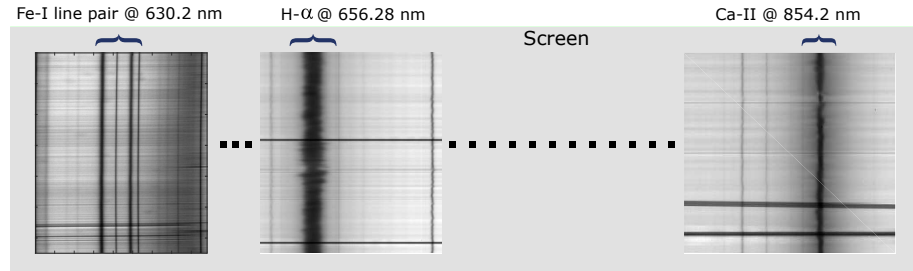


Figure 2.3: Sample spectra from a grating. Note Spectral dispersion is not to scale

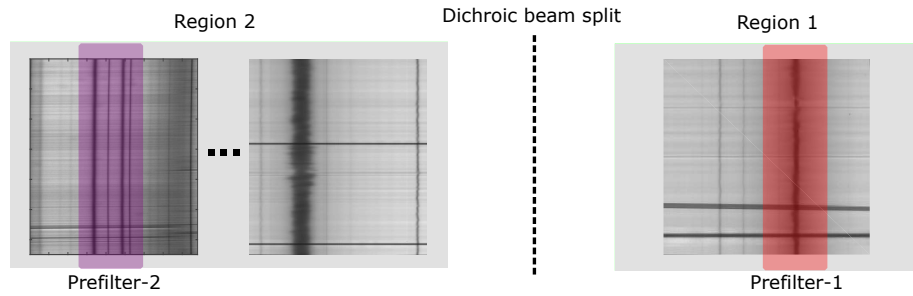


Figure 2.4: The entire spectral band is split into two or more broad band spectra using dichroic beam splitter. Each broad band spectra is then passed through narrow band prefilter

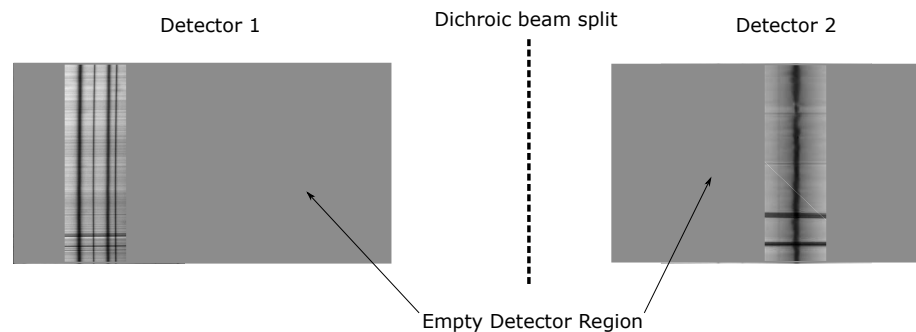


Figure 2.5: Narrow band spectra imaged on a detector

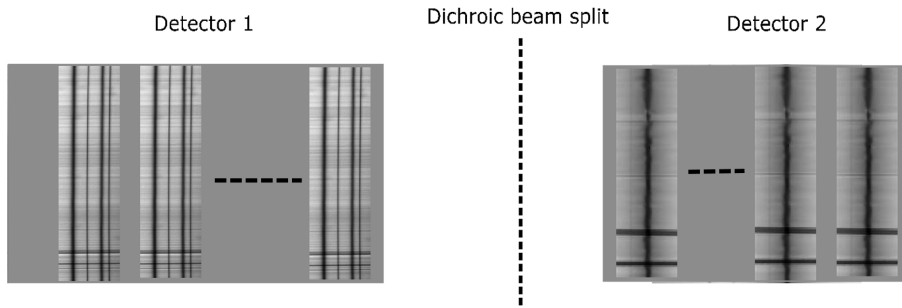


Figure 2.6: Spectra of multiple slit sampling different regions of the **FOV** can occupy the previously unused detector space.

Slit samples a narrow portion of a field. For extended objects like Sun, the slit has to be raster scanned on the **FOV** or vice-versa to generate an image data cube $[x,y,\lambda]$ of the field such that spectral information of the entire **FOV** is recorded. But this is a time consuming process. Dynamic events cannot be recorded through simple raster scan of the field as there are chances of artifacts creeping into the data. Reducing the time taken to raster scan the **FOV** is the only solution to this problem. Consider Figure 2.2a, spectral output shown in this schematic would look like Figure 2.3 on the detector. A small portion of the spectra is selected by placing a dichroic beam-splitter and a narrow band filter (Figure 2.5 and Figure 2.2b). For a 2D image, moving the slit in the plane perpendicular to the optical axis of lens L1 displaces the spectra on the image plane. By placing two or more single slits at different position on the 2D image, their spectra form at physically different location on the detector. Thus with multiple slits (Figure 2.6), the **FOV** gets divided into smaller regions. Now a raster scan has to be performed within the subdivided **FOV** which takes a shorter duration than the raster scan of a single slit on the entire **FOV**. The reduction in time is equal to the number of slits on the **FOV**. But the number of slits that can be placed depends on the spectral dispersion of the spectrograph and bandwidth of the prefilter. Consider Figure 2.5, assuming that the translation of the slit parallel to the dispersion plane displaces the spectra by the same extent on the detector plane, the minimum distance ' ds ' at which the next slit can be placed is equal to the product of linear spectral dispersion of the spectrograph and the passband of the prefilter. For a **FOV** of size x , the number of slits that can be used is integer value of x/ds . The linear spectral dispersion depends on the spectral order in which the grating is operated and the focal length of the imaging optics. Size of the **FOV** is determined by the telescope and magnification of intermediate optical components rendering the image onto the slit. So the design of a spectrograph/spectro-polarimeter depends on

spectral dispersion (determined by the science goal of the instrument) and **FOV** (determined by telescope).

MSSP is a spectro-polarimeter with 5-slits and spectral dispersion of $13.5 \text{ m}\text{\AA}$ per pixel designed specifically for 6 arcmin **FOV** of **MAST**. Following points are discussed in the subsequent sections

- The design of the spectrograph and polarimetric unit
- Calibration of the grating and polarimeter package
- Integration of **MSSP** to **MAST** and operating it with a GUI
- Determining analytically the telescope Mueller matrix for **MAST**
- Obtaining engineering run data and reducing it to Stokes data with data reduction software for **MSSP**
- Inversion of Stokes data and comparison with **HMI**'s observation

MSSP is capable of simultaneously recording Fe I 6302 \AA , Ca II 8542 \AA , He-I 10830 \AA and Fe I 15653 \AA but is currently operational at Fe I 6302 \AA . However the spectroscopic design of **MSSP** takes into account the science needs of all the four spectral lines.

2.2 SPECTROGRAPH DESIGN

MAST is a Coudé focus Gregorian type of telescope with 50 cm primary mirror aperture (Denis et al. [24], Mathew et al. [71], and Venkatakrishnan et al. [123]). This telescope is installed at **USO** on an island at Lake Fatesagar in Udaipur, India. The lake and wide open space provides a turbulence free lower atmospheric condition during most parts of the year. Hence it is logical to assume that the atmospheric seeing is fairly good for high resolution spectro-polarimetry of the Sun. Although the natural "seeing" or Fried parameter r_0 is around 6 cm at the observatory (Kumar et al. [58]), a low order Adaptive Optics (**AO**) system for **MAST** (Sridharan and Bayanna [111]) is under development to attain diffraction limited performance for the telescope. The spectrograph is designed taking into account both the **AO** system and a set of relay lenses used in **AO** for collimation and imaging as they change the plate scale and magnification of the **FOV**.

A water body regulates temperature during day time and improves seeing. For e.g Big bear solar observatory USA

For a 50 cm telescope, resolution limit at 6302 \AA is

$$\theta = \frac{1.22 \times \lambda}{D} = 1.537 \text{ mrad}$$

At 1.537 mrad or 0.3171 arcsec, solar granulations (Nordlund, Stein, and Asplund [74]) and penumbral structures are resolved in the photosphere (Sütterlin [116]). The flux tubes in the penumbra have plasma movement or Evershed flows whose velocity is on an average 1000 m/sec (Evershed [30]). A spectral resolution of $20 \text{ m}\text{\AA}$ or lower is needed to detect wavelength shift for velocities of 1000 m/sec at 6302 \AA

At 8542 Å the telescope's resolution limit reduces to 0.43 mrad, apart from sunspots, chromospheric features like filaments and fibrils can be recorded as well. Although plasma velocity of the penumbral flux tubes are higher in the chromosphere, a lower limit of 1000 m/sec is taken to measure small scale structure velocities like fibrils and mottles (Pontieu et al. [80]). This corresponds to a theoretical spectral resolution of 28.47 mÅ in the near Infra-red region.

The next parameter needed for spectrograph's design is the slit size. The slit width should be equal to half the spatial resolution limit of the telescope in order to sample the spatial features in the FOV. Light from MAST passes through AO system and the exit beam from the AO has a platescale of 5.283 arcsec/mm at 6302 Å at the image plane. So the required slit size is 30 μm according to nyquist criteria (i. e. 0.16 arcsec spatial sample). A slit produces diffraction pattern when monochromatic light is incident on it. The angular deviation of the central maxima in the diffraction pattern is given by

$$\theta = 2 \times \sin^{-1} \left(\frac{\lambda}{d} \right)$$

Mean free path of the photons increases in the chromosphere due to decrease in density. So the size of the smallest resolvable element on the Sun increases. Thus a decrease in telescope resolution, due to longer wavelengths, gets partially compensated with increased spatial scales of smallest resolvable elements. Spatial sampling of the slit follows nyquist criteria

where λ is wavelength of the monochromatic source and d is the slit width. For a beam of light incident on the slit, if the f-ratio or f-number (#) is larger than $1/\tan(\theta)$ i. e. if the angular divergence/-convergence of the beam is smaller than θ then the exit beam from the slit has # equal to $1/\tan(\theta)$. An entrance slit with such a configuration makes the spectrograph independent of the FOV's # (Lin and Versteegh [68] and Sankarasubramanian et al. [93]). The advantage of this configuration is that the spectral resolution and spectral dispersion of the spectrograph is fixed and the spatial scale of the FOV on the slit can be varied. It is later shown that this is adopted in MSSP due to which it can operate in two modes called high resolution mode (for 3 arcmin FOV) and large field mode (for 6 arcmin FOV).

To summarize, a grating spectrograph requires two parameters for its design. Spectral resolution and FOV or slit size. The spectral resolution considered to be 20 mÅ and slit size as 30 μm for our design criteria. The components of a spectrograph are a spectral disperser (grating), a collimator and an imager (see Figure 2.7).

2.2.1 Grating

In this section, the basic design of the grating used in MSSP is worked out. The grating required is inferred from the grating equations and the science goal of the spectrograph. By determining the grove density and grating type, linear spectral dispersion of the spectrograph is obtained from the focal length of collimating and imaging optics (see Table 2.2.1).

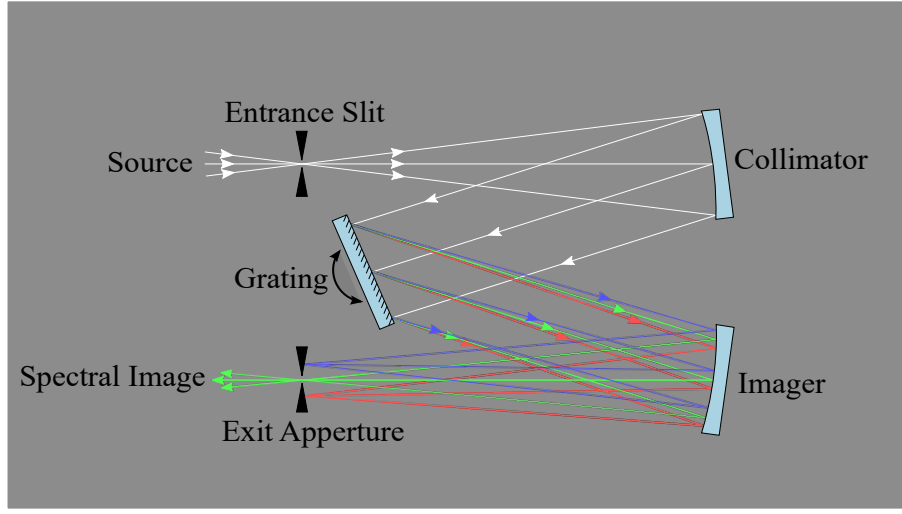


Figure 2.7: A simple reflection grating spectrograph with Czerny-Turner design

Distance between two slits is called pitch of the grating

The grating works on the principle of interference from multiple slits and diffraction from single slit to produce phase difference in the incident wave that constructively or destructively interfere at a point. Consider a reflective grating with each reflecting surface of size b , let the distance between the centers of two adjacent reflecting surface be ' a' ([Figure 2.8](#)). Each reflecting surface can be considered to be a slit of width b and the opaque non reflecting region in between can be considered to be the spacing between slits.

For rays i_1 and i_2 incident on the grating at an angle α with respect to the grating normal, phase difference between the rays is

$$a \times \sin(\alpha)$$

and the phase difference between rays r_1 and r_2 reflected at an angle β is

$$a \times \sin(\beta).$$

So the constructive interference at a point is given by

$$m\lambda = a (\sin(\alpha) + \sin(\beta)) \quad (2.1)$$

where m is the order for which wavelength λ constructively interferes at an angle β . The normalized intensity distribution of λ at different angles of incidence α and angles of reflection β is given by

$$I_\lambda(\theta) = \left(\frac{\sin^2 \left(\frac{aN\pi \sin(\theta)}{\lambda} \right)}{\sin^2 \left(\frac{a\pi \sin(\theta)}{\lambda} \right)} \right) \left(\frac{\sin^2 \left(\frac{b\pi \sin(\theta)}{\lambda} \right)}{\left(\frac{b\pi \sin(\theta)}{\lambda} \right)^2} \right) \quad (2.2)$$

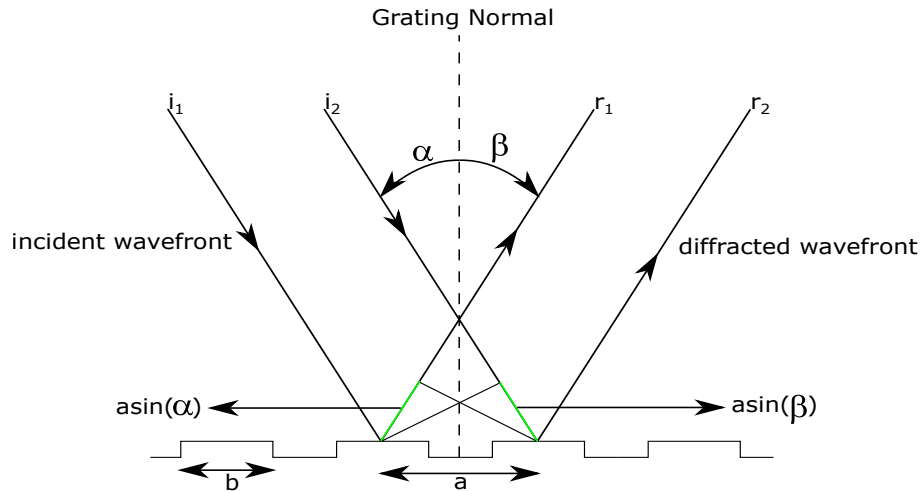


Figure 2.8: Grating working principle

$$= \text{Interference factor} \times \text{Blaze function}$$

where

$$\theta = \sin(\alpha) + \sin(\beta) \quad (2.3)$$

The first part of [Equation 2.1](#) $\left(\frac{\sin^2\left(\frac{aN\pi\sin(\theta)}{\lambda}\right)}{\sin^2\left(\frac{a\pi\sin(\theta)}{\lambda}\right)} \right)$ is the contribution of intensity due to interference of N slits and is a fast varying component. The second part of the equation $\left(\frac{\sin^2\left(\frac{b\pi\sin(\theta)}{\lambda}\right)}{\left(\frac{b\pi\sin(\theta)}{\lambda}\right)^2} \right)$ is the contribution of intensity due to diffraction of light from a single slit ([Kitchin \[54\]](#)). [Figure 2.9](#) is a plot of intensity pattern due to interference from 20 slits at an arbitrary wavelength λ . This pattern is modulated by the broader single slit diffraction pattern also called as the blaze function of the grating as shown in [Figure 2.10](#)

The interference factor (IF) determines the spectral resolution of the grating while the blaze function (BF) determines the efficiency of a grating at wavelength λ in the order m . Spectral resolution is defined from Rayleigh criteria as two wavelength points separated from each other such that the peak transmission of one lies in the minima of the other. In [Equation 2.2](#), I.F reaches minima for angular points

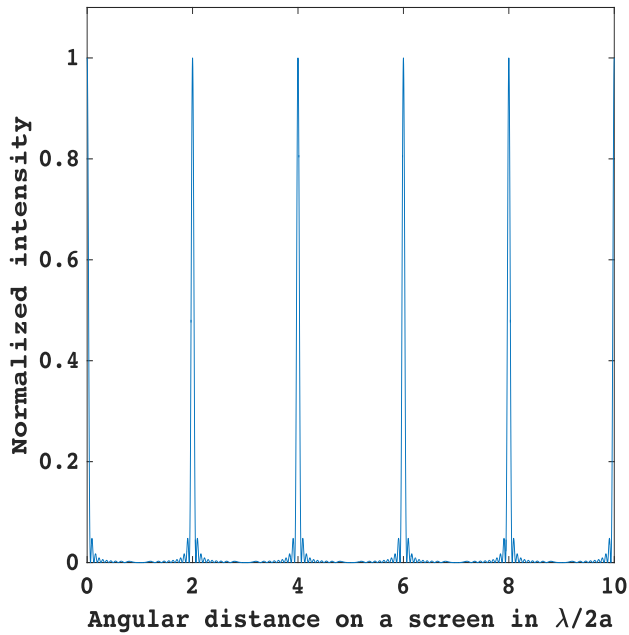


Figure 2.9: Intensity fringe pattern produced from interference of 20 slits. a is the distance between the centers of two slits

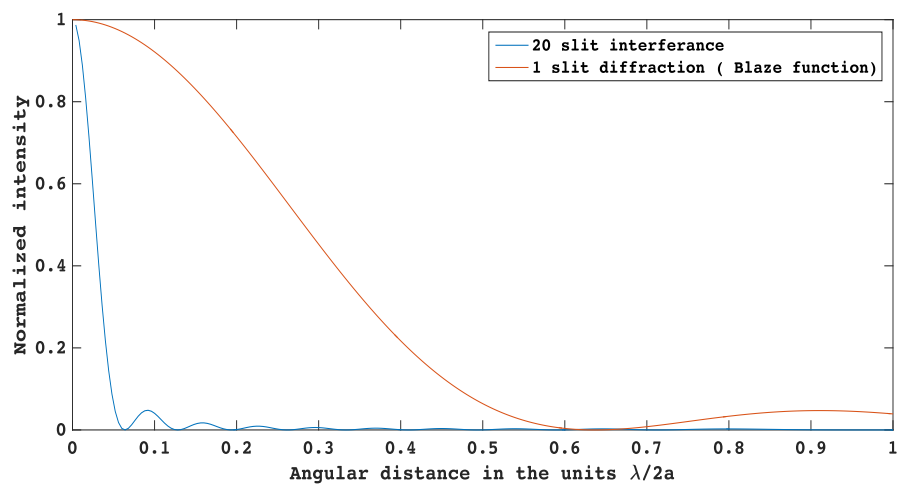


Figure 2.10: Interference pattern modulated by the single slit diffraction pattern

$$\left(\frac{aN\pi \sin(\theta)}{\lambda} \right) = n\pi,$$

except for $n = mN$. Then the angular width between the first minimas on either side of the wavelength maxima is given by

$$d = \frac{2\lambda}{aN\cos(\theta)}.$$

So the angular size for two spectrally resolved wavelength points from Rayleigh criteria is given by

$$s = \frac{\lambda}{aN\cos(\theta)} \quad (2.4)$$

and the spectral resolution is

$$r = s \frac{d\lambda}{d\theta} \quad (2.5)$$

Substituting [Equation 2.3](#) in [2.1](#) and differentiating it, spectral dispersion becomes

$$\frac{d\lambda}{d\theta} = \frac{a\cos(\theta)}{m}. \quad (2.6)$$

By substituting [Equation 2.4](#) in [2.5](#), we obtain the spectral resolution of the grating in terms of physical quantities that define the pitch and size of the grating

$$r = \frac{\lambda}{Nm}. \quad (2.7)$$

The resolving power of the spectrograph is

$$R = \frac{\lambda}{r} = Nm. \quad (2.8)$$

From [Equation 2.8](#), it can be seen that several combinations of N and m gives the same resolving power R . To achieve high R the grating should have a high groove density or operate at high orders but both can't be achieved simultaneously due to manufacturing constraints. This divides the grating design into two types. High groove density (N) holographic grating and high order (m) echelle grating. Holographic gratings have consistent efficiency over broad wavelength range. They are manufactured using interference pattern as a mask on the mirror surface coated with light sensitive material. The masked region is then etched away resulting in grooves which are sinusoidal in shape and results in low operating efficiency of the grating. Holographic grating can't be blazed to high angles due to this high spectral dispersion can't be achieved using this grating. On the contrary, echelle grating achieves high efficiency over a small wavelength region. Also mechanical ruling of the grating grooves allows for high blaze angles and spectral dispersion. As [MSSP](#) operates over

narrow wavelength bands of few angstrom and requires high spectral dispersion, echelle grating is the design choice for **MSSP**.

Echelle grating is a blazed grating whose slits or reflecting surface is tilted to a high degree with respect to the grating normal ([Figure 2.11](#)). As blaze function of a single slit determines the efficiency of the grating ([Equation 2.2](#)), blazing the grooves shifts peak efficiency from 0^{th} order to the blazed angle. Blaze function of [Equation 2.2](#) is modified to

$$BF = \frac{\sin^2 \left(\frac{\pi a \cos(\theta_B)}{\lambda} (\sin(\beta - \theta_B) + \sin(\alpha - \theta_B)) \right)}{\left(\frac{\pi a \cos(\theta_B)}{\lambda} (\sin(\beta - \theta_B) + \sin(\alpha - \theta_B)) \right)^2} \quad (2.9)$$

Echelles are operated in littrow configuration where $\alpha = \theta_B$. As the grooves are drawn mechanically using diamond cutters, the most commonly used blazing angle by the manufacturers for echelles are a standard value of 63.5^0 . With angle of incidence (α) and blaze angle (θ_B) fixed the only parameter needed for the design of our grating is groove size 'a' as it determines the order m from [Equation 2.1](#) and efficiency from [Equation 2.9](#) at which the spectrograph operates in wavelength λ . The spectrograph operates at highest efficiency at those wavelengths for which $\beta = \theta_B$ (from [Equation 2.9](#)), so the groove size is governed by the science goal of the instrument which determines the wavelength of operation of the spectrograph.

As mentioned in [Section 2.1](#), **MSSP** is intended to obtain spectro-polarimetric information from the photosphere and chromosphere. Fe I at 6302 Å or 15653 Å are good lines for diagnostics of photospheric vector fields (Rutten [[90](#)]) and Ca II at 8542 Å (Carlin and Ramos [[17](#)]) or He-I at 10830 Å (Rüedi et al. [[88](#)]) are chosen as diagnostics line for chromospheric magnetic field. Thus wavelength points for which **MSSP** is optimized are 6302, 8542, 10830 and 15653 Å. Consider [Equation 2.1](#) in littrow configuration for wavelength λ_0 diffracting at the blazed angle

$$m_0 \lambda_0 = 2a \times \sin(\theta_B),$$

for a wavelength point $\lambda = \lambda_0 \pm \Delta\lambda$ the order m can be numerically written as

$$m = \left[\frac{2a \times \sin(\theta_B)}{\lambda} \right].$$

Where [] implies round off to nearest integer and

$$\begin{aligned} \lambda \left[\frac{2a \times \sin(\theta_B)}{\lambda} \right] &= a(\sin(\theta_B) + \sin(\beta)), \\ \beta &= \sin^{-1} \left(\frac{\lambda}{a} \left(\left[\frac{2a \times \sin(\theta_B)}{\lambda} \right] \right) - \sin(\theta_B) \right). \end{aligned} \quad (2.10)$$

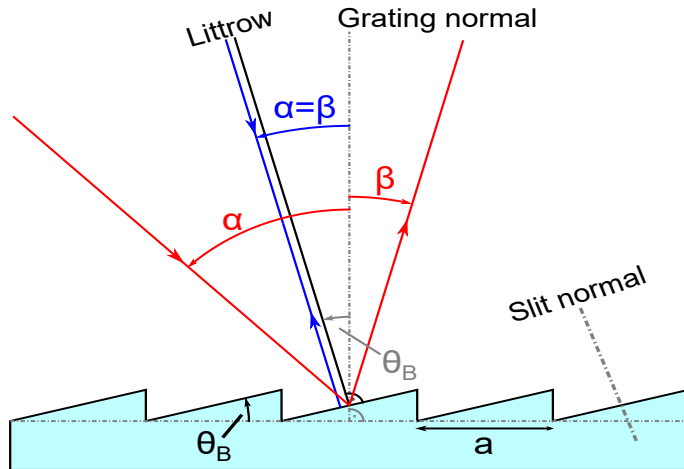


Figure 2.11: Blazed grating with blaze angle θ_B

WAVELENGTH	ORDER (M)	REGION	EFFICIENCY
Fe I line pair at 6302 Å	122	Upper Photosphere	99.57%
Ca II infrared line at 8542 Å	90	Lower Chromosphere	99.88%
He-I at 10830 Å	71	Middle to Upper Chromosphere	99.72%
Fe I at 15653 Å	49	Lower Photosphere	96.59%

Table 2.1: Wavelength order of operation for [MSSP](#)

Substituting [Equation 2.10](#) in [2.9](#) for the four wavelength points mentioned above, we get the groove size as $a = 42.9434 \mu\text{m}$ or groove density of 23.29 lines/mm for blaze function efficiency of 96 % in the spectral lines. The order and efficiency at which each of the four wavelengths operate in [MSSP](#) are given in [Table 2.1](#).

With the order of operation established, we now determine the number of grooves N which has to be illuminated to obtain the desired resolving power for [MSSP](#).

Optics for the spectrograph

In this section, the imaging optics for [MSSP](#) is designed and the number of slits that can be placed on the [FOV](#) of the “multi-slit” spectro-

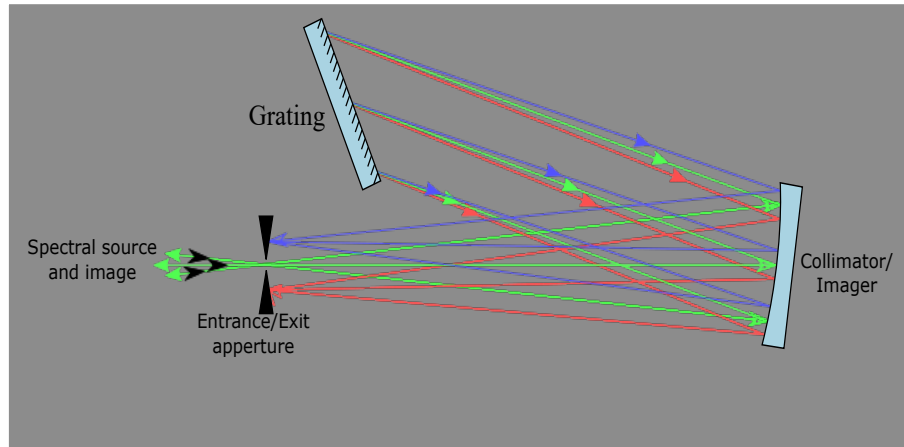


Figure 2.12: Schematic layout of spectrograph in Littrow configuration

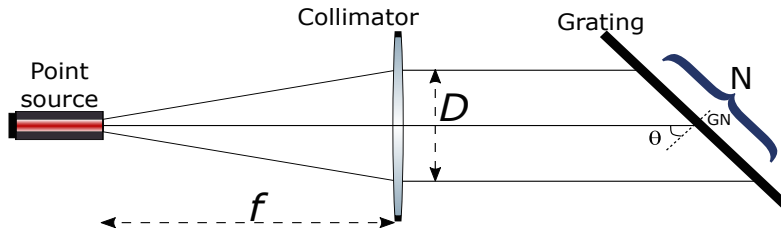
graph is also determined. The optical elements consist of entrance slit, collimator and imager for the grating (as shown in Figure 2.7) and imaging optics for the detector. The design starts off with a single entrance slit using which the focal length of the imager and collimator are determined. Then a DWDM filter is used as a prefilter as illustrated in Figure 2.4 to form a narrow wavelength band on the detector as shown in Figure 2.5. The linear dispersion of this narrow band spectra determines the number of slits that can be placed in the FOV.

2.2.2 Collimator and Imager

Echelle spectrographs are operated in Littrow configuration where the collimating and imaging optics is a single element. In the Littrow configuration the normal of grating's slit lies along the optical axis of the collimator/imager. Figure 2.12 is a schematic layout of spectrograph in littrow configuration. The only design parameter for the collimator/imager is its focal length. As the collimating and imaging optics have the same focal length, magnification of the system is unity.

The focal length is determined by the resolving power R of the grating and width of the entrance slit. From Equation 2.7, the spectral resolving power is determined by the order (m) of the diffracted wavelength λ and the number of grooves (N) illuminated by a point source on the grating. In a slit based spectrograph, the slit can be considered to be made up of a set of point sources that lie parallel to the groove lines. For a slit with width d placed at the entrance aperture, diffraction produced by the slit is

$$n\lambda = d \sin(\theta)$$



N - Number of grooves illuminated

GN - Grating normal

f - focal length of the collimator

D - Collimated beam width

Figure 2.13: Schematic layout of the Collimator

The intensity of light at an angular distance θ due to diffraction is given by

$$I(\phi) = I_0 \left(\frac{\sin(\phi)}{\phi} \right)^2,$$

where

$$\phi = \frac{\pi d \sin(\theta)}{\lambda}.$$

The percentage intensity content in the principle maxima is

$$I_p = \int_{-\pi}^{\pi} I(\phi) d\phi = 0.9028 I_0$$

As 90 % of the intensity lies in the principle maxima, the divergence of light from a point source in the slit can be considered to be equal to twice the angular distance of the first minima from the central maxima. In order to collimate this diverging beam of light the $f\#$ of the collimator must be equal to tangent of the divergence i.e.

$$f\# = \frac{f}{D} = \frac{1}{\tan(2\sin^{-1}(\frac{\lambda}{d}))} \quad (2.11)$$

Equation 2.11 forms the first criteria to determine the focal length of the collimator. The second criteria is the number of grooves that have to be illuminated in the grating. Consider Figure 2.13, a schematic layout of the slit (point source), collimator and grating for a beam of light collimated with a lens of focal length f , the number of grooves illuminated on the grating is

$$N = \frac{gD}{\cos(\theta)}, \quad (2.12)$$

PARAMETER	VALUE
Parent parabola's focal length	152.4 cm
Off axis distance (OAD)	20.32 cm
Diameter of off-axis mirror	25.4 cm
Zonal radius (ZR)	38.1 cm

Table 2.2: Specifications for off-axis parabolic mirror used in MSSP. The abbreviations used here are in accordance with Figure 2.14

where θ is the angle between the grating normal and the optical axis of the collimator. D is the width of the collimated beam and g is the groove density. Substituting Equation 2.12 in 2.11 we get

$$f = \frac{N \cos(\theta)}{g \times \tan(2 \sin^{-1}(\frac{\lambda}{d}))} \quad (2.13)$$

The slit width d is determined by the smallest spatial point which the spectrograph has to sample. The spatial resolution is proportional to observing wavelength. Fe I at 6302 Å is the smallest operating wavelength for MSSP so the slit size is determined based on the spatial resolution of MAST at this wavelength. The plate scale of the FOV at the entrance aperture of MSSP is 0.00528 arcsec/ μ m and the spatial resolution of the telescope is 0.317 arcsec. So the width of the slit needed to sample the spatially resolved point at Nyquist rate is $d = 30 \mu\text{m}$. It must be noted that this plate scale can be varied through magnification of the FOV¹.

Out of the four wavelength regions in Table 2.1, 6302 Å is used to obtain resolving power for MSSP. This is because of the current technological limitation in IR detectors. A large format IR detector has larger pixels than their visible counterparts. So higher spectral resolution at IR range becomes redundant as the detectors are incapable of recording the high resolution spectra.

In Equation 2.13, $\theta = \theta_B$ for littrow configuration. Substituting Equation 2.7 and Equation 2.12 in Equation 2.13, we get

$$f = \frac{\lambda \cos(\theta)}{g \times r \times m \times \tan(2 \sin^{-1}(\frac{\lambda}{d}))}. \quad (2.14)$$

From Equation 2.14, the minimum focal length of the collimator needed for MSSP at $\theta = 63.5^0$, $\lambda = 6302 \text{ \AA}$, $r = 20 \text{ m\AA}$, $g = 23.3 \text{ lines/mm}$, $m = 122$ and $d = 30 \mu\text{m}$ is $f = 117.648 \text{ cm}$.

The collimator/imager used in MSSP is an off-axis parabolic mirror manufactured by SORL® www.sorl.com. The mirror was bought off the shelf from SORL® with the specifications mentioned in Table 2.2.

¹ The platescale obtained here is governed by AO system placed ahead of MSSP. The actual plate scale of MAST is 10.31 arcsec/mm

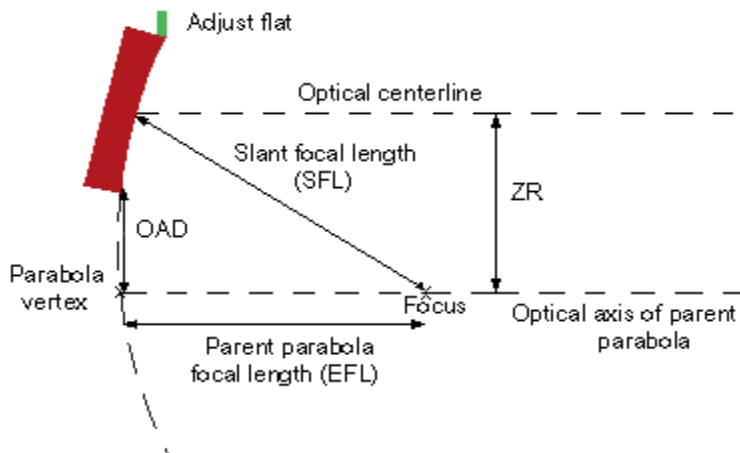


Figure 2.14: Schematic of off-axis-parabolic mirror

Figure 2.14 is the schematic of an off-axis parabolic mirror. The adjust flat is a plane mirror used to align the child's optical axis with parent parabola's optical axis. An off-axis system makes the spectrograph compact hence it was adopted in MSSP's design. It must be noted that this design for MSSP is one among the many possible designs. In Equation 2.14, the slit width d was taken to be $30 \mu\text{m}$ for a plate scale of $0.005528 \text{ arcsec}/\mu\text{m}$ but the plate scale can be magnified to a higher or lower value leading to a more compact or distributed system respectively.

2.2.3 DWDM filter and multi-slit entrance aperture

MSSP would have been a typical slit and grating based spectrograph with the standard components and detector. But the prefilter used in this spectrograph sets it apart from a standard spectrograph. The prefilter has also enabled the placement of multiple slits in the FOV. Technological advancements in fiber optical communication helped in the development of a thin film based filter called DWDM filter. In this section, the working principle of DWDM filter is described. The number of slits that can be placed on the FOV due to DWDM's filter response and spectral dispersion of the grating used in MSSP are determined.

Dense wavelength division multiplexing is a technique used in fiber optical communication systems to increase the volume of transmitted data over an optical fiber. Optical fibers have the capacity to carry large quantity of data using a relatively small transmission path. A single mode fiber has only $8 \mu\text{m}$ thick cores and are capable of transmitting data with very little loss over several hundred kilometers. Data rates of 10 Gbps and higher are transmitted through the fiber in the C and L band with modern fibers.

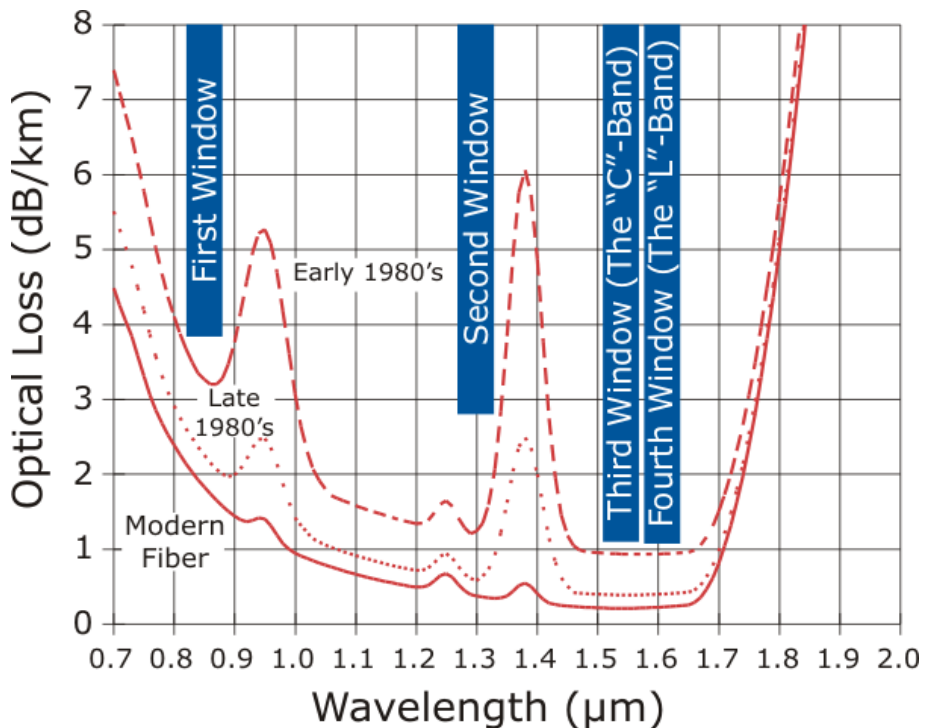


Figure 2.15: Transmission window for glass core optical fiber used in optical communication

Although the data link (which is an optical fiber) had the capacity to carry large data volume, the transmitting sub systems were incapable of delivering this load onto the fiber link. The transmitters were made up of LEDs (light emitting diodes) or wavelength tunable laser cavities. Consider a transmission/reception band like L-band (Figure 2.15) which has a 100 nm bandwidth. The number of data channels that can be transmitted in this band depends on the number of non-overlapping wavelength bands, where each wavelength band corresponds to one channel. LEDs emit light pulses in a broad wavelength range with low power. So a single data transmission channel occupies a large section of the bandwidth and due to low power in transmitted signal, repeaters have to be used frequently. Tunable lasers on the other hand are highly monochromatic so the bandwidth occupied per channel is small. But at a given instance in time, only one laser at a particular wavelength can transmit as it is physically linked to the fiber while another lasers/data transmitters of the same or different wavelength have to be in stand by mode. Due to this a large portion of the bandwidth (L-band in this case) remains unoccupied at any given instance of time. A solution to this problem is to transmit data over multiple channels by wavelength multiplexing several monochromatic laser cavities of slightly different wavelength and non overlapping bandwidth as a single broadband channel. The multiplexed waveband is then physically linked to the fiber enabling multiple lasers/data transmitters to operate simultaneously.

PARAMETER	VALUE
Central wavelength	$6302 \text{ \AA} \pm 0.1 \text{ \AA}$
Pass band (3 dB)	$6 \text{ \AA} \pm 0.1 \text{ \AA}$
Transmission efficiency	80 %
Operating temperature	21°C

Table 2.3: Specifications of DWDM filter used for Fe I at 6302 \AA

This can be perceived with an analogous example. A prism disperses white light into component wavelengths that travel at different angle. Conversely if light from individual wavelength components are incident on the prism at their respective angles of dispersion, they combine into a beam of broad wavelength band as shown in [Figure 2.16](#). In this figure, S_{1-3} are individual sources of polychromatic light that carry data and the prism acts like a wavelength multiplexer and combines the data from these sources into a single band of light. All the three sources can operate simultaneously and the data transmitted by them can be received at the output without ambiguity. In fiber optical communication this light multiplexing is achieved by several ways. One among them is a thin film multiplexer where thin film coatings with variable thickness, refractive index and spacing are used to generate a transmission band (Gerken and Miller [38], Ozoliņš, Bobrovs, and Ivanovs [75], and Yafei Ren et al. [133]).

A thin film DWDM response is shown in [Figure 2.17](#). The filter has a flat top response with a sharp fall-off in transmission at the band stop frequencies f_1 and f_2 . So the filter response is effectively a rectangle with high transmission in the pass band and high attenuation in the band stop region. This technology can be adopted in the field of solar astronomy where a flat top filter is used as a prefilter in a spectrograph to transmit specific wavelength regions while blocking the rest of the band. The illustration in [Figure 2.4](#) and [Figure 2.5](#) shows a DWDM filter transmitting Fe I line pair while attenuating the rest of the wavelength band. A typical spectral profile for Fe I taken from a spectrograph using DWDM filter would look like [Figure 2.18](#). The filter response is compared with the commonly used Fabry-Pérot type interference filter for wavelength selection in spectrographs.

2.2.3.1 DWDM for MSSP

The spectrograph currently operates for Fe I line pair at 6301.5 \AA and 6302.5 \AA . An upgrade will be performed in the future such that MSSP can operate in other wavelengths mentioned in [Table 2.1](#). The DWDM filter used in MSSP has the specifications mentioned in [Table 2.3](#).

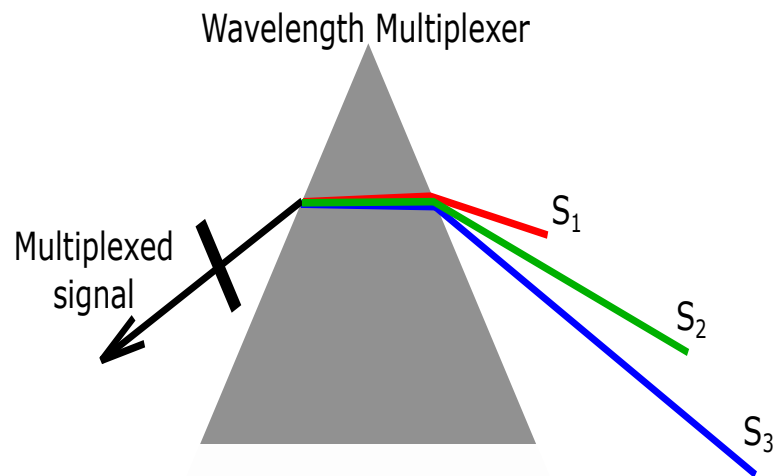


Figure 2.16: Prism as wavelength multiplexer

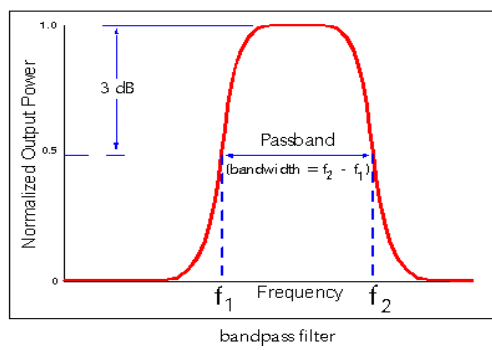


Figure 2.17: DWDM filter response function

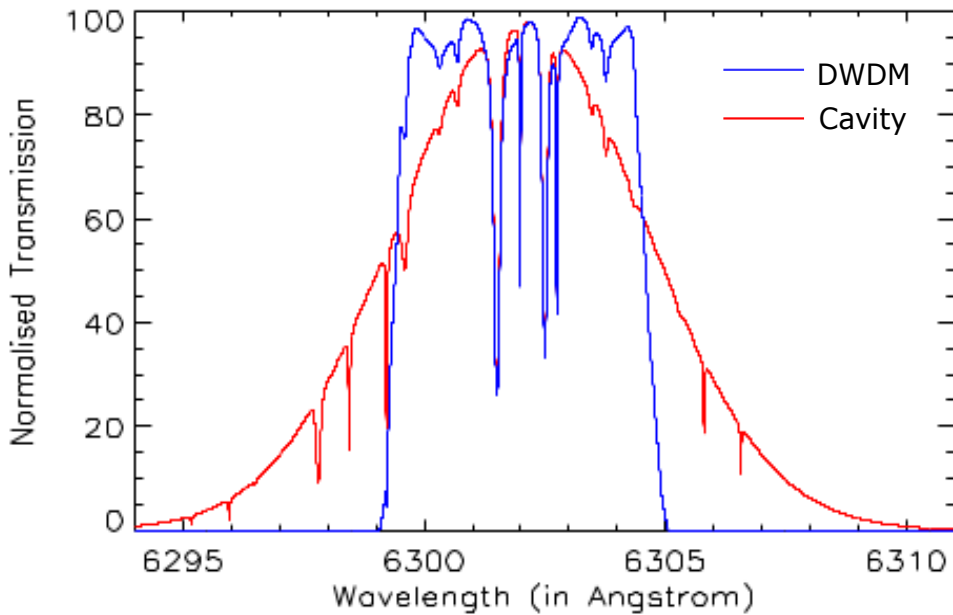


Figure 2.18: Comparison of spectral transmission for DWDM filter and a more commonly used cavity type filter on Fe I line pair

Multi-slit entrance aperture and MSSP modes of operation

MSSP operates in two modes -

- Small FOV diffraction limited mode for 3 arcmin field
- Large FOV non diffraction limited mode for 6 arcmin filed

The number of slits on the FOV is determined from the large field mode of operation for MSSP. The concept of multi-slit and its implementation in MSSP is described below.

In a Littrow configuration the magnification of the system is unity. For a littrow spectrograph using a mirror system for collimation and imaging, the image plane lies on the entrance slit and it consists of a spectrally dispersed image of the slit. Although the spectral image of the slit occupies a large section in the spectral direction, addition of a prefilter reduces the size of the spectra to a small width (Figure 2.5). If a person sees into the spectrograph through the entrance slit aperture, the slit spectra appears to “occupy” certain portion of the FOV on the entrance aperture around the region of the original slit (Figure 2.19). The width D of the single slit spectra on the FOV depends on two parameters, they are linear spectral dispersion of the spectrograph and band pass of the prefilter.

Angular spectral dispersion of a grating is the angular spread in the wavelength of light at a given diffracted angle of the beam. For a constant angle of incidence, the dispersion of the grating is obtained by differentiating Equation 2.1 as a function of wavelength

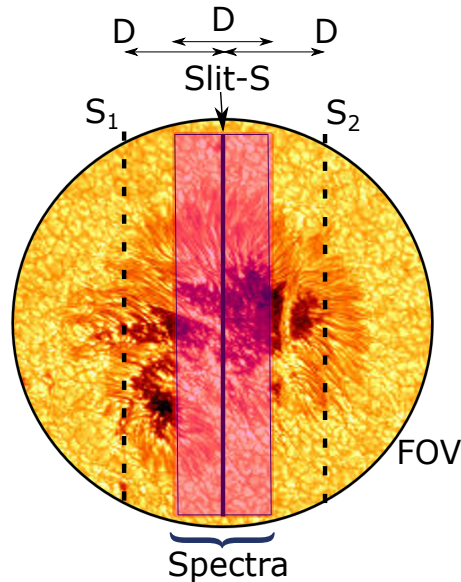


Figure 2.19: Conceptual diagram of multiple slit on the **FOV**. The shaded region of width 'd' is the spectral image of slit-s formed on the entrance aperture. The next slit S_1 or S_2 is placed at distance d from the slit-s to avoid any spectral overlap between the slits

$$\frac{d\beta}{d\lambda} = \frac{m}{a \cos(\beta)},$$

by using [Equation 2.1](#)

$$\frac{d\beta}{d\lambda} = \frac{\sin(\alpha) + \sin(\beta)}{\lambda \cos(\beta)}$$

and linear spectral dispersion on the slit is

$$\frac{dl}{d\lambda} = \frac{f(\sin(\alpha) + \sin(\beta))}{\lambda \cos(\beta)}.$$

Where f is the focal length of the collimator/imager.

For **MSSP** operating at 6302 \AA , linear dispersion will be $\frac{dl}{d\lambda} = 0.95 \text{ mm/\AA}$. The **DWDM** prefilter has a pass band of 6 \AA so the spatial distance occupied by spectral band of a single slit as shown in [Figure 2.19](#) is $d = 5.7282 \text{ mm}$. Hence for an extended field, the next slit can be placed 5.7282 mm away from the 1^{st} slit. If the 1^{st} slit lies at the center of the **FOV** then two slits can be placed on either sides of the 1^{st} slit at a distance of d each as shown in [Figure 2.19](#).

As mentioned earlier **MAST** can operate in two modes. Large field mode with 6 arcmin **FOV** and small field mode with 3 arcmin **FOV**. In large field mode the **AO** system generates an $f/48$ beam with a plate scale of 8.333 arcsec/mm . The 6 arcmin field forms a circular region with

PARAMETER	VALUE
Number of slits	5
Slit width	$30 \mu\text{m} \pm 2 \mu\text{m}$
Slit height	$30 \text{ mm} \pm 3.5 \text{ mm}$
Slit separation	$5.8 \text{ mm} \pm 15 \mu\text{m}$
Minimum scan steps on FOV	194
Field sampled per slit ($f/48$)	0.257 arcsec for 6 arcmin
Field sampled per slit ($f/75$)	0.16 arcsec for 3 arcmin

Table 2.4: Specifications of Multi-slit used in MSSP

a diameter of 43.2 mm on the entrance aperture. For uniform illumination on each of the slit, a square region of length $l = 30.54 \text{ mm}$ is taken in the circular FOV. As the spectral dispersion is $d = 5.7282 \text{ mm}$, MSSP has 5 slits with a separation of 5.8 mm between each slit. The height of each slit is equal to the length of the square region in the FOV. The multi-slit used in MSSP is a chemical etched reflective front surface glass slab with a thickness of 2 cm. It is manufactured by EdmundOptics® <https://www.edmundoptics.com>. Table 2.4 summarizes the specifications of the multi-slit used in the spectrograph.

In 6 arcmin mode, all the slits are illuminated uniformly. The FOV is raster scanned on the slits with a step size equal to the slit width to generate an image of the field. As a rectangular region is scanned over a circular field, the resulting image does not contain the entire 6 arcmin FOV but a square field of 4.2464 arcmin. An illustration of 6 arcmin field with multi-slits is shown in Figure 2.20. The raster scan direction of the FOV is also indicated.

In 3 arcmin high resolution mode, the input beam on the entrance aperture is an $f/75$ beam with a plate scale of 5.333 arcsec/mm . Each slit samples a region of 0.16 arcsec on the FOV which corresponds to the Nyquist rate at diffraction limit for MAST. In this mode the field does not illuminate all the slits uniformly and occupies a smaller region on the slit. But the entire field is recorded producing a 3 arcmin circular field. An illustration of 3 arcmin field on the multi-slit is shown in Figure 2.21. The regions chosen in Figure 2.20 and Figure 2.21 corresponds to 3 and 6 arcmin on the Sun respectively.

The number of scan steps needed for the raster scanner to cover the whole field is equal to the number of slits that can be placed between two adjacent slits. As the distance between two adjacent slits is 5.8 mm, 193.33 slits of $30 \mu\text{m}$ width can be placed between two slits or 194 scan steps are needed to cover the FOV.

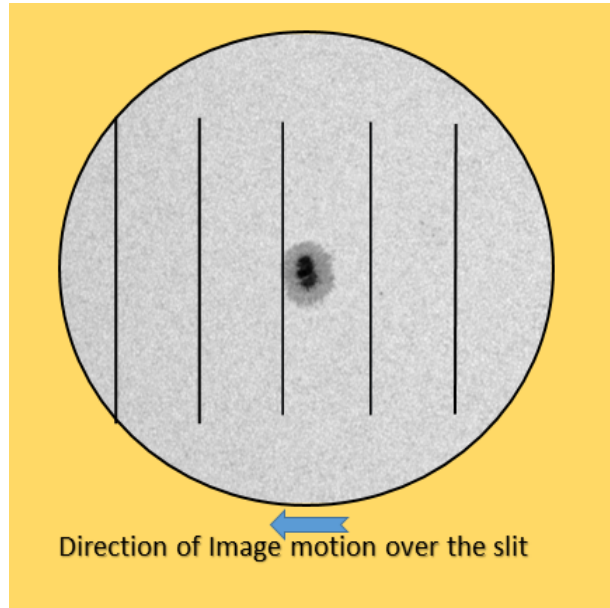


Figure 2.20: 6 arcmin field drawn to scale with multi-slit. The sunspot is NOAA 12526 taken on 31st Mar 2016 from [HMI](#)

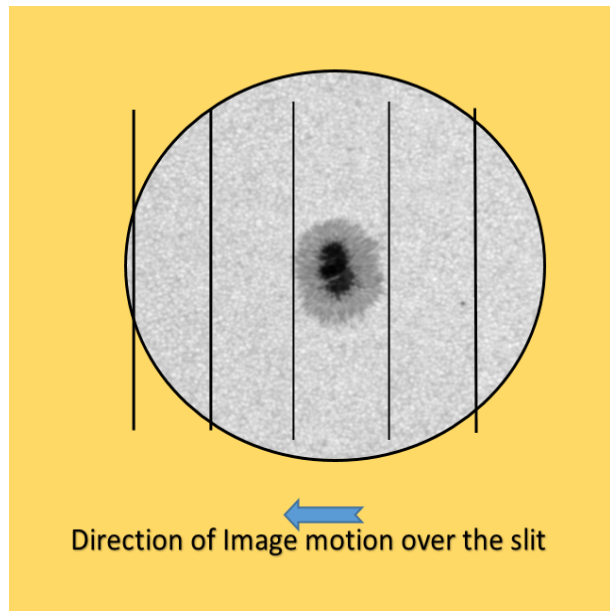


Figure 2.21: 3 arcmin field drawn to scale with multi-slit. The sunspot is NOAA 12526 taken on 31st Mar 2016 from [HMI](#)

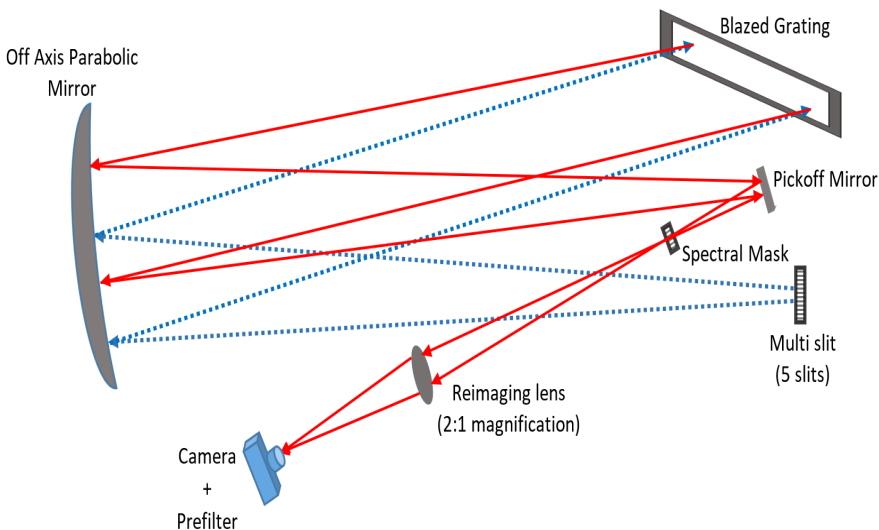


Figure 2.22: Schematic layout of the spectrograph section of MSSP with pick-off mirror and spectral mask

2.2.4 Optics for the detector unit

The spectra is formed at the entrance aperture of the spectrograph with a small offset given by [Equation 2.1](#). But the multi-slit aperture of MSSP occupies a region of $30\text{ cm} \times 30\text{ cm}$ which has an overlay with the spectral image. Thus a detector system with DWDM filter cannot be accommodated at the first image plane. A pickoff mirror (a plane mirror) is used to divert the spectral beam away from the slit and a re-imaging lens is used to image the spectra in the first image plane onto the detector or second image plane. The re-imaging optics serves two purposes

- Magnifies or demagnifies the spectral image produced by the spectrograph to accommodate it onto the detector chip
- Allows for the placement of spectral mask in the first image plane to block unwanted spectra

A schematic layout of the spectrograph with a pickoff mirror, spectral mask, prefilter and detector is shown in [Figure 2.22](#). The detector used for the detection of Fe I at 6302 \AA is pco.2000 from pco.[®] <https://www.pco.de>. It is a charge coupled device with 2048×2048 imaging elements of the size $7.4\mu\text{m} \times 7.4\mu\text{m}$.

For a 2048×2048 detector with pixel size of $7.4\mu\text{m}$ the detection area of the CCD chip is $15.15\text{ mm} \times 15.15\text{ mm}$. But the spectral image occupies an area of $30\text{ mm} \times 30\text{ mm}$. So the re-imaging lens has to de-magnify the spectra by two times. A biconvex lens with a focal length of 250 mm is used for the purpose of reimaging the spectra onto the detector. The purpose of a spectral mask and its use in polarimetric measurements are described in [Section 2.3.2.1](#)

PARAMETER	VALUES
Type	CCD with AR
Pixel size	$7.4 \mu\text{m} \times 7.4 \mu\text{m}$
Number of pixels	2048×2048
Dynamic range	14 - bits

Table 2.5: CCD detector specifications used for the Fe I line pair at 6302\AA

2.3 POLARIMETER UNIT FOR MSSP

Unlike the spectrograph a polarimeter unit is designed specifically for an individual spectral band. [MSSP](#) currently operates at 6302\AA and the polarimetric unit is designed for that wavelength. A polarimeter unit consists of a modulator and an analyzer. In this section the modulation scheme chosen for [MSSP](#) and the implementation of dual beam analyzer system are discussed.

Photosphere is the visible layer of the solar atmosphere where the optical depth of a photon reaches unity i.e. the photon's mean free path is greater than the distance of the atmosphere that lies ahead of it. So the photosphere is the first visible layer of the Sun at which field parameters can be estimated through remote sensing. Characterizing the properties of photosphere in terms of velocity, temperature and magnetic field plays a vital role in determining the physical parameters at higher layers in the solar atmosphere and the coupling between layers. There are many parameters that couple different layers of the solar atmosphere, magnetic field is one such coupling parameter (Lin [65] and Nordlund, Stein, and Asplund [74]). It is believed that they transport energy from lower layers of the atmosphere and deposit them in the upper layers (one of the plausible reasons for coronal heating) and most of the energy transport is contributed from small scale magnetic field. Magnetic field on the photosphere goes from tens of Gauss in the quiet Sun region to few thousands of Gauss in the umbral region of a sunspot. But quiet Sun magnetic fields are the pre-dominant regions where most of the global solar magnetic field is present (Bellot Rubio and Beck [11] and SuÁrez et al. [115]). It is therefore desirable to measure magnetic field of quiet Sun upto the resolving limit of the telescope. The strongest of quiet Sun magnetic fields lie in the network region. However there are two arguments: one which states that high fields of about 1.3 kG exist in small regions with the remaining part of the quiet Sun surrounding this small region being truly quiet (Socas-Navarro and Sanchez Almeida [107]) while a contradicting argument states that most parts of the quiet Sun is made up of low fields of about 400 G while the rest of the region is truly quiet (Lin and Rimmele [67]). Thus more observations of such regions are needed for better understanding of

the magnetic field distribution on the Sun. Magnetic field is measured through the Zeeman effect and anomalous Zeeman effect produced by a radiating element under the influence of magnetic field. These radiations are polarized in nature and measuring their polarization gives a direct handle on the field strength and orientation. A polarimetric accuracy of 0.1 % is necessary to measure field strength of few hundred Gauss (Lin and Rimmele [67]). Thus we design a polarimeter which has equal efficiency in measuring all the Stokes parameters with the measurements taken at high accuracy.

An optical detector is incapable of measuring polarization of light. So a polarimeter is used to modulate or convert the polarization information of light into variation in intensity which is then detected by detector. The modulated intensity is then demodulated back during post-processing to obtain the polarization information. Polarization of light can be represented using four Stokes parameters

$$\begin{pmatrix} I \\ Q \\ U \\ V \end{pmatrix},$$

where I is the total intensity of light, Q and U gives the degree of linear polarization and the orientation of the plane of linear polarization, V is a measure of the direction of rotation of the plane of polarization with time i.e. circular polarization. Among these four parameters only I can be recorded by a detector. The polarimeter unit embeds the information content of other Stokes parameters into the intensity parameter. This process of embedding the information of one parameter into another parameter is called modulation. The efficiency with which one signal gets embedded into the other determines the efficiency of the modulator and the lowest polarization signal that can be measured by the polarimeter.

The modulation calculation is performed via the Mueller matrix of the optical elements used in a polarization modulator. A polarization modulator consists of a retarding element and a polarizing element. The retarding element modulates linear polarization into circular polarization or vice - versa and linear into linear polarization i.e. modulation between Stokes Q and U. The polarizing element modulates linear polarization into intensity and vice - versa. Hence a combination of retarder and polarizer can modulate any Stokes vector into any other Stokes vector. But our parameters of interest are Q, U, V modulation into I. Mueller matrix of a retarder of retardance δ and fast axis angle θ to the polarizer optical axis is

$$M_R(\delta, \theta) = \begin{pmatrix} 1 & 0 & 0 & 0 \\ 0 & g + h\cos(4\theta) & h\sin(4\theta) & -\sin(\delta)\sin(2\theta) \\ 0 & h\sin(4\theta) & g - h\cos(4\theta) & \sin(\delta)\cos(2\theta) \\ 0 & \sin(\delta)\sin(2\theta) & -\sin(\delta)\cos(2\theta) & \cos(\delta) \end{pmatrix} \quad (2.15)$$

where,

$$g = \frac{1}{2}(1 + \cos(\delta)),$$

$$h = \frac{1}{2}(1 - \cos(\delta)).$$

The Mueller matrix of polarizer at an angle ϕ to polarization reference axis is

$$M_P(\phi) = \frac{1}{2} \begin{pmatrix} 1 & \cos(2\phi) & \sin(2\phi) & 0 \\ \cos(2\phi) & \cos^2(2\phi) & \sin(2\phi)\cos(2\phi) & 0 \\ \sin(2\phi) & \sin(2\phi)\cos(2\phi) & \sin^2(2\phi) & 0 \\ 0 & 0 & 0 & 0 \end{pmatrix}. \quad (2.16)$$

2.3.1 Modulator

The retarder is a major component of the polarimeter. Retarder along with the polarizer modulates polarization of light as shown in [Equation 2.17](#).

$$\begin{pmatrix} I' \\ Q' \\ U' \\ V' \end{pmatrix} = [M_P] \times [M_R] \times \begin{pmatrix} I \\ Q \\ U \\ V \end{pmatrix}, \quad (2.17)$$

where

$$I' = aI + bQ + cU + dV$$

Here I' is the modulated intensity containing the information of all Stokes parameters. For [Equation 2.17](#) variation in ϕ, δ, θ in [Equation 2.15](#) and [Equation 2.16](#) gives several I' such that a system of linear equations can be formed as

$$\begin{pmatrix} I'_1 \\ I'_2 \\ I'_3 \\ I'_4 \\ \vdots \end{pmatrix} = \begin{pmatrix} a_1 & b_1 & c_1 & d_1 \\ a_2 & b_2 & c_2 & d_2 \\ a_3 & b_3 & c_3 & d_3 \\ a_4 & b_4 & c_4 & d_4 \\ \vdots & \vdots & \vdots & \vdots \end{pmatrix} \begin{pmatrix} I \\ Q \\ U \\ V \end{pmatrix} \quad (2.18)$$

$$= [O] \begin{pmatrix} I \\ Q \\ U \\ V \end{pmatrix}$$

The coefficients matrix in [Equation 2.18](#) is a $n \times 4$ matrix called the modulation matrix (O) and its inverse is the demodulation matrix (D). The modulation matrix determines how and to what extent a Stokes parameter gets modulated on to intensity. So the modulation efficiency or the extent of modulation defined as

$$E = O^T O,$$

where O^T is the transpose of the modulation matrix O . If $\varepsilon_i, \varepsilon_q, \varepsilon_u, \varepsilon_v$ are the efficiencies of I, Q, U, V respectively then there exists a modulation matrix called optimum modulation matrix for which

$$E = n \begin{pmatrix} \varepsilon_i^2 & 0 & 0 & 0 \\ 0 & \varepsilon_q^2 & 0 & 0 \\ 0 & 0 & \varepsilon_u^2 & 0 \\ 0 & 0 & 0 & \varepsilon_v^2 \end{pmatrix},$$

where

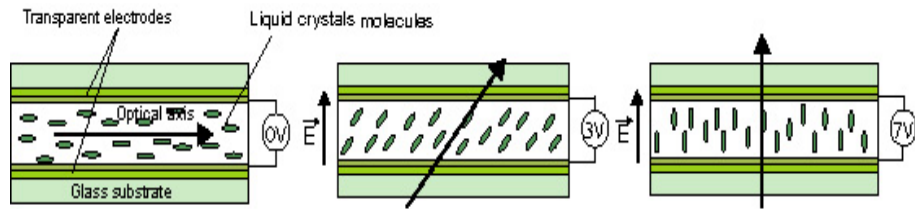
$$\varepsilon_i = 1,$$

and

$$\sum_{q,u,v} \varepsilon^2 = 1.$$

According to the specifications for [MSSP](#), it is necessary to detect all Stokes parameters at the same significance level or equal efficiency. An optimum modulation matrix with equal modulation efficiency is called the balanced modulation matrix. For a four step balanced modulation, the modulation matrix looks like

$$O = \begin{pmatrix} 1 & 1/\sqrt{3} & 1/\sqrt{3} & 1/\sqrt{3} \\ 1 & 1/\sqrt{3} & -1/\sqrt{3} & -1/\sqrt{3} \\ 1 & -1/\sqrt{3} & 1/\sqrt{3} & -1/\sqrt{3} \\ 1 & -1/\sqrt{3} & -1/\sqrt{3} & 1/\sqrt{3} \end{pmatrix}, \quad (2.19)$$



Orientation of the LC molecules (or optical axis) in the phase retarder in function of the applied tension. For 0 V (a), 3 V (b), 7 V (c).

Figure 2.23: Working principle of **LCVR**. An increase in potential makes the molecules get aligned to the direction of electric field. This is also known as Kerr effect.

or

$$O = \begin{pmatrix} 1 & -1/\sqrt{3} & -1/\sqrt{3} & -1/\sqrt{3} \\ 1 & -1/\sqrt{3} & 1/\sqrt{3} & 1/\sqrt{3} \\ 1 & 1/\sqrt{3} & -1/\sqrt{3} & 1/\sqrt{3} \\ 1 & 1/\sqrt{3} & 1/\sqrt{3} & -1/\sqrt{3} \end{pmatrix}, \quad (2.20)$$

where the efficiency of Stokes Q, U, V is $\epsilon = \frac{1}{\sqrt{3}}$.

A combination of [Equation 2.19](#) and [Equation 2.20](#) can be used to achieve beam exchange or beam swapping technique (Semel, Donati, and Rees [101]) where the seeing induced polarization cross-talk is minimized by measuring both the positive and negative states of polarization.

The modulator used in **MSSP** is a pair of Liquid Crystal Variable Retarder (**LCVR**s) bought off the shelf from Meadowlark optics® <http://www.meadowlark.com>. An **LCVR** is made up of liquid crystals that are sensitive to electric field. Applying an electric field across a molecule of liquid crystal orients the molecule in the direction of the field ([Figure 2.23](#), the Kerr effect). As a liquid crystal is chiral, change in orientation of the molecule changes the refractive index of the material in one direction while keeping it constant in the perpendicular direction. This change in refractive index is used to generate retardance in a beam traveling through the liquid crystals. The axis of an **LCVR** defined as θ in [Equation 2.15](#) is along the longest dimension of a molecule of liquid crystal when no potential is applied across the molecule (shown in 1st diagram of [Figure 2.23](#)). For a fixed orientation angle θ , retardance δ is varied to modulate light.

For **MSSP** two **LCVR**s are used at an orientation of $\theta_1 = 0^\circ$ and $\theta_2 = 45^\circ$ with respect to the analyzer ($\phi = 0^\circ$) as shown in [Figure 2.24](#). [Equation 2.15](#) is solved for those values of δ which gives the elements of balanced modulation matrix in [Equation 2.18](#). The retardance values δ_1 and δ_2 which satisfy [Equation 2.19](#) are given in [Table 2.6a](#) and the retardance which satisfy [Equation 2.20](#) are given in [Table 2.6b](#). **LCVR**s inherently cannot attain $\delta = 0^\circ$ as very large potentials are

needed to align all the molecule of the liquid crystal along the field. A typical retardance range of an [LCVR](#) manufactured for visible range or IR is around 45^0 to 315^0 . It can be seen from [Table 2.6](#) that the balanced modulation scheme is generated within the working range of a non-compensated [LCVR](#). Thus a polarimeter for other wavelength bands of [MSSP](#) can be easily implemented with off-the-shelf components from a manufacturer and no customization is necessary for it.

Set-1	1	2	3	4
δ_1	45^0	135^0	135^0	225^0
δ_2	54.74^0	125.26^0	234.74^0	54.74^0

(a) Retardance of [LCVR-1](#) and [LCVR-2](#) which satisfy [Equation 2.19](#)

Set-2	1	2	3	4
δ_1	45^0	135^0	135^0	45^0
δ_2	234.74^0	305.26^0	54.74^0	125.26^0

(b) Retardance of [LCVR-1](#) and [LCVR-2](#) which satisfy [Equation 2.20](#)

Table 2.6: Retardance values of [LCVR](#) for balanced modulation

2.3.2 Analyzer

The analyzer is a polarizer which converts light modulated by the modulator into variation in intensity. The orientation of the analyzer defines the axis of the polarimeter unit and all Stokes parameters are defined with respect to that axis. The analyzer used in [MSSP](#) is a dual beam polarizer which produces two orthogonal states of polarization. I discuss the uses of dual beam and the technique of spectral masking used to implement dual beam polarization in [MSSP](#).

The atmosphere is a turbulent system. A plane wavefront (wave with constant phase) emitted from a source in the sky gets distorted in phase as it passes through this turbulent atmosphere. The phase distorted wavefront causes scintillation of the image of the source. As it was mentioned earlier, the detector is sensitive only to the intensity and variation in intensity of light. So during polarimetric measurements, any fluctuation in intensity caused due to scintillation results in crosstalks among Stokes parameters and a wrong interpretation of the source polarization. As intensity is the strongest signal among all four Stokes parameters, a crosstalk from intensity into other three Stokes parameters is very problematic and makes the polarimeter in-

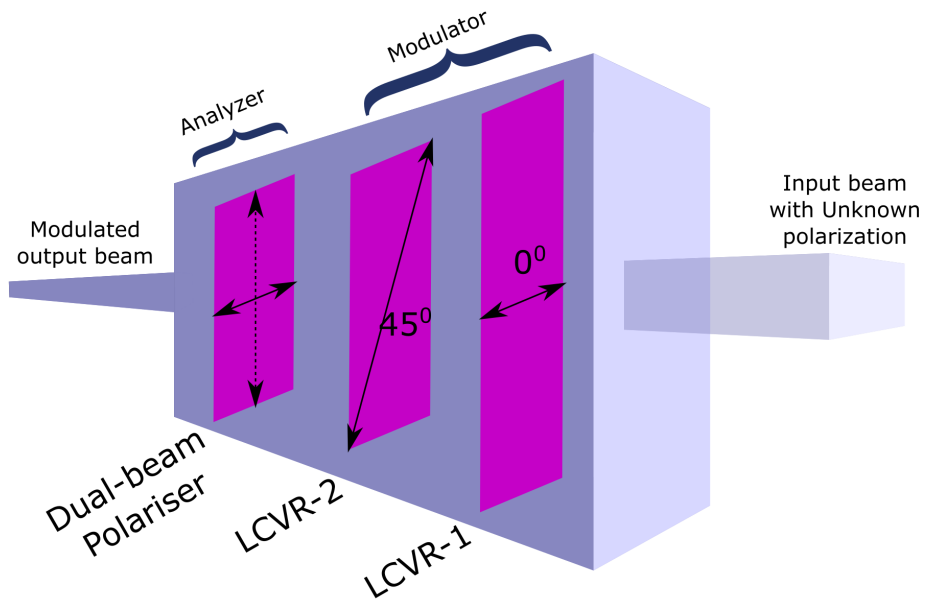


Figure 2.24: Schematic drawing of polarimeter unit used in [MSSP](#)

capable of detecting weak polarization signals. Consider a source S with polarization states

$$S_i(t) = R_i [1 + \beta_i N(t)]$$

where $i = I, Q, U, V$. R_i is the source signal for undistorted wavefront, β_i is the gradient or variation in the intensity of source at different location. For a point source β_i is unity at the source and zero away from it. $N(t)$ is the atmospheric turbulence at some time instance t. If this source is modulated by a polarimeter with [LCVR](#) as modulator, then the resultant Stokes vector at the output of the polarimeter is

$$O_{\delta i}(t) = [M(\delta)] S_i(t) \quad (2.21)$$

From [Equation 2.16](#) for two analyzers orthogonal to each other [Equation 2.21](#) becomes,

$$O_{\delta i}(t) = -O'_{\delta i}(t), \quad (2.22)$$

for $i = Q, U, V$ and

$$O_{\delta I}(t) = O'_{\delta I}(t), \quad (2.23)$$

for Stokes intensity. It can be seen that by combining the output of two orthogonal analyzers crosstalk from Stokes I into normalized Stokes

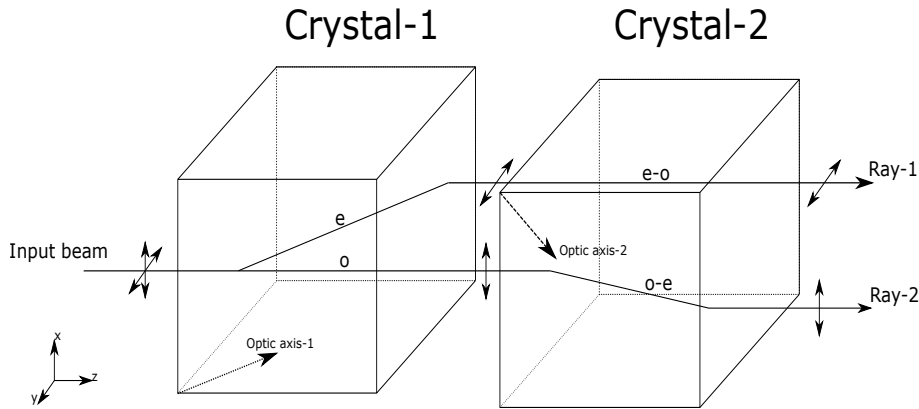


Figure 2.25: Dual beam analyzer schematic drawing for MSSP. o and e-o represents ordinary ray, e and o-e represents extra-ordinary ray

parameters Q/I , U/I , V/I is eliminated (Elmore et al. [27] and Lites [69]).

Dual beam analyzer for MSSP is made up of two calcite polarizing beam displacers placed orthogonal to each other as shown in Figure 2.25. A ray of unpolarized light gets split into two orthogonally polarized rays. One ray is the ordinary ray (o) and the other ray is extra-ordinary (e). The angular displacement η of the e-ray with respect to the o-ray for a positive birefringence crystal is given by,

$$\tan(\eta) = \left(1 - \left(\frac{n_e}{n_o}\right)^2\right) \left(\frac{\tan(oa)}{1 + \left(\frac{n_e}{n_o}\right)^2 \tan(oa)} \right), \quad (2.24)$$

where n_e and n_o are the refractive index for e-ray and o-ray respectively and oa is the angle between o-ray and optical axis of the crystal. It can be seen in Figure 2.25 that for a single crystal, e-ray travels longer distance compared to o-ray due to which the focal plane of e and o images do not lie on the same plane. In order to compensate for the additional path length, a second crystal is introduced in the beam where the roles of o and e ray flip forming o-e and e-o rays. The second crystal introduces additional path length to o-e ray and the resultant image formed by o-e ray and e-o ray lie on the same plane. If d is the linear displacement between o and e-ray from a single crystal then the total displacement of the two crystal system is $d\sqrt{2}$.

2.3.2.1 Spectral mask

In MSSP the spectral image occupies an area of $15 \text{ mm} \times 15 \text{ mm}$ on the detector plane. But not all of the spectral band provides useful information. Consider Figure 2.26, the Fe I line pair occupy a region of

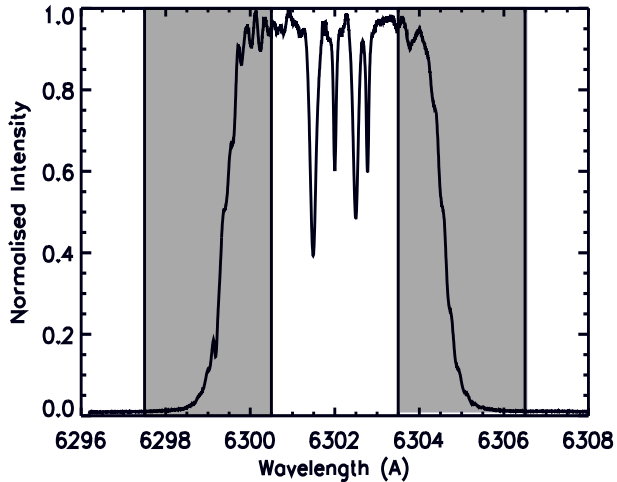
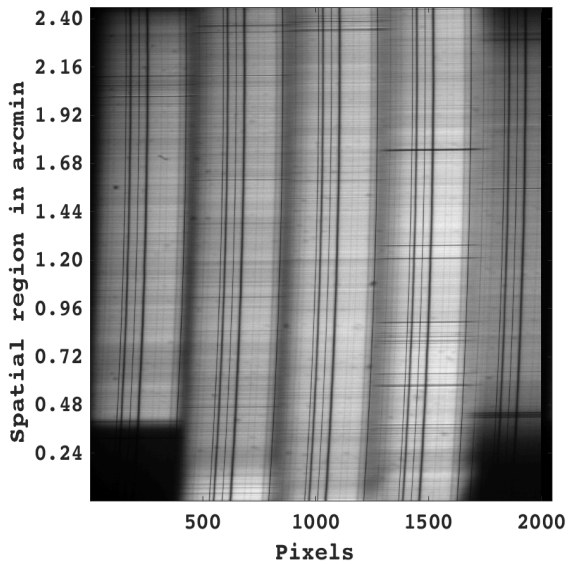


Figure 2.26: DWDM transmits 6 \AA of which the unwanted 1.5 \AA continuum on either sides of the spectra can be blocked using a physical barrier.

3 \AA while the additional 1.5 \AA on either sides constitutes of the solar continuum. The continuum wavelength does not contain any polarization information and is redundant. If the 1.5 \AA continuum region is "masked out" from the spectra then a void region is created between two adjacent spectra whose spatial size corresponds to a spectral dispersion of 3 \AA .

For dual beam polarimetry this void can be accommodated with an identical image of the spectra with orthogonal polarization. The spectral mask is a physical barrier placed at the 1^{st} image plane of the spectrograph as shown in Figure 2.19. It consists of an opaque element with five transparent windows of size $2.9\text{ mm} \times 15\text{ mm}$ placed 5.8 mm away from each other. Figure 2.27a is a 5 slit spectra taken from MSSP without a spectral mask. Figure 2.27b is a dual bream polarimetric image taken after placing the mask.

Specifications of the analyzer used in MSSP is given in Table 2.7. The size of the crystal mentioned in the table is calculated using Equation 2.24.



(a) 5 slit spectral image without a spectral mask

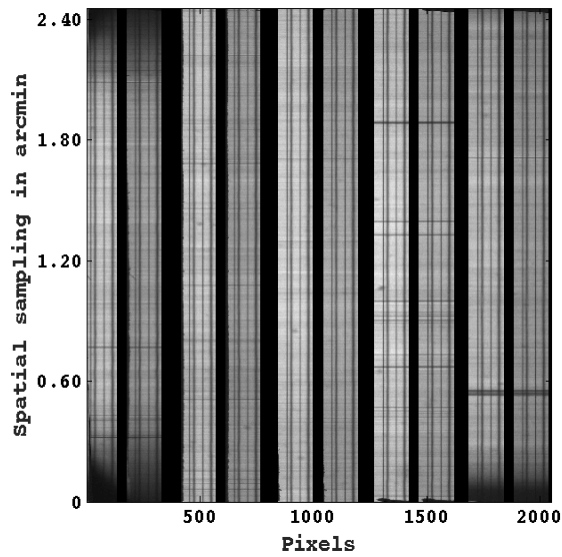
(b) 5 slit spectral image in dual beam mode with a spectral mask placed at the 1^{st} image plane

Figure 2.27: Multi-slit spectra of Fe I line pair at 6302 \AA taken from pco.2000

PARAMETER	VALUE
Material	Calcite
optical axis angle	45^0
Clear aperture	25 mm
Length of single crystal	9.49 mm
Beam separation per crystal	1.0253 mm @ 6302 Å

Table 2.7: Specifications of dual beam analyzer used in [MSSP](#)

2.4 CHARACTERIZATION AND CALIBRATION OF MSSP

[Section 2.2](#) and [2.3](#) describes the design of the spectro-polarimeter. In this section I discuss the performance of [MSSP](#) as a spectro-polarimetric instrument. Parameters like spectral resolution, spectral dispersion are determined. The quality of spectral images recorded by it are evaluated by determining the width of the spectral lines and comparing it with well calibrated space based instruments like Hinode. We also present the calibration of the polarimeter using a GUI created in LabView®. The GUI acts like a general purpose virtual laboratory to calibrate any modulator irrespective of its type and wavelength of operation. We also briefly discuss the procedure followed to setup [MSSP](#) at a component level.

[MSSP](#) is a littrow configuration spectro-polarimeter with 5-slits at the entrance aperture. It consists of a 150 cm focal length off-axis parabolic mirror to collimate the entrance aperture onto the grating. The grating is a mechanically ruled blazed echelle with a groove density of 23.3 *lines/mm* and blazing angle of 63.5^0 . It disperses the collimated beam of light into its constituent wavelength components with an angular dispersion of 2.188 *arcmin/Å* and reflects it back onto the off-axis parabolic mirror. The off-axis parabola images the dispersed beam of collimated light into 5 spectral bands at the first image plane. A pickoff mirror diverts the converging beam of spectra coming from the off-axis mirror onto a detector plane. An opaque spectral mask with 5 transparent windows of 2.9 mm × 30 mm separated by 5.8 mm is placed at the first image plane. A re-imaging lens with a focal length of 250 mm is used to demagnify the masked 1st image plane onto the detector. A polarimeter unit consisting of two [LCVRs](#) oriented at 45^0 and 0^0 and two calcite polarizing beam displacers oriented at 45^0 and 135^0 is placed in front of a [DWDM](#) filter for Fe I at 6302 Å. The filtered spectra from the [DWDM](#) is imaged onto a 15 mm × 15 mm CCD detector.

Although the spectro-polarimeter is designed at the component level, a system level integration onto a single unit requires additional factors like relative placement of each component with respect to each other and optimum angle of incidence such that the optical aberra-

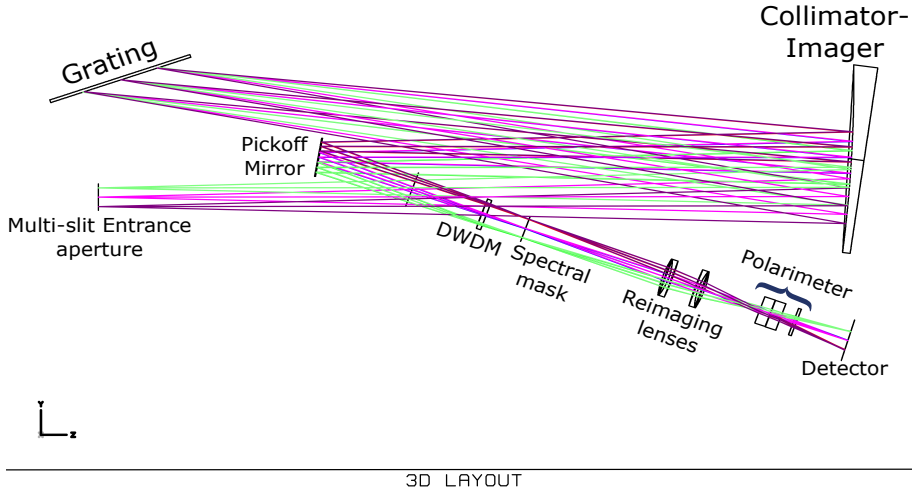


Figure 2.28: Optical layout of MSSP

tions produced by the system is minimal. Design optimization was performed in a ray tracing software called ZEMAX™. The performance optimized and aberration minimized optical diagram of MSSP is shown in Figure 2.28

The pick off mirror is placed 22.5 cm ahead of the 1st image plane and tilted at an angle of 10° clockwise with respect to the z-axis as shown in Figure 2.28. The aberration and imaging performance of the system at the 1st image plane after the pickoff mirror is shown as a spot diagram in Figure 2.29. The airy disk size is determined by the collimator and the chief ray is at 6302 Å. The spot diagram is generated for a point source object placed within a square field of 34 mm such that the center of the field lies at (0,0) and extends to 17 mm on either sides. Nine field points at (0,0) ; (0,17) ; (0,-17) ; (17,0) ; (-17,0) ; (17,17) ; (-17,17) ; (17,-17) and (-17,-17) are taken and their image performance at the 1st image plane is obtained. It can be seen that the spread in chief ray is well within the airy disk of the collimator suggesting the optimal placement of the entrance aperture, collimator, grating and the pickoff mirror.

The optical performance at the detector plane is shown as the spot diagram in Figure 2.30. The following assumptions were taken while drawing the optical layout from the 1st image plane to the detector - DWDM filter is considered to be a parallel plate glass of 1cm thickness, a single beam polarizer is placed at the detector instead of a dual beam polarizer. It can be seen that the chief ray lies within the Airy disk for (0,0) field point while it moves marginally out side the Airy disk at the corner field points.

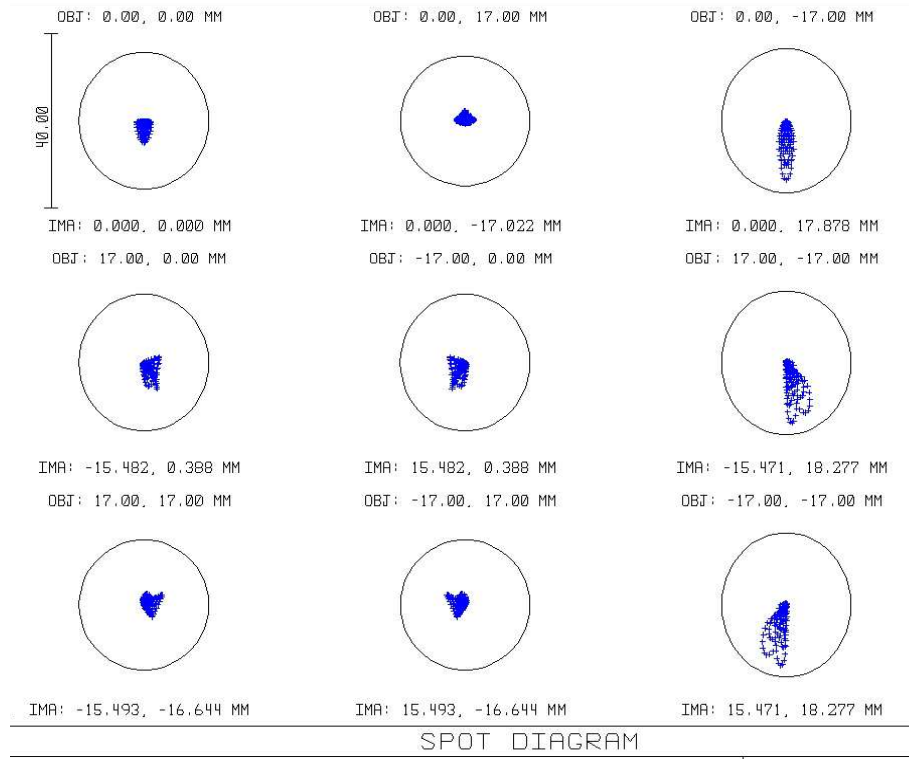


Figure 2.29: The dispersion of chief ray about the airy disk of the collimator at 6302 \AA taken at the 1^{st} image plane formed after the pickoff mirror in Figure 2.28. The object field size is $34 \text{ mm} \times 34 \text{ mm}$

2.4.0.1 *Instrument setup*

A brief description of the instrument setup is given here. The preliminary setup and tests for [MSSP](#) are performed at the optics laboratory in ISAC-ISRO. A heliostat was used as a temporary telescope system for [MSSP](#) to determine spectral dispersion. The setup procedure are as follows

- Multi-slit entrance aperture - The front surface of the multi-slit has a reflective coating. Slits were formed by etching away the reflective coating at specific locations. The multi-slit is aligned to the solar beam coming from the heliostat using back reflection from the reflective front surface. The aligned multi-slit defines the optical axis of [MSSP](#).
- Off-axis Parabola - The off-axis system is aligned to the optical axis in two steps assuming that the optical axis of the parent parabola passes through the center of the multi-slit. The first step is to make the mirror mount perpendicular to the optics bench. An alignment flat as shown in Figure 2.14 is used for this purpose. It is a flat mirror whose normal is parallel to the normal of the mount's surface. Thus the mirror mount and the off-axis mirror come into alignment by aligning the alignment

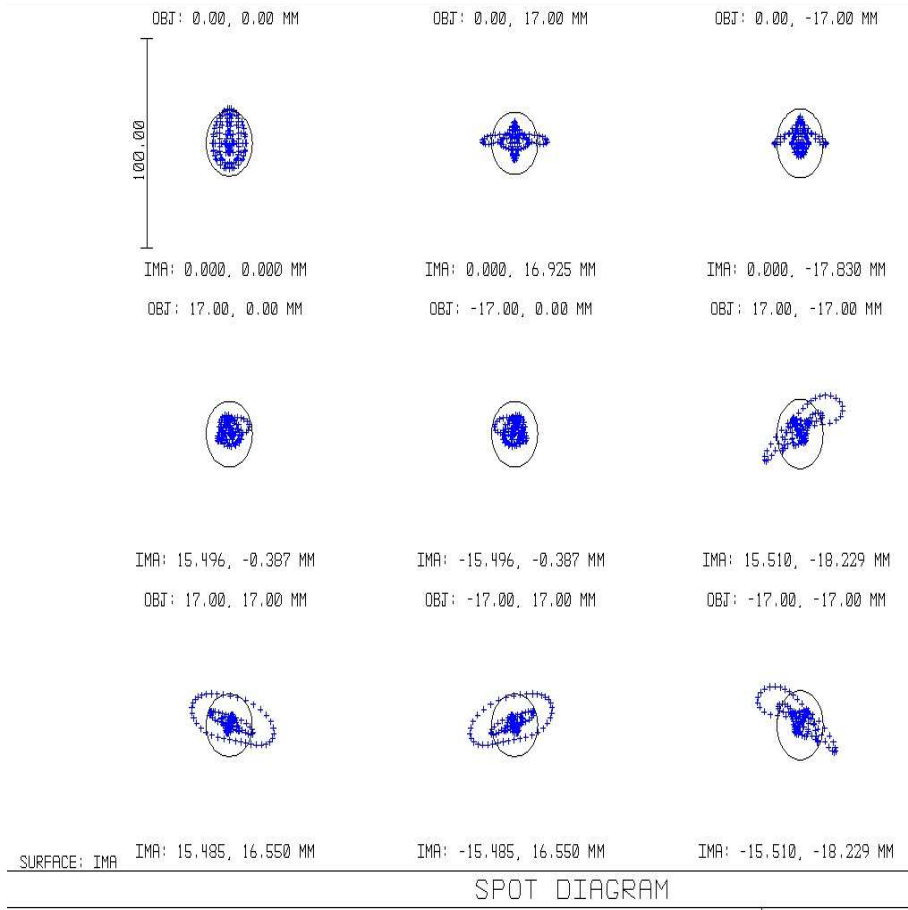


Figure 2.30: The spot diagram of chief ray at the detector plane

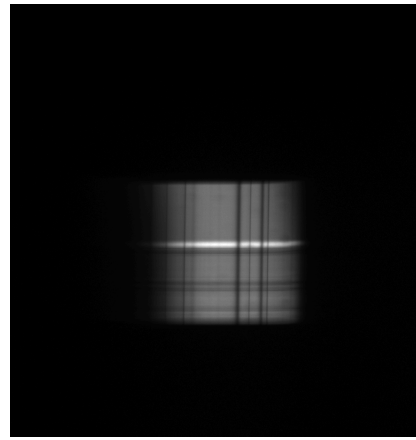
flat to the optical axis of MSSP. In the next step, a laser is incident along the optical center of the off-axis mirror and the mirror is rotated about its optical center until the source and reflected beam are in the plane whose normal is parallel to the length of the slit. The placement of other optical components from the grating to the detector is a simple process and is deemed redundant to mention the same.

The characterization procedure is divided into two parts. First is the characterization of the spectrograph for its spectral resolution and dispersion and the second is calibration of the polarimeter for the relation of voltage vs retardance for each of the two LCVRs.

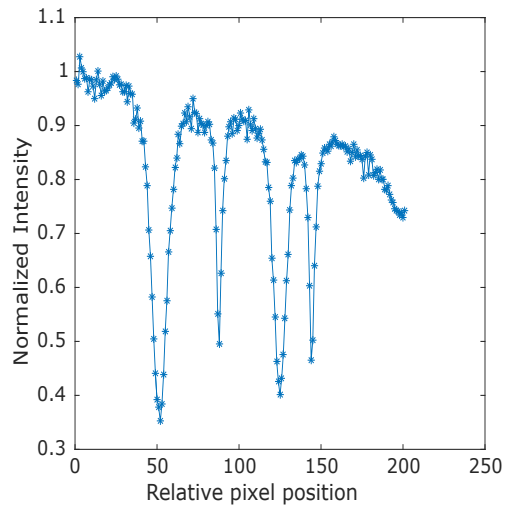
2.4.1 Spectral resolution and dispersion

For the 6302\AA spectral band, the spectral dispersion can be found using the two oxygen telluric lines formed in the Earth's atmosphere. Their absorption spectra are stable and their line cores are formed at 6301.99\AA and 6302.75\AA . An image of the Fe I spectra taken using the heliostat setup is shown in [Figure 2.31a](#) and a wavelength plot along a

cut taken at the center of the spectral image is shown in [Figure 2.31b](#). A Gaussian is fit to the absorption lines and the distance between the mean of the two Gaussian is found to be 111.87 pixels. Therefore the spectral dispersion is $6.7 \text{ m}\text{\AA}/\text{pixel}$ or $0.91 \text{ m}\text{\AA}/\mu\text{m}$ at the 1^{st} image plane. It must be noted that the spectral dispersion at the second focal plane is reduced by half due to de-magnification of the image plane.



- (a) This is a single slit spectra recorded using $2k \times 2k$ pco.200 camera at the 1^{st} image plane. The spectral dispersion of the system is determined using Fe I spectra obtained from calibration setup of [MSSP](#). The spectra has two telluric lines with a stable wavelength of absorption.



- (b) Spectral dispersion along the detector plane sampled at $7.4 \mu\text{m}/\text{pixel}$. The spectral dispersion is obtained as wavelength per pixel using this plot.

Figure 2.31: Fe I spectra obtained from calibration setup of MSSP

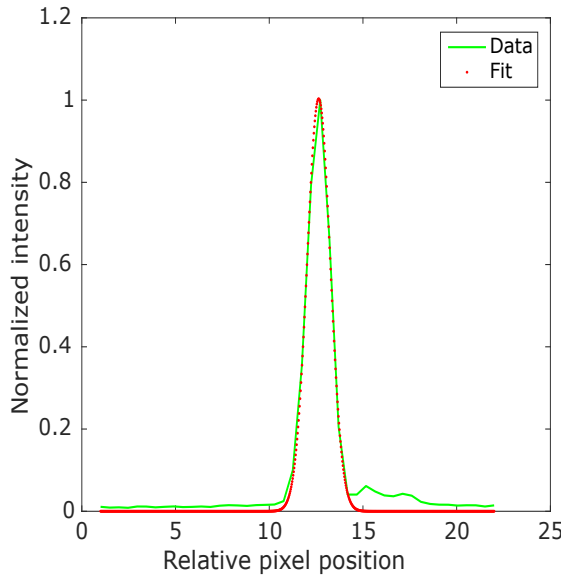


Figure 2.32: Laser profile fitted with a gaussian function to determine spectral dispersion. σ of the Gaussian is 0.9932 pixels

In order to determine the spectral resolution of the spectrograph, a 5 mW He-Ne laser at 632.8 nm was used. The laser width is assumed to be infinitely thin (i.e. perfectly monochromatic) but the spectrograph broadens the line due to its inherent resolution limit. The laser is incident on the center slit and imaged at the detector. A Gaussian is fit to the laser line and the standard deviation σ is found to be 0.99 pixels (± 0.1 along the slit). For a spectral dispersion of $6.7 \text{ m}\text{\AA}/\text{pixel}$, the spectral resolution of the spectrograph is $15.8 \text{ m}\text{\AA}$. Table 2.8 gives a comparison of numerical vs experimental spectral dispersion and resolution. It can be seen that the spectral dispersion is lesser than the expected value. This implies that the de-magnification attained on the detector is less than two times. The reduced de-magnification implies that the spectral image slightly overfills the detector chip by about 12 %.

PARAMETER	THEORITICAL	EXPERIMENTAL
Spectral dispersion	$7.75 \text{ m}\text{\AA}/\text{pixel}$	$6.7 \text{ m}\text{\AA}/\text{pixel}$
Spectral resolution	$15.448 \text{ m}\text{\AA}$	$15.8 \text{ m}\text{\AA} \pm 1.2 \text{ m}\text{\AA}$

Table 2.8: Comparison of theoretical spectral performance and experimental value obtained for MSSP

2.4.2 Polarimeter calibration

The polarimeter unit is made up of two parts. The [LCVR](#) as a modulator and Polarizing Beam Displacer ([PBD](#)) as an analyzer. The cali-

ibration of polarimeter unit involves the characterization of **LCVR** for its retardance at different electric potentials and determining the performance of polarizing beam splitter in terms of image quality and image separation between the dual beam. In this section, we perform the characterization of **LCVR** using a GUI created using LabView. The GUI is generalized and can be used to characterize any modulator. The final integration into one polarimetric unit is performed using another GUI which takes into account the alignment errors and relative position of the modulator and analyzer.

2.4.2.1 *Modulator*

Two **LCVRs** are used as modulator to obtain balanced modulation matrix as shown in [Equation 2.19](#) and [2.20](#). In order to obtain the desired retardance values, the user must have a prior voltage vs retardance curve that maps the voltages to retardance values at a particular wavelength. But the voltage vs retardance curves are highly non linear. A large number of samples are needed to faithfully generate the curve. In order to make the process automatic, a GUI has been developed. The procedure requires a **PBD** or a Wollaston prism as an analyzer. Sunlight is used as the light source with a prefilter of the operating wavelength. A schematic layout of the optical setup is shown in [Figure 2.33](#). The procedure implemented in the GUI is as follows

- a. The GUI prompts the user to align the two beams from the **PBD** to a horizontal plane. A Gauss fit routine runs in the background to ensure that the peak of the two gaussian beams lie in the same horizontal plane.
- b. Once the beams are horizontal a virtual LED turns green and prompts the user to place a linear polarizer ahead of the analyzer such that the polarizer's axis is aligned to one of the orthogonal axis of the analyzer/Wollaston prism. The GUI indicates that the polarizer is aligned to the analyzer when the ratio of the intensities between the two beams is atleast $1:10^4$.
- c. The user is prompted to place the **LCVR**. Upon placement, the modulator (**LCVR** in our case) is cycled through a voltage range of 0 to 10V and the intensity is recorded at each point. Then the GUI analyses the data and infers the voltage (v) at which the **LCVR** has $\delta = 180^\circ$. It sets the **LCVR** to " v " and prompts the user to rotate the **LCVR** about the axis passing through the beam. When the contrast between the two beams flips with respect to the configuration without the **LCVR** then the GUI prompts the user that the setup is ready for calibration. This step ensures that the fast axis of **LCVR** is at 45° with respect to the input polarizer.

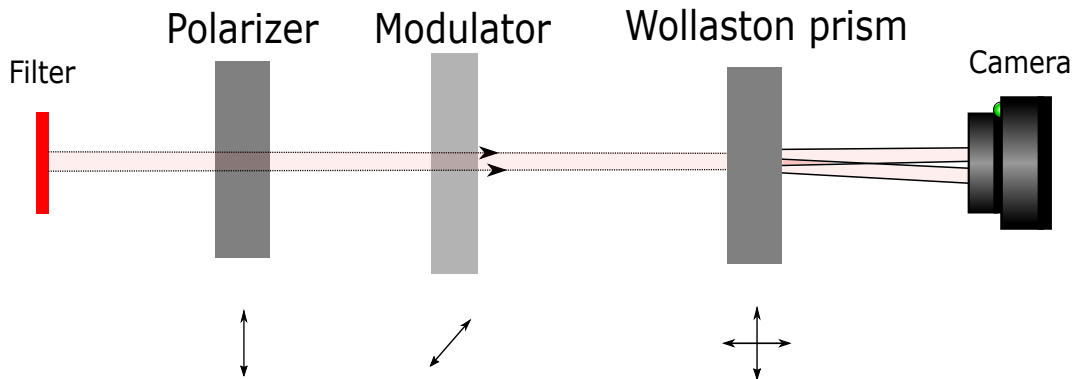


Figure 2.33: Schematic layout of the optical setup to characterize a polarization modulator. The arrow below the polarizer and Wollaston prism indicates the relative position of the transmission axis and the arrow for the modulator indicates the orientation of its fast axis with respect to the polarizer.

- d. The GUI varies the [LCVR](#) voltage in fine steps in the range 0-10V. Upon completion, a text file containing the tabulation of voltage and its corresponding retardance is generated.

This procedure can be extended to a rotation wave-plate where the [LCVR](#) is replaced by the waveplate on a motorized rotation stage.

The voltage retardance relation for the [LCVRs](#) used in [MSSP](#) is shown in [Figure 2.35](#). It must be noted that the 1st [LCVR](#) has a compensator retarder hence the retardance goes to negative values. The curve is generated for an ambient temperature of 21 °C as this is the temperature maintained at the instrument floor in [USO](#) with a variation of ±1 °C.

2.4.2.2 Analyzer

The calcite analyzer for [MSSP](#) is tested for the separation between the images formed by o-ray and e-ray. He-Ne laser at 632.8 nm is used to illuminate the center slit. The dual beam laser image and a corresponding gaussian fit of the profile is shown in [Figure 2.36](#).

The mean Gaussian width of the left and right slit images are 1.09 ± 0.1 pixel and 1.02 ± 0.1 pixel (Although the 2nd decimal point lies within errors, it is given to show the difference in focus between the two beams). The laser width before the placement of the analyzer is 0.99 ± 0.1 pixels. This implies that the beam splitter has introduced a defocus and this corresponds to a decrease in the spectral resolution by 1.63 mÅ. Although the spectral resolution has degraded, its better

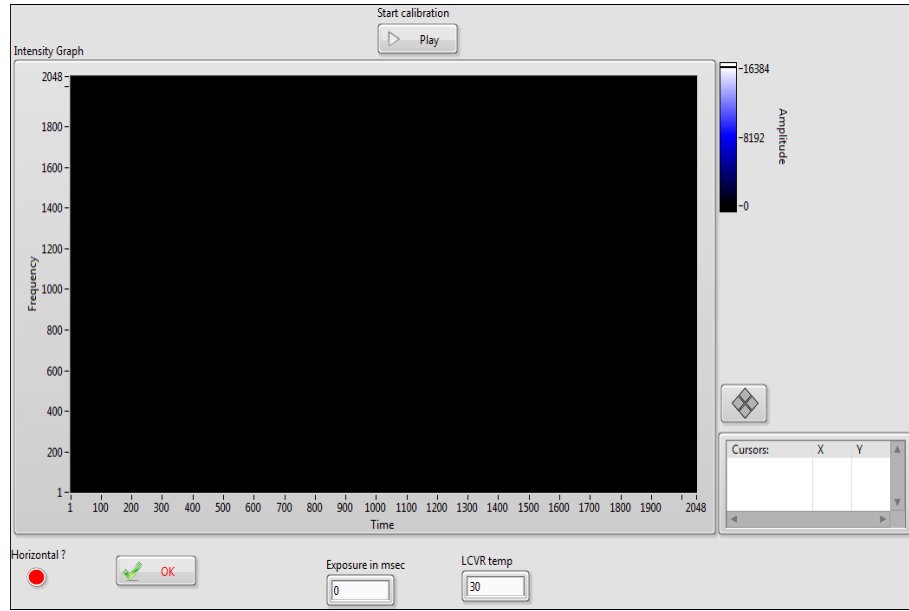


Figure 2.34: Front panel of the GUI designed to calibrate the modulator. Note that the front panel is dynamic i.e. the selection buttons and options given to the user vary according to the procedure which is currently being executed.

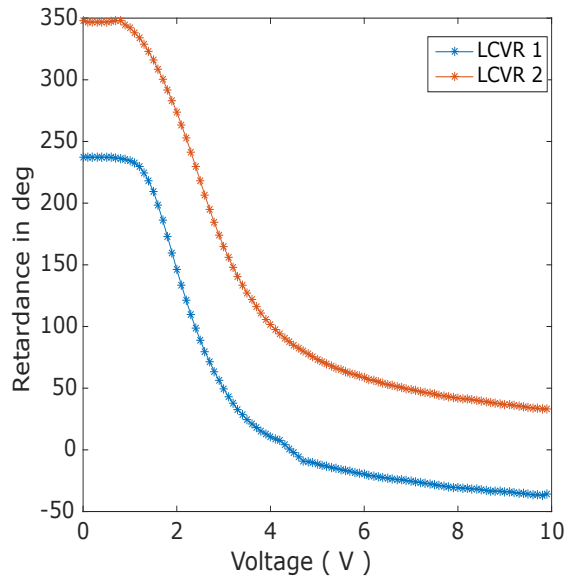
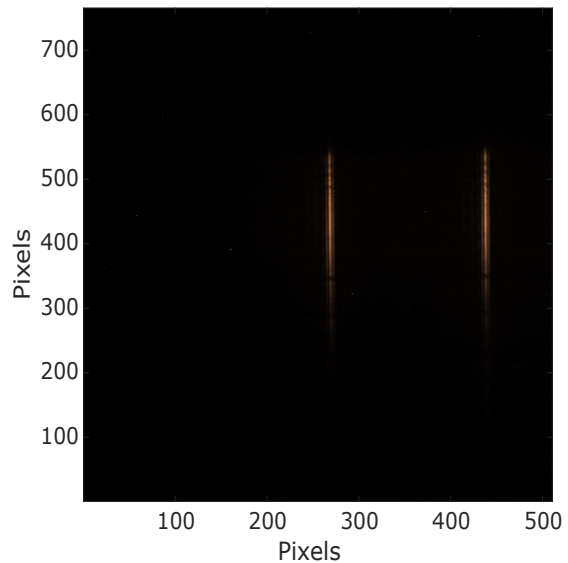
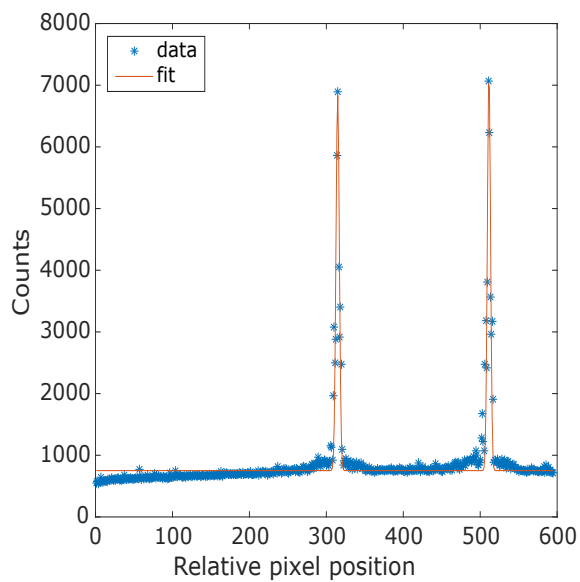


Figure 2.35: The curve represents the relation between voltage and retardance for the two LCVRs used in MSSP. The 1st LCVR has a compensator hence the retardance goes to negative values. Note that this curve is generated at 21 °C ambient temperature.



(a) A dual beam laser image of the center slit



(b) Gaussian profile fit to the laser profile obtained from a cut taken across the dual beam image. The mean width of the left and right Gaussian are 1.09 pixels and 1.02 pixels respectively.

Figure 2.36: Evaluation of the performance of calcite analyzer used in MSSP

than the acceptable levels of $20\text{m}\text{\AA}$ defined from the science goals of **MSSP**.

With the spectrograph and the polarimeter calibrated, **MSSP** is installed at **USO** to be operated with **MAST**.

2.5 INTEGRATING MSSP TO MAST

The laboratory tests for **MSSP** revealed that the spectro-polarimeter performs as expected. The system is integrated into **MAST** as one of the facility instrument of **USO**. This section describes the inclusion of a raster scanning mechanism to **MSSP** to make it an imaging spectro-polarimeter. The spectral focus and imaging capabilities and performance of the 5 slits of the spectro-polarimeter are discussed. As a spectro-polarimeter the instrument must be capable of detecting polarization signals from Sun. But the intermediate optical components introduce polarization known as instrumental polarization. The facility **polcal** placed at the telescope's exit pupil is used to determine the instrument polarization. The integration of **polcal** into **MSSP** data acquisition procedure is discussed. A GUI is designed to operate **MSSP** as a black box. The GUI is highly interactive and an user can utilize the facility instrument with no prior knowledge of the instrument or its working. The section also covers the derivation of analytical model of telescope polarization for **MAST**.

2.5.1 Imaging spectro-polarimeter

The layout of **MSSP** and other instruments at **MAST** is shown in the block diagram of [Figure 2.37](#). The spectro-polarimeter along with the scanning mirror forms the imaging spectro-polarimeter. The scanning mirror is a DC motor driven rotating mirror used to raster scan the **FOV** over the multi-slit entrance aperture. There are three ports at **USO** called the north, south and east port and **MAST** delivers a collimated beam of sunlight only to a single port at any given time. The center of the beam is at a height of 16 cm from the optics bench. But the height of optical axis for **MSSP** is determined by the off-axis parabolic mirror whose center is at a height of 22.5 cm from the optics bench. In order to compensate for the mismatch in beam height and the optical axis of **MSSP**, two mirrors with their normal at an angle of 45^0 with respect to the ground plane is placed in front of **MSSP**. A schematic layout of the two mirror setup is shown in [Figure 2.38](#). The top mirror (M_2) is connected to a rotation stage whose axis of rotation is normal to the optics bench and passes through the center of M_2 . The beam coming from M_2 is collimated and an imaging lens with focal length of f is placed in front of it to form an image over the multi-slit. As the mirror rotates by θ the collimated beam moves over the imaging lens in a plane parallel to the optics bench. The image formed by the lens

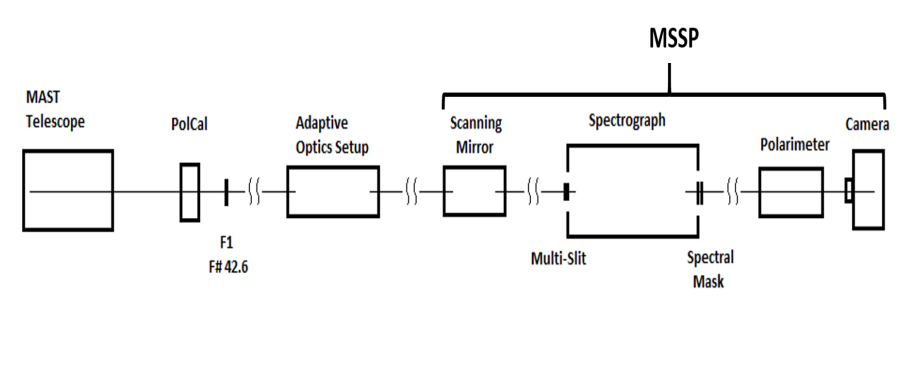


Figure 2.37: Block diagram of instrument layout at [MAST](#)

in-turn moves by $f \times \theta$ over the multi-slit forming a “raster scan” of the [FOV](#). As the slit width is d , the angle of rotation for the scanning mirror to perform a single step in the raster scan is

$$\theta = \frac{d}{f}$$

[MSSP](#) currently operates in 3 arcmin high resolution mode and an imaging lens with $f=50$ cm is used to produce an $f/75$ beam. With the scanning mechanism integrated into the spectro-polarimeter, the imaging capabilities of [MSSP](#) and its spectral performance are tested. USAF 1951 standard resolution target is placed at the first image plane after the polcal unit shown in [Figure 2.37](#). The target is a glass plate with opaque rulings of known size. This opaque pattern forms an image on the multi-slit. These patterns can be considered to be a proxy to the features formed on the Sun. The target image is used to determine the accuracy in scan steps and resolution of the raster image.

[Figure 2.39](#) shows an USAF 19 resolution target. Each horizontal and vertical line belong to a particular element number and a group number. Based on the element number and group number one can find the length and width of the line. For [MSSP](#) the telescope limiting resolution is 0.317 arcsec at 6302 Å. Two spatially resolved elements at the slit plane are $16.5 \mu\text{m}$ apart. Group 5 element 1 horizontal and vertical lines have a separation of $15.63 \mu\text{m}$. According to Rayleigh criteria two spatial points are just resolved when their point spread functions coincide at half power point. [Figure 2.40](#) is a raster scanned image of the resolution target placed at the 1st image plane. A plot of the normalized intensity profile of two adjacent lines in group 5 element 1 is shown in [Figure 2.41](#). It can be seen that the Point Spread Function (PSF) of the lines cross over below the half power point thus the two lines are just resolved as they satisfy Rayleigh criteria. Thus the raster scan of the imaging spectrograph is working well within the telescope’s resolution limit.

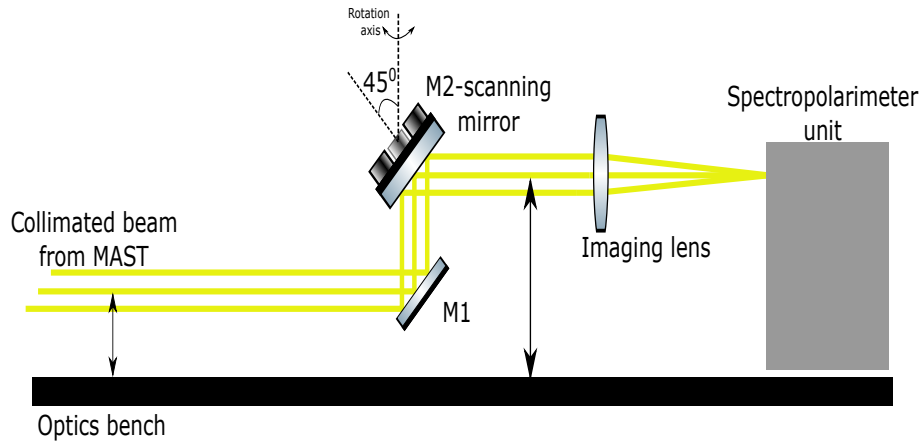


Figure 2.38: Schematic layout of the scanning mechanism used to perform imaging spectro-polarimetry for MSSP

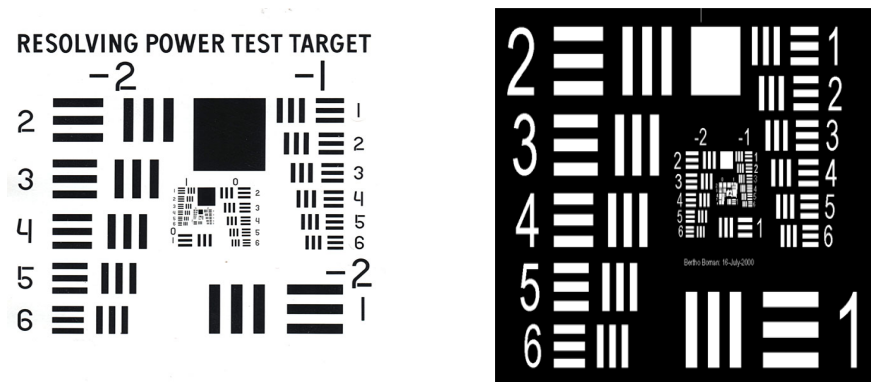


Figure 2.39: USAF 19 resolution target used to test the imaging capabilities of MSSP. Target on the left has positive ruling and the one on right has negative ruling. Note - The two images are not to scale

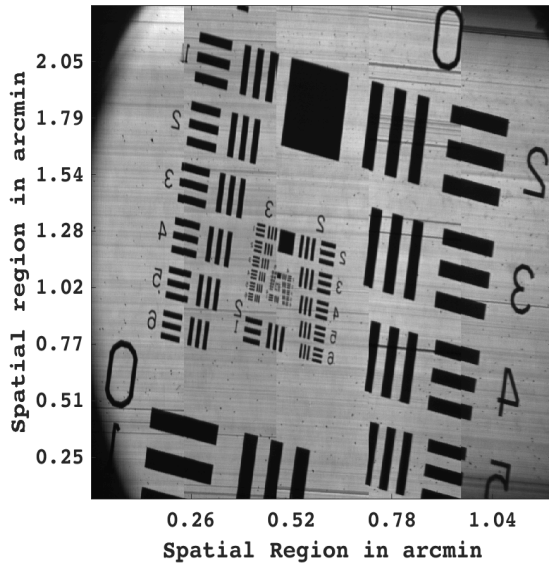


Figure 2.40: Raster scan of the resolution target placed at first image plane of a 3 arcmin field.

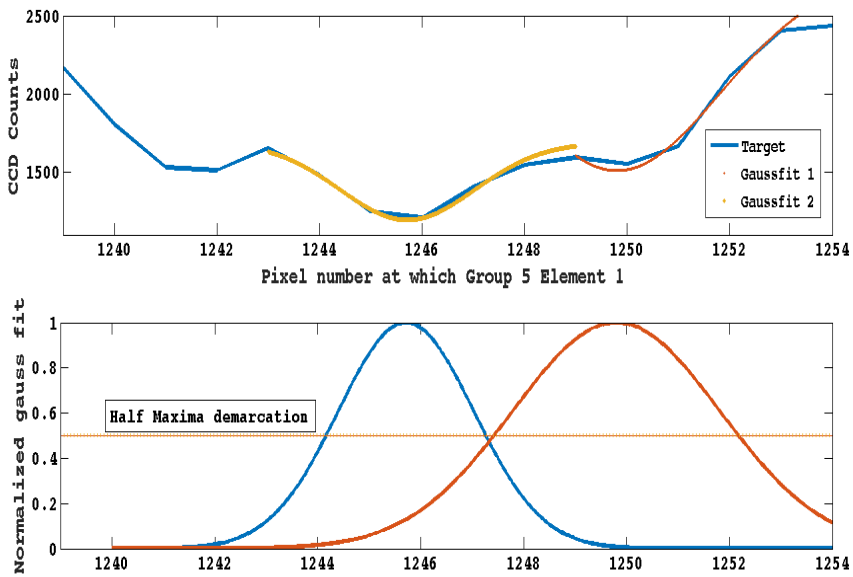


Figure 2.41: Point spread function of two group 5 element 1 lines in USAF 19 resolution target. The contrast is nominal as the target used is a positive ruling type.

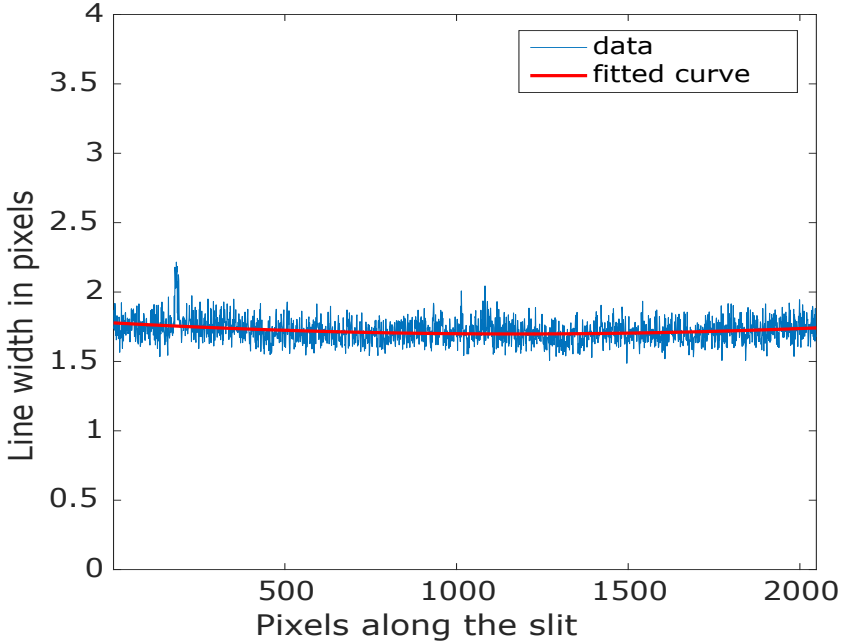


Figure 2.42: A plot of variation in line width of the oxygen telluric line along the slit. The fitted curve is a 2^{nd} degree polynomial whose 1^{st} and 2^{nd} order coefficients determine defocus in the system.

The final test needed to verify the working of the imaging polarimeter and a successful integration to [MAST](#) is the consistency in the focus of the spectral image along the entire slit. Variation in line width of telluric line at 6301.99 \AA is taken for the purpose of focus test. A plot of Telluric line width along the center slit is shown in [Figure 2.42](#). The y-axis is represented in pixels to easily interpret the data. A 2^{nd} degree polynomial is fit to the curve and the coefficients in x and x^2 are of the order of 10^{-4} and 10^{-8} respectively. It can be seen that the non-linearity in line width or the non linearity in focus is negligible. Hence there is no global trend in the variation of spectral width which implies that all the points along the slit are focused at the same plane on the detector.

2.5.2 *polcal* and Telescope polarization

With the successful integration of [MSSP](#) to [MAST](#), the imaging spectro-polarimeter can determine the polarization of light at the slit plane or entrance aperture. But the polarization of light at the slit plane has contribution from the Sun and the instruments that lie in between. The Mirrors and the beam splitters introduce a finite amount of polarization which corrupts the polarization signatures from the Sun. But the instrument induced polarization is constant and can be ex-

tracted out by determining the Mueller matrix of the system. If M_I is the Mueller matrix of the instrument system then,

$$S_D = M_I \times M_T \times S_{\odot},$$

where S_D is the Stokes parameters of light reaching the polarimeter unit, M_T is telescope Mueller matrix and S_{\odot} is the polarization of incoming solar radiation. M_I can be determined by sending a known polarization of light into the system and detecting the change in polarization at the detector. This process is known as ellipsometry and requires a minimum of 16 independent measurements to determine all the elements of the Mueller matrix. At USO ellipsometry is performed using a linear polarizer and zero order rotating retarder to generate known states of polarization. The retarder is rotated in steps of 22.5^0 using a motorized rotation stage. From Figure 2.37, it can be seen that `polcal` corrects for instrument polarization induced from the first image plane F1 up to the detector system of MSSP. Although the instrument induced polarization is assumed to be constant, polarization calibration is performed after every data acquisition to ensure that minor variations in the setup are rectified during post processing.

2.5.2.1 Telescope polarization

To measure weak magnetic fields from a source, its necessary to extract the source polarization with high accuracy (Socas-Navarro et al. [109]). Symmetric systems generally introduce uniform polarization at all orientations (Q, U and V) thus reducing the sensitivity of the system to instrument polarization. But asymmetric systems introduce strong polarization preferentially at arbitrary orientations. Unlike symmetric systems it's difficult to model the polarization characteristics of an asymmetric system.

Telescope polarization is a limiting parameter for many sensitive polarimetric applications. Unlike the back end instruments it is not easy and in some cases its not possible to measure telescope polarization or perform ellipsometry on it. The only viable option in such scenarios are ray-tracing software like ZEMAX™. In some scenarios the system does become fairly simple and analytical models can be built to predict the telescope polarization.

The primary component in determining telescope polarization is the Mueller matrix of a reflecting metal surface. Mueller matrix of a reflecting mirror derived from Fresnels laws of reflection is given by (Kawakami [52])

$$M = \frac{1}{2} \begin{pmatrix} 1 + X^2 & 1 - X^2 & 0 & 0 \\ 1 - X^2 & 1 + X^2 & 0 & 0 \\ 0 & 0 & 2X\cos(\phi) & 2X\sin(\phi) \\ 0 & 0 & -2X\sin(\phi) & 2X\cos(\phi) \end{pmatrix}, \quad (2.25)$$

where X^2 is the ratio of the Fresnel reflection coefficients for the two direction of vibration of light

$$X^2 = \frac{|R_{||}|^2}{|R_{\perp}|^2},$$

and ϕ is the phase difference between $R_{||}$ and R_{\perp} . The mirror surface is coated with a metal of refractive index $n+ik$. So expressing the ratio of amplitudes and phase in terms of the refractive index of the metal and angle of incidence i , we get

$$\tan(\phi) = \frac{2b\sin(i)\tan(i)}{\sin^2(i)\tan^2(i) - (a^2 + b^2)},$$

$$X^2 = \frac{a^2 + b^2 - 2asin(i)\tan(i) + \sin^2(i)\tan^2(i)}{a^2 + b^2 + 2asin(i)\tan(i) + \sin^2(i)\tan^2(i)},$$

where

$$a = \frac{1}{2} \left(n^2 - k^2 - \sin^2(i) + \sqrt{(n^2 - k^2 - \sin^2(i))^2 + 4n^2k^2} \right)$$

and

$$b = \frac{1}{2} \left(k^2 - n^2 + \sin^2(i) + \sqrt{(n^2 - k^2 - \sin^2(i))^2 + 4n^2k^2} \right).$$

By knowing the angle of incidence for a ray of light, the change in polarization on that ray can be determined. By summing all possible angles of incidence of a ray on a telescope surface, one can model the telescope Mueller matrix. Thus the most important criteria to determine telescope polarization is the angle of incidence for a bundle of light. The refractive index on the other hand can be determined experimentally using a small sample piece of metal surface used in the telescope.

[MAST](#) is a 50 cm off-axis parabolic coudé telescope. The optical layout of the telescope is shown in [Figure 2.43](#). The primary (M1) and secondary (M2) mirrors are both off-axis parabolic mirrors with complementary structures. Their focal lengths are 200 cm and 20 cm respectively. Off-axis mirrors are asymmetrical optics and our system has two off-axis mirrors. So the polarization introduced by the telescope is a major concern for spectro-polarimetric instruments. [Table 2.9](#) gives the configuration of the mirror system used in [MAST](#).

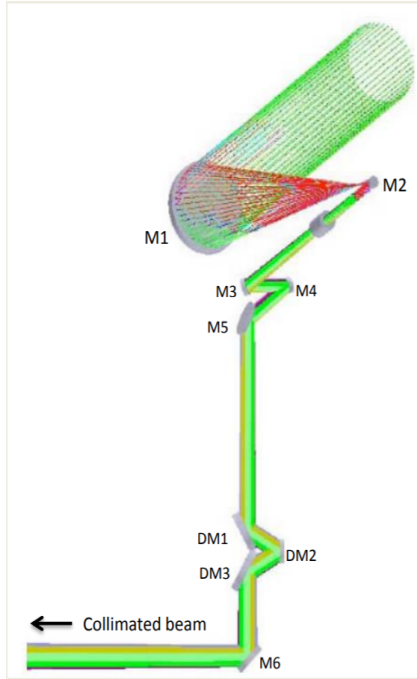


Figure 2.43: Optical layout of MAST

MIRROR NUMBER	TYPE	PARAMETERS
M ₁	Off-axis parabolic	f = 200 cm, OD = 57.5 cm
M ₂	Off-axis parabolic	f = 20 cm, OD = 5.75 cm
M ₃	Plane	N = 45 ⁰
M ₄	Plane	N = 16.85 ⁰
M ₅	Plane	N = 61.85 ⁰
DM ₁	Plane	N = 60 ⁰
DM ₂	Plane	N = 30 ⁰
DM ₃	Plane	N = 60 ⁰
M ₆	Plane	N = 45 ⁰

Table 2.9: Configuration of Mirror system used in MAST. f is focal length, OD is off-axis distance, N is angle between the normal and chief ray.

Although the telescope has two asymmetric mirrors and seven plane mirrors, the working of the telescope is fairly simple and the mirror system can be modeled into a single Mueller matrix. The telescope is an alt-azimuth tracker and it can be divided into three parts. The first part is the main frame which houses the primary mirror (M_1), secondary mirror (M_2) and plane mirror (M_3). This frame moves in the alt and azimuth direction (Figure 2.44a). So at any given time, the rays from the Sun are incident at a constant angle on the mirror system. In order to provide the light beam in a constant direction a coudé mirror system is being used (Figure 2.44b). The coudé mirrors M_4 , M_5 are mounted on a metal frame and moves only in the azimuth direction. The output beam from M_5 has a constant direction but the image formed by it rotates about the axis passing through the center of the beam. Image rotation is problematic for slit based spectrographs as there is no reference image to compensate for image rotation. To over come this problem, a de-rotating mirror system consisting of three plane mirrors are used. Like a dove tail prism, the de-rotating mirrors (DM 1-3) rotate about the center of the beam and produce a stable image of the FOV. The last mirror M_6 channels the beam into one of the three ports in the observatory i. e. the north or south or east port.

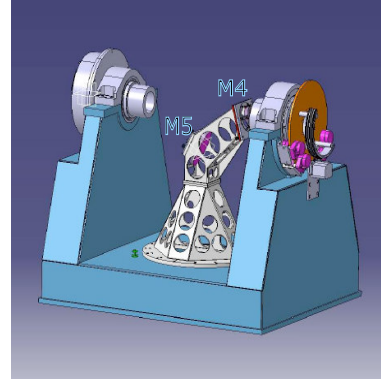
For a ray at the center of the field, angle of incidence on each mirror is constant and the angles are described in Table 2.9. Field motion is tracked using two axis of rotation, namely the alt and azimuth. Hence for any ray in the FOV the angle of incidence is constant through out, irrespective of the position of the object in the sky. This implies that Equation 2.25 can be defined for each mirror as a constant which does not change with time. But it must be noted that the matrix is defined for $R_{||}$ and R_{\perp} and a rotation in parallel and perpendicular planes has to be compensated with rotation matrix

$$R(\theta) = \begin{pmatrix} 1 & 0 & 0 & 0 \\ 0 & \cos(2\theta) & \sin(2\theta) & 0 \\ 0 & -\sin(2\theta) & \cos(2\theta) & 0 \\ 0 & 0 & 0 & 1 \end{pmatrix}.$$

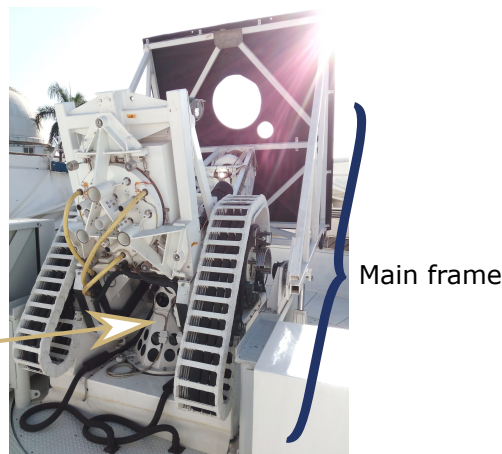
For an observer traveling with the sun's rays into the telescope system, the main frame appears stationary as it comprises of alt and azimuth rotation, the coudé appears to have a rotation only in the alt direction because the train comprises of rotation in the azimuth direction, the derotating mirrors appear to have both alt and azimuth rotation as it rotates in the opposite direction to compensate for image rotation. These relative rotations are directly translated into the rotation of $R_{||}$ and R_{\perp} . So if M_i is the Mueller matrix of the i^{th} mirror then the Mueller matrix of the telescope is



(a) Telescope Main frame move in alt-azimuth direction



(b) Coudé train consisting of M4 and M5 compensates for alt-azimuth motion and directs light in a constant direction



(c) Main frame and coudé train assembled as a complete telescope

Figure 2.44: **MAST** Telescope structure consisting of the main frame and coudé train to track an object in alt-azimuth plane

$$\begin{aligned}
M(\text{alt}, \text{azi}, p) = & M_6 \times \text{rot} \left(-\frac{(\text{alt} + \text{azi})}{2} + \frac{p}{2} \right) \times DM_3 \times DM_2 \times DM_1 \times \\
& \text{rot} \left(\text{azi} + \frac{(\text{alt} + \text{azi})}{2} - \frac{p}{2} \right) \times M_5 \times M_4 \times \\
& \text{rot} ((90 - \text{alt})) \times M_3 \times \text{rot} (90) \times M_2 \times M_1,
\end{aligned} \quad (2.26)$$

where alt and azi are the altitude and azimuth of the Sun during observation, p is the solar paralactic angle. The pole angle is a slow variation caused due to a tilt in Earth's axis of rotation and a tilt in the ecliptic plane with respect to the solar equator. Derotating mirrors compensate for p in order to provide an image of the Sun whose north - south axis is fixed to a particular direction through out the year.

In [Equation 2.26](#), the Mueller matrix of the parabolic mirrors is the average value of the contribution of all the points on the mirror. A parabolic mirror can be assumed to be made up of many small plane mirrors tracing the surface of a parabola ([Sen and Kakati \[102\]](#)). At any given point on the parabola, the small mirror is positioned in such a way that the normal of the mirror surface coincides with the normal of the parabola at that point. So for a collimated beam of light the angle of incidence i of a ray at any point on the parabola is given by

$$\cos(i) = \frac{4f \times \cos(\eta) - h \times \cos(\theta) \times \sin(\eta)}{\sqrt{h^2 + (4f)^2}}, \quad (2.27)$$

where f is the focal length of the parabola, h is the distance of the ray from principle axis, θ is the azimuthal angle of the ray about the principle axis and η is the angle made by the ray with principle axis. Substituting [Equation 2.27](#) in [2.25](#), one obtains the Mueller matrix of the paraboloid at every point on its surface. [Figure 2.45](#) is a simulation of the linear polarization introduced by a symmetric parabolic mirror for an unpolarized input beam. An off-axis parabolic mirror is a section of its parent symmetric paraboloid and [Figure 2.46](#) is a simulated output of the polarization introduced by off-axis mirror whose specifications are equal to that of [MAST](#) primary. It is also stated in [Table 2.9](#) that M_1 and M_2 are complementary to each other. So from the principle of reversibility of light, the Mueller matrix of M_2 is exactly the same as M_1 . Thus by substituting the numerical solution of M_1 and M_2 in [Equation 2.26](#), one obtains the analytical solution to telescope polarization. It is important to note that the refractive index of the mirrors play a very important role in determining the telescope Mueller matrix. For the data analysis performed on [MSSP](#) data (see [Section 2.6](#)), it is assumed that the mirror is coated with silver. An additional oxide layer is not considered for analysis. The true refractive index of the reflective surface can however be obtained experimentally as demonstrated in ([Sankarasubramanian and Venkatakrishnan \[92\]](#)) and references therein.

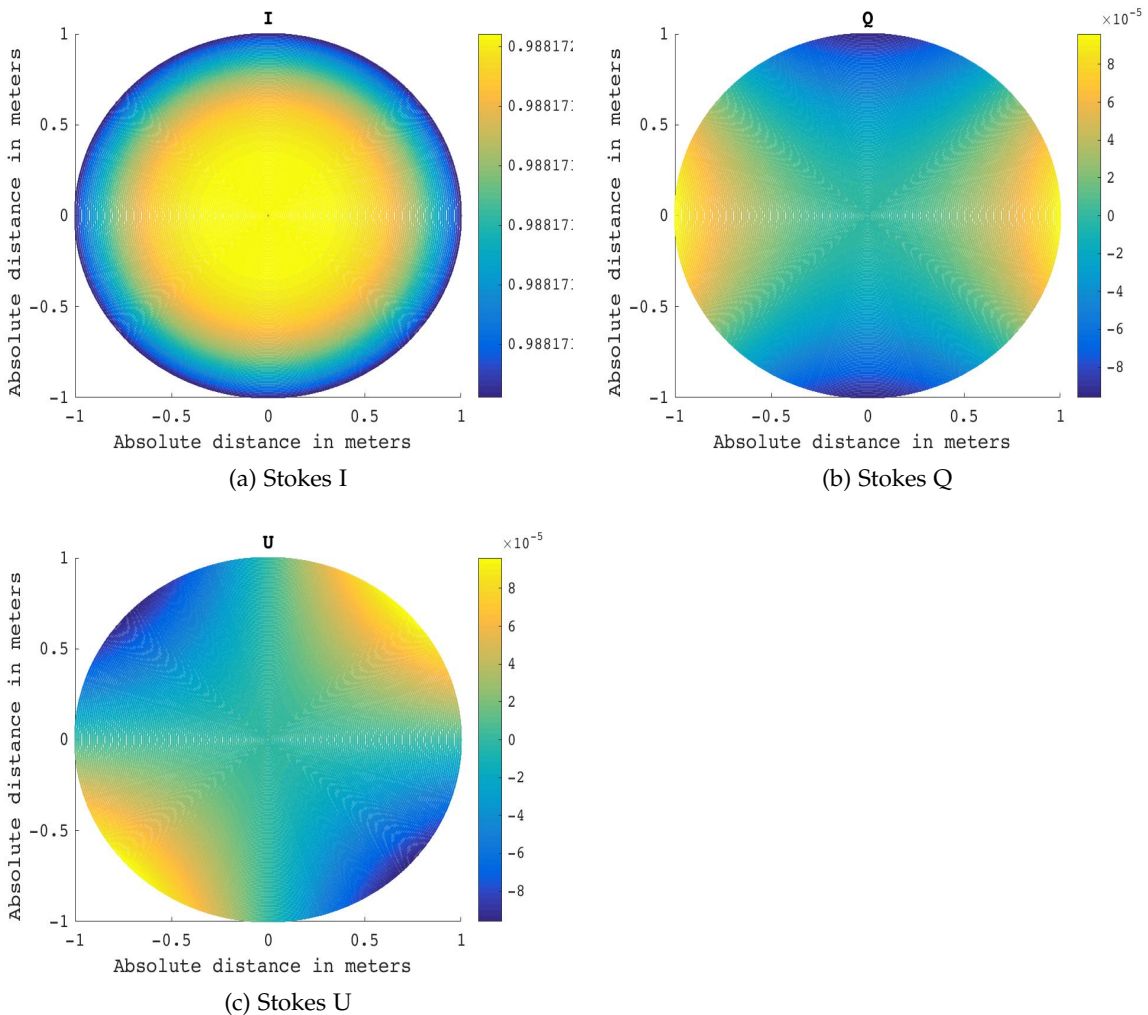


Figure 2.45: Simulation of polarization introduced by parabolic mirror with 1 meter diameter and 2 meters focal length for an unpolarized input at 6302\AA normal to the principle axis of silver coated mirror

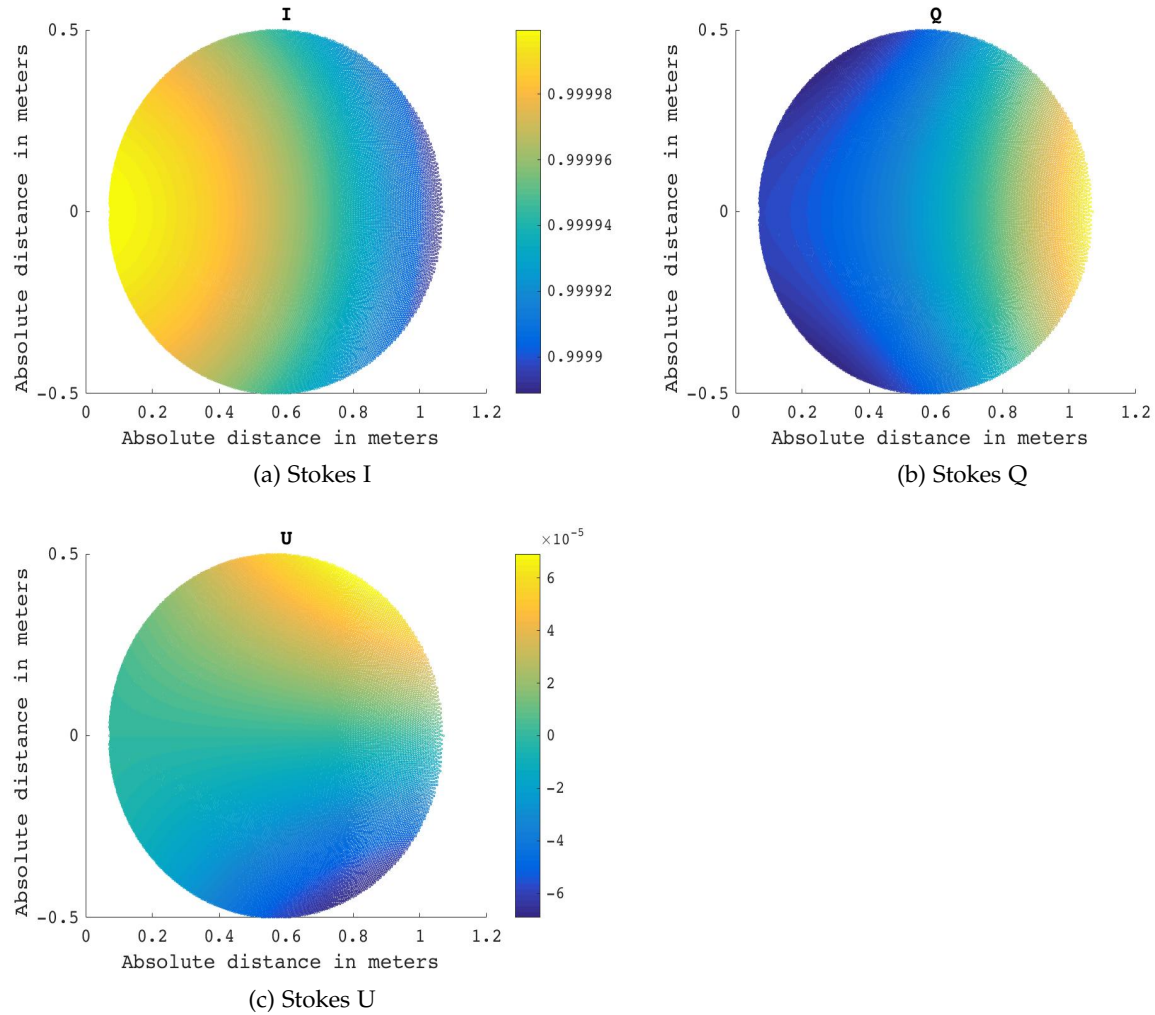


Figure 2.46: Simulation of polarization introduced by off axis parabolic mirror with 0.5 meter diameter, 0.5 meter zonal radius and 2 meters focal length for an unpolarized input at 6302 \AA normal to the principle axis of silver coated mirror. Note that this mirror bears the configuration of [MAST](#) primary.

2.6 DATA ACQUISITION AND ANALYSIS

After designing, calibrating and setting up the instrument at the observatory, it is necessary to operate it on regular basis. It is also important to keep the working of the system as simple as possible such that users are encouraged to take observations from the instrument. The final goal of the developers of this instrument is that the facility should help in improving our understanding on the dynamics of the Sun by providing accurate measurements on polarization of light. Although accuracy in measurements depends on factors like the correctness of voltage vs retardance relation of the modulator or refractive index of the telescope mirrors, a major portion of the accuracy is determined by the data acquisition and data reduction procedure. As an example if the voltage vs retardance is accurate but the synchronization between the modulator and detector is imperfect, errors creep into the system and they cannot be corrected. Similarly if a system like [MSSP](#) is upgraded to work on all 4 wavelength bands mentioned in [Table 2.1](#), new camera and modulator systems have to be interfaced to the PC with synchronization needed between all 4 wavelength bands in order to have simultaneous observation. Hence it is important to develop a GUI which makes the operation of the instrument simple and user friendly. The GUI should also be made in a manner such that it can quickly be adapted for the changes that are made to the instrument. After acquiring the data, it's equally important to reduce the data to a common format followed by the science community. Many reduction procedures are specific to [MSSP](#) and need not be applicable elsewhere. Also for a proper reduction of raw data the technical knowledge of the instrument becomes necessary. In order to avoid erroneous reduction, data reduction codes that reduce the raw data to science ready data have been developed.

This section deals with the description of the GUI developed for [MSSP](#) and the data obtained from it. Performance of [MSSP](#) using data obtained from the engineering run and the data reduction procedure are also being presented. The reduced data is inverted and the magnetic field strength is compared with the results obtained from [HMI](#).

2.6.1 Data Acquisition using a GUI

A general slit based spectrograph has an output similar to [Figure 2.1](#) where the vertical direction contains spatial information of the field sampled by the slit and the horizontal direction contains the spectral information of the field points. In order to build an image of the field like [Figure 2.40](#), the FOV is scanned over the region and to obtain polarimetric information the modulator cycles through the modulation states like [Equation 2.19](#) at each scan step.

The same procedure is followed for a multi-slit spectrograph like **MSSP** using a GUI ([Figure 2.47](#)). The GUI is developed in LabViewTM and it is used to control the camera, **LCVRs**, scanning mirror and polcal unit. The functions performed by the GUI in the order of execution are -

1. System initialization - This step initializes all the components for an observation
 - The scanning mirror which was parked in home position is now brought to scan position.
 - The camera is initialized, camram memory is reset to 0's and the peltier cooler is switched on and set to a predefined temperature.
 - The **LCVRs** are set to 0V and the user is prompted for temperature of operation for the **LCVR**.
 - The polcal unit is checked for connectivity (as it is shared by **MSSP** and a narrow band imager) and initialized to set retarder at 0°.
2. Preparation for observation - In this step the user
 - Is asked to select between spectroscopic observation or spectro-polarimetric observation.
 - Then the user can set the exposure time for the camera and intensity range in the display window.
 - In spectro-polarimetric mode the user can choose to average the observation in two ways
 - a) Average per modulation - If the user wants to average N frames then in this scheme each modulation state is recorded N times and averaged. Then the modulator goes to the next modulation state.
 - b) Average per cycle - If the user wants to average N frames then a complete cycle of modulation is run once then this cycle is added to the next complete cycle until N cycles. The summed up cycles are then averaged i.e. divided by N. Note that both these averaging techniques are done per scan position and the process is repeated for every step advanced in the raster scan.
3. Observation Mode - The observation mode is divided into three parts
 - Data acquisition - The scanning mirror raster scans the image on the field and modulates the spectra at each scan.
 - Flat fielding - The user is prompted to move the telescope to Sun center and perform random walk around the Sun

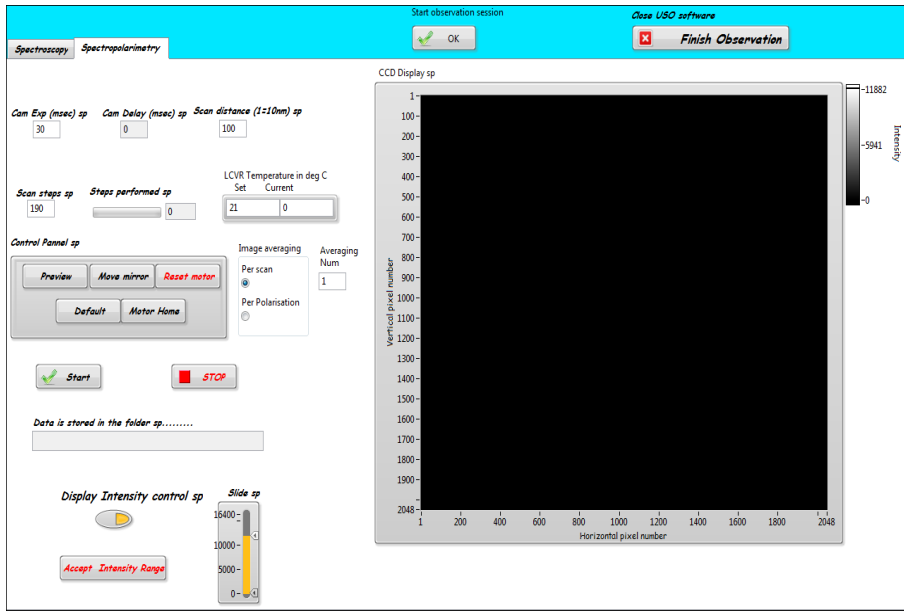


Figure 2.47: A snapshot of the GUI developed to operate [MSSP](#). The GUI varies dynamically according to the operation being performed.

center. While the telescope performs a random walk, the system records the field which will be used as a flat correction image during post processing.

- **polcal** - This step is performed only in spectro-polarimetric mode. The user is indicated that **polcal** is initiated. The zero order retarder unit performs six rotations of 22.5^0 and at each rotation step, four modulations are done using [MSSP](#) polarimeter and the data is stored in the cam-ram of the camera which is then transferred to the PC.
- Dark calibration - The camera used in our setup is a shutter less CCD chip. In order to perform dark calibration the entrance aperture of the spectrograph has to be closed with a lid. The GUI prompts the user to cover the entrance aperture and records dark frames from the CCD which are used in dark correction of the CCD.

After the completion of observation, the user is prompted for more observations. If the user wishes to perform more observations, then, Steps 2 and 3 are repeated else the GUI places the camera in standby, scanning mirror in home position and exits.

2.6.2 Data reduction procedure

The GUI records the data in the standard FITS format (Wells, Greisen, and Harten [[128](#)]). The data set has four parts - spectroscopic or spectro-polarimetric data of the [FOV](#), flat field, dark and polcal data

PARAMETER	VALUE
Sunspot number	NOAA 12653
Sunspot type	α
Observing date	28 th April 2017
Observation start time	10:45 UT
Duration of observation	15 min
Number of steps in raster scan	200
Mode of observation	Spectropolarimetric

Table 2.10: Field details for engineering run observation of an active region

for spectro-polarimetry. The raw data consists of intensity images which are converted to Stokes data and later inverted to get field parameters.

The data set presented in this section is active region NOAA 12653 recorded on 28th April 2017. NOAA 12653 is an α type sunspot with an approximate size of 20×20 arcsec including the penumbra. Details of the observation are given in [Table 2.10](#). A raw spectral image at the center scan position is shown in [Figure 2.27b](#).

The data reduction is done using [MSSP](#) data processing codes, the reduction procedure involves -

1. Spectral curvature removal - The optical path length for a ray originating at the center of the slit is longer than the optical path length of a ray originating at the edge of the slit. Thus a spectral region of wavelength λ has a curvature on the image plane and this curvature is towards the longer wavelength as we move away from the center of the slit ([Figure 2.48](#)). This curvature is removed by tracing the line core of the telluric line at 6301.99 \AA and shifting each spectral band along the slit to the location of the spectral band at the center of the slit.
2. Generating master flat - The flat field images are averaged into a single flat. The telluric lines and iron lines are averaged all along the slit to generate an average line profile. This line profile is used to remove the absorption line features in the spectra. The resultant image is a master flat used for gain table correction ([Figure 2.49](#)). It must be noted that the average line profile removes the spectral features but not the variation in the gain between pixels. So the removal of spectral line in master flat does not introduce any artifacts in the data.
3. Generating Stokes data - The curvature removed data is divided by flat and the resultant gain corrected data is demodulated.

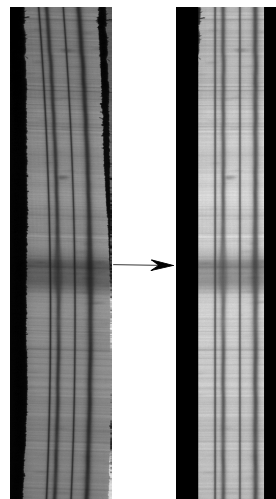


Figure 2.48: An example of correction for spectral curvature of the center slit of [MSSP](#)

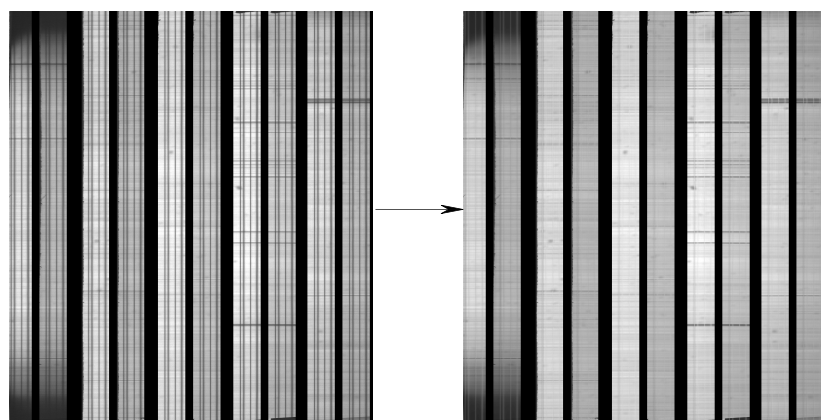


Figure 2.49: Master flat for [MSSP](#) is generated by removing the spectral line in flat data. The images shown in this figure is a the multi-slit spectra taken from $2k \times 2k$ pco.2000 camera.

Each raster scan has four images with intensity I_1, I_2, I_3 and I_4 such that

$$\begin{pmatrix} I_1 \\ I_2 \\ I_3 \\ I_4 \end{pmatrix} = [M_M] \begin{pmatrix} I \\ Q \\ U \\ V \end{pmatrix}_{EA} \quad \text{or}$$

$$[I_I] = [M_M] [S]_{EA}$$

where $[M_M]$ is the modulation matrix given in [Equation 2.19](#) and $[S]_{EA}$ is the Stokes vector for light at entrance aperture of the polarimeter unit. So

$$[S]_{EA} = [M_M]^{-1} [I_I]$$

is the demodulated Stokes data of the recorded intensity images.

4. [polcal](#) correction - The Stokes data is corrected for crosstalk due to instrument polarization by using the Mueller matrix generated using [polcal](#).

$$[S]_F = M_I^{-1} [S]_{EA}$$

where M_I is the Mueller matrix of the instrument system that introduces polarization into the incoming light. For NOAA 12653 the recorded instrument polarization was

$$M_I = \begin{pmatrix} 1.0000 & -0.0976 & 0.0116 & -0.0194 \\ -0.1680 & 0.4130 & -0.0499 & 0.0461 \\ -0.0171 & -0.0877 & -0.0464 & 0.4025 \\ -0.0159 & -0.0666 & -0.4226 & -0.1229 \end{pmatrix}.$$

5. Removal of telescope polarization - The telescope Mueller matrix M_T given by [Equation 2.26](#) is generated for a silver coated mirror at 6302 Å (n=0.05686, k=4.2559) such that

$$[S]_{\odot} = M_T^{-1} [S]_F$$

where Stokes vector $[S]_{\odot}$ is the polarized light coming from the source which in this case is NOAA 12653. [Figure 2.50](#) shows the telescope and polcal corrected profiles against the uncorrected ones. It must be noted that a residual of 7-10% is present in the corrected data due to systematics and assumption that the mirror surface is made up of bare silver.

6. Science ready data - In this step, the 5 slits in dual beam are segregated into two portions where each portion contains 5 slits of one of the orthogonal polarization. The Stokes Q, U and V data is normalized with Stokes I and the dual beam are combined

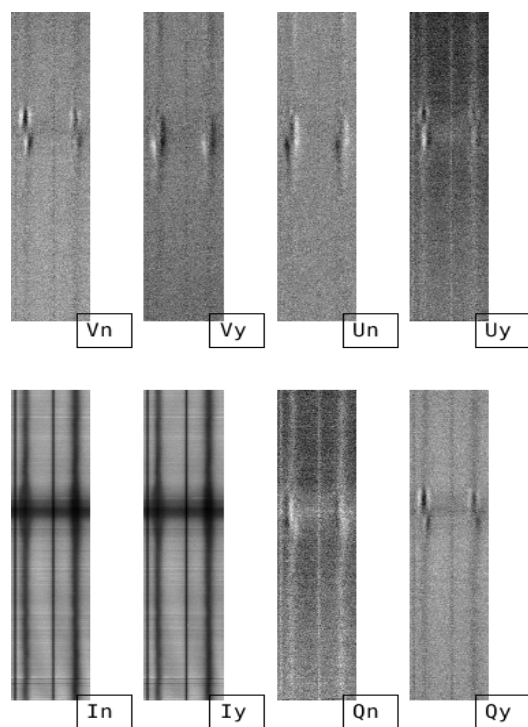


Figure 2.50: Stokes data with polcal and telescope polarization correction.

The subscript *n* stands for not corrected data and the subscript *y* stands for corrected data. A residual of 7-10% remains after the corrections.

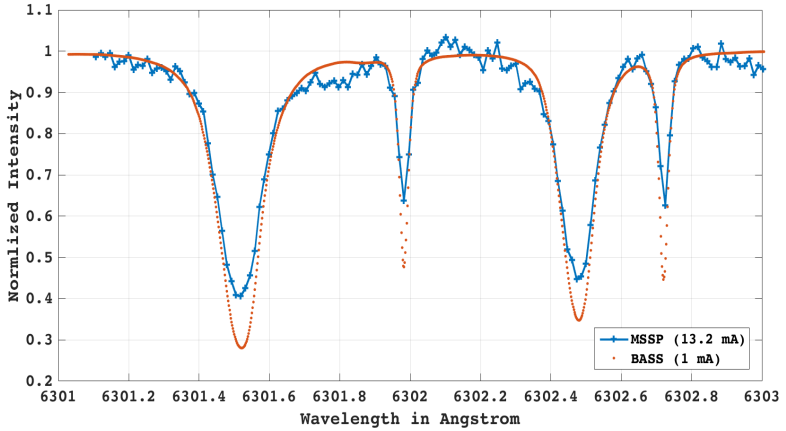


Figure 2.51: A plot of spectra obtained from [MSSP](#) and comparison with [BASS](#) solar atlas gives an estimate of stray light fraction

using the relation [Equation 2.22](#) and [Equation 2.23](#). Now each slit has a portion of the entire [FOV](#) in the 200 raster scanned images. The images are stacked in sequence such that the first 200 images are from slit 1, the next 200 images are from slit 2 and so on until the 5th slit. The final stacked images of the raster scan contains the entire [FOV](#) sampled by the entrance aperture (e. g. [Figure 2.40](#)). This data is now in the standard form of data obtained from any slit based spectrograph and can be utilized to perform magnetic field inversion or other scientific analysis.

2.6.2.1 Vector magnetic field for NOAA 12653

The extraction of magnetic field from Stokes profiles using radiative transfer equation (Baur et al. [8]) is implemented using many inversion codes. The inversion code used for extracting vector magnetic field of NOAA 12653 is NICOLE (Socas-Navarro et al. [110]). NICOLE is capable of multi threading the inversion process so that large field can be inverted sufficiently quickly using a cluster of computers. The other reason for the use of NICOLE is its capability to consider Non-LTE conditions for spectral lines like Ca II at 8542 Å and other chromospheric lines. As [MSSP](#) is going to be upgraded in the future to observe in those wavelength bands, NICOLE is a logical choice.

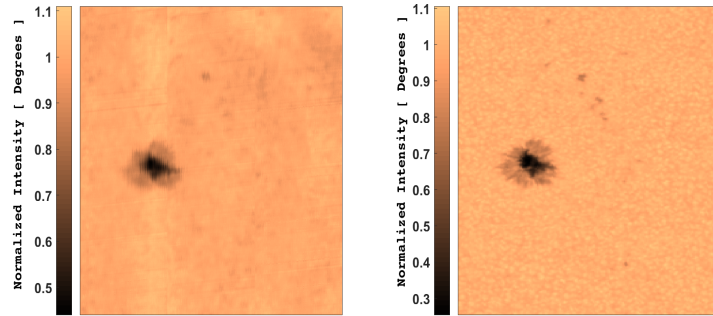
As it was intended to test the working of [MSSP](#) and compare its results with [HMI](#), NOAA 12653 is inverted for a single atmosphere model i. e. Milne-Eddington atmosphere. Stray light is any unwanted light that pollutes the purity of the spectra. A proper estimate of stray light fraction is needed in order to perform inversions. [Figure 2.51](#) is a plot of Fe I line pair obtained from [MSSP](#) and overplotted with BASS solar atlas spectra in the same wavelength range. A stray light fraction of 20-25% exists in the data.

The magnetic field parameters extracted from NOAA 12653 recorded by [MSSP](#) and inverted using NICOLE is shown in [Figure 2.52](#). The region under consideration is a $93.6'' \times 144.23''$ field. It can be seen that the vector magnetic field (line of sight vector with inclination and azimuth angle) of the region recorded using [MSSP](#) has comparable results to [HMI](#) data except for blur caused due to atmospheric seeing. Thus the engineering run of the instrument is successfully completed and the instrument is ready for regular science observation.

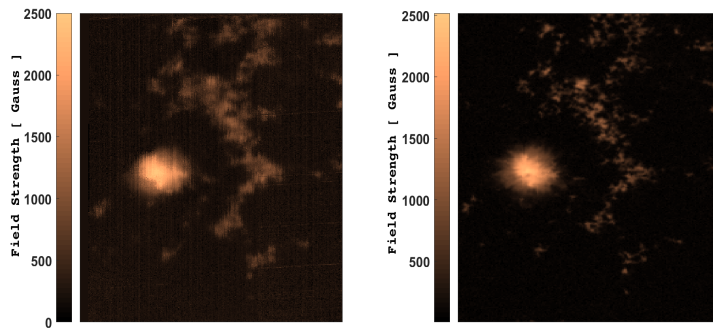
2.7 CONCLUSION AND FUTURE WORK

This chapter dealt with the construction of [MSSP](#) from the component level keeping in view the science goals of the instrument as the development constraint. The chapter began with a comparison between slit based spectrograph and [FP](#) based spectrograph. It was found that a slit based spectrograph can truly simultaneously perform spectroscopy at multiple wavelengths and has higher efficiency when working with high spectral resolutions than a [FP](#). But one of the major draw backs of a slit spectrograph is the time required to develop an image of the field through raster scan. As the spectrograph type chosen for observations was a slit and grating, a conceptual diagram explaining the possibility of utilizing a small section of the spectra for a specific purpose and utilizing the remaining space of the detector to place multiple slits was developed. This reduced the time taken for the raster scan. Keeping scientific goals in mind, the spectrograph for our purpose was designed at four wavelength points. The choice of each component and the parameters specifying the component were explained taking the science goal into consideration. An added advantage was given with the use of [DWDM](#) filter and its nearly rectangular filter response. The polarimeter was then designed with dual beam analyzer to reduce Stokes I cross-talk and a standard balanced modulation scheme.

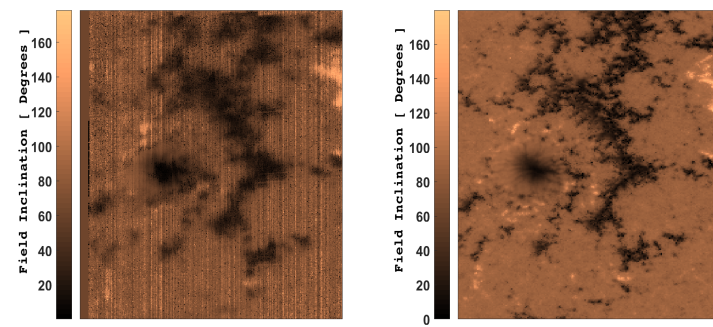
With the development of the instrument, tests were conducted to verify the performance of the spectrograph in terms of spectral resolution and dispersion. Modulator's voltage versus retardance relation was found and a spectral mask technique was proposed to operate [MSSP](#) in dual beam mode. Upon verifying the working of [MSSP](#), it was integrated to [MAST](#) and imaging capabilities were obtained due to scanning mirror mechanism. Two sources of concern for polarization measurements i. e. instrument polarization and telescope polarization were addressed separately. One with experimentally obtained correction values and the other obtained through a theoretical model. The crosstalk was removed with a residual of 7-10%. Finally a data set was obtained during the engineering run using the user friendly GUI developed for [MSSP](#). The data were reduced from a raw form to science ready form and inverted. The inverted results were compared



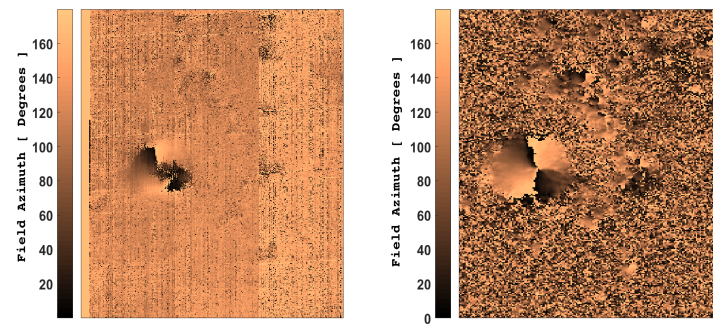
(a) Continuum intensity map of the field



(b) Line of sight magnetic field



(c) Magnetic field inclination



(d) Azimuthal orientation of the magnetic field

Figure 2.52: Vector magnetic field of NOAA 12653 obtained from NICOLE and recorded by [MSSP](#) (left image) and compared with [HMI](#) observations (right image). The area of the region represented in the figure is $93.6'' \times 144.23''$

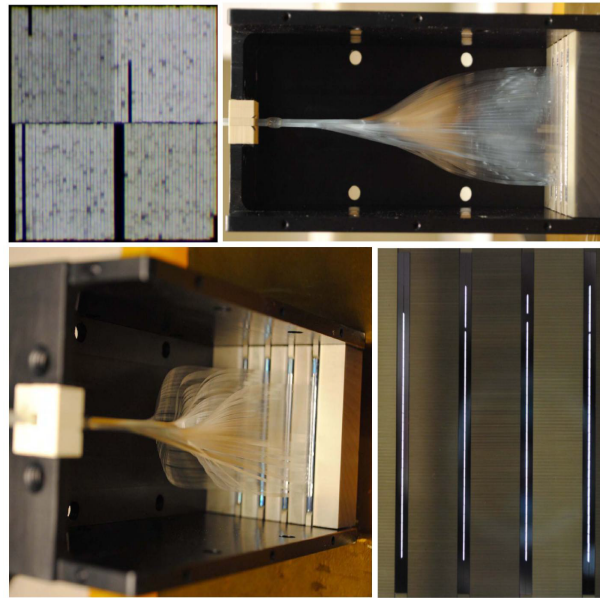


Figure 2.53: Concept of fiber bundle sampling the image in 2D and reorienting it into 1D multi-slit. The image was taken from Schad et al. [95]. From top left moving in clockwise are 1 - fiber bundle sampling 2D FOV; 2 & 3 - side view of the reorientation of 2D fiber into 1D slits; 4 - 1D slits which form the entrance aperture of the spectrograph.

with HMI and were found to have a close match. Thus the development, testing and working of the imaging spectro-polarimeter was presented in this chapter.

It can be seen that MSSP was built for four wavelengths with an emphasis on simultaneity in measurements. The advantage of multi-wavelength measurement in determining atmosphere parameters are shown in the next chapter.

The future work of multi-wavelength observation will begin as soon as the AO system becomes available. The upgrade requires new cameras and DWDM filters. Apart from multi-wavelength upgrade there lies an important performance enhancement system for MSSP. The new system is yet again borrowed from fiber optical communication. With the advent of single mode fiber technology, the core diameter has shrunk to $8 \mu\text{m}$. If multiple fibers are stacked at the image plane of the FOV such that they sample the region with high density then these fibers can be reoriented into multiple slits at the entrance aperture of the spectrograph. This effectively converts a 2D field into a 1D slit as shown in Figure 2.53. This would reduce the time taken to image the field from raster scan to a single snapshot. Such techniques are being tested (Lin [65], Lin and Versteegh [68], and Schad et al. [95]) to improve spectro-polarimetric capabilities.

3

SPECTRO-POLARIMETRIC INVERSION

OVERVIEW

In this chapter, the results obtained from the inversion of two absorption lines Fe-I at 6302 Å and Ca-II at 8542 Å which are formed at the photosphere and lower chromosphere respectively, are presented. The data is obtained from SOLIS-VSM. An inversion code called NICOLE is used to derive the atmospheric field parameters (Socas-Navarro et al. [110]). The field parameters obtained at the photosphere are verified with HMI's measurements while the ones obtained at chromosphere are verified using PFSS. This chapter highlights the type of data received from MSSP, its interpretation and expected results. The chapter concludes by placing an introductory note on hyper-spectral imaging.

3.1 INTRODUCTION

MSSP described in the previous chapter is capable of obtaining spectral information at different wavelengths simultaneously. As mentioned in Section 1.2, it is necessary to deduce the field information at different heights in order to understand the coupling between the layers of the solar atmosphere and the transport of energy between them. As spectral lines are formed at different heights, simultaneous measurements of such lines become mandatory. The four wavelengths at which MSSP is designed to operate are Fe-I at 6302 Å, Fe-I at 15653 Å, Ca-II at 8542 Å and He-I at 10830 Å which corresponds to mid-photosphere, lower photosphere, lower chromosphere and upper chromosphere respectively. MSSP is currently operating at a single wavelength band Fe-I at 6302 Å. Spectro-polarimetric data obtained from SOLIS-VSM (Balasubramaniam and Pevtsov [5] and Henney, Keller, and Harvey [44]) which observes in Fe-I at 6302 Å and Ca-II at 8542 Å lines was inverted in order to determine the field configuration at photosphere and lower chromosphere. The diagnostic capabilities of calcium 8542 Å (Kuridze et al. [59]) for measuring chromospheric field is shown by Socas-Navarro et al. [110]. Thus the results presented in this chapter serves as a preamble to the data and results expected from upgraded MSSP.

The field strength of a typical sunspot has been inferred to have a gradient of 4 G/km by inverting the IR line of Fe-I formed at the photosphere (Mathew et al. [70]). This may be valid for a few hundred kilometers at the photosphere and not the whole atmosphere because

such a trend would lead to zero magnetic field at a height of 750 km for a strong 3 kG sunspot. Further, the contribution function of the IR line is well within the photosphere so it would be inappropriate to infer field parameters at chromospheric heights. In order to obtain an average gradient in the field between photosphere and chromosphere, inverting the lines formed at the appropriate heights would generate reliable results. We use the data obtained from SOLIS to deduce the magnetic field at photosphere and lower chromosphere for a simple ' α ' class sunspot. The change in field strength at these two heights will provide the average gradient of magnetic field as α 's have a dominant monopolar spot and a nearly evenly spread out field of opposite polarity.

3.2 DESCRIPTION OF THE INSTRUMENT AND DATA

3.2.1 SOLIS-VSM

SOLIS is a synoptic facility for solar observation dedicated for the study of long term evolution of the Sun (Balasubramaniam and Pevtsov [5], Henney, Keller, and Harvey [44], and Keller [53]). SOLIS-VSM is a vector magnetograph placed on a 50 cm telescope. It consists of a single slit and grating based spectrograph and records the image of the entire Sun at two wavelength bands viz Fe-I at 6302 Å and Ca-II at 8542 Å. The images are recorded sequentially and not simultaneously with a typical data acquisition session taking about an hour. Hence, there exists a time delay of about an hour between the field parameters obtained at two different heights of the solar atmosphere. Due to this delay, complex flaring active regions cannot be studied. On the other hand, a simple active region like an α type sunspot which evolves at time scales of a day or more is a suitable candidate.

The VSM records full Stokes spectra at both the wavebands. A modulator unit is placed in front of the slit along with a prefilter and polarization calibration unit for each waveband. A beam splitter is used as an analyzer at the detector. The slit samples a 1 arcsec field on the Sun and the image is raster scanned to build the 2D image. Time taken to record one frame is 0.6 sec for Fe and 1.2 sec for Ca. The spectral resolution of the device is 50 mÅ.

3.2.2 Active region NOAA 12683

The synoptic data presented in this chapter is for an active region NOAA 12683 recorded on 30th September 2017. The active region is an alpha type sunspot. MSSP records a square region of size 4.242 arcmin² on the Sun in its large field mode. Thus a region of 4.242 arcmin² is chosen around the sunspot. It occupies 255×255 pixels on the detector in SOLIS-VSM. The sunspot has two umbrae separated

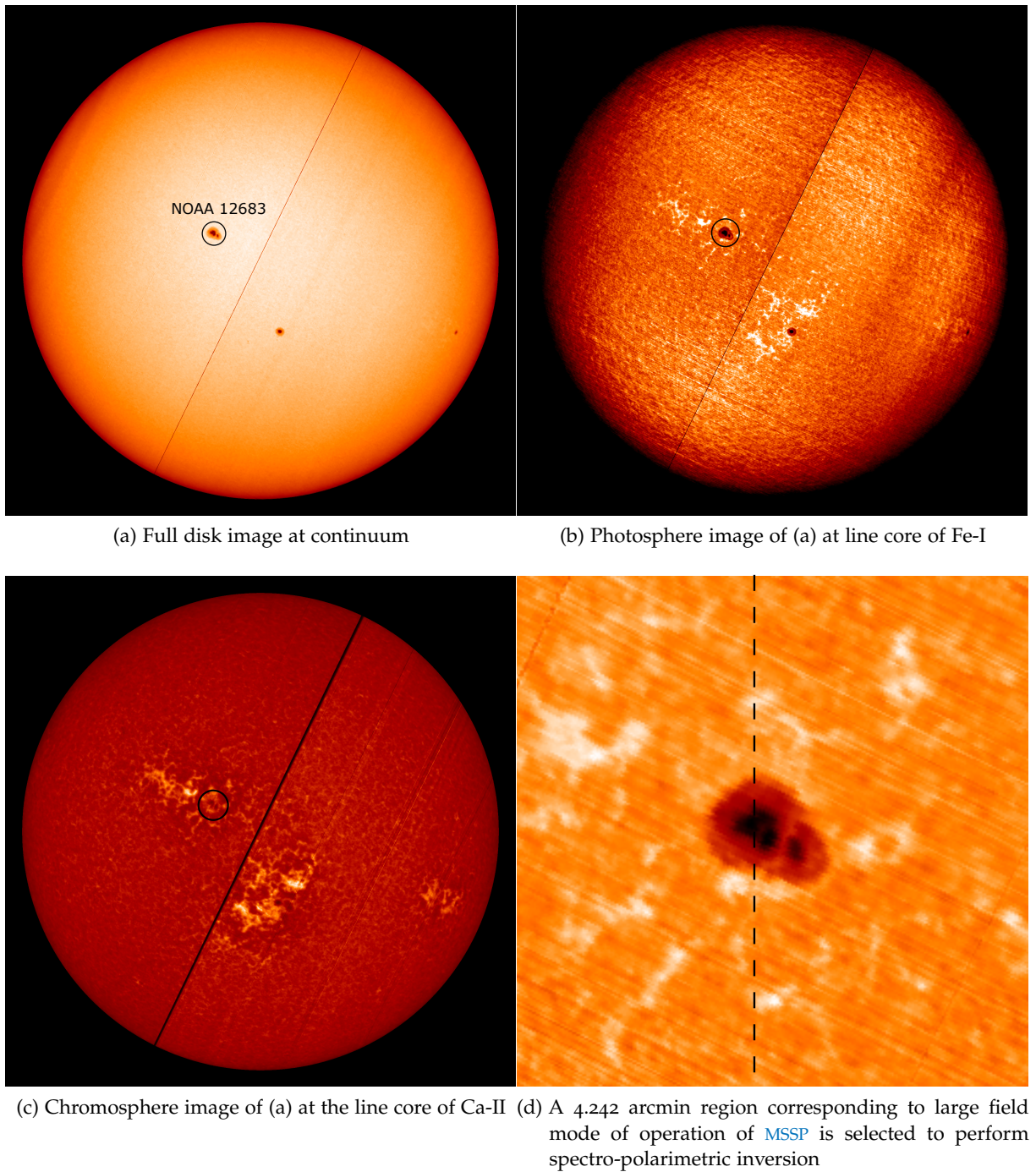


Figure 3.1: A synoptic image of Sun recorded by SOLIS-VSM on 30th September 2017 is shown in the figure. The α -sunspot NOAA 12683 who's photospheric and chromospheric field obtained is marked in (a), (b) and (c) with a zoomed in image shown in (d). The Dashed line in (d) is chosen to represent field strength and inclination in [Figure 3.6](#).

PARAMETER	VALUE
Wavelength sample	21.4 mÅ/pix
Starting wavelength	6300.938 Å
Number of wavelength points	93

(a) Spectral sample for Fe-I line pair at 6302 Å

PARAMETER	VALUE
Wavelength sample	36.5 mÅ/pix
Starting wavelength	8540.5 Å
Number of wavelength points	93

(b) Spectral sample for Ca-II at 8542 Å

Table 3.1: Spectral parameters for the data set taken from SOLIS on 30th Sep 2017

by a light bridge and a distinct common penumbra surrounds it. The spatial resolution is 1 arcsec and the spectral parameters for the data set is given in [Table 3.1](#).

3.2.3 NICOLE - inversion code

In order to obtain the field parameters from the Stokes spectra of the Region of Interest (ROI), [Equation 1.3](#) has to be solved numerically. Iron line formed at the photosphere is in an LTE atmosphere while calcium line formed at chromospheric heights is in a non-LTE regime. Hence, a code that numerically synthesizes Stokes spectra for a non-LTE atmosphere and minimizes the difference between synthetic and observed Stokes spectra is chosen. NICOLE (Socas-Navarro et al. [110]) is an open source inversion code (available at <http://www.iac.es/proyecto/inversion/codes/nicole.php>) and the inversion code performs LTE inversion on iron line and non-LTE inversion on calcium line to extract the model atmospheric parameters (Socas-Navarro [106]). Steps involved in a typical inversion for LTE and non-LTE atmosphere is given in [Appendix A](#). As NLTE inversions are computationally intensive, NICOLE offers parallel processing where multiple CPU cores invert multiple pixels simultaneously. The data set presented in this chapter was inverted using the “vikram-HPC” super computer cluster at the Physical Research Laboratory, Ahmedabad.

⁵¹² CPU cores were used for parallel processing and inversion

3.2.4 Data reduction and input parameters to NICOLE

The Stokes data given as an input to the code is a [255×255×93] data cube with the first two dimensions being spatial (x,y) and third di-

mension being wavelength λ . Stokes I is normalized with respect to the quiet Sun continuum while Stokes-Q, U and V are normalized with respect to Stokes-I. After providing the data, the user has to configure NICOLE to invert the data. NICOLE has a configuration file which determines the input settings for the inversion. A typical inversion requires information regarding the stray light fraction, instrument profile, filling fraction, spectral parameters, atomic line transition and model atmosphere.

Stray light and instrument profile are obtained by performing Monte-Carlo simulation using a gaussian profile to fit the FTS spectra and observed data. Atomic line transitions are specific to the element and its ionization state. NICOLE has an inbuilt atomic line database which is set to iron and calcium for our analysis. A model atmosphere is the initial guess value of the field parameters which an user provides to the inversion code. The code generates a synthetic spectra from the model atmosphere and compares it with the observed spectra. It then alters the values of the model atmosphere to minimize χ^2 given in [Equation 1.8](#). The model atmospheric values which give the best fit or the least possible χ^2 within the user specified number of iterations is considered to be the physical conditions of the real atmosphere at the time of recording the data. The FALC model (Fontenla et al. [32]) is given as the initial model atmosphere for both photospheric and chromospheric inversion (de la Cruz Rodríguez et al. [20], Leenaarts et al. [61], and Leenaarts et al. [62]).

FTS spectra is obtained using a Fourier transform spectrometer

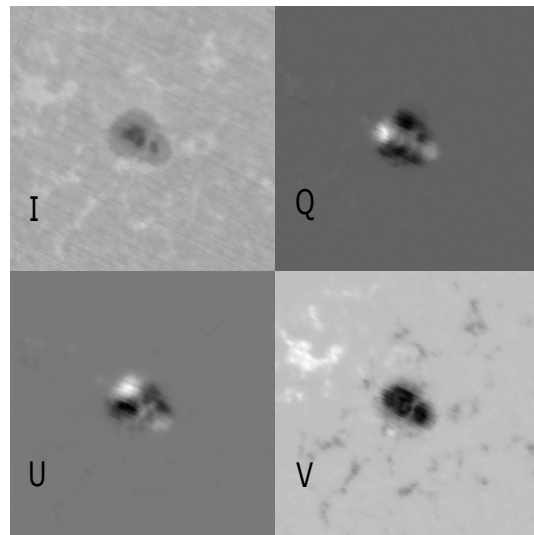
3.3 RESULTS

In this section the results obtained from spectro-polarimetric inversion of NOAA 12683 are presented and validated. The photospheric fields are compared with [HMI](#) and chromospheric fields are compared with results obtained from [PFSS](#).

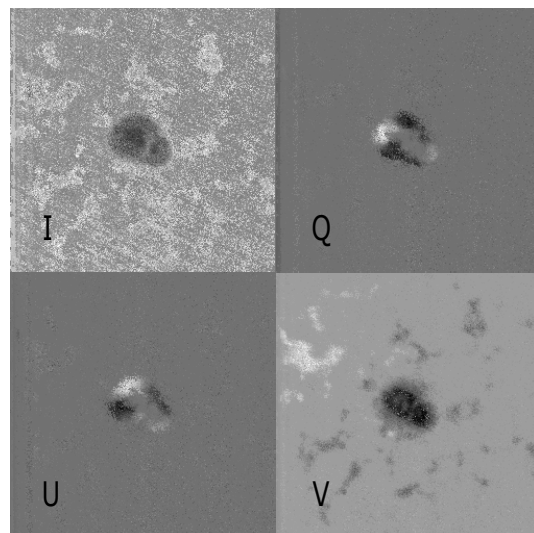
3.3.1 Field values and comparison with standard results

The base of the photosphere is that region at which the optical depth τ reaches unity for a photon with wavelength equal to 500 nm. The Fe-I line forms at an average height of 150-200 km from the $\tau_{500} = 1$ surface (Bruls, Lites, and Murphy [15]). Stokes data of the 4.242×4.242 arcmin 2 ROI is shown in [Figure 3.2a](#). A section of the synthesized data cube of the Stokes spectra is shown in [Figure 3.2b](#). The corresponding magnetic field strength, inclination and azimuth are shown in [Figure 3.3](#). The vector magnetic field parameters are compared with the values obtained from [HMI](#).

From MHD simulations it is estimated that Ca-II line forms at an average height of 1.5 - 2 Mm from the solar surface which corresponds to the lower chromosphere (Carlin and Ramos [17]). The field strength



(a) Observed Stokes I, Q, U, V for a 4.242×4.242 arcmin 2 field as shown in Figure 3.1d



(b) Synthetic Stokes I, Q, U, V generated for the values shown in (a)

Figure 3.2: A Model atmosphere generated by fitting the observed spectra with a synthesized spectra for Fe-I line pair at 6302 Å. The observed and synthesized spectra of 4.242×4.242 arcmin 2 field are shown in (a) and (b) respectively.

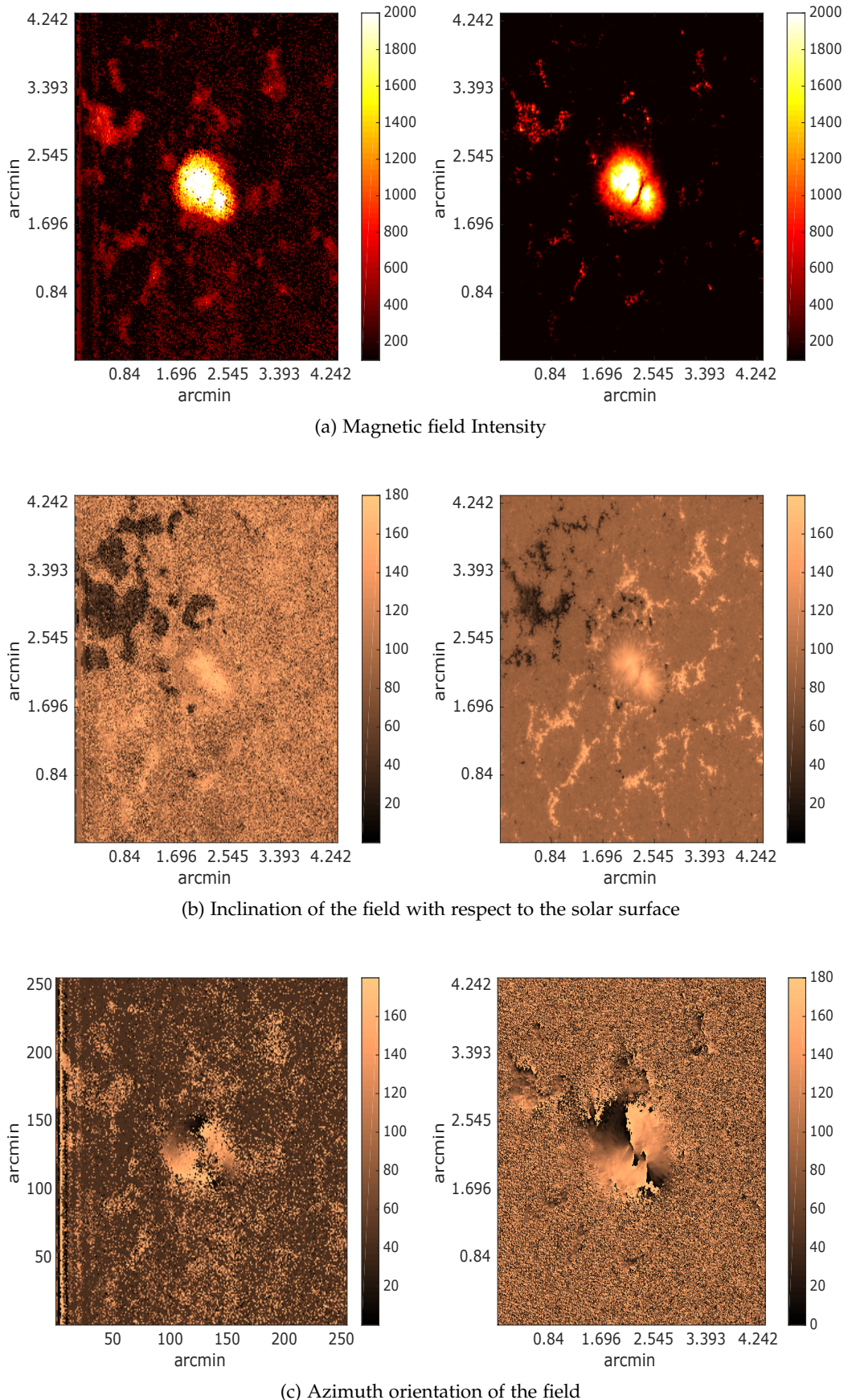


Figure 3.3: Comparison of the photospheric field strength, inclination and azimuth obtained from NICOLE - LTE inversion (left) of Fe-I line pair with standard HMI's results (right) of the same 4.242×4.242 arcmin 2 region defined in Figure 3.1d

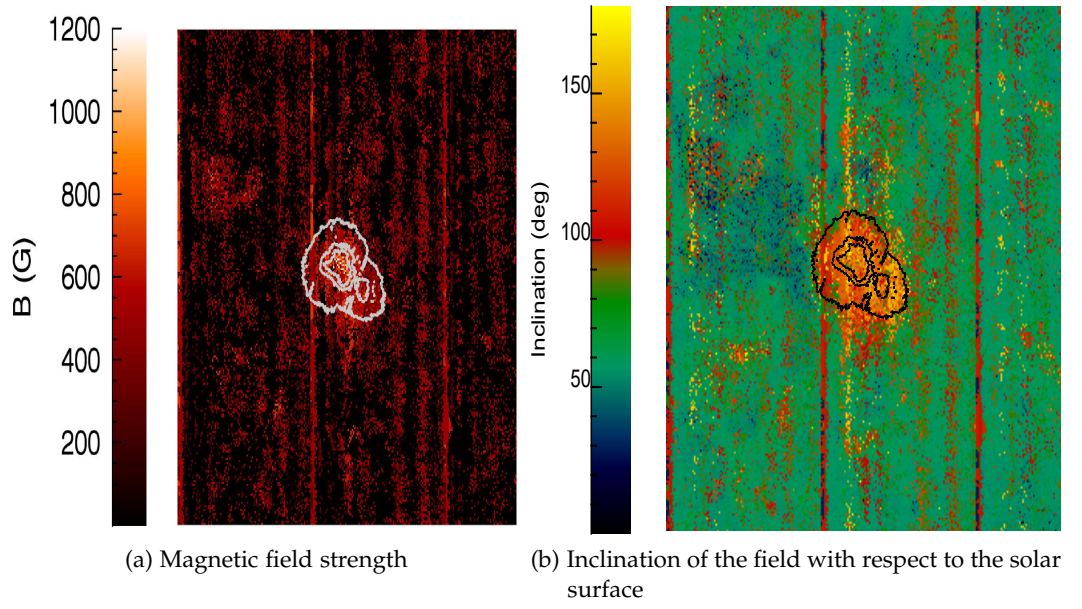


Figure 3.4: Chromospheric magnetic field strength and inclination obtained from NICOLE - NLTE inversion of Ca-II for the same 4.242×4.242 arcmin 2 field.

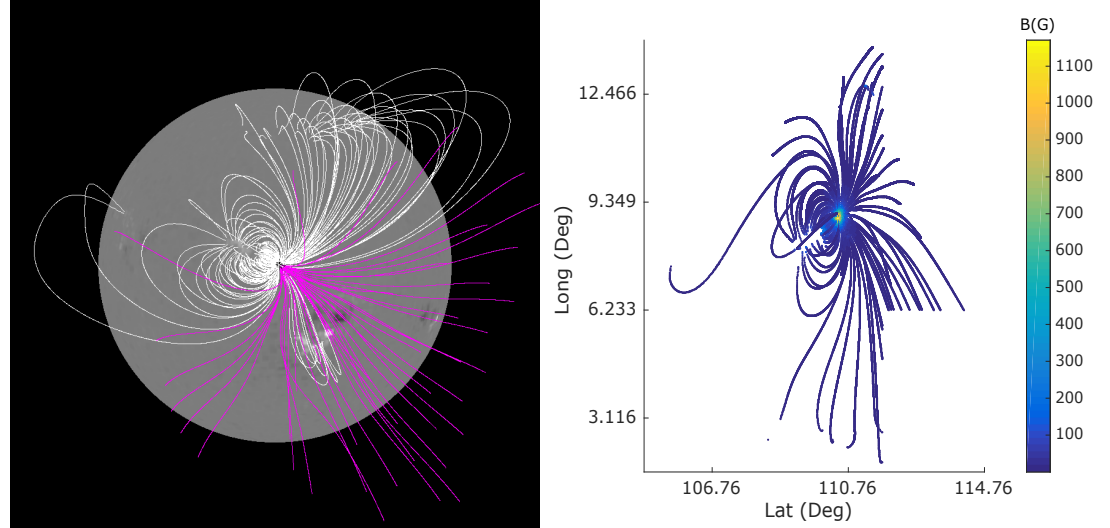
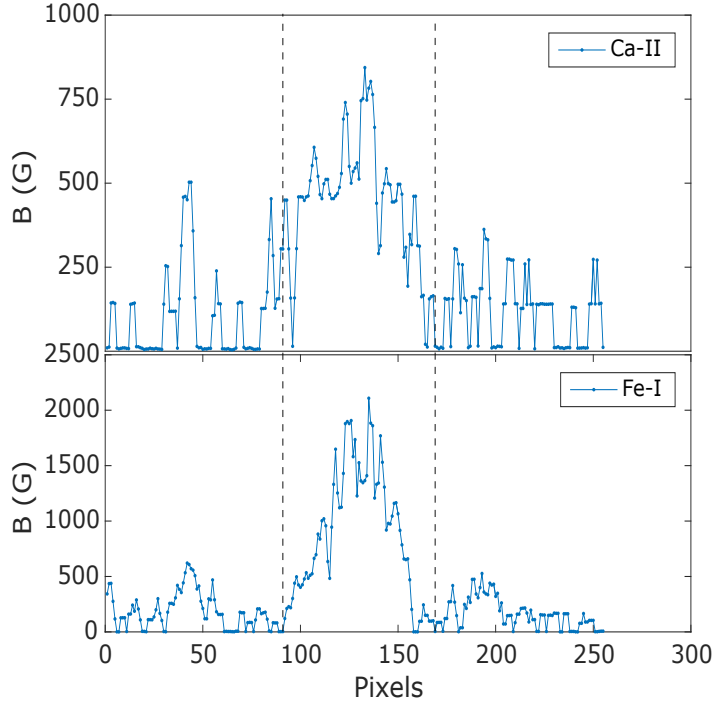


Figure 3.5: PFSS hairy Sun image (left) shows the divergence of field lines from the photosphere to corona over NOAA 12683. The pink lines represent open field lines. Magnetic flux at the lower chromosphere from 1 to 2 Mm is shown in the image on the right. This region also corresponds to the formation of Ca-II. Hence the magnetic flux obtained from PFSS at 1-2 Mm corresponds to the expected field strength obtained from Ca-II inversion.

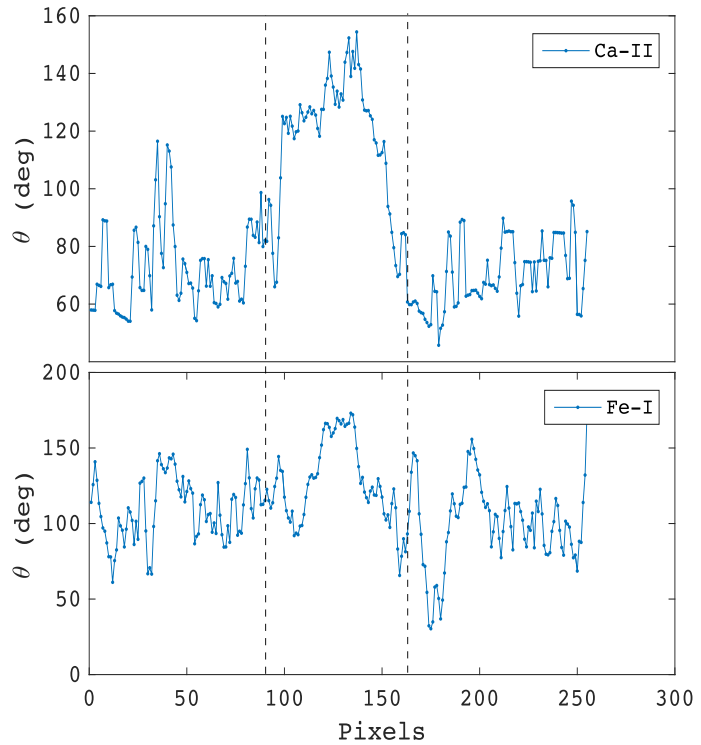
and inclination obtained from NLTE inversion of Ca-II is shown in [Figure 3.4](#). Potential field models are used on regular basis to extrapolate the photospheric magnetic field to coronal heights (Tadesse et al. [117]). Potential force source extrapolation of the photospheric field using the *SSWIDL-pfss* module (Riley et al. [85], Schatten, Wilcox, and Ness [96], and Staley [112]) was performed to verify the magnitude of the field strength obtained at the chromospheric heights. The “hairy Sun” image which represents the extrapolated field lines from the photosphere upto the corona is shown in [Figure 3.5](#). The photospheric region chosen has $L = [104.76 : 116.48]$ and $B = [7.97 : 17.35]$ which encompasses the active region NOAA 12683. The pink lines represent open field lines and the white lines represent closed field lines. A section of the atmosphere lying between $1.002 R_{\odot}$ to $1.0028 R_{\odot}$ which corresponds to the $1.5 - 2$ Mm region of the solar atmosphere is chosen and the magnetic flux at that region is plotted in [Figure 3.5](#). The flux values are comparable to the field strength obtained from inversion with a marginal difference of 100 G between the two results.

3.3.2 Field strength and temperature

A region along the y-axis is chosen from the [ROI](#) as shown in [Figure 3.1d](#). The field parameters at photosphere and chromosphere are compared along this region. A plot of field strength and inclination at photosphere and chromosphere along the selected line is shown in [Figure 3.6a](#). It is found that the field strength at the chromosphere is about 1000 G lower than the photosphere. Thus the field gradient is 1 G/km between the photosphere and lower chromosphere. It must be noted that the chromospheric field has also occupied a larger region due to field divergence as indicated by the magnetic field inclination shown in [Figure 3.6b](#). Thus the field is more uniform at the chromosphere and diverges at a lesser rate beyond the lower chromosphere. Due to non simultaneous observation and low spatial/spectral resolution, individual comparison of field parameters at the umbra and penumbra were not performed. Although it must be noted that this problem will not exist for [MSSP](#). The temperature stratification over the [ROI](#) with varying optical depth or height in the solar atmosphere is shown in [Figure 3.7](#). A plot of the variation in the temperature values in the umbra, penumbra and quiet Sun with increasing optical depth or decreasing height is shown in [Figure 3.7b](#). The temperature stratification was obtained by simultaneously fitting the calcium and iron line intensity in NICOLE.



(a) The field strength is lower and falls slowly as one moves away from the active region at the chromosphere. This suggests a more uniform field distribution at the chromosphere than photosphere.



(b) The field inclination occupies a broader region in the chromosphere with smaller variation.

Figure 3.6: A plot of chromospheric and photospheric field and inclination across a 255 pixel region as shown by a dashed line in Figure 3.1d. The two dashed lines in (a) and (b) is the approximate extent sunspot region in the chromosphere.

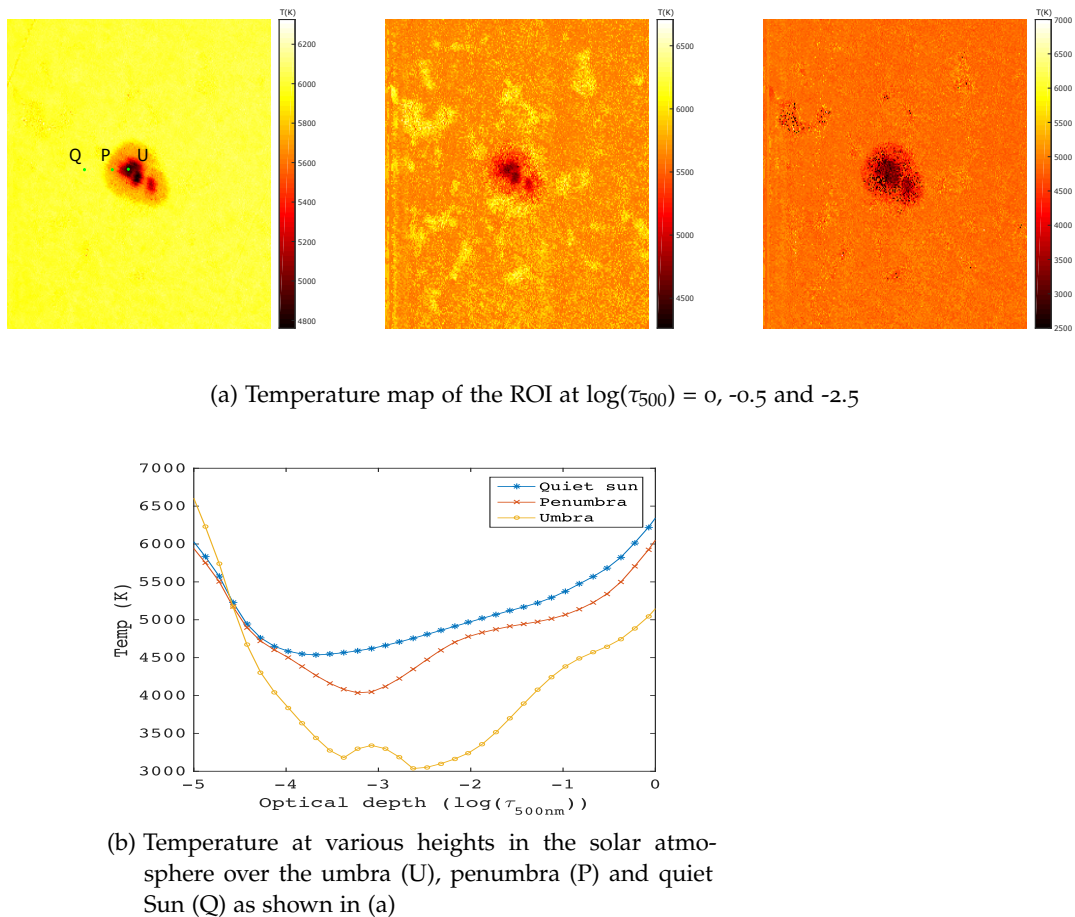


Figure 3.7: A map of the atmospheric temperature at various heights as obtained from the inverted model atmosphere

3.4 CONCLUSION

Absorption lines at different wavelength are formed at different heights based on the transition state, temperature, density and ionization of the element. Each line has a contribution function that gives the information of the atmosphere upto a particular height. In order to study a broader region of the solar atmosphere, simultaneous observation of multiple lines formed at multiple wavebands have to be performed.

Two lines were chosen to study the photospheric and lower chromospheric region. The Fe-I and Ca-II lines provide field information at these two heights and the temperature stratification between the two layers. It was found that a field gradient of 1 G/km exists rather than the 4 G/km as reported by Mathew et al. [70] in the umbral region of an α sunspot. As statistical measurements of coronal fields show that the typical field strength over an active region is about 50 G (Lin, Kuhn, and Coulter [64] and Lin, Penn, and Tomczyk [66]), the field diverges slowly beyond the lower chromosphere due to a more uniform and a greatly inclined field. Stratification of temperature between 100 km and 2 Mm region was obtained through simultaneous fit of photospheric and chromospheric line intensities. There is a large difference in time cadence and time period of observation for Fe-I and Ca-II. Due to this, plasma flows are different at different parts of the atmosphere. Thus a comparison of plasma velocity between photosphere and lower chromosphere is not given in this chapter.

The magnetic field parameters and other physical parameters like velocity and temperature of the solar atmosphere can be improvised by increasing the spectral resolution and time cadence of observation. Although [MSSP](#) meets these criteria, it requires few minutes to generate a hyper spectral cube by scanning the [ROI](#). It would be of great advantage if the entire hyper-spectral cube of the [ROI](#) is generated in a single snap shot. Such a device can be used to study the field configuration and its variation during dynamic events like a flare. Such instruments are called snapshot spectroscopes. We describe the development of one such device in the next chapter.

Part II
SNAPSHOT SPECTROSCOPY

4

SNAPSHOT SPECTRAL IMAGING

OVERVIEW

In this chapter, the concept of snapshot spectral imaging by sampling the pupil plane is discussed. Three instrument designs based on pupil sampling are proposed and one of the design is used to build an instrument called [LAS](#). The ability of this instrument to perform snapshot spectroscopy is tested at [USO](#) using [MAST](#). Snapshot and multi-spectral capabilities of [LAS](#) are demonstrated by recording the Ever-shed flow in sunspot penumbra at Fe-I 6301.5 Å and oscillations in prominence at H- α 6562.8 Å.

4.1 INTRODUCTION

Spectroscopy provides a plethora of information about the [FOV](#). A spectral image of the field consists of two spatial dimensions (say x-direction and y-direction) and one spectral dimension (wavelength- λ). A data cube which is made up of two spatial and one spectral dimension is called a hyper spectral cube or Hyper Spectral Image ([HSI](#)) and the dimensions are represented as [x, y, λ] as shown in [Figure 4.1](#). Each small cube in [Figure 4.1](#) represents a spatio-spectral point which corresponds to some spectral information of a spatial point in a 2D image. Traditionally there are three methods to generate hyper spectral cube of 2D field they are -

1. **Push broom scanning** :- A single spatial point is taken from a 2D spatial region and its spectra is obtained through dispersers like prism or grating. Then a different spatial point is taken from the field to repeat the process. The scanning mechanism involves movement in x and y direction to generate a spectral map of the whole field point by point which when combined forms a hyper spectral cube of the field.
2. **1D line scanning** :- This is a slit and grating based spectrgraph and the mechanism involves a slit which samples a 1D region of the 2D field and generates a wavelength map along all the points in that 1D field. This slit is moved or raster scanned over the 2D field to generate a hyper cube image of the field.
3. **Wavelength scanning** :- This method involves a filter wheel or Fabry-Pérot interferometer where the spatial information of a 2D image is obtained at a particular wavelength. The hyper

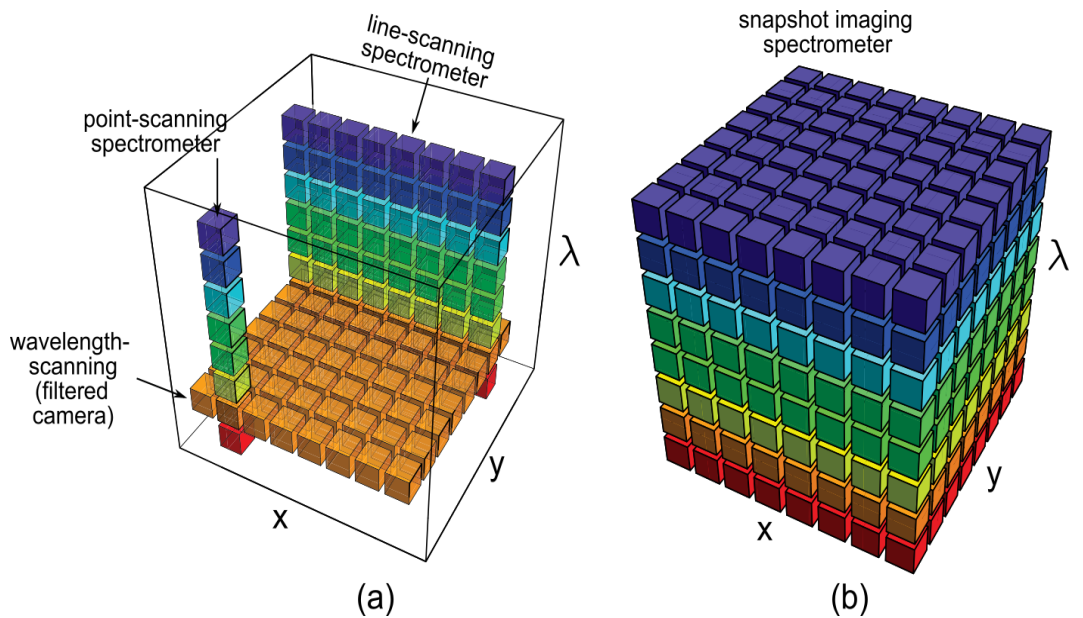


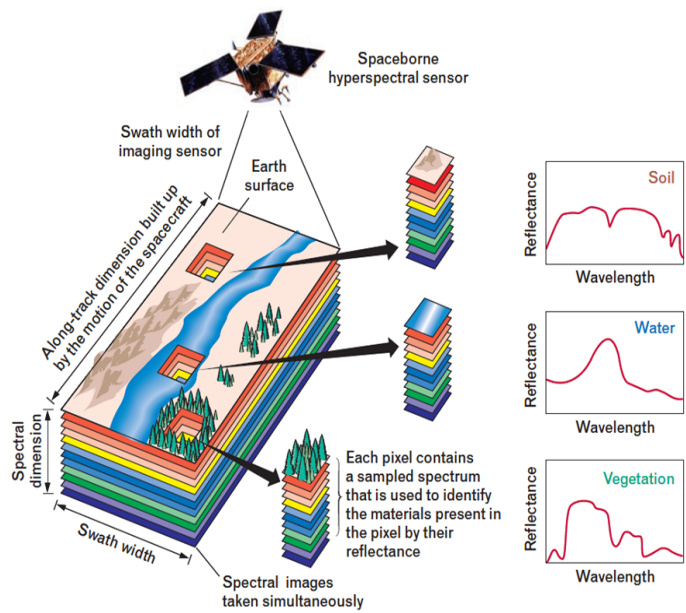
Figure 4.1: A hyper spectral data cube with the three axis representing two spatial dimension and one spectral dimension (Illustration borrowed from Hagen and Kudenov [43]). (a) Represents the three scanning mechanisms commonly used to generate a hyper spectral cube. (b) Represents a hypercube of an object consisting of the three dimensions $[x, y, \lambda]$ obtained in a snapshot

spectral cube is generated by obtaining several images of the 2D field at different wavelength points.

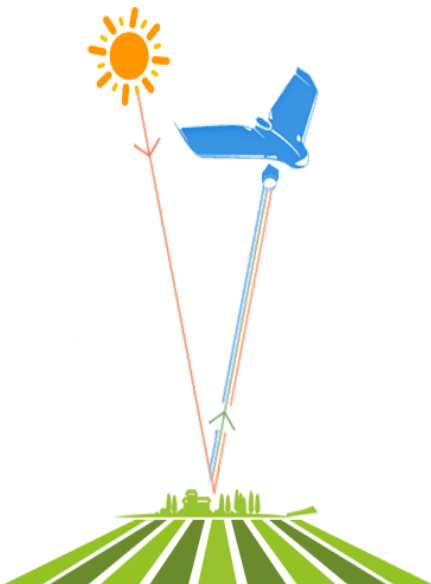
It is always necessary to generate the spectral information of an object before its spectral characteristics change or the object moves out of the FOV. E.g. Consider a satellite used for remote sensing where a patch of vegetation, soil and water body as shown in Figure 4.2a are to be imaged for their spectral signatures. If the satellite is at a low Earth orbit and has a small swath area (spatial region that can be scanned at given instance in time) and can accommodate only one or few topographic features then multiple transits have to be performed over the region to generate the hyper spectral cube of the entire region. But the spectral signatures of the field can vary with angle of irradiance of the Sun (Jensen and Lulla [47]). So for each transit of the satellite over the same field, solar irradiance and hence the spectra of the field varies. In order to over come this issue snapshot spectroscopic techniques were adopted in remote sensing. Snapshot spectroscopy is a method of obtaining the hyper spectral cube in a single image frame i.e. a 3D data cube of $[x, y, \lambda]$ is generated using a 2D detector plane. Several techniques exist for snapshot spectral imaging (Hagen and Kudenov [43]) of which three are adopted in astronomy.

Snapshot spectroscopic techniques were first developed for astronomy but had an immense growth due to remote sensing.

The snapshot hyperspectral techniques used in astronomy are -



(a) A satellite swath region consists of multiple geological features of variable spectral information



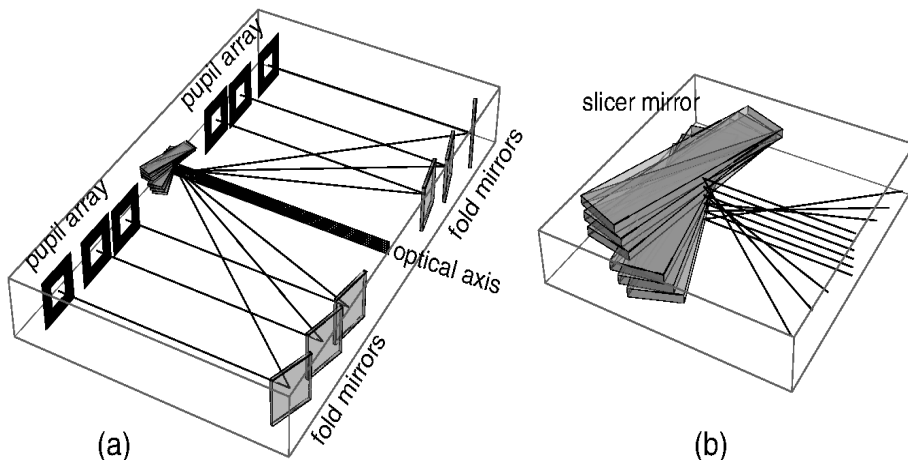
(b) The reflectance or spectral signature of the geological feature can vary with position of the sun

Figure 4.2: A satellite imaging system used to illustrate the necessity of fast hyper spectral imaging.

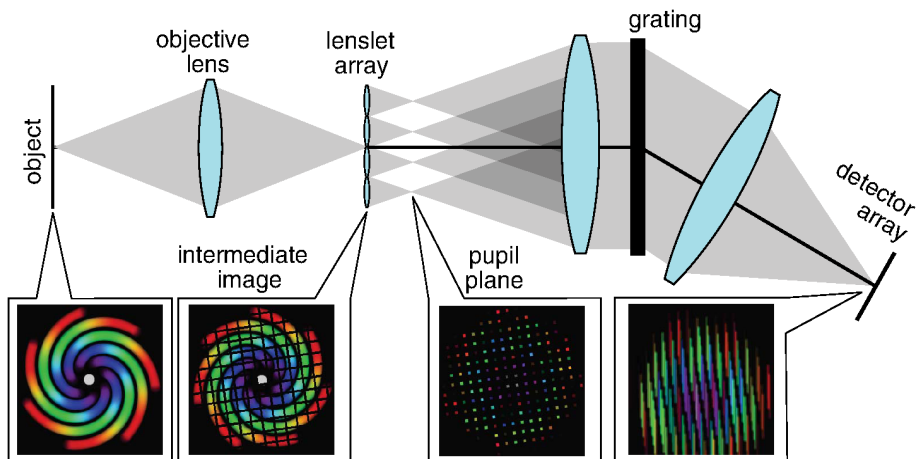
- Snapshot spectroscopy with facet mirrors - A set of closely spaced mirrors with slightly different angles such that an object whose image formed on this mirror is divided into several small regions. Each region is fed to a separate spectrograph units and a spectrum is obtained (Weitzel et al. [127]). Then the divided regions and their respective spectra are combined to form HSI of the object (Figure 4.3a).
- Snapshot spectroscopy with lenslets on the image plane - An image of a 2D field formed by the telescope or an imaging lens is sampled by a set of lenslets. The image sampled by the lenslet gets shrunk or demagnified and occupies a small region with a void surrounding it. Each of the demagnified images are collimated and spectrally dispersed using a grating. The dispersed spectra when re-imaged forms a spectral streak of the demagnified image thus giving wavelength information at multiple points on the 2D field as shown in Figure 4.3b (Courtes et al. [19]).
- Snapshot spectroscopy with fiber bundle - An optic fiber bundle is placed at the image plane of the telescope. The fibers are oriented in such a way that the 2D field sampled by the fibers are converted to 1D slit structure. A grating is used to obtain the spectra of the 1D slit. As we obtain the spectral information of every point on the 1D slit, we effectively have the spectra of the 2D image forming a HSI as shown in Figure 4.3b (Fletcher-Holmes and Harvey [31]).

Although the snapshot techniques described above are in the main stream stellar astronomy e.g. (Erskine et al. [28, 29] and Ge, Erskine, and Rushford [37]), solar observations are yet to implement these techniques in main stream observation. This is because of the difficulty that lies in the implementation part of the technique. For e.g. the fiber bundle are fragile and are sensitive to polarization in multi-mode. Unlike stellar astronomy where point objects are spread across the FOV, solar astronomy has a continuous field. The packing fraction of the fibers have to be high in order to faithfully sample the FOV. Thus special single mode fibers with high packing fraction are needed to perform fiber bundle based snapshot spectroscopy. For more details on an instrument built on this concept, the reader is referred to Lin [65], Lin and Versteegh [68], and Schad et al. [95].

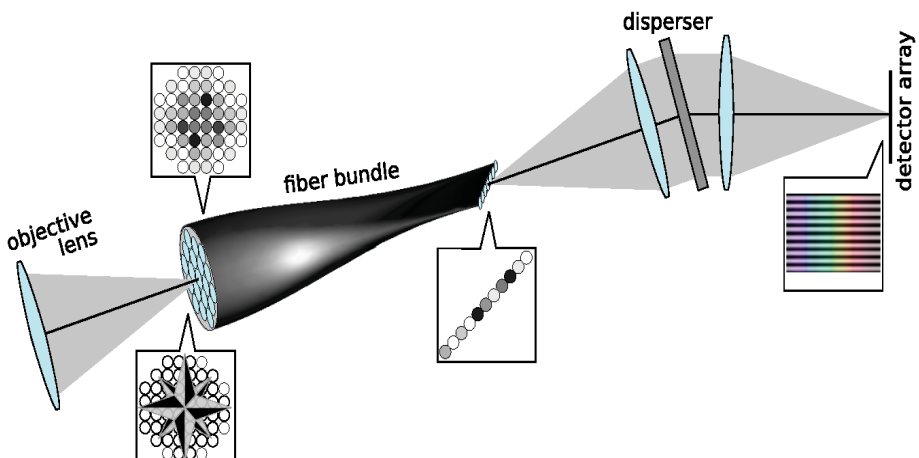
A device with snapshot capabilities would provide immense information about the dynamics of the Sun. Global oscillations (Duvall et al. [26]), prominence and filament eruptions (Arregui, Oliver, and Ballester [3], Ballegooijen and Martens [6], and Parenti [76]), small scale oscillation of fibrils and sunspot (Giovanelli [39], Pontieu et al. [80], and Sütterlin [116]) and other dynamic features of the Sun can be studied in great detail. It can be seen that all the snapshot instruments



(a) Facet mirror slicers divide the image and divert it into multiple spectrographs. (b) A zoomed image of the facet mirrors.



(b) Lenslet array samples the image plane and the void created due to demagnification is used for spectral dispersion



(c) A fiber bundle samples a 2D image plane and re-formats it into 1D slit which is dispersed using a spectrograph

Figure 4.3: Snapshot spectroscopic concepts used in stellar astronomy. Images are taken from [43]

mentioned above sample the image plane and uses a grating spectrograph to obtain multi spectral capabilities. A novel instrument technique is developed that is simple in design and easy to implement. This device (named lenslet array spectroscope [LAS](#)) achieves snapshot capabilities by sampling the pupil rather than the image plane and uses a Fabry-Pérot interferometer as a spectrograph. The following sections describe the detail of the instrumentation and are organized as follows -

- The concept of sampling the pupil plane and performing hyperspectral imaging using [FP](#),
- Optical design for instruments to perform pupil sampling,
- [LAS](#), a snapshot spectrograph development and laboratory testing,
- Demonstration of snapshot capabilities by recording Evershed flow in sunspot NOAA-12526 and oscillations in a prominence region.

4.2 WORKING PRINCIPLE

An [FP](#) (Perot and Fabry [79]) consists of two parallel plates with their inner surface made highly reflective. The etalon works on the principle of multiple reflection ([Figure 4.4](#)) where the maximum intensity of transmission occurs at wavelengths

$$m\lambda = 2\mu d \cos(\theta), \quad (4.1)$$

where

- μ is refractive index of medium between the parallel plates
- d is separation between the plates
- λ is wavelength at peak transmission
- θ is angle of incidence of a poly-chromatic beam
- m is wavelength order

It is well known that for a ray incident at a small angle θ the change in the peak transmitted wavelength for an etalon is given by

$$\Delta\lambda = \left(\frac{\lambda_0}{2} \right) \left(\frac{\theta}{\mu} \right)^2, \quad (4.2)$$

where λ_0 is the wavelength transmitted for normal incidence. So for a point source if the diverging beam of light is collimated and incident on an [FP](#), all rays are transmitted at the same wavelength that satisfies [Equation 4.1](#) and the resultant image formed on the screen has a single transmitted wavelength of the source for a given order. Conversely for a point source if converging rays are incident on the

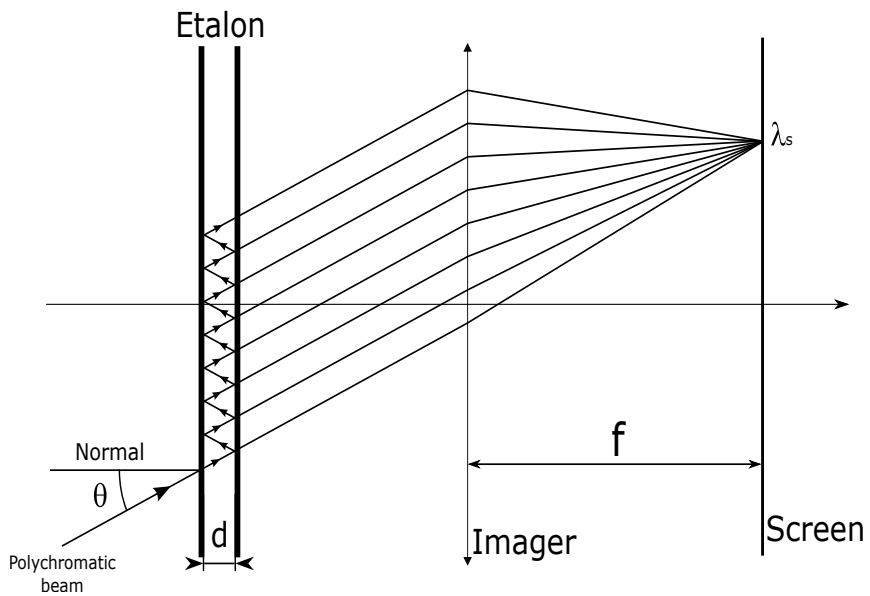


Figure 4.4: A parallel plate etalon transmitting multiple wavelength peaks λ_s which interfere constructively on a screen

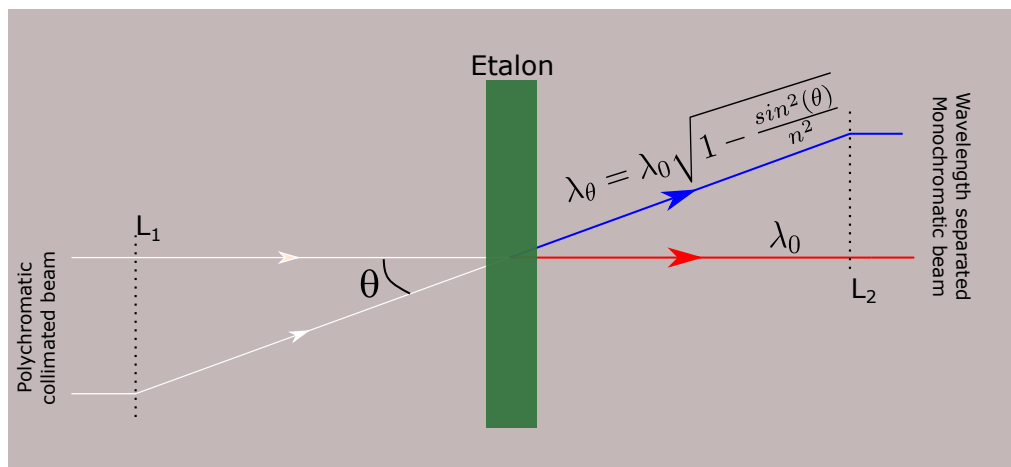


Figure 4.5: Blue shift in transmitted wavelength for a ray traveling at an angle with respect to the ray traveling normal to the etalon

FP, the resultant image of the point source on the screen consists of a set of wavelength points defined by [Equation 4.2](#).

Combining the effect of collimated and converging beam, one can produce a multi-wavelength image of a 2D field. In [Figure 4.5](#), an illustration of the combination of collimating and converging beam is shown. First a set of parallel rays coming from a point source after collimation strikes lens L₁ and forms a converging beam. After passing through the etalon this beam has a gradient of wavelength defined by the equation

$$\lambda_\theta = \lambda_0 \sqrt{1 - \frac{\sin^2(\theta)}{n^2}}.$$

Upon re-collimation using lens L₂ we obtain a parallel beam whose wavelength varies spatially. In the case of [Figure 4.5](#) the variation is from red to blue as we move from the bottom of the beam to the top end of the beam. For an infinitesimally small point, each ray uniquely defines the point. Thus by taking small pencil of rays in the collimated beam, one can define unique images of the point source at different wavelength. Selecting a pencil bundle of rays in the collimated beam is equivalent to sampling the pupil plane. From [Figure 4.5](#) it can be seen that collimated beam or parallel rays exist before lens L₁ and after lens L₂, thus pupil sampling can be done in either of the two regions.

This principle can be extended to multiple points or a 2D region where the entire 2D field is considered to be made up of multiple small points and the collimated beam from each of this point (or a group of points) are sampled and incident on the etalon at variable angles. The resultant image is a spatio-spectral plane of the 2D field where multiple images of every field point exists at a different wavelength thus forming a snapshot spectroscopic image of the field.

4.3 OPTICAL DESIGN

From [Figure 4.5](#), it can be seen that the pupil plane (or the region where a bundle of rays emitted from a point source are parallel to each other) exists at two locations, a region before lens L₁ and a region after lens L₂. The first region is considered to be object plane and the second region is considered to be image plane in our design. Two optical layouts are presented where one sampled the object plane and the second samples the image plane.

In [Section 4.1](#), it is shown that the image is sampled using a lenslet array or optic fiber bundle. The “sampled” image is spectrally dispersed, using a grating, to obtain a snapshot hyperspectral cube. Pupil sampling is similar to image sampling. Lenslets are used to sample the pupil instead of the image and a set of collimating and imaging lenses (L₁ and L₂ in [Figure 4.5](#)) along with a Fabry-Pérot is used to

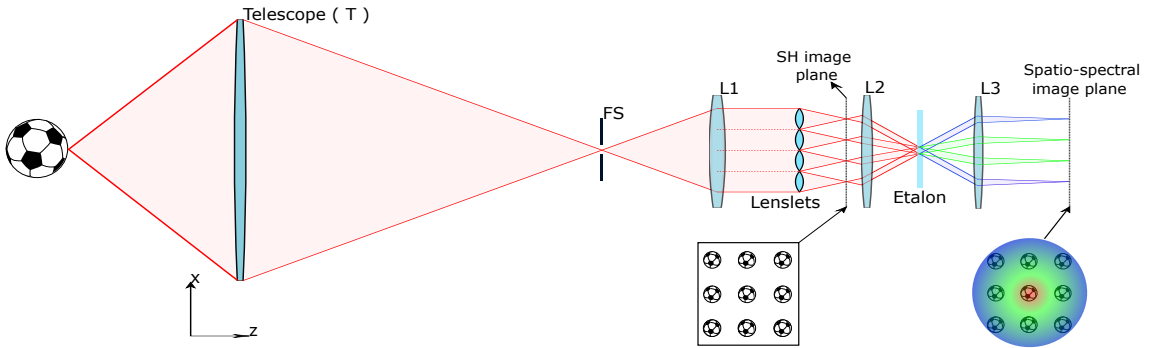


Figure 4.6: Optical design for object plane sample.

obtain a snapshot hyperspectral cube. The sampling element (lenslet) is merely used to divide the pupil plane into smaller sections and does not contribute to the spectral capabilities of the instrument. A modified Fresnel lens or a set of concentric mirrors or a lenslet array can be used for the purpose of sampling the pupil.

Optical design-1 : Sampling the object pupil

Figure 4.6 is an optical diagram that works on the principle of object plane sample. The design uses a lenslet array for the purpose of sampling. As shown in the figure, an object either at finite distance like a vegetation or water body in the case of remote-sensing or prominence and Evershed flow at near infinity as in the case of solar astronomy, can be imaged using a telescope. The telescope (T) forms an image of the field. This field is restricted to a particular size based on the ROI using a field stop. A collimating lens L₁ collimates the beam exiting the field stop. The collimated beam is now the “object plane”. The lenslet array samples this pupil plane and forms individual identical images of the ROI at the focal plane of the lenslet. The images formed at the focal plane are similar to the ones formed in Shack Hartmann wavefront sensor, hence this plane is called as SH image plane in **Figure 4.6**. The lenslet images are re-collimated using lens L₂. This lens is similar to the lens l₁ illustrated in **Figure 4.5** and the sampled pupil is made to pass through the etalon at angles which are determined by the focal length of lens L₂. If d is the distance of an object from the optic axis of the system in the SH image plane then

$$\theta = \tan^{-1} \left(\frac{d}{f} \right), \quad (4.3)$$

where f is the focal length of lens L_2 . Using [Equation 4.3](#) in [Equation 4.2](#), we obtain the shift in wavelength or the wavelength sample for the field. As d increases the peak transmitted wavelength decreases. The lens L_3 , which is analogous to l_2 in [Figure 4.5](#), images the wavelength sampled pupil onto the spatio-spectral plane. The spatio-spectral plane is the image plane where the wavelength decreases according to the relation in [Equation 4.2](#). As the wavelength depends on angle, symmetry exist along the radial direction i.e. all points at the same radial distance from the optic axis is at the same wavelength. Multiple images formed at the SH image plane are distributed in this plane thus a field point in the [ROI](#) gets sampled at multiple wavelength points. This is true for every point on the [ROI](#) thus a hyper spectral cube of the 2D field is obtained in a single snapshot.

Optical design-2 : Sampling the image pupil

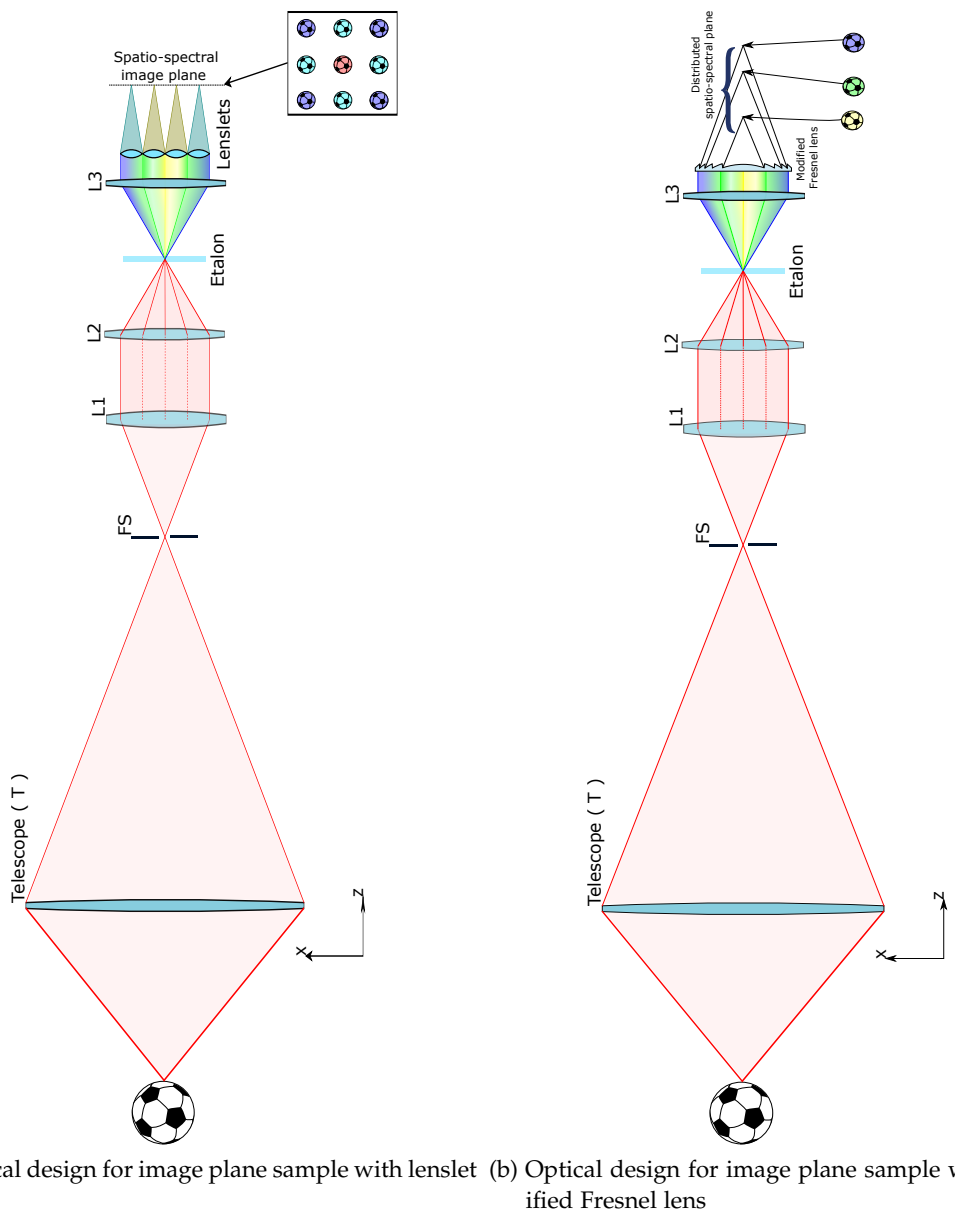
[Figure 4.7](#) is an optical diagram that works on the principle of image plane sample. The variation in wavelength continues to follow the relation given in [Equation 4.3](#) but unlike the object plane the image plane sampling is simpler in design and can have two types of sampling mechanisms they are -

- Sampling a section or a region
- Sampling an annular ring

The optical diagram in [Figure 4.7a](#) is an example of region or a section of the pupil plane being sampled. The lenses L_2 and L_3 are equivalent to l_1 and l_2 given in [Figure 4.5](#). A pupil plane with varying wavelength is formed after L_3 . A section sampled in this plane produces an image whose wavelength is equal to an average of that section. Although each image formed has a uniform wavelength across the [ROI](#), the bandwidth or the [FWHM](#) of the transmission band is broadened. The sampling element used in this system is a lenslet array. The size of each lenslet determines the wavelength averaging in the resultant image. As multiple images of different wavelength sample are formed on the detector plane, a hyper spectral cube of the [ROI](#) are obtained in a single snapshot.

Sampling the pupil after the FP results in averaging the wavelength as the pupil consists of concentric wavelength bands whose width depends on the spectral resolution of the FP

The optical diagram in [Figure 4.7b](#) is an example of the pupil plane being sampled as an annular ring. The advantage of sampling an annular ring instead of a region is that all the points in the pupil that correspond to a particular wavelength are imaged into a single [ROI](#). The thinner is the annulus the better is spectral purity of the image. The minimum size of the annular ring can be determined using the transmission bandwidth of the [FP](#). But a major drawback of this system is the use of a custom made sampling element (or a modified Fresnel's lens in this case). If the wavelength samples varies due to a change in the magnification between L_2 and L_3 , a new Fresnel's lens



(a) Optical design for image plane sample with lenslet (b) Optical design for image plane sample with modified Fresnel lens

Figure 4.7: Optical design for image plane sample

has to be used that meets the [FP](#)'s criteria of spectral broadening and pupil size due to magnification of the lens system. Also, the 2D images formed at different locations on the optic axis (corresponding to different wavelength) has to be diverted into the detector plane using facet mirrors. But this design provides the highest spectral purity and simplest post processing images of the [ROI](#) among all the optical designs presented.

When the three designs are compared for their simplicity and performance, it can be seen that -

- [Figure 4.6](#) is simple in design and nominal in spectral resolution. But the spread of spatial images on a spectral plane i.e. the spatio-spectral plane in this design requires the highest amount of post-processing to extract the hyper spectral cube of the 2D field.
- [Figure 4.7a](#) is the simplest in terms of design and produces images that do not require intense post processing but the spectral resolution of each image is the poorest among the three designs.
- [Figure 4.7b](#) is the design that produces the highest spectral resolution and the brightest image for a given wavelength among all the three designs but requires custom designed optical component.

4.4 LENSLET ARRAY SPECTROSCOPE (LAS)

From the three designs described in [Section 4.3](#), the optical diagram shown in [Figure 4.6](#) is simple in design and provides nominal spectral sampling without the use of customized optical elements hence that design is chosen for the development of the instrument and the instrument is called lenslet array spectroscope. In this section, experiments conducted to verify the optical diagram and working principle of [LAS](#) are presented.

In [Figure 4.6](#), the specifications of the instruments used are termed as follows -

f_p	Focal length of the telescope
S	Aperture of the telescope
FS	Size of the field stop
f_1	Focal length of lens L_1
f_{ll}	Focal length of the lenslet
p	Pitch or distance between two lenslets
f_2	Focal length of lens L_2
μ	Refractive index of the space between FP plates
f_3	Focal length of lens L_3

For the instrument to obtain a hyperspectral cube in the range λ_a to λ_b where $\lambda_a < \lambda_b$ we have,

$$\lambda_0 = \lambda_b.$$

Using [Equation 4.2](#) and [Equation 4.3](#)

$$\lambda_a \geq \lambda_n = \lambda_b - \left[\left(\frac{\lambda_b}{2} \right) \times \left(\frac{\arctan(r_n/f_2)}{\mu} \right)^2 \right],$$

where λ_n is the wavelength for any image at a distance of r_n in the SH image plane. A given wavelength range is achieved with several combination of object plane size r_n and f_2 but the magnification between lens L_2 and L_3 sets an upper limit to r_n beyond which two adjacent ROI overlap over each other. From geometry the maximum size of object plane is

$$r_n = \frac{f_{ll} \times FS \times S}{f_p \times p}.$$

If the wavelength at any point in the spatio-spectral plane is

$$\lambda_i = \lambda_0 - \Delta\lambda \quad (4.4)$$

then the linear spectral dispersion on the spatio-spectral plane is obtained by using [Equation 4.2](#) in [Equation 4.4](#) and differentiating with wavelength to get

$$\frac{dl}{d\lambda} = \frac{-\mu}{\lambda_0 \theta} \times f_3.$$

The optical layout drawn in [Figure 4.6](#) assumes that the presence of lenslets will not affect the relation between wavelength and angle of incidence. It also assumes that the collimating and imaging lenses determine the wavelength range and linear spectral dispersion of the system. Thus the working of [LAS](#) depends on two factors. The validity of [Equation 4.2](#) for the optical layout chosen and the principle of operation explained in [Section 4.3](#) using [Figure 4.5](#). Two experiments are conducted to validate the above two factors. It must be noted that a Fabry-Pérot interferometer is used instead of a fixed etalon for our experiment. In [Section 4.6](#), a description is provided to replace [FP](#) with a fixed etalon for future operations of [LAS](#).

4.4.1 Experiment to validate relation between wavelength and angle of incidence

In this experiment, a He-Ne laser source at 632.8 nm is used as the object. A collimated beam is incident on the lenslet array. The lenslets sample the pupil and lens L_2 collimates the beam which is incident at

Element	Value
SH lenslets pitch	1 mm
SH lenslets focal length	45 mm
L_2 focal length	18 cm
Fabry-Pérot type	Air spaced
L_3 focal length	50 cm

Table 4.1: Configuration of LAS for monochromatic source

different angles on the FP. From [Equation 4.1](#), it can be seen that for a fixed wavelength λ if there is a change in the distance “d” between the plates of the FP then the peak transmitted wavelength occurs at

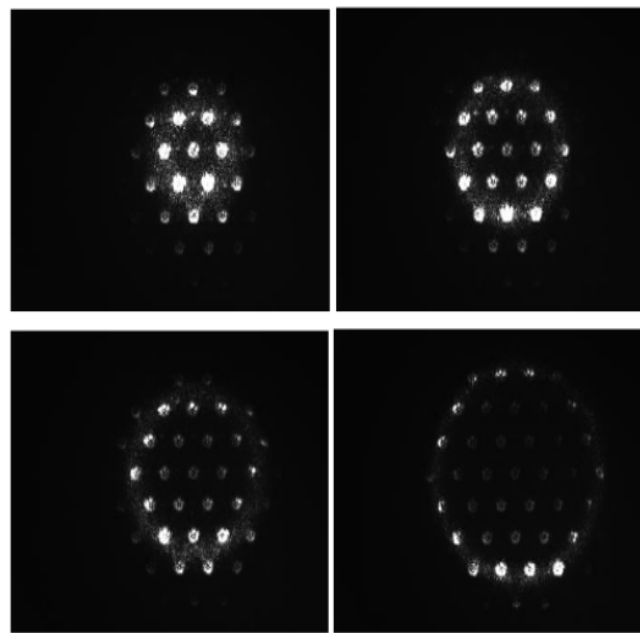
$$\theta = \cos^{-1} \left(\frac{m\lambda}{d} \right).$$

So a change in the wavelength with angle of incidence is analogous to change in the distance between the plates for a monochromatic source. The specifications of the lens system used in the experiment is given in [Table 4.1](#).

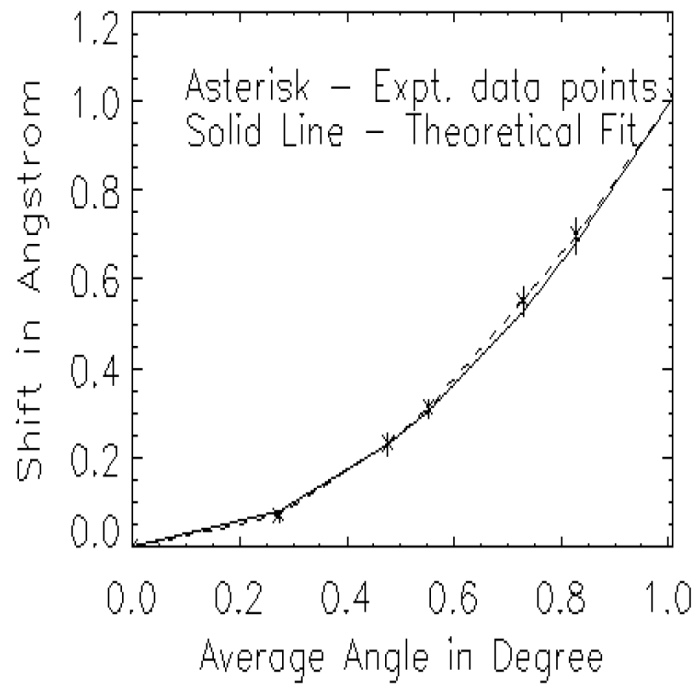
Lens L_3 images the lenslet on a detector plane and the peak intensity of the laser beam is plotted against its angular distance from the optic axis in [Figure 4.8b](#). It can be seen that the experimental values match the theoretical prediction with less than 10 mÅ deviation. Thus the position, shape and presence of the lenslets does not affect the relation between wavelength and angle of incidence (Gosain, Sankarasubramanian, and Venkatakrishnan [40] and Sankarasubramanian et al. [94]).

4.4.2 Pupil plane variation in wavelength

The second assumption was that variation in wavelength is determined by lens L_2 and not the lenslet array. In order to verify this assumption the entire LAS instrument was setup without the lenslets on an 8 inch Cassegrain telescope at USO. The setup involved sampling the 6301.5 Å iron line and the 6301.99 Å telluric line simultaneously on the pupil’s image. In [Figure 4.6](#), if the lenslet array is removed then the pupil gets imaged onto the detector. This assumption is true as the focal length of the lenslets are small (0.45 cm) and causes a very small defocus when compared to a large focal length of lens L_2 (20 cm). [Table 4.2](#) gives the parameters of the telescope and lens L_1 , L_2 , L_3 used in the optical setup for this experiment.

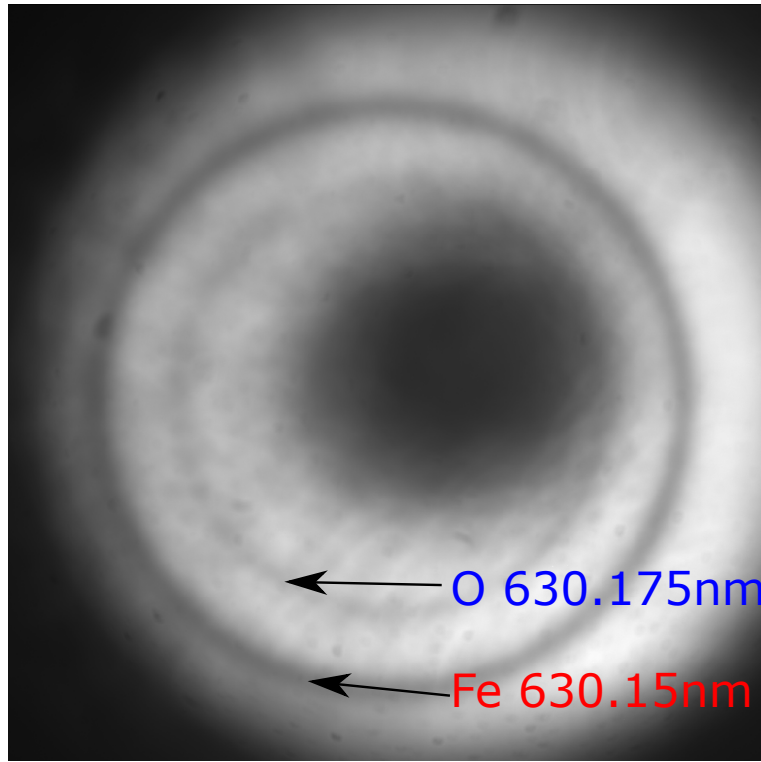


(a) Peak intensity of the laser beam moves outward with increase in spacing between FP plates. The image sequence is top left, top right, bottom left, bottom right.

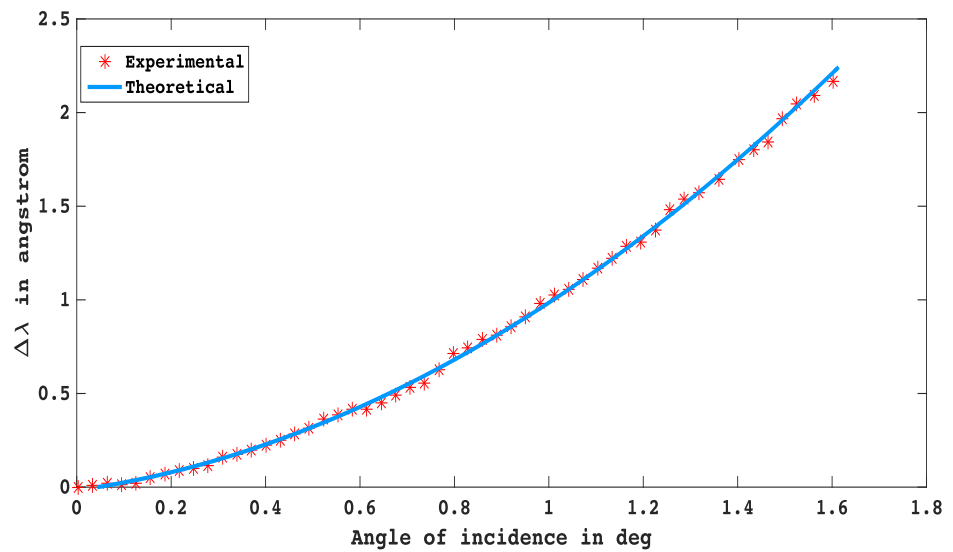


(b) A plot of position of peak transmitted intensity with angular distance from optic center.

Figure 4.8: The experimental validation of variation in wavelength with angle of incidence for LAS



(a) Pupil image of the Cassegrain telescope obtained using LAS with a 4 \AA prefilter. The variation in wavelength across the pupil can be clearly seen with two concentric annular rings of absorption line corresponding to Fe-I and telluric line. The central dark portion is the obscuration in the primary mirror of the telescope



(b) A plot of the position of the line core of telluric line as a function of distance from the optic axis.

Figure 4.9: Experimental results to validate the variation in wavelength along the pupil for LAS

Element	Value
Telescope aperture	20.32 cm
L_1 focal length	10 cm
L_2 focal length	20 cm
Fabry-Pérot type	Air spaced
L_3 focal length	20 cm

Table 4.2: Configuration for field test on Cassegrain telescope

[Figure 4.9a](#) is the image of the pupil at the detector plane. It can be seen that the iron and telluric lines are visible and form concentric circles on the pupil image. Thus the working principle described in [Section 4.3](#) is satisfied where variation in wavelength is determined by lens L_2 . The line core of oxygen telluric line can be considered to be a monochromatic point with low intensity. Thus the experiment conducted with the laser source is repeated (increasing the spacing between the plates of the FP) and the position of the telluric line is plotted as a function of angle of incidence. It is found that the shift in the line satisfies the theoretical prediction ([Figure 4.9b](#)).

Thus from the results obtained using the monochromatic source, it is found that the optical design performs as expected in the presence of a pupil sampler. Also the experiments conducted using a Cassegrain telescope on the absorption line pair reveals that the design complies with the assumption that lens L_2 causes the change in wavelength (on the pupil's image) irrespective of the presence of a pupil sampler (lenslet array in this case).

4.5 DATA ACQUISITION AND ANALYSIS

The laboratory tests conducted on [LAS](#) provided results which matched with the working principles of the instrument. In order to test the working of [LAS](#) as a snapshot spectroscopic instrument, the device was set up on the [MAST](#). [MAST](#) is a 50 cm off-axis telescope at [USO](#) (Denis et al. [24] and Mathew et al. [71]). Unlike the 20.32 cm Cassegrain telescope used for the laboratory test of the instrument, [MAST](#)'s primary mirror is an off axis parabola and does not have a central obscuration. Hence it provides a uniform illumination across the pupil image.

It was shown in [Chapter 3](#) that the spectral information obtained at multiple wavelength bands provide information of the physical parameters at various heights in the solar atmosphere. The core element in [LAS](#) is an etalon. In a parallel plate element, the reflected orders are complimentary to the transmitted orders. So this reflected light can be utilized to obtain hyperspectral cube of the field at different wave-

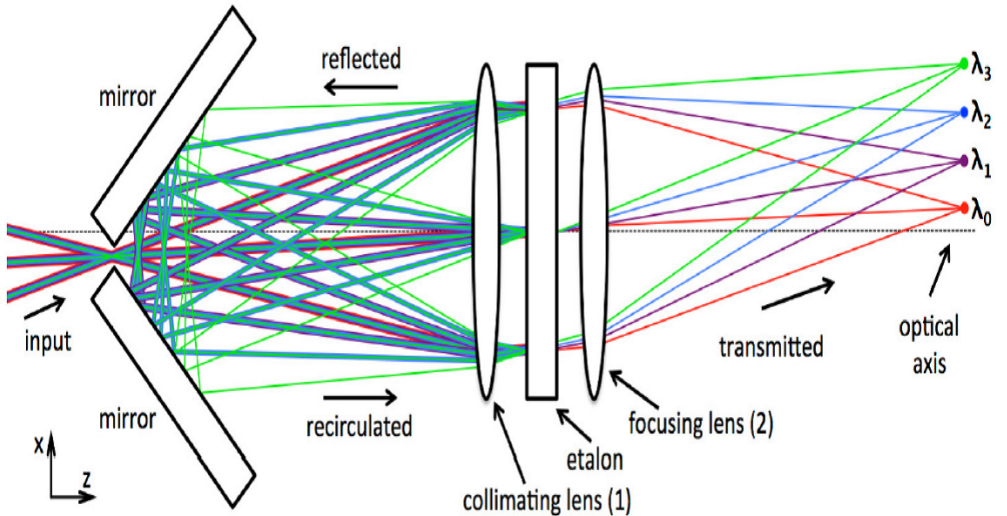


Figure 4.10: Conceptual diagram of etalon light re-circulation technique where reflected light is circulated back to the etalon at a different angle. The conceptual diagram presented here is borrowed from [113].

length bands by transmitting the light back to the etalon at different angles. This process is known as etalon re-circulation (Jennings and Boyle [46] and Stephen, Krainak, and Fahey [113]) where a mirror is used to divert the reflected light back into the etalon at some angle. Using the re-circulation technique **LAS** can obtain snapshot hyperspectral image at multiple wavelength bands.

In order to test the snapshot capabilities of **LAS** along with multi wavelength band imaging, the Evershed flow in sunspot penumbra at 6301.5 Å and solar prominence at H- α 6562.8 Å were recorded. The data acquisition and data analysis procedure are as follows -

Data acquisition

Note:- The sunspot was recorded on Mar 31st 2016 and the prominence was recorded on 23rd May 2017

A GUI is designed in LabView™ for data acquisition (Figure 4.11). The GUI allows for a quick configuration of the **FP** and camera system to acquire data and store in the standard FITS format (Wells, Greisen, and Harten [128]). The GUI can be upgraded to accommodate a polarimeter unit for the future run of the instrument. The standard procedure for acquiring data using a CCD detector is to record the science data of the **ROI** followed by flat and dark frames.

As any single image has both spectral and spatial information, science image for this instrument is a single snapshot of the field. But to study the dynamics of the field one can record several frames in a sequence which provides the time evolving features of the field.

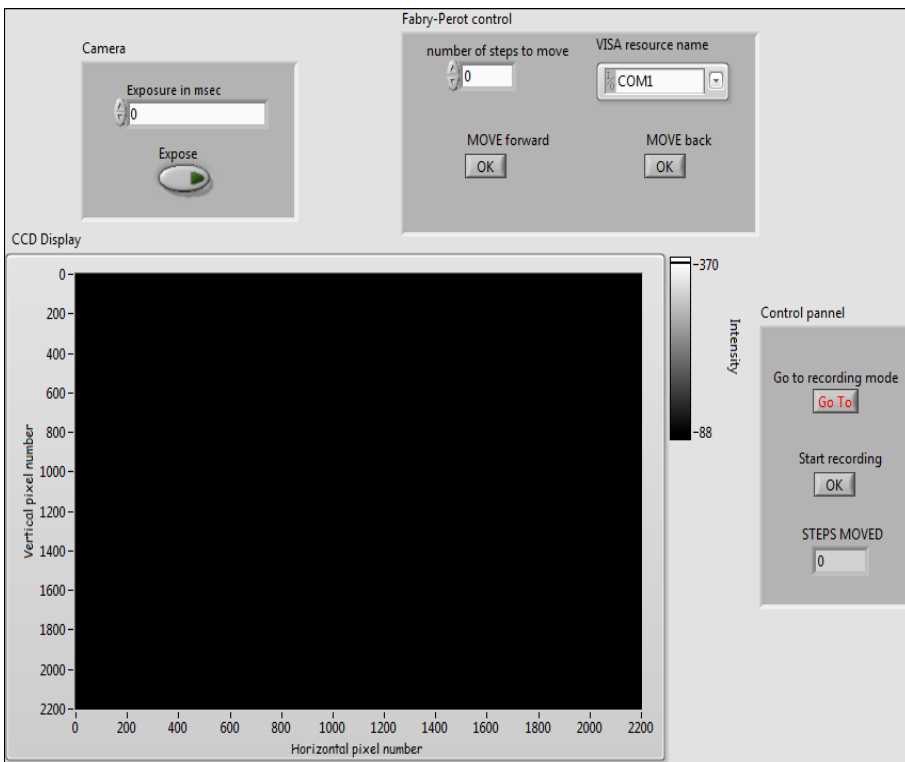


Figure 4.11: GUI to operate [LAS](#) at [USO](#). The GUI can control the camera and the [FP](#) interferometer. It can be upgraded to include a polarimeter unit

Flat field on the other hand requires a wavelength scan. This can be explained as follows-

Consider the pupil plane in [Figure 4.9a](#) for a snapshot of the pupil where each pixel on the detector is exposed to a different wavelength. In order to obtain the hyperspectral cube of a field, different pixels that correspond to the same field but at different wavelengths in the spatio-spectral plane have to be combined. As flat fielding is performed to correct the difference in gain between pixels, each pixel should be exposed to the same wavelength of light. In order to expose different pixels to the same wavelength, the spacing between [FP](#) plates are changed and a frame is recorded for each spacing. During post processing the whole frame is masked away except for those regions whose pixels are in the continuum and this process is repeated for every frame. The combination of all such frames lead to a final frame where every pixel is exposed to the same wavelength. This frame is called the master flat and is used for gain correction among different pixels in the recorded data.

Two independent data sets were taken to determine the snapshot capabilities of [LAS](#). The data sets were also intended to test the multi spectral band imaging through etalon re-circulation. The specification of the focal length of the lens used to obtain the data are given in [Table 4.3](#).

Element	Value
Telescope aperture	50 cm
Field stop	0.5 cm
L_1 focal length	50 cm
SH lenslets pitch	0.1 cm
SH lenslets focal length	4.5 cm
L_2 focal length	20 cm
Fabry-Pérot type	Air spaced
L_3 focal length	30 cm

Table 4.3: Configuration of [LAS](#) for data observation

Data analysis

Two different regions were recorded using [LAS](#). They were sunspot NOAA 12526 at 6302 Å absorption line and a prominence at 6562.8 Å emission line. This data intends to demonstrate the following capabilities of [LAS](#) -

- Snapshot and multi spectral band capabilities of [LAS](#),
- Ability to correct for low order atmospheric seeing. Hence can be used in telescopes even if [AO](#) system is not available,
- Can observe both emission and absorption line features.

A typical image obtained from the instrument is shown in [Figure 4.14a](#). Each lenslet image consist of the same [ROI](#) or spatial region spread in the spectral plane forming a spatio-spectral image. In order to obtain a hyperspectral cube from the spatio-spectral plane, it is necessary to determine the wavelength at each pixel and also recognize spatially equivalent point in each lenslet.

1. Determining the wavelength at each pixel :- The wavelength at every point is known using [Equation 4.2](#) and [4.3](#) provided the position of the starting wavelength λ_0 is known. In order to determine the position of λ_0 , a set of wavelength tuned flat images are considered. [Figure 4.12](#) illustrates the procedure to determine the position of λ_0 . The absorption lines form concentric circles as seen in [Figure 4.9a](#). Now the position of these lines are traced by choosing a column and row of pixels and stacking them for each scan position. The stacked image of row

pixels forms an image which traces an arcs of the absorption line. This arc is a segment of a circle whose y-coordinate of the center lies at the y-coordinate of starting wavelength λ_0 . A circle is fit to this arc using the method described by (Pratt [81]) or (Tauber [118]). Repeating the process for the column image gives x-coordinate of λ_0 . Thus the position of λ_0 and hence the wavelength at every point on the spatio-spectral plane is known. A master flat can be generated using the position [x_0 , y_0] of the λ_0 . Figure 4.13a and 4.13b illustrates the procedure of generating a master flat. In Figure 4.13a, R_1 is the position of 6301.5 Å absorption line. Region inside the circle is red continuum while region outside is the blue continuum. As the spacing of the FP increases the red continuum occupies a greater region as shown in Figure 4.13b. Thus by selecting the appropriate wavelength region from each flat frame, a master flat whose image is made up of pixels from the same wavelength is obtained.

2. Determining spatially equivalent points :- As every lenslet samples the same ROI, recognizing the center of each lenslet gives a handle on the position of every other point in that lenslet. Thus selecting a region in one lenslet can determine the location of a spatially equivalent point in all other lenslets across the spatio-spectral plane. As the lenslet boundary has a high contrast with respect to its surroundings, Hough transform (Atherton and Kerbyson [4] and Yuen et al. [134]) is applied on the image and the boundary or the location of the center of each lenslet is determined. Figure 4.13 shows the selection of each lenslet performed using Hough transform.

The next step is to determine the position of a solar feature within each lenslet. LAS is operated without the aid of AO system. The optical layout from L₁ upto the SH image plane in Figure 4.6 is similar to a Shack Hartmann wavefront sensor used in adaptive optics (Beckers [9] and Rimmeli [86]). For a distorted wavefront sampled by the lenslets, the images formed on the SH image plane is displaced and this displacement is arbitrary in each lenslet. So a spatio-spectral image of the ROI consists of randomly displaced field points with respect to each lenslet. In order to determine the displacement of the field in each lenslet and hence the spatially equivalent point in each lenslet, two techniques are adopted. One technique is for absorption line feature and the other is for emission line feature. Each technique is described by taking their respective observation as example -

Sunspot NOAA 12526 - absorption line feature

The sunspot is recorded on 31st Mar 2016 using a 3 Å pass band filter centered at 6302 Å. From the configuration given in Table 4.3,

the wavelength sample is $500 \text{ m}\text{\AA}$ for a 6×6 lenslet array. The field recorded using [LAS](#) is shown in [Figure 4.14a](#). The displacement of the sunspot within each lenslet is determined using normalized auto-correlation (Jianwen Luo and Konofagou [48]) with the sunspot in the center of the 6×6 lenslet array taken as a template. The peak correlation shown as bright points in [Figure 4.14b](#) is the position of the sunspot in that lenslet. The displacement of this peak with respect to the center of the lenslet determines the shift in the spot in that lenslet. Knowing this displacement, one can find the spatially equivalent point of a field in all the lenslets. As the wavelength of each pixel in the spatio-spectral plane is known, a spectral distribution of each spatial point in the [ROI](#) can be obtained. [Figure 4.15](#) is a plot of wavelength information of one such point in the [ROI](#). The intensity distributed with wavelength is fit with a gaussian. A shift of the core of the absorption line gives the information of line of sight velocity of that field point. [Figure 4.16a](#) shows the continuum intensity of the 1 arcmin [ROI](#) and [Figure 4.16c](#) is an image of the line of sight velocity at every field point. It can be seen that the penumbral region clearly shows Evershed flow (Evershed [30]) with the plasma having velocity of $1.2\text{-}1.4 \text{ km/sec}$. This velocity map was generated using a single CCD frame which was exposed for 300 msec . Also, the image was corrected to 1^{st} order for atmospheric seeing using normalized auto-correlation. Thus one can perform snapshot spectroscopy under seeing limited condition without the use of [AO](#) system. The results obtained from [LAS](#) are compared with the intensity and Dopplerogram images of [HMI](#) as shown in [Figure 4.16b](#) and [Figure 4.16d](#) respectively. The images obtained from [HMI](#) are downgraded to the resolution limit of [LAS](#) at [MAST](#) which is about 2 arcsec . Seeing reduces the resolution further and it was found that the resolution reduced to 4 arcsec at the time of acquiring this data.

Prominence - emission line feature

A prominence at solar $L = 127^{\circ}51'18.2''$ and $B = 25^{\circ}41'16.44''$ is recorded using a 1.5 \AA band pass prefilter centered at 6562.8 \AA . All configurations in this setup remains the same as given in [Table 4.3](#) except that the [FP](#) is tilted at an angle of 1.9° with respect to the optical axis. Tilting the [FP](#) is equivalent to making the beam incident at an angle to the [FP](#). As etalon re-circulation depends on the concept of varying the angle of incidence of the back reflected beam on to the [FP](#), tilting the [FP](#) implies that the device is tested for re-circulation capabilities. The prominence image recorded using [LAS](#) is shown in [Figure 4.17a](#). By tilting the [FP](#), the position of starting wavelength is moved out of the lenslet array field. [Figure 4.17b](#) shows an arc running over a set of wavelength equivalent points drawn with its center on $[x_0, y_0]$. A set of 950 frames with a time cadence of 1 sec is recorded to determine the evolution of prominence region. Unlike the

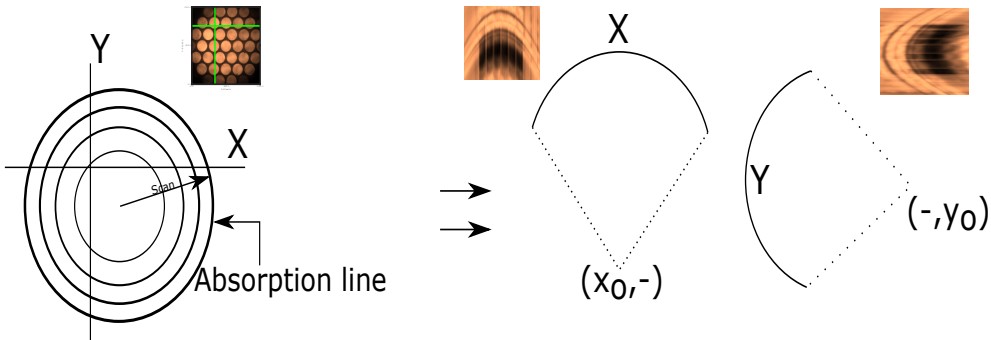
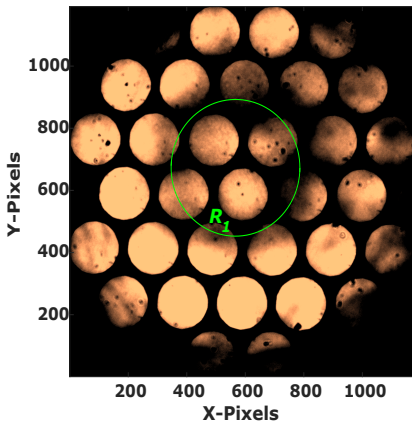


Figure 4.12: Illustration to determine the location of the starting wavelength λ_0

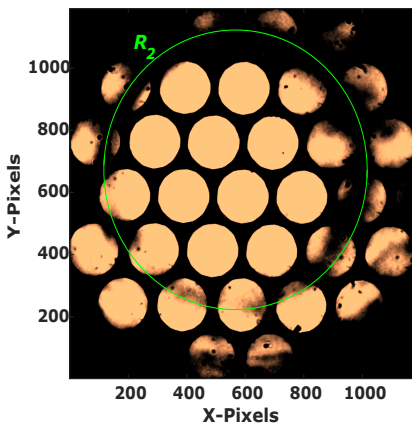
absorption line, the relative position of the prominence in each lenslet cannot be determined using normalized auto-correlation. Instead we assume that the atmospheric seeing causes shift in the region about a mean point. As seeing is a random process the mean position is nothing but the expectation of the random distribution i.e. $\langle E(x) \rangle$ and $\langle E(y) \rangle$ along two orthogonal axis x and y respectively. Once the mean position of a feature is obtained within a lenslet, the shift of the feature with respect to the mean value in every individual frame of the time sequence data can be determined and corrected. Upon correction, the hyper spectral cube can be obtained in the same manner as described for the case of absorption line. Figure 4.18a shows prominence region in line core obtained by combining the wavelength information from all the lenslets at a particular snapshot. The velocity of the field is obtained in all the 950 frames and it is found that waves propagate through the plasma in the prominence (Arregui, Oliver, and Ballester [3], Ballegooijen and Martens [6], and Parenti [76]). A phase plot which represents the difference in velocity or propagation of wave in the field of view is shown in Figure 4.18c. Two points P_1 and P_2 that are at opposite phase location is chosen and the velocity at that point is plotted for all 950 frames or 16 min of data in Figure 4.18d. The propagation of wave in plasma manifests as change in line of sight plasma velocity. Thus LAS has successfully demonstrated its snapshot capabilities with the ability to work in multiple wavelength band through etalon re-circulation.

4.6 DESIGN ENHANCEMENTS AND FUTURE WORK

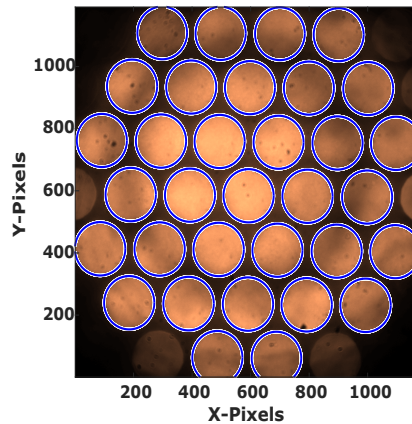
It is seen that the LAS although by design uses a fixed etalon and does not use a Fabry-Pérot interferometer, performs data acquisition with an interferometer. The main reason for this is to determine the coordinates $[x_0, y_0]$ of the stating wavelength λ_0 and to obtain a master flat. As both needed a wavelength scan, an interferometer which can change the spacing between the plates is being used. Etalons are



(a) A particular region R_1 whose pixels are at same wavelength

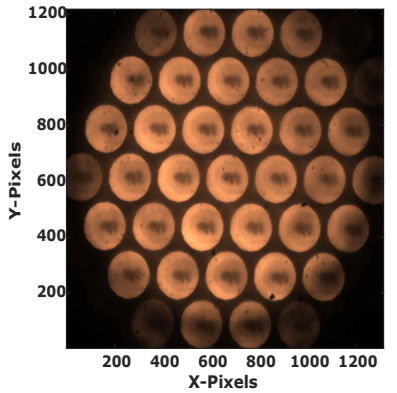


(b) The region for the same wavelength defined in (a) expands outward as the spacing between the FP plates are increased

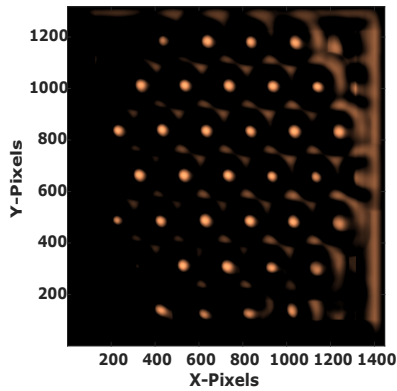


(c) Master flat is generated by combining small regions as shown in (a) and (b). Then Hough transform is used to determine the boundary of each lenslet.

Figure 4.13: Generation of master flat and determining the position of the lenslets using hough transform



(a) Sunspot NOAA 12526 recorded on 31st Mar 2016 using a 3 Å prefilter. The field stop samples a ROI of 1 arcmin



(b) Normalized auto-correlation peaks obtained using a lenslet template from (a). The peaks represent the position of a sunspot in the lenslet and relative shift between the peaks are used to correct for the displacement in the image due to seeing

Figure 4.14: Absorption line feature sunspot NOAA12526 recorded using LAS

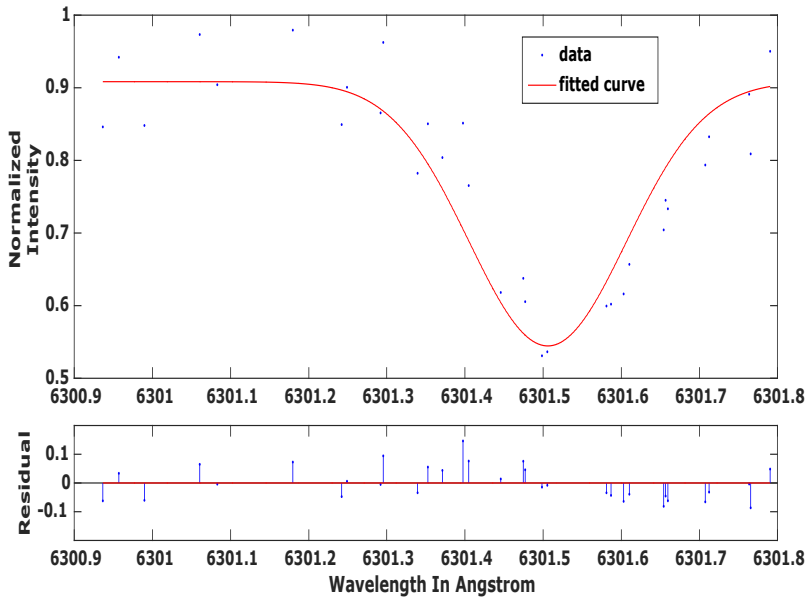


Figure 4.15: A plot of absorption line Fe-I at 6301.5 \AA obtained from a single snapshot image. The residuals of the fit are shown below.

easier to handle and they only require a temperature controlled oven to maintain the position of the peak transmitted wavelength. The design strategy described below can be used to replace the Fabry-Pérot interferometer with a fixed etalon -

- Flat field using etalon :- Tilting the Etalon causes a shift in transmitted wavelength (Frenkel and Lin [33]). So the etalon can perform a wavelength scan by tilting on two axis. If the detector is divided into four quadrants as shown in Figure 4.19a, then the etalon can tilt in x and z-axis of Figure 4.6. Tilt shifts one quadrant to blue wavelength while the diagonally opposite quadrant to redder wavelength. Thus by tilting in four directions wavelength scan can be achieved and a master flat can be generated
- Wavelength centering :- The location of $[x_0, y_0]$ in the spatio-spectral plane is nothing but the focal point of all the rays that are incident normally on the etalon's surface. If a light source emits wavefront which are parallel to the surface of the etalon then the wavefront gets imaged at $[x_0, y_0]$. An illustration of the same is shown in Figure 4.19b. Thus by using a calibration lamp in tandem with the etalon, position of λ_0 and all other wavelength points in the spatio-spectral plane can be determined

Thus by using a tilt mechanism and a calibration lamp one can replace the FP interferometer with a fixed etalon system.

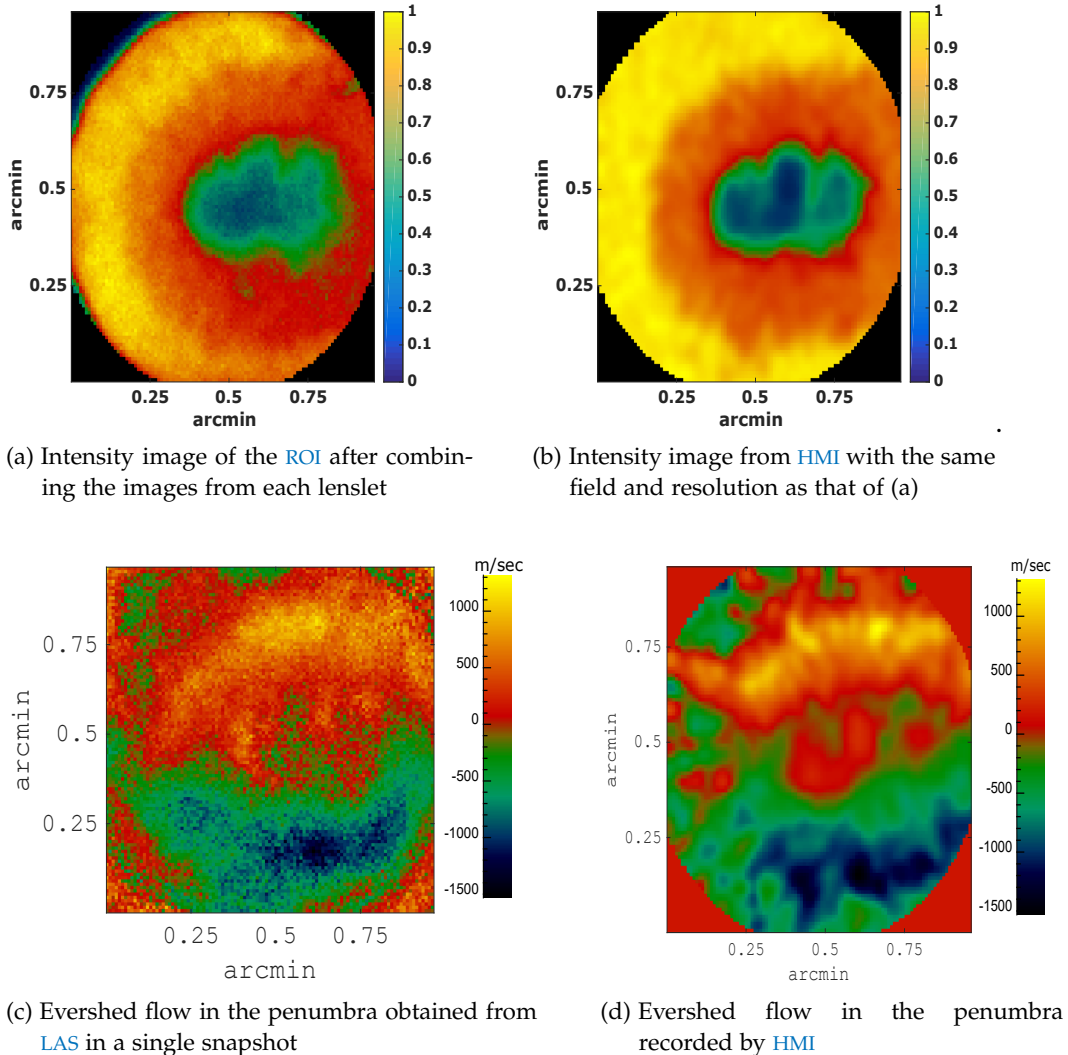
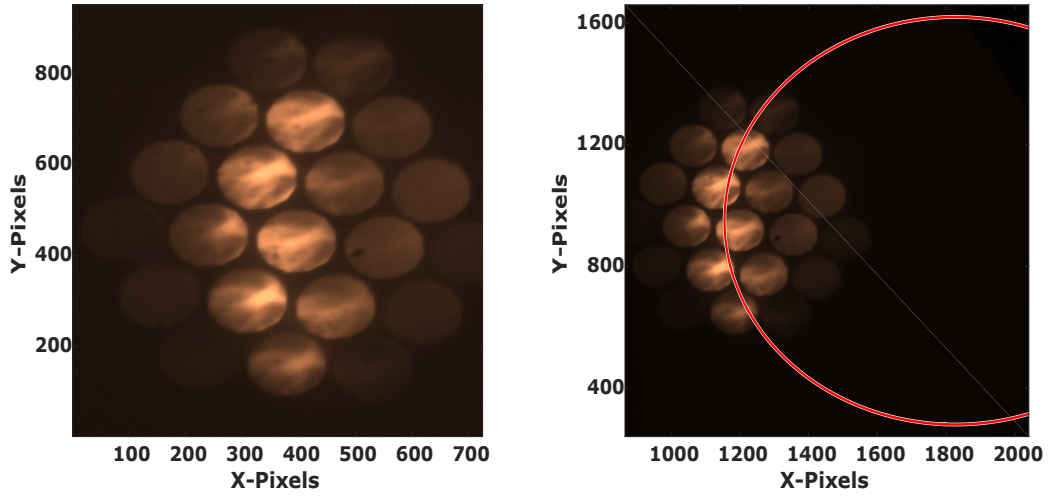


Figure 4.16: Comparison of continuum intensity and velocity obtained by LAS with that of HMI



(a) Prominence recorded in the H- α emission line (b) Uniform wavelength points with the central wavelength λ_0 lying outside the lenslet array field

Figure 4.17: Emission line feature at 6562.8 Å recorded by tilting the etalon by 1.9^0 . With all other configurations remaining the same as sunspot observation, light re-circulation mechanism is demonstrated in this figure.

Future work

[LAS](#) is a very versatile device. Although designed for solar astronomy the instrument can be utilized in other fields like remote-sensing or medicine (Korb, Gentry, and Li [56] and Shahidi et al. [103]). An important enhancement of [LAS](#) is the ability of the device to perform snapshot spectropolarimetry. Each pixel on the detector plane consists of a spatial field which corresponds to a spectral region. But the variation in spatial points is determined by the telescope resolution and the spectral resolution is determined by the resolving power of the etalon. If several detector pixels are placed within a spatially unresolved element of the telescope then they essentially contain the same spatial information. Similarly, if several detector pixels are placed within a spectrally unresolved element they contain the same wavelength information. For a spatio-spectral plane the resolving limit is the intersection of spatial and spectral resolution on the detector plane. So if several detector pixels are placed within the spatio-spectrally unresolved element then they contain the same information and are redundant in terms of hyperspectral imaging. But if each of the spatio-spectral point is modulated using a modulator analyzer unit then the resultant image plane is a spatio-spectropolarimetric plane. Spatial light modulators (SLM) have been used in several applications like projector system and LCD monitors where retarder at

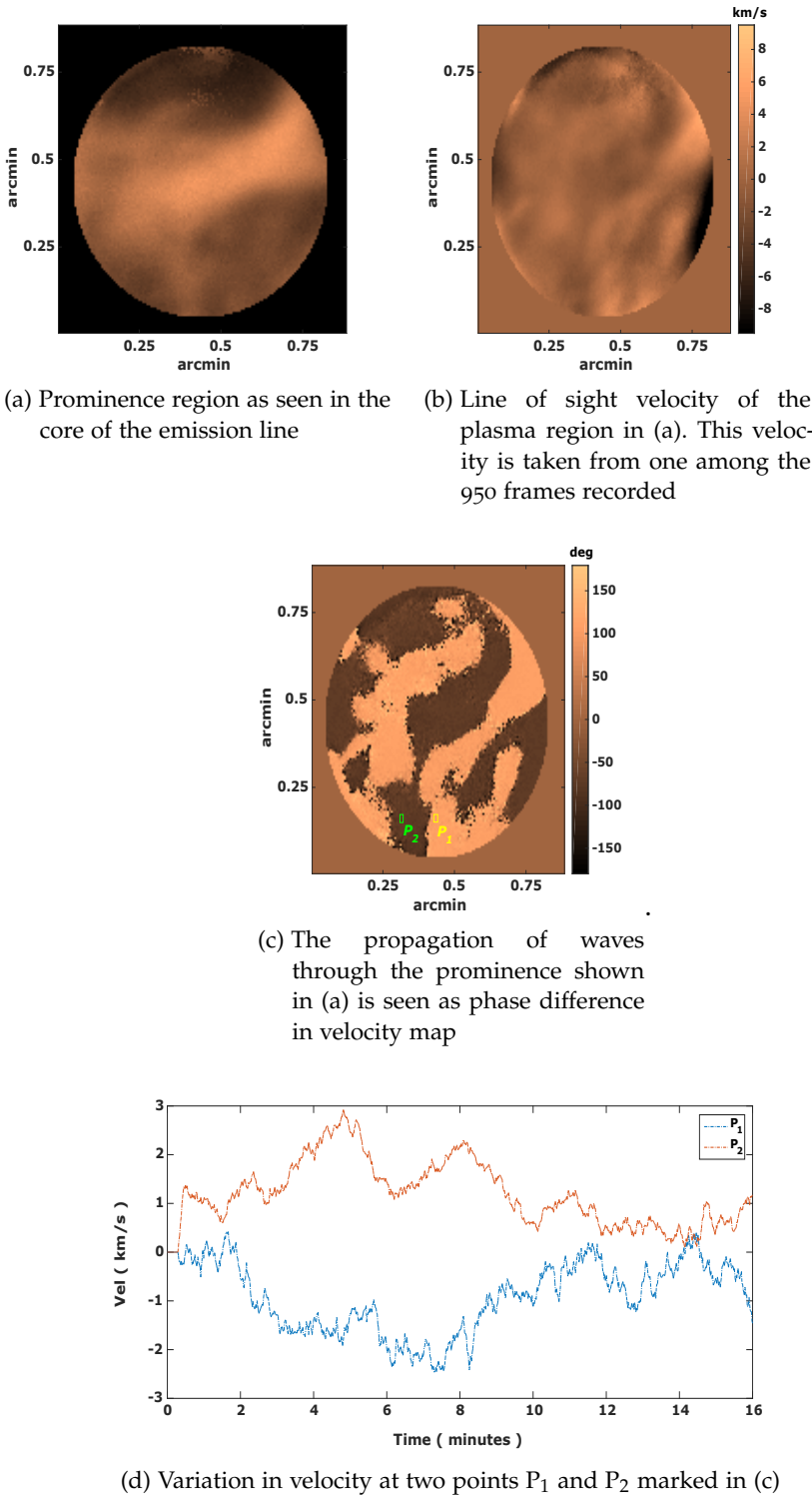


Figure 4.18: Dynamic events (wave propagation) obtained using sequence of snapshot images recorded by [LAS](#)

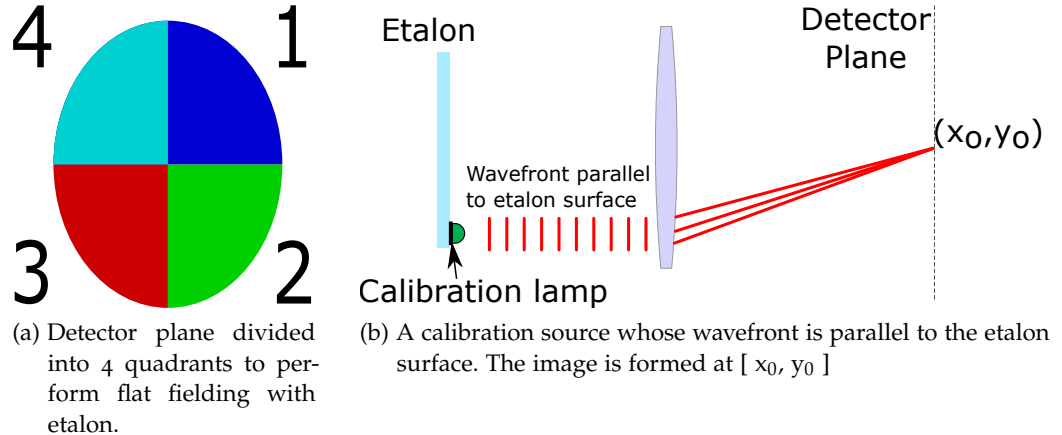


Figure 4.19: Design enhancements for LAS to perform snapshot spectroscopy using a fixed etalon

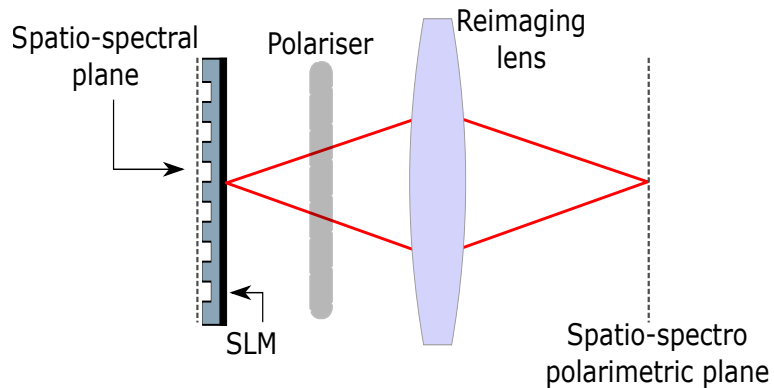


Figure 4.20: Conceptual diagram of using a spatial light modulator (SLM) to enhance LAS to perform snapshot spectropolarimetry

miniature level modulate light over a pixel. This device can be placed at the spatio-spectral plane and the pixels within a resolving element are modulated with different modulation scheme such that they contain the same spatio-spectral information but different polarimetric information. The resultant image on the detector is a snapshot spec-tropolarimetric image of the field. A conceptual diagram of the same is shown in Figure 4.20.

4.7 CONCLUSION

The problem of traditional spectrometers and their short coming in terms of speed were the driving force in the field of remote sensing to come up with new spectroscopic techniques. The ability to perform snapshot spectroscopy i. e. obtain a hyper spectral cube of [x, y, λ] in a single 2D frame was the solution to overcome the limitation in speed of traditional spectrometers. Several snapshot techniques came up as shown in Hagen and Kudenov [43] of which three techniques were

used in stellar astronomy. Although these techniques were used as main stream spectroscopic instruments in stellar astronomy, light intensity and several other factors link resolution and intensity crosstalk prevented their implementation in solar astronomy until recent times. Fiber and image sampling lenslet array are used as the snapshot techniques in solar astronomy. These instruments sample the image plane and use a grating spectrograph for spectral dispersion. Thus modifying the wavelength range or performing spectroscopy at multiple bands is not feasible.

A new class of snapshot spectroscopic instruments which sample the pupil rather than the image plane is presented in this chapter. The instrument design has three iterations with each design having its own merit and demerit as described in [Section 4.3](#). The working principle of the instrument is simple and the wavelength range of operation can be changed just by changing the focal length of the imaging and collimating lenses. This device also has multi wavelength band operation capabilities where the reflected light from the back surface of the etalon is recirculated back to the etalon at different angle of incidence.

Among the three optical designs presented the object pupil sample was developed into [LAS](#). The working principles of [LAS](#) were tested using a He-Ne laser light and solar spectra in the 6302 \AA region for the validity of the optical design. The instrument is then placed at [MAST](#) and its snapshot capabilities at two wavelength regions are tested. The instrument performs as predicted from the design and promises the capabilities of snapshot spectropolarimetry. This instrument can also be flown to space for studying the dynamics of the Sun at greater detail without the hindrance of the atmospheric seeing. As an example the coronal magnetic field configuration can be studied during the time of re-connection and the occurrence of flare or coronal mass ejection using [LAS](#). But it must be noted that the coronal magnetic field is weak and the next chapter describes the modulation techniques for measuring the coronal magnetic field. Overall [LAS](#) is a promising new instrument with a novel concept that can be used for snapshot spectroscopic study of the solar atmosphere.

Part III
POLARIZATION CROSSTALK

5

EVALUATION OF POLARIZATION CROSSTALK FOR CORONAL FIELD MEASUREMENTS

OVERVIEW

In this chapter, a polarimeter unit being developed for EVELC to measure the coronal magnetic field is discussed. The corona is pervaded by weak magnetic field, the inference of which requires high accurate and high precision spectropolarimetric observations. Because of large scatter in the atmosphere and varying seeing conditions, inferring such weak magnetic fields from ground based observations is very challenging. So the polarimeter designed here is for space based instruments intended to measure the line of sight magnetic field from the corona. The systematics and crosstalk parameters for such a space based system is simulated and a laboratory experiment is conducted to verify the same. The modulation scheme, experiments and results are presented in this chapter.

5.1 INTRODUCTION

The Sun is a dynamic star with the atmosphere broadly classified into four regions viz the photosphere, chromosphere, transition region and the corona. It is known that the solar atmosphere is coupled from the photosphere to the corona (Ballegooijen et al. [7], Schrijver and Title [97], and Wedemeyer-Böhm, Lagg, and Nordlund [126]). Although Sun has been studied for a long time and in recent times with great detail, several unanswered questions still remain. The coronal heating is one such example. There is a huge rise in temperature from 6000 K at the photosphere to a million kelvin at the corona, a 100 times in a span of just 3000 km as seen in [Figure 5.1](#). Several models and MHD simulations (e.g. Abbott and Fisher [1], Gudiksen and Nordlund [41], and Klimchuk [55]) are performed to match the observations and determine the energy transport mechanism from the lower layers of the atmosphere to the upper layers. The energy transport mechanisms can be mechanical or non mechanical with magnetic (currents) and non magnetic components. There are two mechanisms proposed for coronal heating viz., the AC heating and the DC heating mechanism. The former mechanism involves mechanical waves called Alfvén waves (Alfvén and Lindblad [2]) which are MHD waves produced due to turbulent convection of granulations in the photosphere. These waves travel through the coronal flux tubes and dump their energy in the corona. The later mechanism is related to magnetic field

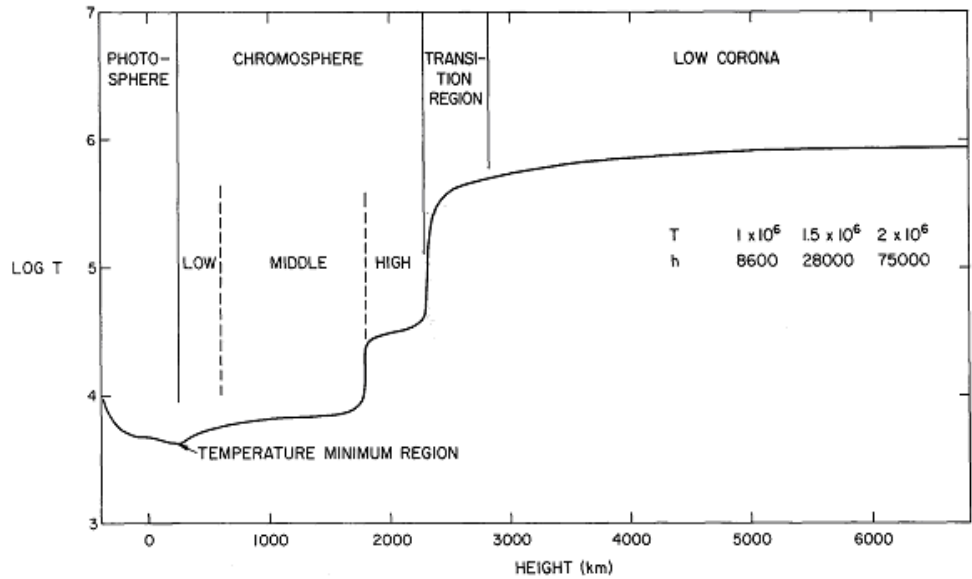


Figure 5.1: Temperature stratification of the solar atmosphere with height.
Nearly a 100 fold jump in temperature can be seen near 2500 km

re-connection where small scale re-connections which produce nano and micro-flares dump a part of released magnetic energy into the corona. Information on the vector magnetic field in the photosphere, chromosphere and corona is crucial in understanding the physical mechanisms which produce magnetic re-connection and validate the correctness of models which describe the process. Thus the mechanisms and models built on it rely on observable like magnetic energy and the correctness in the measured coronal magnetic fields (Wiegemann et al. [129]).

Coronal magnetic field is weak which is in the order of tenths of Gauss (estimated through indirect measurements (Nakariakov and Ofman [73] and Van Doorsselaere et al. [121])) and Zeeman effect is one of the most widely used magnetic diagnostics (Chapter 1). The extent of split in the wavelength of the spectral line in Angstrom due to Zeeman effect is given by

$$\Delta\lambda = 4.67 \times 10^{-10} \cdot g \cdot \lambda^2 \cdot B$$

where

g Landé factor

λ Wavelength in Å

B Magnetic field strength in gauss

Thus in order to obtain the polarization signature from weak coronal fields, the Landé factor or a measure of sensitivity of the atom to magnetic field should be high and wavelength of observation should

ELEMENT	λ in $[\mu\text{m}]$	LOG I $\text{erg cm}^{-2} \text{s}^{-1} \text{sr}^{-1}$	s/n FOR V	LOG T _e
Fe XIII	1.0746	1.35	5.6×10^{-4}	6.22
Si IX	3.9346	-0.17	1.5×10^{-3}	6.04
Si X	1.43	0.73	4.5×10^{-4}	6.13
Mg VIII	3.027	-0.36	5.6×10^{-4}	5.92
Fe XIII	1.0797	0.72	2.3×10^{-4}	6.22
Fe XIV	0.5303	1.36	1.5×10^{-4}	6.30
Fe XI	0.7891	0.96	1.5×10^{-4}	6.10
Fe X	0.6374	1.12	1.5×10^{-4}	6.03
S IX	1.252	-0.07	7.2×10^{-5}	6.0
Si VII	2.481	-0.71	7.0×10^{-5}	5.8

Table 5.1: Coronal forbidden transition lines with their corresponding Stokes V signal for longitudinal magnetic field of 50 G in a coronal loop over a typical active region with kG field in the photosphere. Values taken from Judge [49]

preferably be long. Due to the extremely high temperature of 10^6 K and low density of 10^{-10}kg/m^3 in the corona several forbidden spectral lines exist in the infrared region (Judge [49]) and the properties of some of the lines are given in Table 5.1.

In order to determine the vector magnetic field of a region all four Stokes parameters are necessary. Due to the low intensity of coronal radiation, the brighter photosphere has to be occulted and the corona has to be observed in the halo region around the occulter as shown in Figure 5.2. Due to this configuration, the Stokes V signal corresponding to the line of sight magnetic field is the weakest among all the four Stokes parameters. Table 5.1 also gives the relative strength of Stokes V with respect to the intensity of the line. It can be seen that among all the lines presented, Si IX at $3.9346 \mu\text{m}$ has the highest signal to noise ratio for Stokes V followed closely by Fe XIII at $1.0746 \mu\text{m}$. Although the polarized signal strength of Si IX is the highest, being at mid IR, detection of this line needs special detector system such as HgCdTe which requires cryo cooling to reduce thermal noise. Alternately detector system needed to detect Fe XIII is simpler and similar to a normal CCD hence the iron line is a preferred choice for coronal field diagnostics by most observers.

The polarization signatures of transverse field (linear polarization component) is 100 times stronger than longitudinal field (circular polarization component) for Fe XIII when observing the halo corona (Lin, Kuhn, and Coulter [64], Lin, Penn, and Tomczyk [66], and Tomczyk et al. [119]). Table 5.1 gives the Stokes V strength for a 50 G field in the coronal loops above a typical active region that has field strength of the order of kG in the photosphere. As Stokes V is the



Figure 5.2: Corona viewed as a halo by occulting the photosphere

weakest signal and is of the order of 10^{-4} times the total intensity, polarimeter system designed for measuring these weak fields should have a sensitivity of $10^{-4}I$ or the noise levels due to systematic and random errors in the system which causes a polarization crosstalk should be less than 0.01%. A major hindrance in achieving high sensitivity polarimeter at ground based observatory is the atmosphere. Not only does the atmospheric seeing limit the spatial resolution but also produces polarization crosstalk, increases background thus reducing Signal to Noise Ratio ([SNR](#)) ([Penn \[78\]](#)). Thus a space observatory is the ideal choice for mapping vector fields of the corona. Although space observatory is free from atmospheric turbulence, satellite jitter and drift causes image motion ([Section 5.2](#)) which has to be accounted while designing the polarimeter.

So a system has to be designed such that it is capable of performing simultaneous measurements at multiple wavelength to obtain height varying information of the field and also have polarimetric sensitivity of 0.01% to measure polarization produced by coronal field. Both the instruments [MSSP](#) presented in [Chapter 2](#) and [LAS](#) presented in [Chapter 4](#) are capable of multi wavelength simultaneous observation. But the polarimeter unit designed for these systems uses [LCVR](#) modulator which is yet to be qualified for space environment and a birefringent crystal has to be used instead (as such crystals have been flown in the past).

EVELC (Raghavendra Prasad et al. [[84](#)]) is a modified version of [MSSP](#) that will observe the corona on board ADITYA-L1 (Seetha and Megala [[99](#)]), a space observatory to study the Sun and to be launched by Indian Space Research Organization - ISRO. This chapter discusses the design of the modulator unit for EVELC and results on polariza-

tion crosstalk obtained from laboratory experiment on a birefringent crystal retarder unit.

5.2 SATELLITE AOCS - JITTER AND DRIFT

The Attitude and Orbit Control System ([AOCS](#)) is a subsystem of the satellite that maintains the orientation of the satellite. The [AOCS](#) is used for positioning the satellite for telemetry-telecommand and to accurately point at an object in the sky. For a typical satellite the subsystem consists of a redundant set of star sensors, Earth sensors and Sun sensors which communicates with the central [AOCS](#) processor unit. The processor is linked to the reaction wheel, momentum wheel and thrusters. Based on the input from the sensors, the processor corrects for the position of the satellite through a process called three-axis stabilization or body stabilization where the momentum of the momentum wheel is increased or decreased electrically or mechanically in one direction to produce an equal and opposite effect on the satellite. There are three degrees of rotation about which a satellite rotates and gets positioned/oriented in space. They are, the yaw, pitch and roll. For a satellite dedicated for astronomical observations the roll axis is oriented along the observing target [Figure 5.3](#).

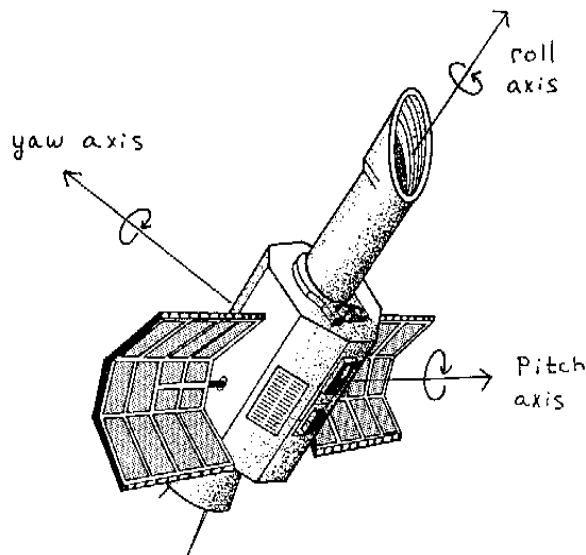


Figure 5.3: The three axis of rotation along which a satellite is stabilized

The extent and rate of correction for an astronomical satellite depends on the accuracy and stability required during the time of observation. When the field drifts beyond a specified limit the reaction wheels are triggered to bring the field back to the desired location. The [AOCS](#) can be considered to be equivalent to an active optics system of a ground based telescopes. For an object under observation

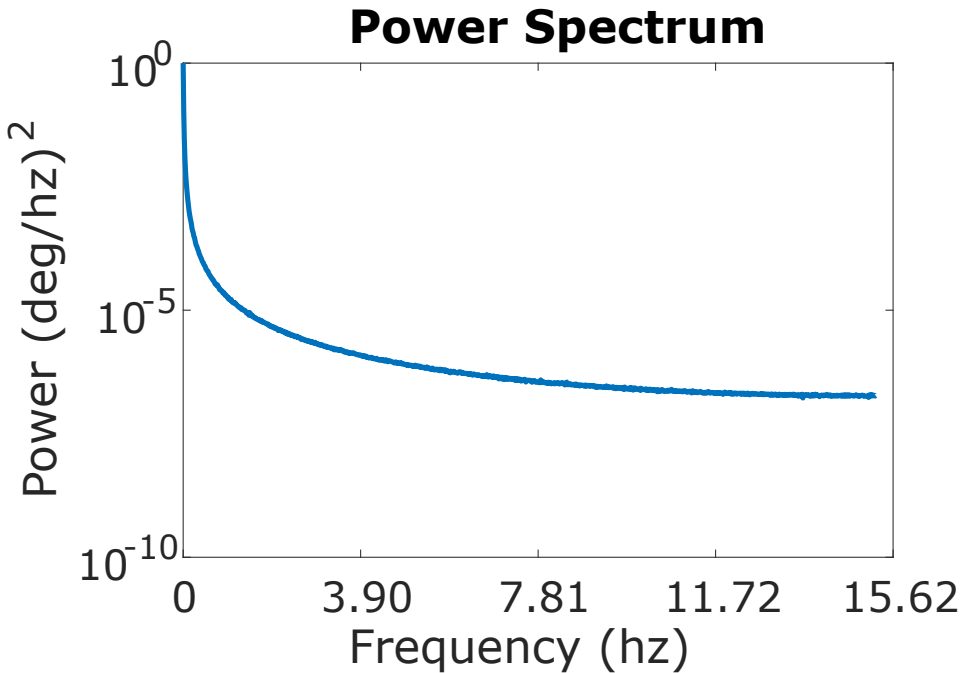


Figure 5.4: Powerspectra of the random motion of a star image on the star-sensor of the satellite taken with a refresh rate of 64 msec.

the mis-alignment in the satellite position and residual after the correction done by the AOCS translates to random motion of the object's image on the detector plane. This random motion can be classified into two types. The slow varying component called the drift and a fast varying or high frequency component called jitter. Figure 5.4 is the power-spectra of the data taken from a star sensor on board a LEO satellite with a refresh rate or correction rate of 64 msec. The data corresponds to the random motion of a star's image on the star sensor which includes the satellite drift and jitter. This random motion is equivalent to atmospheric seeing. Although the image motion is much smaller than that caused due to atmospheric seeing, it has to be taken into account while generating the modulation matrix for coronal polarimeter as small crosstalk of 10^{-4} into Stokes V can result in wrong interpretation of the fields.

Unlike LEO satellites, EVELC on-board ADITYA-L1 is going to be placed at a relatively stable environment, the first Lagrange point, hence the satellite jitter would be lesser when compared to the powerspectra of Figure 5.4. But the polarimeter is designed taking into consideration the higher power such that the system's performance will be well within the expected range.

5.3 POLARIMETER DESIGN

A polarimeter is composed of a modulator and an analyzer. The polarimeter for EVELC will consist of a single birefringent crystal retarder as the modulator and a calcite beam displacer as a dual beam analyzer. The dual beam analyzer splits a single image into two orthogonally polarized images. Such a design is used to eliminate intensity to linear and circular polarization crosstalk (Lites [69]). All other design parameters for the analyzer is obtained in the manner described in Chapter 2 and the design of the modulator is described in this section.

The crystal retarder is used to modulate light by rotating the retarder. If M_R is the muller matrix of a retarder then

$$M_R(\delta, \theta) = \begin{pmatrix} 1 & 0 & 0 & 0 \\ 0 & g + h\cos(4\theta) & h\sin(4\theta) & -\sin(\delta)\sin(2\theta) \\ 0 & h\sin(4\theta) & g - h\cos(4\theta) & \sin(\delta)\cos(2\theta) \\ 0 & \sin(\delta)\sin(2\theta) & -\sin(\delta)\cos(2\theta) & \cos(\delta) \end{pmatrix},$$

$$g = \frac{1}{2}(1 + \cos(\delta)),$$

$$h = \frac{1}{2}(1 - \cos(\delta)), \quad (5.1)$$

and if M_P is the muller matrix of the polarizer then

$$M_P(\phi) = \frac{1}{2} \begin{pmatrix} 1 & \cos(2\phi) & \sin(2\phi) & 0 \\ \cos(2\phi) & \cos^2(2\phi) & \sin(2\phi)\cos(2\phi) & 0 \\ \sin(2\phi) & \sin(2\phi)\cos(2\phi) & \sin^2(2\phi) & 0 \\ 0 & 0 & 0 & 0 \end{pmatrix}.$$

The well known balanced modulation matrix can be obtained using two rotating retarders (e.g. Nagaraju et al. [72]). But the modulator system designed here is used in a space instrument and mass constraint prevents the use of multiple rotating retarders. The modulated light from a single rotating retarder with analyzer at 0° is

$$M_P \times M_R.$$

As the detector can detect only the variation in intensity, the modu-

lated intensity for an input Stokes $\begin{pmatrix} I \\ Q \\ U \\ V \end{pmatrix}$ is given by

$$I_i = 0.5I + ((g + h * \cos(4\theta_i)) * Q) + ((h * \cos(4\theta_i - 90^\circ)) * U) + ((f * \sin(2\theta_i)) * V) \quad (5.2)$$

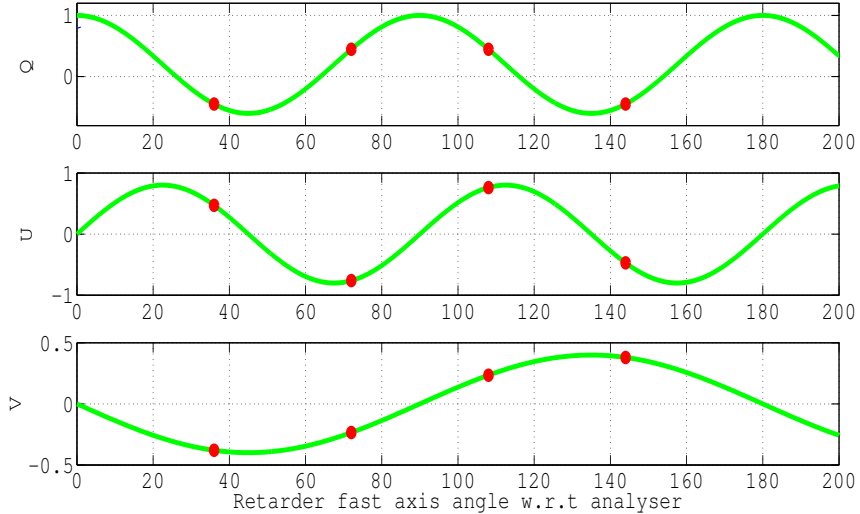


Figure 5.5: Modulated output of Stokes Q , U , V for $\delta = 127^0$ retarder with sampling points for nearly balanced modulation shown as red dots

where g and h are taken from [Equation 5.1](#) and

$$f = 0.5\sin(\delta)$$

For nearly balanced modulation using a single crystal retarder we get retardance $\delta = 127^0$ with the fast axis oriented at $\theta = [36^0, 72^0, 108^0, 144^0]$. The modulated Q , U , V signal from a $\delta = 127^0$ retarder is shown in [Figure 5.5](#).

It must be noted that the samples in [Figure 5.5](#) are taken at discrete points. Discrete sampling would imply stepping where the retarder moves to a particular value of θ and stops for each measurement. For a realistic space based polarimeter, this start and stop motion would introduce torque on the satellite which unnecessarily causes additional jitter and eventually crosstalk in measurement. To avoid this, the retarder is rotated continuously and the camera is exposed at particular instance of time when the the retarder is at the desired angle. This method causes a range of Q , U , V values to be measured instead of a single point. Thus in [Figure 5.5](#), the sample points are replaced by a window whose center coincides with the red dots. But such a configuration leads to high degree of asymmetry and eventually large systematics and crosstalks in the system. If ' O ' is the modulation matrix of the retarder analyzer system then the coefficients of the modulation matrix are the area under the curve of the modulation windows chosen. The efficiency in modulating different Stokes parameters are given by the efficiency matrix

$$A = O^T O$$

$$= n \begin{pmatrix} \epsilon_I^2 & a & b & c \\ d & \epsilon_Q^2 & e & f \\ g & h & \epsilon_U^2 & i \\ j & k & l & \epsilon_V^2 \end{pmatrix}, \quad (5.3)$$

where

- n Number of modulations or unique window positions
- ϵ_i Efficiency with which a Stokes parameter is modulated
- a to l Systematics.

For an orthogonal set of modulations, the off diagonal elements in 'A' become zero. It must be noted that an orthogonal modulation matrix can't be achieved using a single crystal retarder because of the dc or constant term introduced by the retarder while modulating Stokes Q. The term 'g' in the [Equation 5.2](#) of output intensity from a rotating retarder and fixed analyzer system causes a dc shift in Stokes Q. I to Q crosstalk is eliminated using dual beam and Q to I crosstalk is neglected due to weak Stokes Q signals over stronger Stokes I. Thus the optimum modulation matrix for a single crystal retarder is one whose efficiency matrix is diagonal neglecting non zero 'a' and 'd' in [Equation 5.3](#). But the nearly balanced modulation matrix has non zero off diagonal elements apart from 'a' and 'd'. This introduces systematics and cross-talk into Stokes V which prevents the system from achieving 0.01% sensitivity.

With balanced modulation not feasible for coronal magnetic field measurements, a custom developed modulation matrix is necessary which caters for the needs of EVELC to specifically measure weak Stokes V signals. So criteria of the retardance and position angle of the modulator for this instrument are -

- Uniform sampling window such that efficiency matrix A is a diagonal matrix (excluding elements a and d)
- High efficiency in measuring Stokes V signal with equal efficiency of measurement for Q and U i.e. $\epsilon_V \geq \epsilon_Q = \epsilon_U$
- Low crosstalk of 10^{-2} or lesser from Stokes Q, U to V (as Q and U are 100 times stronger than V)

For a continuously rotating modulator of retardance δ uniform sampling occurs at those angles of θ for which

$$\theta_2 = (2n + 1) \frac{\pi}{2} - \theta_1 \quad n = 0, 1, 2, \dots, \quad (5.4)$$

such that if

$$U_1 = \sin(2\theta_1),$$

then

$$U_2 = \sin(2\theta_2) = -\sin(2\theta_1) = -U_1, \quad (5.5)$$

and

$$A = n \begin{pmatrix} \epsilon_I^2 & a & 0 & 0 \\ a & \epsilon_Q^2 & 0 & 0 \\ 0 & 0 & \epsilon_U^2 & 0 \\ 0 & 0 & 0 & \epsilon_V^2 \end{pmatrix}, \quad (5.6)$$

where U_1 and U_2 are Stokes U at θ_1 and θ_2 respectively.

For a detector system which has 50 % duty cycle over the modulation cycle, the sampling windows that satisfy the criteria Equation 5.4 and 5.5 are represented in Figure 5.6 and Figure 5.7 and their corresponding efficiency curve as a function of retardance is given in Figure 5.8 and Figure 5.9 respectively.

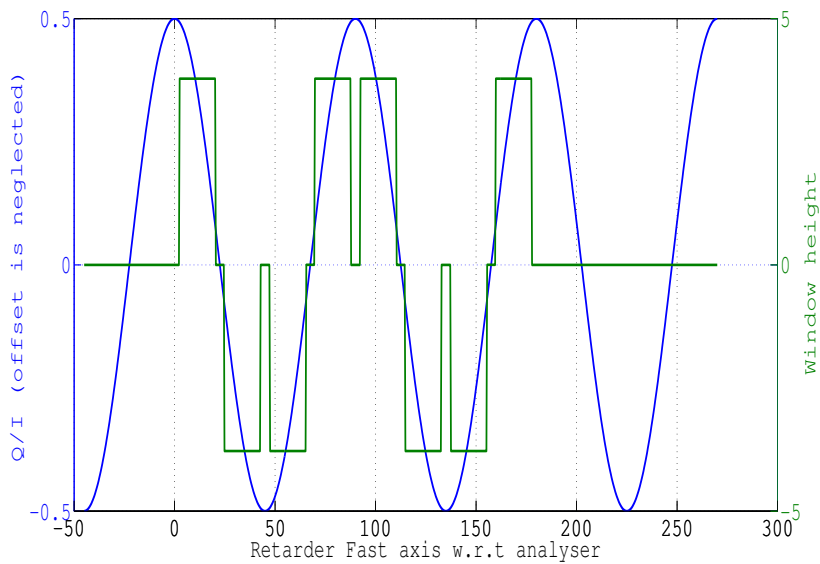


Figure 5.6: Uniform intensity sampling with farthest spacing between the samples

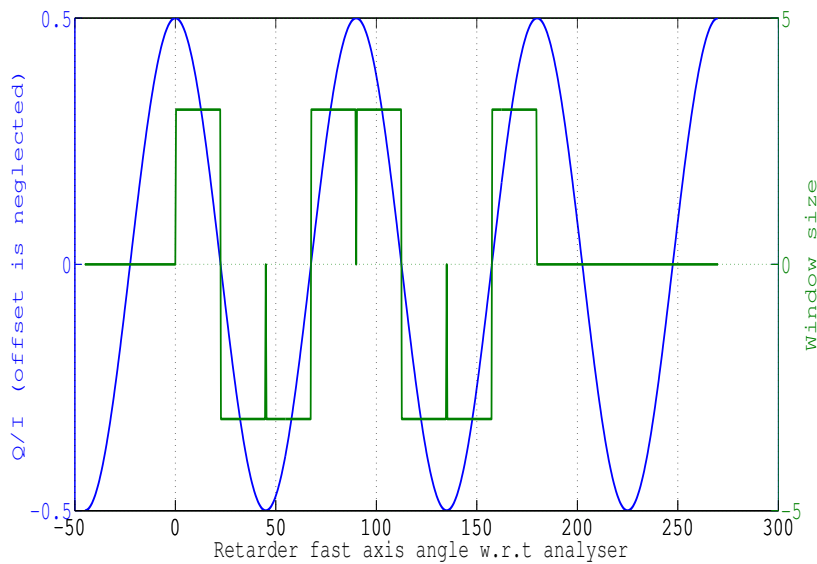


Figure 5.7: Uniform intensity sampling with the closest spacing between samples

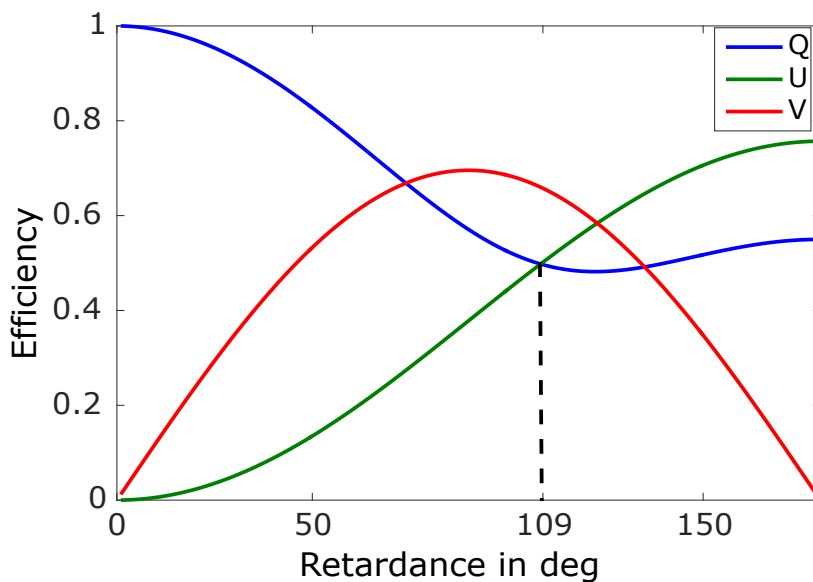


Figure 5.8: Normalized efficiency of detecting a Stokes parameter with the window position defined in Figure 5.6 as a function of retardance.

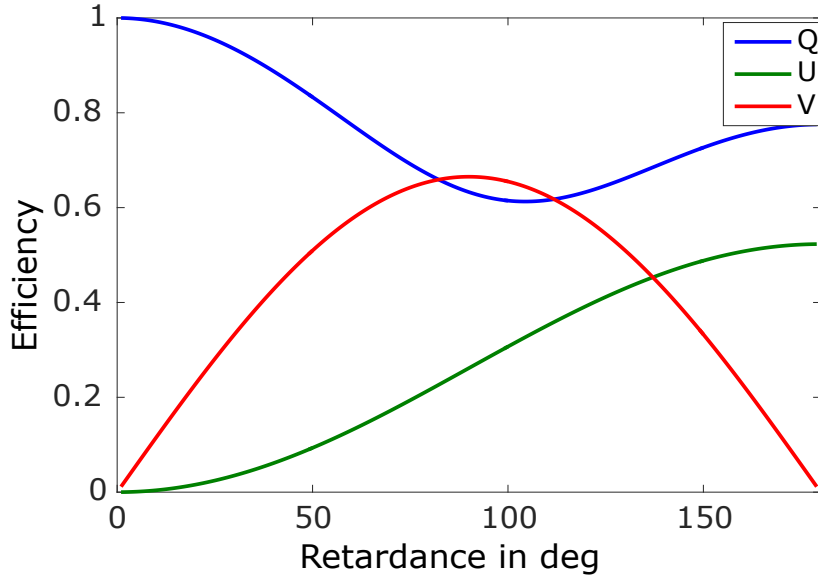


Figure 5.9: Normalized efficiency of detecting a Stokes parameter with the window position defined in Figure 5.7 as a function of retardance

For a system with uniform sampling window out of all the possible ranging from maximum spacing among the window to minimum spacing between them, it is found that the windows with largest spacing between samples (Figure 5.6) modulates Q and U Stokes parameters with equal efficiency (Figure 5.8) when a retarder of retardance $\delta = 109^0$ is used, while window with minimum spacing between adjacent channels (Figure 5.7) has the highest efficiency in modulating Stokes V (Figure 5.9). The final modulation matrix among the two possible modulation schemes is determined based on the crosstalk introduced by each matrix.

For a source whose Stokes parameters can be written as (Lites [69]),

$$S_i = R_i[1 + \beta_i N(t)],$$

where

- S_i Input Stokes vector for the modulator,
- R_i Source intensity,
- β_i Gradient in source intensity,
- $N(t)$ Noise due to random motion.

We have the variation in the source signal due to some random noise $N(t)$ introduced by the atmosphere or the satellite jitter and the variation is amplified with gradient in the source β_i . For a point source, this gradient is the highest and for an extended source of infinite size with uniform intensity this value is zero. So for a constant “seeing” the extent of crosstalk depends on the shape, size and uniformity of the source under observation. If $G(t)$ is the modulation function then

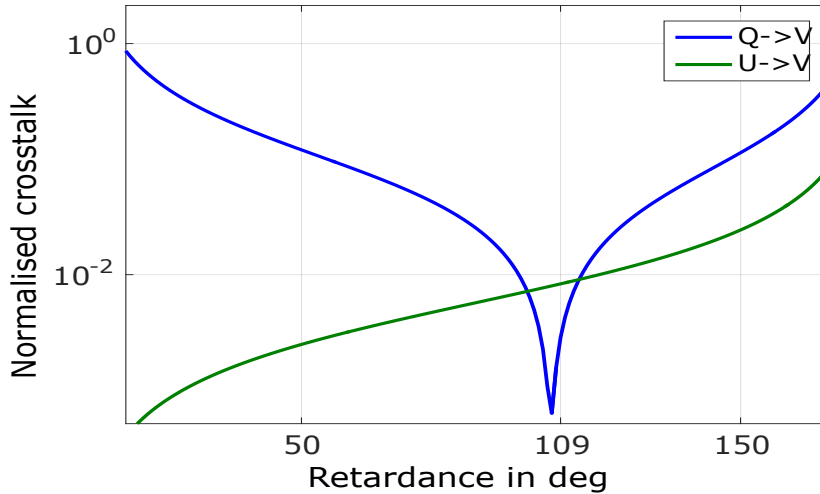


Figure 5.10: The crosstalk from linear to circular polarization is shown as a function of retardance. The crosstalk level is at 10^{-2} for retarder rotating at 1 Hz and 50% duty cycle of the detector

the crosstalk (σ_{ri}) from one Stokes parameter (r) to the other (i) due to seeing/jitter $N(t)$ can be represented in the frequency domain as -

$$\sigma_{ri}^2 = (R_i \beta_i)^2 \int_0^\infty P_N(v) |H_{ri}(v)|^2 dv, \quad (5.7)$$

where

- $P_N(v)$ Power in the noise or jitter at frequency v ,
- H_{ri} Fourier transform of the product of sampling, window r and Stokes parameter i.

The power spectra of noise or jitter in the satellite is obtained from the star sensor data as described in [Section 5.2](#). For a refresh rate of 64 ms the satellite power spectra of jitter is given in [Figure 5.4](#). This is considered to be P_N in [Equation 5.7](#). The function H_{ri} depends on the window size used in the modulator. For a dutycycle of 50 % and a rotation rate of 1 Hz the window size of the modulator depicted in [Figure 5.6](#) and [Figure 5.7](#) is 31.25 ms. The value of the integral given in [Equation 5.7](#) which represents the normalized source independent crosstalk is computed for different retardance. The crosstalk for first sampling windows used in [Figure 5.6](#) is shown in [Figure 5.10](#) and the crosstalk for second sampling window used in [Figure 5.7](#) is shown in [Figure 5.11](#).

Discussion -

The modulator designed for EVELC should generate optimum modulation matrix which satisfies [Equation 5.6](#) and has high efficiency in modulating Stokes V. It is also desired to have equal efficiency in

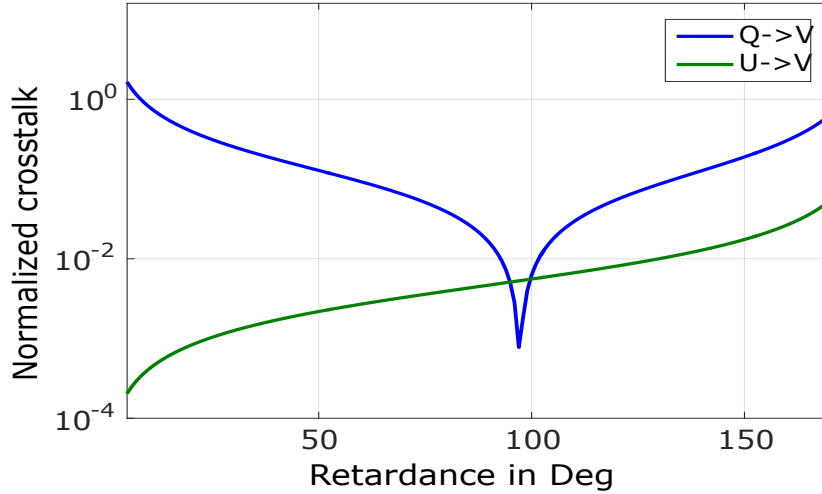


Figure 5.11: Crosstalk of Q and U into V for second sampling window generated using the same conditions as described in Figure 5.10

modulating linear polarization. Two sets of modulation satisfy these conditions along with low crosstalk of 10^{-2} into Stokes V for a 1 Hz rotating retarder at 50 % dutycycle of the detector. But the first modulation scheme called the first window has equal efficiency in modulating both Stokes Q and U at $\delta = 109^\circ$. The modulation matrix of the polarimeter is given by

$$O = \begin{bmatrix} 1 & 0.7168 & 0.5225 & 0 \\ 1 & -0.0424 & 0.5225 & -0.8370 \\ 1 & -0.0424 & -0.5225 & -0.8370 \\ 1 & 0.7168 & -0.5225 & 0 \\ 1 & 0.7168 & 0.5225 & 0 \\ 1 & -0.0424 & 0.5225 & 0.8370 \\ 1 & -0.0424 & -0.5225 & 0.8370 \\ 1 & 0.7168 & -0.5225 & 0 \end{bmatrix}$$

and the efficiency matrix of the system is

$$A = 8 \begin{bmatrix} 1 & 0.3372 & 0 & 0 \\ 0.3372 & 0.2578 & 0 & 0 \\ 0 & 0 & 0.2730 & 0 \\ 0 & 0 & 0 & 0.3503 \end{bmatrix}$$

5.4 EXPERIMENTAL VERIFICATION AND DESIGN ENHANCEMENT

The simulated results for linear to circular polarization crosstalk was obtained using the formulation given in (Lites [69]). In order to ver-

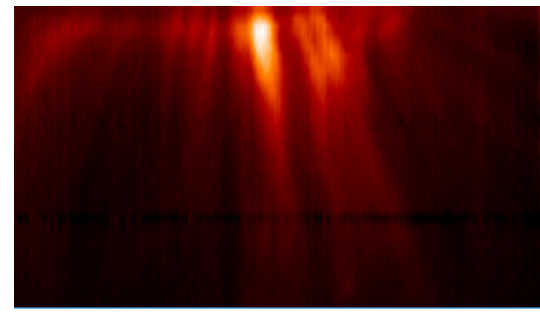
ify the applicability of the polarimeter to real time observation of the corona, an experiment was setup where the “satellite jitter” is introduced into the source and the resultant noise in measured polarization of the source is computed. If the system is capable of reaching noise levels of $10^{-4}I$ then the modulation matrix can be implemented for coronal vector magnetic field measurements.

Artificial jitter

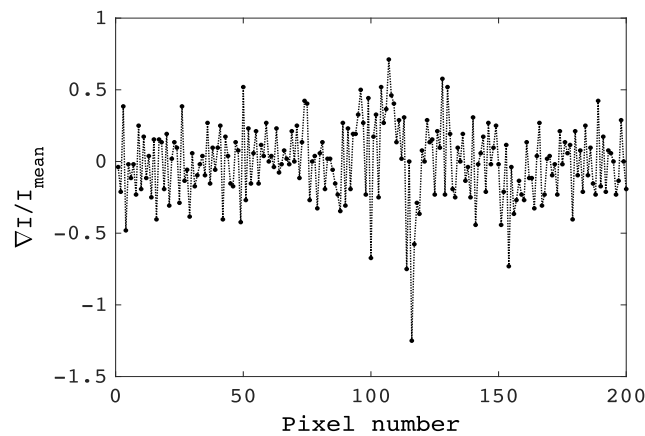
The experiment relies on the re-creation of the jitter experienced by the satellite and the resultant image motion on the detector when EVELC observes the corona. Satellite jitter translates to a random motion of a point source about a region on the detector. The amplitude of that motion is determined by the rate of correction performed by the AOCS of satellite. The powerspectra in [Figure 5.4](#) gives the information about the extent to which a point moves from its mean position and the frequency with which such a motion occurs. This is also valid for an extended source like corona. Consider a coronal image taken at Fe XIII 1.0746 μm as shown in [Figure 5.12a](#), a region at a distance of $1.05 R_{\odot}$ is taken from the image (the coronagraph in EVELC images the corona from $1.05 R_{\odot}$). Variation in the source intensity about the mean intensity from pixel to pixel at $1.05 R_{\odot}$ is plotted in [Figure 5.12b](#) and the standard deviation is found to be 26 %. The plate scale of the image is 2.51 arcsec/pix thus the variation in intensity for a typical quiet Sun coronal image is 10.35 % of intensity per arcsec. This is used as the base value in intensity fluctuation for our experiment.

The experimental setup is shown in [Figure 5.13](#). In order to produce artificial jitter, a current controlled laser diode was used whose intensity fluctuates with an amplitude variation of 10.35% per arcsec and follows the power spectral distribution shown in [Figure 5.4](#). The experiment is devised to test the linear to circular crosstalk. For a linearly polarized source, the extent of circular polarization measured by the polarimeter should be 10^{-4} or lesser in order to conclude the working of the polarimeter. A Glan Thompson polarizer with an extinction ratio of $10^5:1$ is used to produce linearly polarized light. The retarder is a zero order (at 632.8 nm) calcite crystal mounted on a mechanized rotation stage and the analyzer is a wollaston prism used to produce dual beam. As the experiment is setup to measure polarimetric accuracy and not imaging capabilities, using a wollaston prism instead of a [PBD](#) will not affect the outcome of the experiment.

As the laser diode fluctuates the motorized rotation stage rotates the retarder which causes a modulation in the intensity of the linearly polarized light. Images are captured by the detector at specific window angles [13, 31, 58, 76, 103, 121, 148, 166] as shown in [Figure 5.6](#). For the purpose of simplicity and synchronization between the retarder position and camera record trigger, the whole experi-



(a) Image of quiet Sun corona taken in Fe XIII
1.0746 μm . The y-axis covers 1.05 - 1.5 R_\odot



(b) Variation in source intensity about the mean value taken at
1.05 R_\odot from Figure 5.12a

Figure 5.12: Variation in source intensity for a typical quiet Sun corona taken at Fe XIII 1.0746 μm line

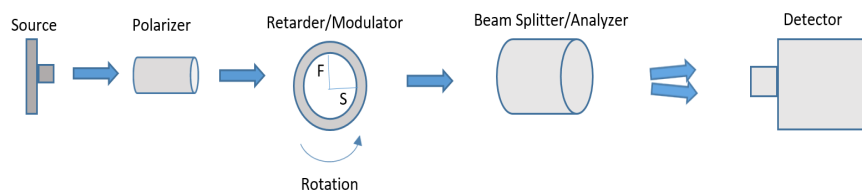


Figure 5.13: Experimental setup to validate the ability of modulation matrix for EVELC

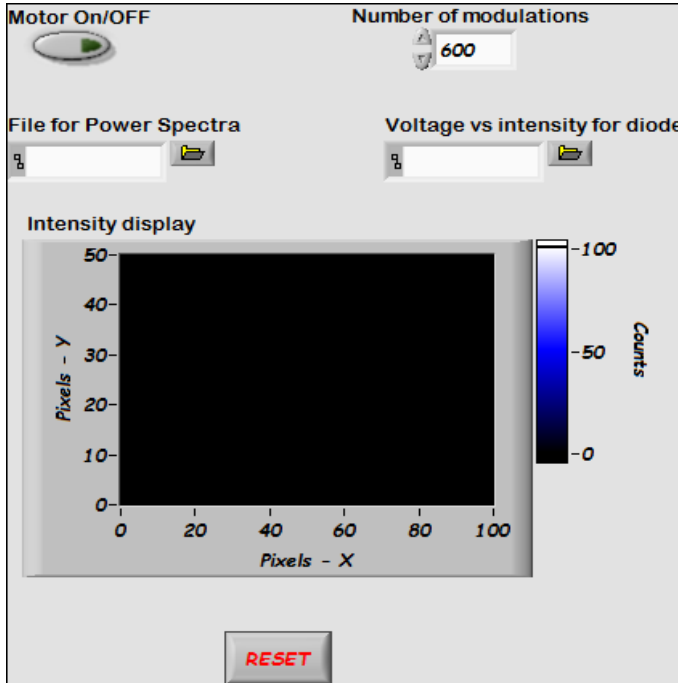


Figure 5.14: A simple GUI developed to test the modulation scheme generated for EVELC. The GUI takes the powerspectra and diodes characteristics as input files to generate fluctuation that are similar to a LEO satellite

ment is conducted using a GUI created in LabView and is shown in [Figure 5.14](#).

Each set of modulated images consist of 8 images which are then demodulated using the demodulation matrix obtained as

$$D = A^{-1}O,$$

where A and O are efficiency matrix and modulation matrix respectively. The demodulated output is

$$\begin{pmatrix} I + \delta I \\ Q + \delta Q \\ U + \delta U \\ V + \delta V \end{pmatrix} = D \times \begin{pmatrix} I_1 \\ I_2 \\ \vdots \\ I_8 \end{pmatrix},$$

where δi is the crosstalk in i^{th} Stokes parameter obtained from a single measurement. As jitter is random

$$\langle i + \delta i \rangle = i.$$

For a large data set or modulations $\langle i + \delta i \rangle_{n+1} - \langle i + \delta i \rangle_n = 0$. Thus for our experiment the difference in the time averaged value of Stokes V should tend towards zero if the modulator has no systematics and the crosstalk values obtained have no residuals. [Figure 5.15](#) is a plot of

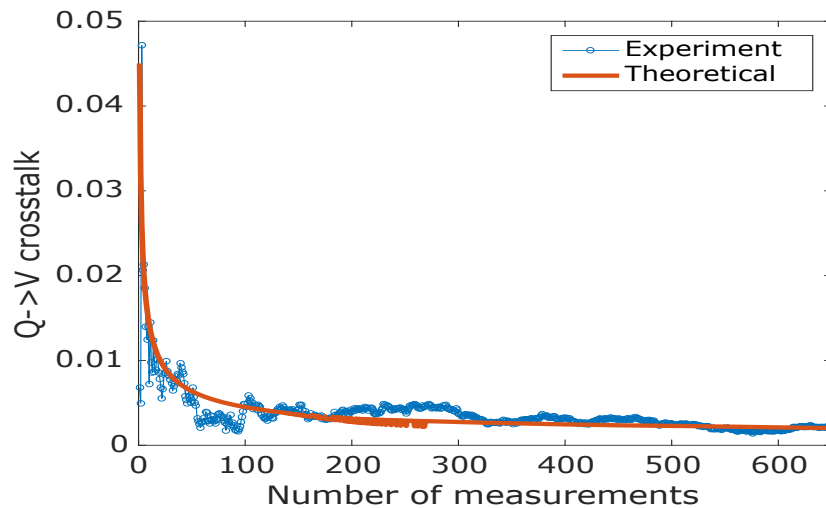


Figure 5.15: Plot of residual Stokes V signal for a Q input. The predicted curve is obtained by simulating the expected crosstalk from the system using [Equation 5.7](#)

the difference in the residual Stokes V signal obtained using the experimental setup with increasing number of averaged frames. The predicted plot is obtained by computing the intensity fluctuation given to the diode and using [Equation 5.7](#) to obtain the residual crosstalk. The crosstalk values are averaged and subtracted from the previous set of averaged values with one lesser frame. It can be seen in [Figure 5.15](#) that the crosstalk levels are tending to zero with increase in the number of averaged frames. Thus the modulation matrix is free from systematics and can be used for coronal polarimetry.

Design enhancement

Unlike a fixed modulator like [LCVR](#) a crystal retarder rotates to modulate the incoming light. A crystal retarder can be considered to be a parallel plate glass slab due to which an incoming light undergoes multiple reflections before exiting the crystal. But due to birefringence, the interference pattern formed on the screen due to multiple reflections are polarized. This interference pattern is called polarization channel ([Semel \[100\]](#)) and affects the sensitivity of the modulator as rotating the retarder rotates the fringe pattern causing crosstalk. The retarder like the glass plate can be kept in a converging beam to diffuse the polarized channels on the detector plane as shown in [Figure 5.16b](#). For a glass plate the total intensity of transmitted light from primary ray and 1^{st} multi reflected ray is given by

$$I_T = I_P + I_r + \sqrt{I_P I_r} \cos(\phi),$$

where I_P is intensity of primary ray, I_r is intensity of secondary ray caused due to reflection at the air glass boundary & ϕ is the phase

difference between primary and secondary rays. For collimated beam the interference term $\sqrt{I_p I_r} \cos(\phi)$ is large of the order of $10^{-2}I$ (Figure 5.16a). But by placing the glass plate in a converging / diverging beam, the extent of interference between the primary and secondary ray can be reduced to $10^{-6}I$ (Note this number is obtained for a 10 mm glass slab placed in an f/7 beam)

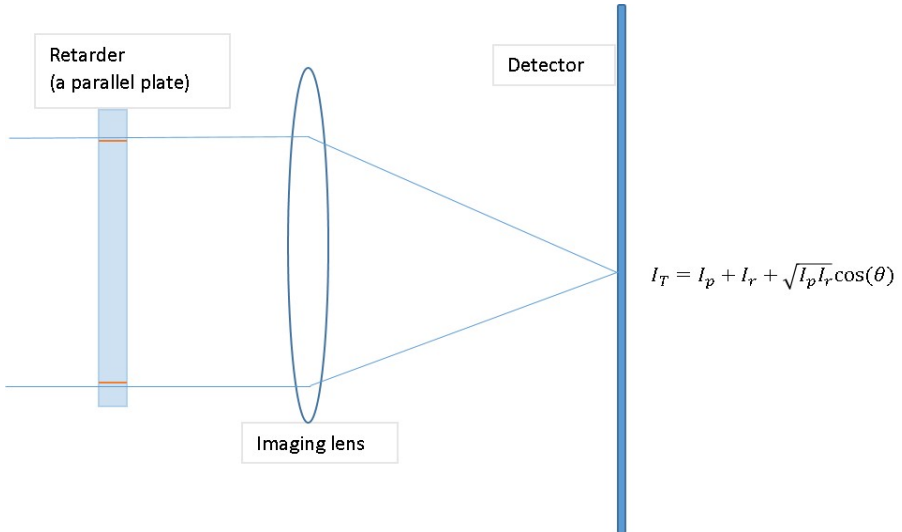
5.5 CONCLUSION

Coronal magnetic field measurements are important to understand the dynamics of the Sun and to solve many unresolved problems in solar physics. Unlike photospheric magnetic fields the field strength of coronal loops is of the order of few tenths of Gauss. Also the corona is visible in optical and IR wavelength only when the photosphere is blocked by an occulter. Due to this the observer predominantly sees longitudinal field thus measuring weak signatures of Stokes V which is a 100 times weaker than Stokes Q and U. In order to measure these weak fields, one has to avoid the turbulent atmosphere and use a space observatory for field measurements. But a space observatory requires special space qualified components for instrumentation. Due to this, a birefringent crystal retarder is used as a modulator instead of LCVR. Further mass and stability constraints limit the number of retarders being used. It is also necessary to modulate the input light by rotating the retarder continuously instead of discrete steps to avoid jerks in the satellite system from start and stop motion of the retarder. Due to continuous rotation, balanced modulation matrix cannot be achieved from a single crystal retarder. Hence, a custom modulation matrix is developed which requires a single continuously rotating crystal retarder. It has high Stokes V efficiency and low crosstalk arising from satellite jitter. Two modulation schemes (with two different window/sampling positions) which satisfy the above criteria are developed and are called first and second modulation scheme. The first modulation scheme has an added advantage of nearly equal efficiency for Stokes Q and U hence it is chosen over the second modulation scheme. The linear to circular crosstalk is within the range of 10^{-2} required for the 100 times weaker Stokes V signal. An experiment was conducted on the simulated modulation matrix using a zero order quarter wave plate crystal and current controlled laser diode. The intensity fluctuation of the diode mimicked a satellite's jitter over typical quiet Sun coronal region at $1.05 R_\odot$. The experimental results matched the predicted values hence confirming the modulation matrix designed for a space based observatory. The chapter concludes with a minor design enhancement of the polarimeter where the modulator is placed in a converging beam instead of a collimated beam to minimize polarization fringes.

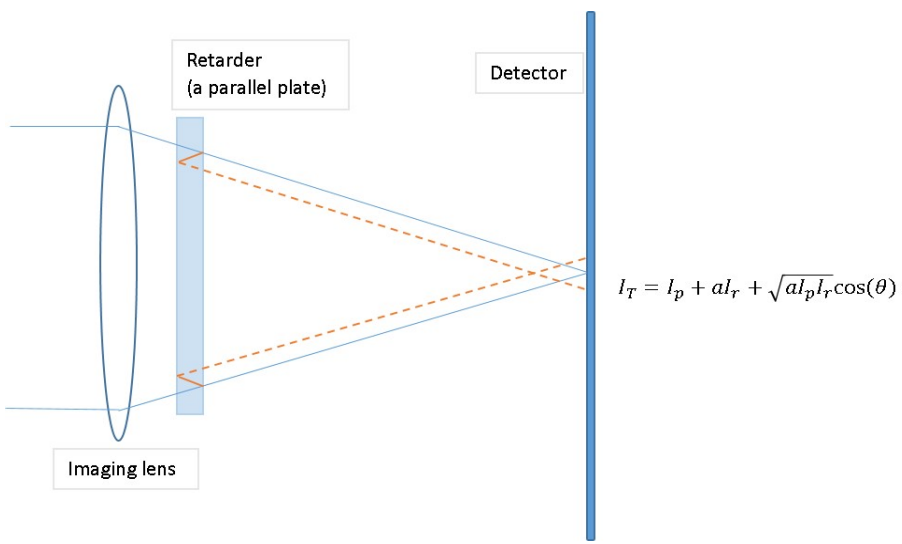
f/7 beam is a configuration taken from EVELC. A space based instrument dedicated to measure coronal magnetic field

Both MSSP and LAS are capable of measuring coronal lines and EVELC is a modified version of MSSP which will be on board ADITYA-L1 mission

The retarder is zero order at 632.8 nm



(a) Retarder in collimated beam produces strong polarized channels as secondary transmission interfere with the primary transmitted ray



(b) Retarder in converging beam produces weak polarization channels as secondary transmission is decoupled from the primary rays and forms an image ahead of the primary transmitted beam. Thus the interference between the two beams is reduced by a factor of "a" equal to the defocus.

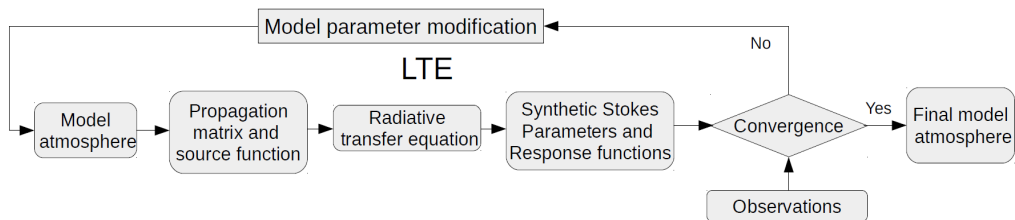
Figure 5.16: Design enhancement for EVELC polarimeter for higher polarization sensitivity

Thus an instrument set is developed in this thesis which performs fast or snapshot spectroscopy for all the layers of the solar atmosphere hence enhancing the capabilities of solar observation in better understanding of the working of the Sun.

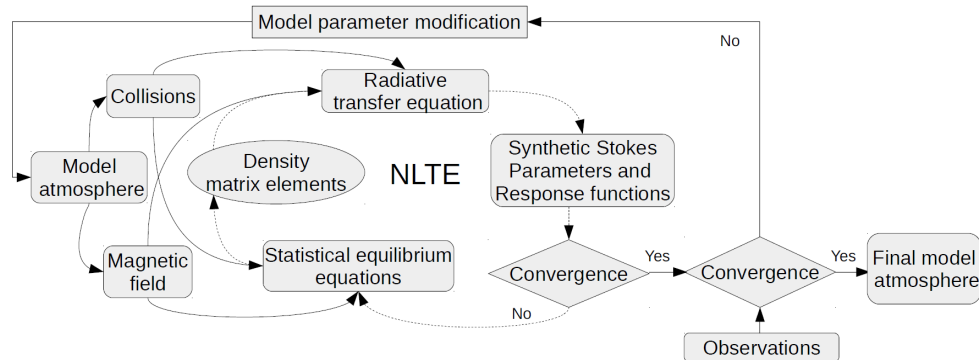
A

APPENDIX

Spectropolarimetric inversion is a process of obtaining the field parameters of a magnetic atmosphere. As the field parameters are non linear, numerical solutions are obtained through χ^2 minimization. The numerical solution is classified into two types based on the thermodynamic state of the atmosphere. They are atmosphere at [LTE](#) and atmosphere at [non-LTE](#).



(a) Flow chart to obtain field parameters for a [LTE](#) atmosphere



(b) Flow chart to obtain field parameters for a [non-LTE](#) atmosphere

Figure A.1: Procedure followed to obtain field parameters of the solar atmosphere numerically. Image credits Yadav [132]. Concept borrowed from del Toro Iniesta and Ruiz Cobo [23]

There are several inversion programs that are used to obtain the numerical solution (refer <http://www.iac.es/proyecto/inversion/index.php>). NICOLE (Socas-Navarro et al. [110]) is an inversion program that can be used to solve both the [LTE](#) and [non-LTE](#) atmosphere. The inputs to the code are -

- Stokes I, Q, U and V spectra in [x,y, λ] dimensions as input file.
- Model atmosphere having the same dimensions as input stokes spectra. This serves as the initial guess value for the system to obtain a numerical solution.

- Stray light fraction or instrument profile and fill factor of the spectra.
- Nodes or heights in the atmosphere at which the numerical solution has to be obtained.

The Nodes chosen for the inversion conducted in [Chapter 3](#) are as follows -

NODES	PHYSICAL PARAMETER
8	Temperature
6	Velocity
1	Magnetic field in along x
1	Magnetic field in along y
1	Magnetic field in along z

The inversion was performed for photosphere and lower chromosphere. The nodes for the magnetic field are placed at the height at which the spectral line core is formed for a non magnetic atmosphere. Note that the total height of the model atmosphere is taken to be 3000 Km.

BIBLIOGRAPHY

- [1] W P Abbett and G H Fisher. "A Coupled Model for the Emergence of Active Region Magnetic Flux into the Solar Corona." In: *The Astrophysical Journal* 582.1 (2003), p. 475. URL: <http://stacks.iop.org/0004-637X/582/i=1/a=475> (cit. on p. 137).
- [2] H. Alfvén and B. Lindblad. "Granulation, Magneto-Hydrodynamic Waves, and the Heating of the Solar Corona." In: *Monthly Notices of the Royal Astronomical Society* 107.2 (June 1947), pp. 211–219. DOI: [10.1093/mnras/107.2.211](https://doi.org/10.1093/mnras/107.2.211). URL: <http://adsabs.harvard.edu/abs/1947MNRAS.107..211A> <https://academicoup.com/mnras/article-lookup/doi/10.1093/mnras/107.2.211> (cit. on p. 137).
- [3] Iñigo Arregui, Ramón Oliver, and José Luis Ballester. "Prominence Oscillations." In: *Living Reviews in Solar Physics* 9.2 (2012). DOI: [10.12942/lrsp-2012-2](https://doi.org/10.12942/lrsp-2012-2). URL: <https://doi.org/10.12942/lrsp-2012-2> <http://link.springer.com/10.12942/lrsp-2012-2> (cit. on pp. 106, 125).
- [4] T.J. Atherton and D.J. Kerbyson. "Size invariant circle detection." In: *Image and Vision Computing* 17.11 (Sept. 1999), pp. 795–803. DOI: [10.1016/S0262-8856\(98\)00160-7](https://doi.org/10.1016/S0262-8856(98)00160-7). URL: <http://www.sciencedirect.com/science/article/pii/S0262885698001607> <http://linkinghub.elsevier.com/retrieve/pii/S0262885698001607> (cit. on p. 123).
- [5] K. S. Balasubramaniam and Alexei Pevtsov. "Ground-based synoptic instrumentation for solar observations." In: *Proceedings of SPIE - The International Society for Optical Engineering*. Ed. by Silvano Fineschi and Judy Fennelly. Vol. 8148. October 2011. Sept. 2011, p. 814809. DOI: [10.1117/12.892824](https://doi.org/10.1117/12.892824). URL: <http://proceedings.spiedigitallibrary.org/proceeding.aspx?doi=10.1117/12.892824> (cit. on pp. 89, 90).
- [6] A. A. van Ballegooijen and P. C. H. Martens. "Formation and eruption of solar prominences." In: *The Astrophysical Journal* 343 (Aug. 1989), p. 971. DOI: [10.1086/167766](https://doi.org/10.1086/167766). URL: <http://adsabs.harvard.edu/doi/10.1086/167766> (cit. on pp. 106, 125).
- [7] A. A. van Ballegooijen et al. "Heating of the Solar Chromosphere and Corona by ALFVÉN Wave Turbulance." In: *The Astrophysical Journal* 736.1 (July 2011), p. 3. DOI: [10.1088/0004-637X/736/1/3](https://doi.org/10.1088/0004-637X/736/1/3). arXiv: [1105.0402](https://arxiv.org/abs/1105.0402). URL: <http://stacks.iop.org/0004-637X/736/i=1/a=3?key=crossref.06c2b3609946a44553286bea16126541> (cit. on p. 137).

- [8] T. G. Baur et al. "THE DETERMINATION OF VECTOR MAGNETIC FIELDS FROM STOKES PROFILES." In: *Solar Physics* 70.2 (Apr. 1981), pp. 395–410. DOI: [10.1007/BF00151343](https://doi.org/10.1007/BF00151343). URL: <http://link.springer.com/10.1007/BF00151343> (cit. on p. 84).
- [9] Jacques M. Beckers. "Adaptive Optics for Astronomy: Principles, Performance, and Applications." In: *Annual Review of Astronomy and Astrophysics* 31.1 (Sept. 1993), pp. 13–62. DOI: [10.1146/annurev.aa.31.090193.000305](https://doi.org/10.1146/annurev.aa.31.090193.000305). URL: <http://adsabs.harvard.edu/abs/1993ARA&D.31..13B> (cit. on p. 123).
- [10] N. Bel and B. Leroy. "Analytical Study of Magnetoacoustic Gravity Waves." In: *Astronomy and Astrophysics* 55 (1977), p. 239. URL: <http://adsabs.harvard.edu/abs/1977A&A...55..239B> (cit. on p. 9).
- [11] Luis R. Bellot Rubio and Christian Beck. "Magnetic Flux Cancellation in the Moat of Sunspots: Results from Simultaneous Vector Spectropolarimetry in the Visible and the Infrared." In: *The Astrophysical Journal* 626.2 (June 2005), pp. L125–L128. DOI: [10.1086/431648](https://doi.org/10.1086/431648). URL: <http://stacks.iop.org/1538-4357/626/i=2/a=L125> (cit. on p. 44).
- [12] Arnold O Benz. "Flare Observations." In: *Living Reviews in Solar Physics* 5.1 (2008), pp. 1–64. DOI: [10.12942/lrsp-2008-1](https://doi.org/10.12942/lrsp-2008-1). URL: <http://adsabs.harvard.edu/abs/2008LRSP....5....1B> (cit. on p. 6).
- [13] H. A. Bethe. "Energy Production in Stars." In: *Physical Review* 55.5 (Mar. 1939), pp. 434–456. DOI: [10.1103/PhysRev.55.434](https://doi.org/10.1103/PhysRev.55.434). URL: <https://link.aps.org/doi/10.1103/PhysRev.55.434> (cit. on p. 2).
- [14] H. A. Bethe and C. L. Critchfield. "The Formation of Deuterons by Proton Combination." In: *Physical Review* 54.4 (Aug. 1938), pp. 248–254. DOI: [10.1103/PhysRev.54.248](https://doi.org/10.1103/PhysRev.54.248). URL: <https://link.aps.org/doi/10.1103/PhysRev.54.248> (cit. on p. 2).
- [15] J. H. M. J. Bruls, B. W. Lites, and G. A. Murphy. "Non-LTE formation heights of Stokes profiles of Fe I lines." In: *Solar Polarimetry* 11. 1991, pp. 444–444 (cit. on p. 93).
- [16] J. Trujillo Bueno, N. Shchukina, and A. Asensio Ramos. "A substantial amount of hidden magnetic energy in the quiet Sun." In: *Nature* 430.6997 (July 2004), pp. 326–329. DOI: [10.1038/nature02669](https://doi.org/10.1038/nature02669). arXiv: [0409004 \[astro-ph\]](https://arxiv.org/abs/0409004). URL: <http://www.nature.com/doifinder/10.1038/nature02669> (cit. on p. 9).

- [17] E. S. Carlin and A. Asensio Ramos. "CHROMOSPHERIC DIAGNOSIS WITH Ca II LINES: FORWARD MODELING IN FORWARD SCATTERING. I." In: *The Astrophysical Journal* 801.1 (Feb. 2015), p. 16. DOI: [10.1088/0004-637X/801/1/16](https://doi.org/10.1088/0004-637X/801/1/16). arXiv: [1412.5386](https://arxiv.org/abs/1412.5386). URL: <http://stacks.iop.org/0004-637X/801/i=1/a=16?key=crossref.8922f1cf3cff117759d495aef584bf22> (cit. on pp. 30, 93).
- [18] P. F. Chen. "Coronal Mass Ejections: Models and Their Observational Basis." In: *Living Reviews in Solar Physics* 8 (2011). DOI: [10.12942/lrsp-2011-1](https://doi.org/10.12942/lrsp-2011-1). arXiv: [arXiv:0905.3272v1](https://arxiv.org/abs/0905.3272v1). URL: <http://link.springer.com/10.12942/lrsp-2011-1> (cit. on p. 6).
- [19] G. Courtes et al. "A New Device for Faint Objects High Resolution Imagery and Bidimensional Spectrography." In: *Instrumentation for Ground-Based Optical Astronomy*. New York, NY: Springer New York, 1988, pp. 266–274. DOI: [10.1007/978-1-4612-3880-5_26](https://doi.org/10.1007/978-1-4612-3880-5_26). URL: http://link.springer.com/10.1007/978-1-4612-3880-5%7B%5C_%7D26 (cit. on p. 106).
- [20] J. de la Cruz Rodríguez et al. "Non-local thermodynamic equilibrium inversions from a 3D magnetohydrodynamic chromospheric model." In: *Astronomy & Astrophysics* 543.September (July 2012), A34. DOI: [10.1051/0004-6361/201218825](https://doi.org/10.1051/0004-6361/201218825). arXiv: [1205.3171](https://arxiv.org/abs/1205.3171). URL: <http://www.aanda.org/10.1051/0004-6361/201218825> (cit. on p. 93).
- [21] J. C. Del Toro Iniesta and B. Ruiz Cobo. "Stokes profiles inversion techniques." In: *Solar Physics* 164.1-2 (Mar. 1996), pp. 169–182. DOI: [10.1007/BF00146631](https://doi.org/10.1007/BF00146631). URL: <http://link.springer.com/10.1007/BF00146631> (cit. on p. 13).
- [22] Jose Carlos del Toro Iniesta. *Introduction to Spectropolarimetry*. Vol. 18. 6. Cambridge: Cambridge University Press, 2003, p. 252. DOI: [10.1017/CBO9780511536250](https://doi.org/10.1017/CBO9780511536250). arXiv: [arXiv:1011.1669v3](https://arxiv.org/abs/1011.1669v3). URL: <http://www.amazon.com/dp/0521036488%20http://ebooks.cambridge.org/ref/id/CB09780511536250> (cit. on pp. 4, 12, 19).
- [23] Jose Carlos del Toro Iniesta and Basilio Ruiz Cobo. "Inversion of the radiative transfer equation for polarized light." In: *Living Reviews in Solar Physics* 13.1 (Dec. 2016), p. 4. DOI: [10.1007/s41116-016-0005-2](https://doi.org/10.1007/s41116-016-0005-2). URL: <http://link.springer.com/10.1007/s41116-016-0005-2> (cit. on pp. 13, 159).
- [24] Stefan Denis et al. "Multi-Application Solar Telescope: assembly, integration, and testing." In: ed. by Larry M. Stepp, Roberto Gilmozzi, and Helen J. Hall. July 2010, p. 773335. DOI: [10.1117/12.858007](https://doi.org/10.1117/12.858007). URL: <http://proceedings.spiedigitallibrary.org/proceeding.aspx?doi=10.1117/12.858007> (cit. on pp. 24, 119).

- [25] Franz-Ludwig Deubner and Douglas Gough. "Helioseismology: Oscillations as a Diagnostic of the Solar Interior." In: *Annual Review of Astronomy and Astrophysics* 22.1 (Sept. 1984), pp. 593–619. DOI: [10.1146/annurev.aa.22.090184.003113](https://doi.org/10.1146/annurev.aa.22.090184.003113). URL: <http://www.annualreviews.org/doi/10.1146/annurev.aa.22.090184.003113> (cit. on p. 2).
- [26] T. L. Duvall et al. "Time-distance helioseismology." In: *Nature* 362.6419 (Apr. 1993), pp. 430–432. DOI: [10.1038/362430a0](https://doi.org/10.1038/362430a0). URL: <http://www.nature.com/doifinder/10.1038/362430a0> (cit. on pp. 2, 19, 106).
- [27] David F. Elmore et al. "<title>Advanced Stokes polarimeter: a new instrument for solar magnetic field research</title>." In: ed. by Dennis H. Goldstein and Russell A. Chipman. Dec. 1992, pp. 22–33. DOI: [10.1117/12.138795](https://doi.org/10.1117/12.138795). URL: <http://proceedings.spiedigitallibrary.org/proceeding.aspx?articleid=996882> (cit. on p. 51).
- [28] David J Erskine et al. "Measuring Precision Wideband Stellar Spectra using a Dispersed Interferometer." In: (2010), pp. 10–12 (cit. on p. 106).
- [29] David J Erskine et al. "Ten-fold spectral resolution boosting using TEDI at the Mt. Palomar NIR Triplespec spectrograph." In: ed. by Howard A. MacEwen and James B. Breckinridge. Sept. 2011, p. 81460M. DOI: [10.1117/12.892664](https://doi.org/10.1117/12.892664). URL: <http://proceedings.spiedigitallibrary.org/proceeding.aspx?doi=10.1117/12.892664> (cit. on p. 106).
- [30] J. Evershed. "Radial movement in sun-spots." In: *Monthly Notices of the Royal Astronomical Society* 69.5 (Mar. 1909), pp. 454–458. DOI: [10.1093/mnras/69.5.454](https://doi.org/10.1093/mnras/69.5.454). URL: <https://academic.oup.com/mnras/article-lookup/doi/10.1093/mnras/69.5.454> (cit. on pp. 24, 124).
- [31] David William Fletcher-Holmes and Andrew Robert Harvey. "Real-time imaging with a hyperspectral fovea." In: *Journal of Optics A: Pure and Applied Optics* 7.6 (June 2005), S298–S302. DOI: [10.1088/1464-4258/7/6/007](https://doi.org/10.1088/1464-4258/7/6/007). URL: <http://stacks.iop.org/1464-4258/7/i=6/a=007?key=crossref.0398431f7b92705694d0bcb679f258c2> (cit. on p. 106).
- [32] J. M. Fontenla et al. "Semiempirical Models of the Solar Atmosphere. I. The Quiet- and Active Sun Photosphere at Moderate Resolution." In: *The Astrophysical Journal* 639.1 (Mar. 2006), pp. 441–458. DOI: [10.1086/499345](https://doi.org/10.1086/499345). URL: <http://stacks.iop.org/0004-637X/639/i=1/a=441> (cit. on p. 93).
- [33] Anatoly Frenkel and Chinlon Lin. "Angle-tuned etalon filters for optical channel selection in high density wavelength division multiplexed systems." In: *Journal of Lightwave Technology*

- 7.4 (Apr. 1989), pp. 615–624. DOI: [10.1109/50.19087](https://doi.org/10.1109/50.19087). URL: <http://ieeexplore.ieee.org/document/19087/> (cit. on p. 128).
- [34] A.B. Galvin et al. “Solar Wind Composition: First Results from SOHO and Future Expectations.” In: *American Astronomical Society Meeting Abstracts #188*. Vol. 28. Bulletin of the American Astronomical Society. May 1996, p. 897. URL: <http://adsabs.harvard.edu/abs/1996AAS...188.4905G> (cit. on p. 1).
- [35] R. A. Garcia et al. “Tracking Solar Gravity Modes: The Dynamics of the Solar Core.” In: *Science* 316.5831 (June 2007), pp. 1591–1593. DOI: [10.1126/science.1140598](https://doi.org/10.1126/science.1140598). URL: <http://www.sciencemag.org/cgi/doi/10.1126/science.1140598> (cit. on p. 2).
- [36] G. Allen Gary. “PLASMA BETA ABOVE A SOLAR ACTIVE REGION: RETHINKING THE PARADIGM.” In: *Solar Physics* 203.1 (2001), pp. 71–86. DOI: [10.1023/A:1012722021820](https://doi.org/10.1023/A:1012722021820). URL: <http://link.springer.com/10.1023/A:1012722021820> (cit. on p. 8).
- [37] J Ge, D J Erskine, and M Rushford. “An externally dispersed interferometer for sensitive Doppler extrasolar planet searches.” In: *Publ. Astron. Soc. Pac. (USA)* 114.799 (2014), pp. 1016–28. DOI: [10.1086/342011](https://doi.org/10.1086/342011). URL: <http://dx.doi.org/10.1086/342011> (cit. on p. 106).
- [38] Martina Gerken and David A B Miller. “Multilayer thin-film coatings for optical communication systems.” In: *Optical Interference Coatings*. Washington, D.C.: OSA, 2004, ThD2. doi: [10.1364/OIC.2004.ThD2](https://doi.org/10.1364/OIC.2004.ThD2). URL: <http://www.opticsinfobase.org/abstract.cfm?URI=OIC-2004-ThD2%20https://www.osapublishing.org/abstract.cfm?uri=OIC-2004-ThD2> (cit. on p. 37).
- [39] R. G. Giovanelli. “Oscillations and waves in a sunspot.” In: *Solar Physics* 27.1 (Nov. 1972), pp. 71–79. DOI: [10.1007/BF00151771](https://doi.org/10.1007/BF00151771). URL: <http://link.springer.com/10.1007/BF00151771> (cit. on pp. 6, 19, 106).
- [40] S Gosain, K Sankarasubramanian, and P Venkatakrishnan. “A New Technique for Solar Imaging Spectro-polarimetry using Shack-Hartmann and Fabry-Perot.” In: *Second ATST-EAST Meeting: Magnetic Fields from the Photosphere to the Corona*. Vol. 463. ii. 2012, pp. 301–306. URL: <http://adsabs.harvard.edu/abs/2012ASPC..463..301G> (cit. on p. 116).
- [41] Boris Vilhelm Gudiksen and Ake Nordlund. “An Ab Initio Approach to the Solar Coronal Heating Problem.” In: *The Astrophysical Journal* 618.2 (Jan. 2005), pp. 1020–1030. DOI: [10.1086/426063](https://doi.org/10.1086/426063). arXiv: [0407266 \[astro-ph\]](https://arxiv.org/abs/0407266). URL: <http://adsabs.harvard.edu/abs/2005ApJ...618..1020G>

- harvard.edu/abs/2005ApJ...618.1020G%20http://stacks.iop.org/0004-637X/618/i=2/a=1020 (cit. on p. 137).
- [42] GMHJ Habets and J R W Heintze. "Empirical bolometric corrections for the main-sequence." In: *Astronomy and Astrophysics Supplement Series* 46 (1981), pp. 193–237 (cit. on p. 1).
- [43] Nathan Hagen and Michael W Kudenov. "Review of snapshot spectral imaging technologies." In: *Optical Engineering* 52.9 (Sept. 2013), p. 090901. DOI: [10.1117/1.OE.52.9.090901](https://doi.org/10.1117/1.OE.52.9.090901). URL: <http://opticalengineering.spiedigitallibrary.org/article.aspx?doi=10.1117/1.OE.52.9.090901> (cit. on pp. 104, 107, 132).
- [44] C. J. Henney, C. U. Keller, and J. W. Harvey. "SOLIS-VSM Solar Vector Magnetograms." In: *Astronomical Society of the Pacific Conference Series* (Dec. 2006). Ed. by R. Casini and B. W. Lites, p. 92. arXiv: [0612584 \[astro-ph\]](https://arxiv.org/abs/0612584). URL: <http://adsabs.harvard.edu/abs/2006ASPC..358...92H%20http://arxiv.org/abs/astro-ph/0612584> (cit. on pp. 89, 90).
- [45] John Jefferies, Bruce W. Lites, and A. Skumanich. "Transfer of line radiation in a magnetic field." In: *The Astrophysical Journal* 343 (Aug. 1989), p. 920. DOI: [10.1086/167762](https://doi.org/10.1086/167762). URL: <http://adsabs.harvard.edu/doi/10.1086/167762> (cit. on p. 12).
- [46] Donald E. Jennings and R. J. Boyle. "Multichannel Fabry-Perot spectrometer for infrared astronomy." In: *Applied Optics* 25.24 (Dec. 1986), p. 4520. DOI: [10.1364/AO.25.004520](https://doi.org/10.1364/AO.25.004520). URL: http://www.ncbi.nlm.nih.gov/entrez/query.fcgi?db=pubmed%7B%5C&%7Dcmd=Retrieve%7B%5C&%7Dopt=AbstractPlus%7B%5C&%7Dlist%7B%5C_%7Duids=related:XmS6X7I%7B%5C_%7D8NsJ%7B%5C%7D5Cnhttp://adsabs.harvard.edu/abs/1986ApOpt..25.4520J%20https://www.osapublishing.org/abstract.cfm?URI=ao-25-24-4520 (cit. on p. 120).
- [47] John R. Jensen and Kalmesh Lulla. "Introductory digital image processing: A remote sensing perspective." In: *Geocarto International* 2.1 (Mar. 1987), pp. 65–65. DOI: [10.1080/10106048709354084](https://doi.org/10.1080/10106048709354084). URL: <http://eeg.geoscienceworld.org/cgi/doi/10.2113/gsegeosci.13.1.89%20http://www.tandfonline.com/doi/abs/10.1080/10106048709354084> (cit. on p. 104).
- [48] Jianwen Luo and Elisa E Konofagou. "A fast normalized cross-correlation calculation method for motion estimation." In: *IEEE Transactions on Ultrasonics, Ferroelectrics and Frequency Control* 57.6 (June 2010), pp. 1347–1357. DOI: [10.1109/TUFFC.2010.1554](https://doi.org/10.1109/TUFFC.2010.1554). URL: <http://www.ncbi.nlm.nih.gov/pubmed/20529710%20http://www.ncbi.nlm.nih.gov/entrez/query.fcgi?artid=PMC4123965%20http://ieeexplore.ieee.org/document/5480177/> (cit. on p. 124).

- [49] P. G. Judge. "Spectral Lines for Polarization Measurements of the Coronal Magnetic Field. I. Theoretical Intensities." In: *The Astrophysical Journal* 500.2 (June 1998), pp. 1009–1022. DOI: [10.1086/305775](https://doi.org/10.1086/305775). URL: <http://stacks.iop.org/0004-637X/500/i=2/a=1009> (cit. on p. 139).
- [50] P. G. Judge et al. "Photon Mean Free Paths, Scattering, and Ever-Increasing Telescope Resolution." In: *Solar Physics* 290.3 (2015), pp. 979–996. DOI: [10.1007/s11207-014-0643-2](https://doi.org/10.1007/s11207-014-0643-2). arXiv: [1409.7866](https://arxiv.org/abs/1409.7866) (cit. on p. 14).
- [51] Philip G. Judge. "Observations of the Solar Chromosphere." In: *Solar MHD Theory and Observations: A High Spatial Resolution Perspective*. Ed. by J. Leibacher, R. F Stein, and H. Uitenbroek. Astronomical Society of the Pacific Conference Series, 2006, p. 259. URL: <http://adsabs.harvard.edu/abs/2006ASPC..354..259J> (cit. on p. 6).
- [52] Shojiro Kawakami. "Light propagation along periodic metal–dielectric layers." In: *Applied Optics* 22.16 (Aug. 1983), p. 2426. DOI: [10.1364/AO.22.002426](https://doi.org/10.1364/AO.22.002426). URL: <http://www.ncbi.nlm.nih.gov/pubmed/18196150%20https://www.osapublishing.org/abstract.cfm?URI=ao-22-16-2426> (cit. on p. 69).
- [53] C.U. Keller. "The SOLIS Vector-Spectromagnetograph (VSM)." In: *Advanced Solar Polarimetry – Theory, Observation, and Instrumentation*. Ed. by M. Sigwarth. 2001, p. 16. URL: <http://adsabs.harvard.edu/abs/2001ASPC..236...16K> (cit. on p. 90).
- [54] Christopher R Kitchin. *Astrophysical Techniques*. Taylor & Francis, 2013, p. 550 (cit. on p. 27).
- [55] James A. Klimchuk. "On Solving the Coronal Heating Problem." In: *Solar Physics* 234.1 (Mar. 2006), pp. 41–77. DOI: [10.1007/s11207-006-0055-z](https://doi.org/10.1007/s11207-006-0055-z). arXiv: [0511841 \[astro-ph\]](https://arxiv.org/abs/0511841). URL: <http://link.springer.com/10.1007/s11207-006-0055-z> (cit. on p. 137).
- [56] C L Korb, B M Gentry, and S X Li. "Edge technique Doppler lidar wind measurements with high vertical resolution." In: *Applied optics* 36.24 (1997), pp. 5976–5983. DOI: [10.1364/AO.36.005976](https://doi.org/10.1364/AO.36.005976) (cit. on p. 130).
- [57] Masahito Kubo, Toshifumi Shimizu, and Bruce W. Lites. "The Evolution of Vector Magnetic Fields in an Emerging Flux Region." In: *The Astrophysical Journal* 595.1 (Sept. 2003), pp. 465–482. DOI: [10.1086/377333](https://doi.org/10.1086/377333). URL: <http://stacks.iop.org/0004-637X/595/i=1/a=465> (cit. on p. 9).
- [58] Brajesh Kumar et al. "Site Characterization Using Solar H α Images." In: *Solar Physics* 241.2 (Apr. 2007), pp. 427–437. DOI: [10.1007/s11207-007-0387-3](https://doi.org/10.1007/s11207-007-0387-3). URL: <http://link.springer.com/10.1007/s11207-007-0387-3> (cit. on p. 24).

- [59] D Kuridze et al. "Spectroscopic Inversions of the Ca II 8542 Å Line in a C-class Solar Flare." In: *The Astrophysical Journal* 846.1 (2017), p. 9. DOI: [10.3847/1538-4357/aa83b9](https://doi.org/10.3847/1538-4357/aa83b9). URL: <http://iopscience.iop.org/article/10.3847/1538-4357/aa83b9/pdf> (cit. on p. 89).
- [60] Henny J. G. L. M. Lamers and Joseph P. Cassinelli. *Introduction to Stellar Winds*. May. Cambridge: Cambridge University Press, 1999, p. 24600. DOI: [10.1017/CBO9781139175012](https://doi.org/10.1017/CBO9781139175012). URL: <http://ebooks.cambridge.org/ref/id/CBO9781139175012> (cit. on p. 1).
- [61] Jorrit Leenaarts et al. "THE EFFECT OF ISOTOPIC SPLITTING ON THE BISECTOR AND INVERSIONS OF THE SOLAR Ca II 854.2 nm LINE." In: *The Astrophysical Journal* 784.1 (Mar. 2014), p. L17. DOI: [10.1088/2041-8205/784/1/L17](https://doi.org/10.1088/2041-8205/784/1/L17). arXiv: [arXiv:1401.5019v2](https://arxiv.org/abs/1401.5019v2). URL: <http://stacks.iop.org/2041-8205/784/i=1/a=L17?key=crossref.27b9d691c8846ad765baf6b7c190faea> (cit. on pp. 20, 93).
- [62] J. Leenaarts et al. "THREE-DIMENSIONAL NON-LTE RADIATIVE TRANSFER COMPUTATION OF THE CA 8542 INFRARED LINE FROM A RADIATION-MHD SIMULATION." In: *The Astrophysical Journal* 694.2 (Apr. 2009), pp. L128–L131. DOI: [10.1088/0004-637X/694/2/L128](https://doi.org/10.1088/0004-637X/694/2/L128). arXiv: [arXiv:0903.0791v1](https://arxiv.org/abs/0903.0791v1). URL: <http://stacks.iop.org/1538-4357/694/i=2/a=L128?key=crossref.fbd3d1445077a46c9ac28dcfc4449468> (cit. on p. 93).
- [63] Hua-bai Li. *The Tai Chi in Star Formation*. Vol. 44. 2053-2571 8. Morgan & Claypool Publishers, Nov. 2017. DOI: [10.1088/978-1-6817-4293-9](https://doi.org/10.1088/978-1-6817-4293-9). arXiv: [1011.1669](https://arxiv.org/abs/1011.1669). URL: <http://arxiv.org/abs/1011.1669%20http://dx.doi.org/10.1088/978-1-6817-4293-9> (cit. on p. 11).
- [64] H. Lin, J. R. Kuhn, and R. Coulter. "Coronal Magnetic Field Measurements." In: *The Astrophysical Journal* 613.2 (2004), pp. L177–L180. DOI: [10.1086/425217](https://doi.org/10.1086/425217). URL: <http://stacks.iop.org/1538-4357/613/i=2/a=L177> (cit. on pp. 100, 139).
- [65] Haosheng Lin. "SPIES: the spectropolarimetric imager for the energetic sun." In: ed. by Ian S. McLean, Suzanne K. Ramsay, and Hideki Takami. Vol. 8446. Sept. 2012, p. 84461D. DOI: [10.1117/12.926830](https://doi.org/10.1117/12.926830). URL: <http://proceedings.spiedigitallibrary.org/proceeding.aspx?doi=10.1117/12.926830> (cit. on pp. 19, 44, 87, 106).
- [66] Haosheng Lin, Matthew J. Penn, and Steven Tomczyk. "A New Precise Measurement of the Coronal Magnetic Field Strength." In: *The Astrophysical Journal* 541.2 (Oct. 2000), pp. L83–L86. DOI: [10.1086/312900](https://doi.org/10.1086/312900). URL: <http://stacks.iop.org/1538-4357/541/i=2/a=L83> (cit. on pp. 100, 139).

- [67] Haosheng Lin and Thomas Rimmele. "The Granular Magnetic Fields of the Quiet Sun." In: *The Astrophysical Journal* 514.1 (Mar. 1999), pp. 448–455. doi: [10.1086/306925](https://doi.org/10.1086/306925). arXiv: [1105.0387](https://arxiv.org/abs/1105.0387). URL: <http://stacks.iop.org/0004-637X/514/i=1/a=448> (cit. on pp. 44, 45).
- [68] HaoSheng Lin and Alex Versteegh. "VisIRIS: a visible/IR imaging spectropolarimeter based on a birefringent fiber-optic image slicer." In: ed. by Ian S. McLean and Masanori Iye. Vol. 6269. September 2005. June 2006, 62690K. doi: [10.1117/12.670852](https://doi.org/10.1117/12.670852). URL: <http://proceedings.spiedigitallibrary.org/proceeding.aspx?doi=10.1117/12.670852> (cit. on pp. 25, 87, 106).
- [69] Bruce W Lites. "Rotating waveplates as polarization modulators for Stokes polarimetry of the sun: evaluation of seeing-induced crosstalk errors." In: *Applied Optics* 26.18 (Sept. 1987), p. 3838. doi: [10.1364/AO.26.003838](https://doi.org/10.1364/AO.26.003838). URL: <https://osapublishing.org/abstract.cfm?URI=ao-26-18-3838> <http://www.ncbi.nlm.nih.gov/pubmed/20490150> (cit. on pp. 51, 143, 148, 150).
- [70] S. K. Mathew et al. "Three dimensional structure of a regular sunspot from the inversion of IR Stokes profiles." In: *Astronomy & Astrophysics* 410.2 (Nov. 2003), pp. 695–710. doi: [10.1051/0004-6361:20031282](https://doi.org/10.1051/0004-6361:20031282). URL: <http://www.aanda.org/10.1051/0004-6361:20031282> (cit. on pp. 89, 100).
- [71] Shibu K. Mathew et al. "First Observations from the Multi-Application Solar Telescope (MAST) Narrow-Band Imager." In: *Solar Physics* 292.8 (Aug. 2017), p. 106. doi: [10.1007/s11207-017-1127-y](https://doi.org/10.1007/s11207-017-1127-y). URL: <http://link.springer.com/10.1007/s11207-017-1127-y> (cit. on pp. 24, 119).
- [72] K. Nagaraju et al. "An efficient modulation scheme for dual beam polarimetry." In: *arXiv preprint arXiv:0710.1694* ooooo (Oct. 2007), pp. 307–318. arXiv: [0710.1694](https://arxiv.org/abs/0710.1694). URL: <http://arxiv.org/abs/0710.1694> <http://arxiv.org/pdf/0710.1694.pdf> (cit. on p. 143).
- [73] V. M. Nakariakov and L. Ofman. "Determination of the coronal magnetic field by coronal loop oscillations." In: *Astronomy & Astrophysics* 372.3 (June 2001), pp. L53–L56. doi: [10.1051/0004-6361:20010607](https://doi.org/10.1051/0004-6361:20010607). arXiv: [arXiv:0901.0974v2](https://arxiv.org/abs/0901.0974v2). URL: <http://www.aanda.org/10.1051/0004-6361:20010607> (cit. on p. 138).
- [74] Åke Nordlund, Robert F. Stein, and Martin Asplund. "Solar Surface Convection." In: *Living Reviews in Solar Physics* 6 (2009). doi: [10.12942/lrsp-2009-2](https://doi.org/10.12942/lrsp-2009-2). URL: <http://link.springer.com/10.12942/lrsp-2009-2> (cit. on pp. 24, 44).

- [75] O. Ozoliņš, V. Bobrovs, and G. Ivanovs. "DWDM Transmission Based on the Thin-Film Filter Technology." In: *Latvian Journal of Physics and Technical Sciences* 48.3 (Jan. 2011), pp. 55–65. DOI: [10.2478/v10047-011-0021-x](https://doi.org/10.2478/v10047-011-0021-x). URL: <http://www.degruyter.com/view/j/lpts.2011.48.issue-3/v10047-011-0021-x/v10047-011-0021-x.xml> (cit. on p. 37).
- [76] Susanna Parenti. "Solar Prominences: Observations." In: *Living Reviews in Solar Physics* 11.1 (2014), pp. 1–88. DOI: [10.12942/lrsp-2014-1](https://doi.org/10.12942/lrsp-2014-1). URL: <http://link.springer.com/10.12942/lrsp-2014-1> (cit. on pp. 106, 125).
- [77] Eugene N Parker. "Hydromagnetic Dynamo Models." In: *Astrophysical Journal* 122 (1955), p. 293. URL: <http://adsabs.harvard.edu/full/1955ApJ...122..293P> (cit. on pp. 6, 9).
- [78] Matthew J. Penn. "Infrared Solar Physics." In: *Living Reviews in Solar Physics* 11.1 (2014), p. 12942. DOI: [10.12942/lrsp-2014-2](https://doi.org/10.12942/lrsp-2014-2). URL: <http://link.springer.com/10.12942/lrsp-2014-2> (cit. on p. 140).
- [79] a. Perot and Charles Fabry. "On the Application of Interference Phenomena to the Solution of Various Problems of Spectroscopy and Metrology." In: *The Astrophysical Journal* 9 (Feb. 1899), p. 87. DOI: [10.1086/140557](https://doi.org/10.1086/140557). URL: <http://adsabs.harvard.edu/doi/10.1086/140557> (cit. on p. 108).
- [80] B De Pontieu et al. "High-Resolution Observations and Modeling of Dynamic Fibrils." In: *The Astrophysical Journal* 655.1 (2007), p. 624. URL: <http://stacks.iop.org/0004-637X/655/i=1/a=624> (cit. on pp. 25, 106).
- [81] Vaughan Pratt. "Direct least-squares fitting of algebraic surfaces." In: *Proceedings of the 14th annual conference on Computer graphics and interactive techniques - SIGGRAPH '87*. Vol. 21. 4. New York, New York, USA: ACM Press, 1987, pp. 145–152. DOI: [10.1145/37401.37420](https://doi.org/10.1145/37401.37420). URL: <http://portal.acm.org/citation.cfm?doid=37401.37420> (cit. on p. 123).
- [82] D.N. Rachkovsky. "Magnetic rotation effects in spectral lines." In: *Izvestiya Ordona Trudovogo Krasnogo Znameni Krymskoj Astrofizicheskoy Observatorii* 28 (1962), pp. 259–270. URL: <http://adsabs.harvard.edu/abs/1962IzKry..28..259R> (cit. on p. 12).
- [83] D.N. Rachkovsky. "The reduction for anomalous dispersion in the theory of absorption line formation in a magnetic field." In: *Izvestiya Ordona Trudovogo Krasnogo Znameni Krymskoj Astrofizicheskoy Observatorii* 37 (1967), pp. 56–61. URL: <http://adsabs.harvard.edu/abs/1967IzKry..37..56R> (cit. on p. 13).

- [84] B. Raghavendra Prasad et al. "Visible Emission Line Coronagraph on Aditya-L1." In: *Current Science* 113.4 (2017), pp. 613–615. DOI: [10.18520/cs/v113/i04/613-615](https://doi.org/10.18520/cs/v113/i04/613-615) (cit. on p. 140).
- [85] Pete Riley et al. "A Comparison between Global Solar Magnetohydrodynamic and Potential Field Source Surface Model Results." In: *The Astrophysical Journal* 653.2 (Dec. 2006), pp. 1510–1516. DOI: [10.1086/508565](https://doi.org/10.1086/508565). URL: [http://adsabs.harvard.edu/abstract%7B%5C%7Dservice.html%20http://stacks.iop.org/0004-637X/653/i=2/a=1510](http://adsabs.harvard.edu.ezp-prod1.hul.harvard.edu/abstract%7B%5C%7Dservice.html%20http://stacks.iop.org/0004-637X/653/i=2/a=1510) (cit. on p. 97).
- [86] T.R. Rimmele. "Recent advances in solar adaptive optics." In: *SPIE Conference Series* 5490 (2004), pp. 34–46. DOI: [10.1117/12.551764](https://doi.org/10.1117/12.551764) (cit. on p. 123).
- [87] L R Bellot Rubio. "Stokes Inversion Techniques: Recent Advances and New Challenges." In: *Solar Polarization Workshop 4* (2006) 358.1996 (Jan. 2006), p. 12. arXiv: [0601483 \[astro-ph\]](https://arxiv.org/abs/astro-ph/0601483). URL: <http://arxiv.org/abs/astro-ph/0601483> (cit. on p. 13).
- [88] I Rüedi et al. "Infrared lines as probes of solar magnetic features. X. HeI 10830Å as a diagnostic of chromospheric magnetic fields." In: *Astronomy and Astrophysics* 293.October (1995), pp. 252–262 (cit. on p. 30).
- [89] B Ruiz Cobo. "Inversión de la ecuación de transporte radiativo." PhD thesis. The University of La Laguna, 1993. URL: <https://dialnet.unirioja.es/servlet/tesis?codigo=11934> (cit. on p. 4).
- [90] Robert J Rutten. "The NLTE Formation of Iron Lines in the Solar Photosphere." In: 1988, pp. 185–210. DOI: [10.1007/978-94-009-4023-9_23](https://doi.org/10.1007/978-94-009-4023-9_23). URL: <http://link.springer.com/10.1007/978-94-009-4023-9%7B%5C%7D23> (cit. on p. 30).
- [91] Sean G Ryan and Andrew J Norton. *Stellar Evolution and Nucleosynthesis*. January. 2010. URL: <http://www.cambridge.org/gb/academic/subjects/physics/astrophysics/stellar-evolution-and-nucleosynthesis?format=HB%7B%5C%7D&isbn=9780521196093%7B%5C%7DRiGLLZfqiyyCcQWqP.97> (cit. on p. 2).
- [92] K. Sankarasubramanian and P. Venkatakrishnan. "Ellipsometry of coelostat coatings using a Babinet compensator: Simulation of the experimental accuracy." In: *Solar Physics* 167.1-2 (Aug. 1996), pp. 1–7. DOI: [10.1007/BF00146324](https://doi.org/10.1007/BF00146324). URL: <http://link.springer.com/10.1007/BF00146324> (cit. on p. 74).
- [93] K. Sankarasubramanian et al. "The Diffraction Limited Spectro-Polarimeter: a new instrument for high-resolution solar polarimetry." In: *Proceedings of SPIE*. Ed. by Silvano Fineschi and Mark A. Gummin. Vol. 5171. Feb. 2004, p. 207. DOI: [10.1117/12.508790](https://doi.org/10.1117/12.508790). URL: <http://spiedigitallibrary.org/proceeding>.

- aspx ? doi = 10 . 1117 / 12 . 508790 % 20http : / / proceedings . spiedigitallibrary . org / proceeding . aspx ? doi = 10 . 1117 / 12 . 508790 (cit. on p. 25).
- [94] K. Sankarasubramanian et al. "A novel solar spectroscopic concept using shack-Hartmann and Fabry-Perot." In: *Journal of Optics (India)* 41.2 (2012), pp. 114–116. DOI: [10.1007/s12596-012-0074-0](https://doi.org/10.1007/s12596-012-0074-0) (cit. on p. 116).
- [95] Thomas Schad et al. "Polarization properties of a birefringent fiber optic image slicer for diffraction-limited dual-beam spectropolarimetry." In: ed. by Suzanne K. Ramsay, Ian S. McLean, and Hideki Takami. July 2014, 91476E. DOI: [10.1117/12.2057125](https://doi.org/10.1117/12.2057125). URL: <http://proceedings.spiedigitallibrary.org/proceeding.aspx?doi=10.1117/12.2057125> (cit. on pp. 87, 106).
- [96] Kenneth H Schatten, John M Wilcox, and Norman F Ness. "A model of interplanetary and coronal magnetic fields." In: *Solar Physics* 6.3 (Mar. 1969), pp. 442–455. DOI: [10.1007/BF00146478](https://doi.org/10.1007/BF00146478). URL: <http://link.springer.com/10.1007/BF00146478> (cit. on p. 97).
- [97] Carolus J. Schrijver and Alan M. Title. "The Magnetic Connection between the Solar Photosphere and the Corona." In: *The Astrophysical Journal* 597.2 (Nov. 2003), pp. L165–L168. DOI: [10.1086/379870](https://doi.org/10.1086/379870). URL: [http://iopscience.iop.org/1538-4357/597/i=2/a=L165](http://iopscience.iop.org/1538-4357/597/2/L165%20http://stacks.iop.org/1538-4357/597/i=2/a=L165) (cit. on p. 137).
- [98] H. Schunker and P. S. Cally. "Magnetic field inclination and atmospheric oscillations above solar active regions." In: *Monthly Notices of the Royal Astronomical Society* 372.2 (Oct. 2006), pp. 551–564. DOI: [10.1111/j.1365-2966.2006.10855.x](https://doi.org/10.1111/j.1365-2966.2006.10855.x). URL: <https://academic.oup.com/mnras/article-lookup/doi/10.1111/j.1365-2966.2006.10855.x> (cit. on p. 9).
- [99] S Seetha and S Megala. "Aditya-L1 mission." In: *Current Science* 113.4 (2017), pp. 610–612. DOI: [10.18520/cs/v113/i04/610-612612](https://doi.org/10.18520/cs/v113/i04/610-612612) (cit. on p. 140).
- [100] M Semel. "Spectropolarimetry and polarization-dependent fringes." In: *Astronomy & Astrophysics* 401.1 (Apr. 2003), pp. 1–14. DOI: [10.1051/0004-6361:20021606](https://doi.org/10.1051/0004-6361:20021606). URL: <http://www.aanda.org/10.1051/0004-6361:20021606> (cit. on p. 154).
- [101] M. Semel, J.-F. Donati, and D. E. Rees. "Zeeman-Doppler imaging of active stars. 3: Instrumental and technical considerations." In: *Astronomy and Astrophysics* 278 (1993), pp. 231–237. URL: <http://adsabs.harvard.edu/abs/1993A&7B%5C%7D26A..278..231S> (cit. on p. 48).

- [102] A K Sen and M Kakati. "Instrumental polarization caused by telescope optics during wide field imaging." In: *Astronomy and Astrophysics Supplement Series* 126.1 (Nov. 1997), pp. 113–119. DOI: [10.1051/aas:1997254](https://doi.org/10.1051/aas:1997254). URL: <http://aas.aanda.org/10.1051/aas:1997254> (cit. on p. 74).
- [103] A.M. Shahidi et al. "Regional variation in human retinal vessel oxygen saturation." In: *Experimental Eye Research* 113 (Aug. 2013), pp. 143–147. DOI: [10.1016/j.exer.2013.06.001](https://doi.org/10.1016/j.exer.2013.06.001). URL: <http://linkinghub.elsevier.com/retrieve/pii/S0014483513001401> (cit. on p. 130).
- [104] Kazunari Shibata and Tetsuya Magara. "Solar Flares: Magnetohydrodynamic Processes." In: *Living Reviews in Solar Physics* 8 (2011). DOI: [10.12942/lrsp-2011-6](https://doi.org/10.12942/lrsp-2011-6). URL: <http://link.springer.com/10.12942/lrsp-2011-6> (cit. on p. 6).
- [105] A. Skumanich, C. Smythe, and E. N. Frazier. "On the statistical description of inhomogeneities in the quiet solar atmosphere. I - Linear regression analysis and absolute calibration of multi-channel observations of the Ca/+ emission network." In: *The Astrophysical Journal* 200.1 (Sept. 1975), p. 747. DOI: [10.1086/153846](https://doi.org/10.1086/153846). URL: <http://adsabs.harvard.edu/abs/1975ApJ...200..747S> %20<http://adsabs.harvard.edu/doi/10.1086/153846> (cit. on p. 9).
- [106] H. Socas-Navarro. "The Three-dimensional Structure of a Sunspot Magnetic Field." In: *The Astrophysical Journal* 631.2 (Oct. 2005), pp. L167–L170. DOI: [10.1086/497334](https://doi.org/10.1086/497334). URL: <http://stacks.iop.org/1538-4357/631/i=2/a=L167> (cit. on p. 92).
- [107] H. Socas-Navarro and J. Sanchez Almeida. "Magnetic Properties of Photospheric Regions with Very Low Magnetic Flux." In: *The Astrophysical Journal* 565.2 (Feb. 2002), pp. 1323–1334. DOI: [10.1086/324688](https://doi.org/10.1086/324688). URL: <http://stacks.iop.org/0004-637X/565/i=2/a=1323> (cit. on p. 44).
- [108] Hector Socas-Navarro et al. "Spinor: Visible and Infrared Spectro-Polarimetry at the National Solar Observatory." In: *Solar Physics* 235.1-2 (May 2006), pp. 55–73. DOI: [10.1007/s11207-006-0020-x](https://doi.org/10.1007/s11207-006-0020-x). URL: <http://link.springer.com/10.1007/s11207-006-0020-x> (cit. on pp. 19, 20).
- [109] H. Socas-Navarro et al. "Characterization of telescope polarization properties across the visible and near-infrared spectrum." In: *Astronomy & Astrophysics* 531 (July 2011), A2. DOI: [10.1051/0004-6361/201015804](https://doi.org/10.1051/0004-6361/201015804). arXiv: [1009.2866](https://arxiv.org/abs/1009.2866). URL: <http://www.aanda.org/10.1051/0004-6361/201015804> (cit. on p. 69).

- [110] H. Socas-Navarro et al. "An open-source , massively parallel code for non-LTE synthesis and inversion of spectral lines and Zeeman-induced Stokes profiles." In: *Astronomy & Astrophysics* 7-577 (2015), pp. 1–10. DOI: [10.1051/0004-6361/201424860](https://doi.org/10.1051/0004-6361/201424860). arXiv: [1408.6101 \[astro-ph.SR\]](https://arxiv.org/abs/1408.6101) (cit. on pp. 84, 89, 92, 159).
- [111] Rengaswamy Sridharan and A. R. Bayanna. "Low-order adaptive optics for the meter aperture solar telescope of Udaipur Solar Observatory." In: *Society of Photo-Optical Instrumentation Engineers (SPIE) Conference Series*. Ed. by Silvano Fineschi and Mark A. Gummin. Vol. 5171. March 2016. Feb. 2004, p. 219. DOI: [10.1117/12.509230](https://doi.org/10.1117/12.509230). URL: <http://proceedings.spiedigitallibrary.org/proceeding.aspx?doi=10.1117/12.509230> (cit. on p. 24).
- [112] T. D. Staley. "Lucky imaging: beyond binary stars." In: (Apr. 2014). arXiv: [1404.5907](https://arxiv.org/abs/1404.5907). URL: <http://arxiv.org/abs/1404.5907> (cit. on p. 97).
- [113] Mark A. Stephen, Michael A. Krainak, and Molly E. Fahey. "Lateral-transfer recirculating etalon spectrometer." In: *Optics Express* 23.23 (2015), p. 30020. DOI: [10.1364/OE.23.030020](https://doi.org/10.1364/OE.23.030020). URL: <https://www.osapublishing.org/abstract.cfm?URI=oe-23-23-30020> (cit. on p. 120).
- [114] Michael Stix. *The Sun*. Astronomy and Astrophysics Library. Berlin, Heidelberg: Springer Berlin Heidelberg, 2002. DOI: [10.1007/978-3-642-56042-2](https://doi.org/10.1007/978-3-642-56042-2). URL: <http://link.springer.com/10.1007/978-3-642-56042-2> (cit. on p. 6).
- [115] Orozco David SuÁrez et al. "Strategy for the Inversion of Hinode Spectropolarimetric Measurements in the Quiet +n." In: *Publications of the Astronomical Society of Japan* 59.sp3 (Nov. 2007), S837–S844. DOI: [10.1093/pasj/59.sp3.S837](https://doi.org/10.1093/pasj/59.sp3.S837). arXiv: [0709.2033](https://arxiv.org/abs/0709.2033). URL: [http://uk.arxiv.org/abs/0709.2033v1%20https://academic.oup.com/pasj/article-lookup/doi/10.1093/pasj/59.sp3.S837](https://academic.oup.com/pasj/article-lookup/doi/10.1093/pasj/59.sp3.S837) (cit. on p. 44).
- [116] P Sütterlin. "The size of penumbral fine structure." In: *Astronomy & Astrophysics* 374.3 (Aug. 2001), pp. L21–L24. DOI: [10.1051/0004-6361:20010872](https://doi.org/10.1051/0004-6361:20010872). URL: <http://www.aanda.org/10.1051/0004-6361:20010872> (cit. on pp. 24, 106).
- [117] Tilaye Tadesse et al. "A Comparison Between Nonlinear Force-Free Field and Potential Field Models Using Full-Disk SDO/HMI Magnetogram." In: *Solar Physics* 289.3 (Mar. 2014), pp. 831–845. DOI: [10.1007/s11207-013-0364-y](https://doi.org/10.1007/s11207-013-0364-y). arXiv: [arXiv:1212.5639v2](https://arxiv.org/abs/1212.5639v2). URL: <http://link.springer.com/10.1007/s11207-013-0364-y> (cit. on p. 97).
- [118] G. Taubin. "Estimation of planar curves, surfaces, and non-planar space curves defined by implicit equations with applications to edge and range image segmentation." In: *IEEE*

- Transactions on Pattern Analysis and Machine Intelligence* 13.11 (1991), pp. 1115–1138. DOI: [10.1109/34.103273](https://doi.org/10.1109/34.103273). URL: <http://ieeexplore.ieee.org/document/103273/> (cit. on p. 123).
- [119] S. Tomczyk et al. “An instrument to measure coronal emission line polarization.” In: *Solar Physics* 247.2 (2008), pp. 411–428. DOI: [10.1007/s11207-007-9103-6](https://doi.org/10.1007/s11207-007-9103-6) (cit. on p. 139).
 - [120] Wasaburo Unno. “Line Formation of a Normal Zeeman Triplet.” In: *Publications of the Astronomical Society of Japan* 8 (1956), pp. 108–125. URL: <http://adsabs.harvard.edu/abs/1956PASJ.....8..108U> (cit. on pp. 12, 13).
 - [121] Tom Van Doorsselaere et al. “Coronal magnetic field measurement using loop oscillations observed by Hinode/EIS.” In: *Astronomy & Astrophysics* 487.2 (Aug. 2008), pp. L17–L20. DOI: [10.1051/0004-6361:200810186](https://doi.org/10.1051/0004-6361:200810186). arXiv: [arXiv:0708.1752](https://arxiv.org/abs/0708.1752). URL: <http://www.aanda.org/10.1051/0004-6361:200810186> (cit. on p. 138).
 - [122] A. H. Vaughan et al. “Stellar rotation in lower main-sequence stars measured from time variations in H and K emission-line fluxes. I - Initial results.” In: *The Astrophysical Journal* 250 (Nov. 1981), p. 276. DOI: [10.1086/159372](https://doi.org/10.1086/159372). URL: <http://adsabs.harvard.edu/doi/10.1086/159372> (cit. on p. 9).
 - [123] P Venkatakrishnan et al. “The Multi Application Solar Telescope.” In: *Current Science* 113.4 (2017), pp. 686–690. DOI: [10.18520/cs/v113/i04/686-690](https://doi.org/10.18520/cs/v113/i04/686-690) (cit. on p. 24).
 - [124] Shuo Wang et al. “RESPONSE OF THE PHOTOSPHERIC MAGNETIC FIELD TO THE X_{2.2} FLARE ON 2011 FEBRUARY 15.” In: *The Astrophysical Journal* 745.2 (Feb. 2012), p. L17. DOI: [10.1088/2041-8205/745/2/L17](https://doi.org/10.1088/2041-8205/745/2/L17). arXiv: [1112.3948](https://arxiv.org/abs/1112.3948). URL: <http://arxiv.org/abs/1112.3948%7B%5C%7D0Ahttp://dx.doi.org/10.1088/2041-8205/745/2/L17%20http://stacks.iop.org/2041-8205/745/i=2/a=L17?key=crossref.30c4425a2fad28fbecebb53e73a3fe32> (cit. on pp. 19, 20).
 - [125] David F. Webb and Timothy A. Howard. “Coronal Mass Ejections: Observations.” In: *Living Reviews in Solar Physics* 9 (2012). DOI: [10.12942/lrsp-2012-3](https://doi.org/10.12942/lrsp-2012-3). URL: <http://link.springer.com/10.12942/lrsp-2012-3> (cit. on p. 6).
 - [126] S. Wedemeyer-Böhm, A. Lagg, and Å Nordlund. “Coupling from the Photosphere to the Chromosphere and the Corona.” In: *Space Science Reviews* 144.1-4 (Apr. 2009), pp. 317–350. DOI: [10.1007/s11214-008-9447-8](https://doi.org/10.1007/s11214-008-9447-8). arXiv: [0809.0987](https://arxiv.org/abs/0809.0987). URL: <http://link.springer.com/10.1007/s11214-008-9447-8> (cit. on p. 137).

- [127] L Weitzel et al. “3D: The next generation near-infrared imaging spectrometer.” In: *Astronomy and Astrophysics Supplement Series* 119.3 (Nov. 1996), pp. 531–546. DOI: [10.1051/aas:1996266](https://doi.org/10.1051/aas:1996266). URL: <http://aas.aanda.org/10.1051/aas:1996266> (cit. on p. 106).
- [128] D C Wells, E W Greisen, and R H Harten. “FITS: A Flexible Image Transport System, 1981.” In: *Astronomy & Astrophysics Supplement Series* 44 (), p. 363 (cit. on pp. 79, 120).
- [129] T. Wiegmann et al. “Testing non-linear force-free coronal magnetic field extrapolations with the Titov-Démoulin equilibrium.” In: *Astronomy & Astrophysics* 453.2 (July 2006), pp. 737–741. DOI: [10.1051/0004-6361:20054751](https://doi.org/10.1051/0004-6361:20054751). URL: <http://www.scopus.com/inward/record.url?eid=2-s2.0-33745753921%7B%5C&%7DpartnerID=40%7B%5C&%7Dmd5=980c5b2098a57631c06b3b1a067ed914%20> <http://www.aanda.org/10.1051/0004-6361:20054751> (cit. on p. 138).
- [130] O. C. Wilson. “Chromospheric variations in main-sequence stars.” In: *The Astrophysical Journal* 226 (Dec. 1978), p. 379. DOI: [10.1086/156618](https://doi.org/10.1086/156618). URL: <http://adsabs.harvard.edu/doi/10.1086/156618> (cit. on p. 9).
- [131] Olin C. Wilson, Arthur H. Vaughan, and Dimitri Mihalas. “The Activity Cycles of Stars.” In: *Scientific American* 244.2 (Feb. 1981), pp. 104–119. DOI: [10.1038/scientificamerican0281-104](https://doi.org/10.1038/scientificamerican0281-104). URL: <http://www.nature.com/doifinder/10.1038/scientificamerican0281-104> (cit. on p. 9).
- [132] Rahul Yadav. “Spectropolarimetric Studies of Sunspot and its Fine-structure.” PhD thesis. MLSU, 2017, p. 210 (cit. on p. 159).
- [133] Yafei Ren et al. “Investigation on the Wavelength Division Multiplexing optical thin-film filter.” In: *The 19th Annual Wireless and Optical Communications Conference (WOCC 2010)*. IEEE, May 2010, pp. 1–4. DOI: [10.1109/WOCC.2010.5510621](https://doi.org/10.1109/WOCC.2010.5510621). URL: <http://ieeexplore.ieee.org/document/5510621/> (cit. on p. 37).
- [134] HK Yuen et al. “Comparative study of Hough Transform methods for circle finding.” In: *Image and Vision Computing* 8.1 (Feb. 1990), pp. 71–77. DOI: [10.1016/0262-8856\(90\)90059-E](https://doi.org/10.1016/0262-8856(90)90059-E). URL: <http://linkinghub.elsevier.com/retrieve/pii/026288569090059E> (cit. on p. 123).
- [135] Harold Zirin and Alan Stein. “Observations of Running Penumbra Waves.” In: *The Astrophysical Journal* 178 (Dec. 1972), p. L85. DOI: [10.1086/181089](https://doi.org/10.1086/181089). URL: <http://adsabs.harvard.edu/doi/10.1086/181089> (cit. on p. 19).

- [136] Cornelis Zwaan. "On the appearance of magnetic flux in the solar photosphere." In: *Solar Physics* 60.2 (Dec. 1978), pp. 213–240. DOI: [10.1007/BF00156523](https://doi.org/10.1007/BF00156523). arXiv: [arXiv:1011.1669v3](https://arxiv.org/abs/1011.1669v3). URL: <http://link.springer.com/10.1007/BF00156523> (cit. on pp. 6, 9).